DGK Ausschuss Geodäsie (DGK)
der Bayerischen Akademie der Wissenschaften

Reihe C | Dissertationen | Heft Nr. 947

Benjamin Tennstedt

Concept and Evaluation of a Hybridization Scheme for Atom Interferometers and Inertial Measurement Units

München 2025

Verlag der Bayerischen Akademie der Wissenschaften, München

ISSN 0065-5325 ISBN 978-3-7696-5359-5

DGK Ausschuss Geodäsie (DGK)
der Bayerischen Akademie der Wissenschaften

Reihe C Dissertationen Heft Nr. 947

Concept and Evaluation of a Hybridization Scheme for Atom Interferometers and Inertial Measurement Units

Von der Fakultät für Bauingenieurwesen und Geodäsie
der Gottfried Wilhelm Leibniz Universität Hannover
zur Erlangung des akademischen Grades
Doktor-Ingenieur (Dr.-Ing.)
genehmigte
Dissertation

von

M.Sc. Benjamin Tennstedt

München 2025

Verlag der Bayerischen Akademie der Wissenschaften, München

ISSN 0065-5325 ISBN 978-3-7696-5359-5

Adresse des Ausschusses Geodäsie (DGK)
der Bayerischen Akademie der Wissenschaften:

Ausschuss Geodäsie (DGK) der Bayerischen Akademie der Wissenschaften
Alfons-Goppel-Straße 11 ● D – 80 539 München
Telefon +49 – 89 – 23 031 1113 ● Telefax +49 – 89 – 23 031 - 1283 / - 1100
e-mail post@dgk.badw.de ● http://www.dgk.badw.de

Prüfungskommission: Vorsitzender: Prof. Dr.-Ing. habil. Jürgen Müller
Referent Prof. Dr.-Ing. Steffen Schön
Korreferenten: PD Dr.-Ing. Hamza Alkhatib
Univ.-Prof. Mag. Dr. habil. Thomas Pany

Tag der mündlichen Prüfung: 09.09.2024

Diese Dissertation ist auf dem Server des Ausschusses Geodäsie (DGK)
der Bayerischen Akademie der Wissenschaften unter <http://dgk.badw.de/>
sowie auf dem Server der Leibniz Universität Hannover unter
<https://repo.uni-hannover.de/items/4cb927cb-0518-4b1b-b5b1-5d875e17ac2d> elektronisch publiziert

ISSN 0065-5325 ISBN 978-3-7696-5359-5

Abstract

By measuring accelerations and angular rates with the help of inertial measurement units (IMU), attitude, velocity and position of a mobile platform in motion can be computed. The integration of errors inherent to the signals leads to a drift of the solution over time. In order to reduce this drift while keeping the advantages of an autonomous measurement principle, quantum sensors are a promising concept. In experiments with cold atom interferometers (CAI), great sensitivities and long term stability for the measurement of accelerations and angular rates have been demonstrated. This technology uses wave-particle characteristics of atoms, which are manipulated by a series of light pulses in order to realize different interferometer schemes. In the Mach-Zehnder pulse pattern, the internal states are split, reversed and recombined, making the setup sensitive to accelerations as well as angular rates. Accurate measurement with this technology is limited to a small bandwidth of signals. The preparation of the atomic wave packet needs time in which the assembly is not able to measure. Additionally, the sinusoidal observation equation of the CAI is generally ambiguous. For those reasons, hybridization with high rate, large bandwidth conventional inertial sensors is the proposed scheme for mobile applications. Up to now, this combination has mainly been explored for stationary experiments with accelerometers only. A full quantum inertial navigation system (QINS) demands inclusion of gyroscope measurement as well as experiments in dynamic applications to validate the models and to further understand the behavior of CAI. The final step toward such a QINS consequently has not yet been taken.

This thesis pursues an engineering approach to model CAI and QINS. Using methods from the navigation and physics community, a kinematic model for the center of mass of the atom wave packet is developed and applied, the velocity and position of the atoms computed, and the phase shift ambiguity solved. This allows to integrate gyroscope measurements in the formulation, as well as lever arm and misalignment between the sensor frame of the CAI and the IMU, enabling a parametrization of the often unknown transfer function between the systems. The error state kinematics of the wave packets furthermore allow an assessment of the limits of the CAI and the hybridization in the light of dynamic applications. With the help of an extended Kalman filter (EKF), the biases of the classical IMU are estimated. It can be shown that the acceleration biases are always observable, while the observability of the gyroscope biases demands a displacement or velocity of the atoms perpendicular to the sensitive axis. The requirements to observe state vector augmentations like misalignments and lever arms are discussed. The stability analysis results in a steady state formulation of the QINS. Under stationary conditions, the performance gain of the QINS is evaluated. It can be shown that the QINS navigation solution mainly profits from the long term stability of CAI.

An additional focus of this study is the optimal configuration of CAI and IMU, supporting future system integrators in designing high performance QINS. Different designs are presented and evaluated, one centered on a complete IMU with high accuracy CAI support, yielding the best overall performance with positioning errors of less than ten meters after one hour of free inertial navigation, the other one centered on the CAI with high rate accelerometer support for applications under stationary conditions which further enhances the sensitivity to accelerations by an order of magnitude. The methods are demonstrated experimentally based on a static, one dimensional CAI data set. Furthermore, noise models for the application in the EKF are derived. The remaining methods under dynamic conditions are verified with the help of dedicated simulations.

Keywords: Cold Atom Interferometry, Inertial Measurement Units, Inertial Navigation

Zusammenfassung

Durch Erfassung von Beschleunigungen und Drehraten mittels Trägheitssensorik (IMU) lassen sich die Orientierung, Geschwindigkeit und Position einer mobilen Plattform berechnen. Die Integration von Unsicherheiten in den Signalen führt zu einer allmählichen Drift der Lösung. Zur Reduktion dieser Drift bei gleichzeitiger Wahrung der Autonomie des Messprinzips sind Quantensensoren ein vielversprechendes Konzept. Experimente mit Atominterferometrie auf Basis kalter Atome (CAI) lassen auf hohe Genauigkeit und Stabilität der Messung von Beschleunigungen und Winkelgeschwindigkeiten hoffen. Diese Technologie macht sich Welle-Teilchen-Eigenschaften der Atome zu Nutze, welche mittels gezielter Lichtpulse manipuliert werden um Informationen über Beschleunigungen und Drehraten zu extrahieren. Akurate Messungen sind jedoch auf kleine Bandbreiten der Signale limitiert. Dies liegt einerseits an der Zeit, die zur Kühlung der Atome benötigt wird und in welcher keine Messung möglich ist. Andererseits ist die sinusförmige Messgleichung des CAI im Allgemeinen mehrdeutig. Aus diesen Gründen ist eine Hybridisierung mit klassischen Inertialsensoren mit hoher Rate und großer Bandbreite ein oft diskutierter Ansatz für mobile Anwendungen. Diese Kombination wurde bisher hauptsächlich in stationären Experimenten unter Nutzung einzelner Beschleunigungsmesser untersucht. Ein vollständiges Quanteninertialnavigationssystem (QINS) erfordert die Einbeziehung von Gyroskopmessungen sowie Experimenten in dynamischen Anwendungen zur Validierung der Modelle und zum besseren Verständnis des Verhaltens von CAI.
Die vorliegende Arbeit verfolgt einen ingenieurwissenschaftlichen Ansatz zur Modellierung von CAI und QINS. Unter Verwendung von Methoden aus der Navigations- und Physik-Community wird ein kinematisches Modell für den Massenschwerpunkt der Atom-Wellenpakete entwickelt, mit welchem sich die Geschwindigkeit und Position der Atome beschreiben und die Mehrdeutigkeit der Phasenverschiebung lösen lässt. Dadurch können Gyroskopmessungen sowie Hebelarm und Fehlausrichtung zwischen dem Sensorrahmen des CAI und der IMU in die Formulierung integriert werden, was eine Parametrisierung der oft unbekannten Übertragungsfunktion zwischen den Systemen ermöglicht. Die Fehlerzustandskinematik der Wellenpakete ermöglicht darüber hinaus eine Abschätzung der Grenzen des CAI und der Hybridisierung im Hinblick auf dynamische Anwendungen. Ein erweitertes Kalman-Filter (EKF) wird vorgestellt, mit dem sich systematische Fehler der klassischen IMU schätzen lassen. Im Rahmen einer Beobachtbarkeitsanalyse wird gezeigt, dass die Beschleunigungsbias immer beobachtbar sind, während die Schätzung der Drehratenbias eine Positionsverlagerung oder Geschwindigkeit der Atome senkrecht zur Messachse des CAI erfordert. Die Beobachtbarkeit weiterer systematischer Effekte wie Fehlausrichtung und Hebelarm wird diskutiert. Eine Steady-State Formulierung des QINS wird erarbeitet, welche eine Abschätzung des Performance-Gewinns des QINS ermöglicht. Den Ergebnissen zufolge wird die Verbesserung der Navigationslösung insbesondere durch die Langzeitstabilität des CAI erzielt.
Ein zusätzlicher Schwerpunkt dieser Arbeit sind die Untersuchungen zu einer optimalen Konfiguration von CAI und IMU, welche Methoden und Formeln für den Entwurf zukünftiger hochperformanter QINS bieten. Es werden unterschiedliche QINS-Designs vorgestellt und bewertet. Eine Positionsgenauigkeit von weniger als zehn Metern nach einer Stunde freier inertialer Navigation scheint möglich, während sich unter stationären Bedingungen eine weitere Genauigkeitssteigerung der Beschleunigungsmessung um eine Größenordnung erzielen lässt. Die Methoden werden experimentell anhand eines statischen, eindimensionalen CAI-Datensatzes demonstriert. Darüber hinaus werden Rauschmodelle für den Einsatz im EKF abgeleitet. Anwendungen der Methodik unter dynamischen Bedingungen werden mit Hilfe dedizierter Simulationen verifiziert.

Schlagwörter: Kaltatominterferometrie, Trägheitssensorik, Inertialnavigation

Acronyms

6DOF Six Degrees of Freedom

AD Allan Standard Deviation

ARW Angular Random Walk

AtoS Atom Strapdown

AV Allan Variance

BEC Bose-Einstein Condensate

CAI Cold Atom Interferometer

DCM Direction Cosine Matrix

ECEF Earth-Centered Earth-Fixed

ECI Earth-Centered Inertial

EKF Extended Kalman Filter

FOG Fiber Optic Gyroscope

GNSS Global Navigation Satellite System

HRG Hemispherical Resonator Gyroscope

IEEE Institute of Electrical and Electronics Engineers

IMU Inertial Measurement Unit

INS Inertial Navigation System

KF Kalman Filter

LSE Least-Squares Estimation

LiDAR Light Detection and Ranging

MC Monte Carlo

MEMS Micro-Electromechanical System

MLE Maximum Likelihood Estimation

MOT Magneto-Optical Trap

ODE Ordinary Differential Equation

OMR Opto-Mechanical Resonator

PSD Power Spectral Density

Q-Flex Quartz Flexure Sensor

QINS Quantum Inertial Navigation System

RLG Ringlaser Gyroscope

STD Standard Deviation

VRW Velocity Random Walk

Contents

1 Introduction

Inertial navigation is the art of estimating position, velocity and attitude; the so-called kinematic states. This is realized by an integration of measured angular rates, which yield information about the orientation in a certain reference frame, and accelerations, which can be transformed to said reference frame in order to compute the velocity and position. The problem that arises from this way of dead-reckoning is the drift of the solution. Only a few seconds of free inertial navigation can lead to a position uncertainty of several meters. One way of countering this deterioration of the navigation performance is the use of sensor systems which measure an absolute quantity. Examples are radar, long range navigation based on radio pulses, e.g. LORAN-C (1950-1990), and Global Navigation Satellite Systems (GNSS). The latter technique is the state of the art for modern global absolute positioning, and is getting more relevant even to this day. Examples are the American Global Positioning System (GPS), the Russian Globalnaja Nawigazionnaja Sputnikowaja Sistema (GLONASS), the Chinese Beidou, the European Galileo and a number of other national and private owned systems.

Those cooperative systems require a large infrastructure. Furthermore, a line-of-sight between the components, e.g. satellite and platform-mounted receiver antenna, is necessary. Another disadvantage is the low signal strength of the microwave signals, which makes the system easily affected by jamming attempts in the corresponding frequency range. A similar problem arises from the more sophisticated spoofing attacks, in which signals are designed to make the receiver believe they were transmitted from the navigation satellites. While for some civilian applications this would be a nuisance at most, in fully automatic applications like autonomous driving it can lead to accidents and more severe situations. Other absolute techniques like Light Detection and Ranging (LiDAR) and the use of ranging stations (pseudolites) additionally require knowledge about the position of the stations, or environmental features, respectively.

The answer to the improvement of purely autonomous inertial navigation thus appears to be the use of higher quality inertial sensors. Hemispherical resonator gyroscopes (HRG), ring laser gyroscopes (RLG) and fiber optic gyroscopes (FOG) can reach very high levels of accuracy, with a drift at the $8 \times 10^{-5}\,\mathrm{deg/h}$ level. For high-end commercial accelerometers the options with respect to high accuracy are mainly found in shape of mechanical pendulous force-feedback systems (Groves, 2015) and some other promising technologies like vibrating fiber optics accelerometers and surface acoustic wave accelerometers (El-Sheimy & Youssef, 2020). The common issue is the long-term stability, which somewhat limits the achievable position accuracy for free inertial terrestrial navigation over extended periods of time (Lawrence, 2001; Titterton & Weston, 2009).

One of the most promising high accuracy options is cold atom interferometry (CAI) (Kasevich & Chu, 1992). Compared with other accelerometer technologies, CAI based systems

exhibit unprecedented levels of sensitivity and long-term stability, cf. Fig. 1.1. This technology is furthermore sensitive to angular rates, in principle making it possible to design a full inertial measurement unit based on a single technology. The performance of CAI prototypes for angular rate measurements at least compares to current technologies like RLG, FOG and HRG. However, there is a number of challenges that need to be tackled when opting for this

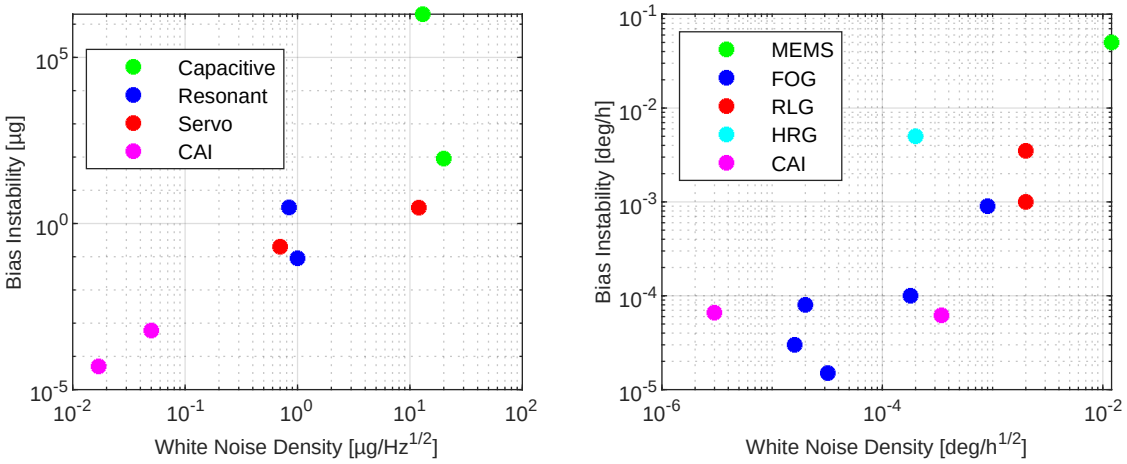

Figure 1.1: CAI in comparison to other inertial sensor technology. The colored dots represent prototypes or commercial products of inertial sensors which will partly be covered in the later chapters. Left: one-axis CAI gravimeters yield superior sensitivity and long-term stability as compared to classical accelerometer technologies (Sources[1]). Right: in comparison to other gyroscope technology (Sources[2]), CAI has promising long-term stability and sensitivity. In comparison to high-end FOG, the performance gap is not as large.

novel design. Due to its limited dynamic range associated with the ambiguity of the sinusoidal observation equation, CAI alone is not expected to be applicable to highly dynamic trajectories. Thus, **hybridization**, i.e. the combination of high accuracy CAI with classical high rate inertial sensors for synergistic effects, is an often discussed concept. Up to date, a fully integrated quantum inertial navigation system (QINS) for mobile terrestrial applications has not yet been realized. The research in this field is highly dynamic and work in this direction so far can be divided in three categories:

A first category are **experimental setups** in a static mode. Classical sensors are applied in order to increase the dynamic range of the atom interferometer, or simply to enable operating the interferometry in the presence of ambient vibrations (Cheiney et al., 2018; Fang et al., 2016; Gouët et al., 2008; Lautier et al., 2014; Merlet et al., 2009; Zhang et al., 2019).

Aside from the experiments in static mode, **mobile applications** have been demonstrated as well. This includes parabolic flight experiments (Battelier et al., 2016; Geiger et al., 2011) and marine applications (Bidel et al., 2018, 2020). Here, an alternative scheme is using gravimetry in conjunction with gravity map matching techniques. While this method allows absolute positioning and thus exhibit no drift of the positioning solution, the accuracy is comparably low and in the order of several hundreds of meters (L. Wu et al., 2017). A mobile marine quantum gravimeter without the need of a stabilization was presented by the company *Vector Atomic* (VectorAtomic, 2023). Another airborne gravimetry campaign is

[1] Capacitive: Rudolf et al. (2014); Serrano et al. (2014). Resonant: Han et al. (2021); Mustafazade et al. (2020). Servo: Honeywell (2020); iMAR (2017b). CAI: Freier et al. (2016); Vermeulen et al. (2018).

[2] MEMS: SBG-Systems (2022). FOG: Cordova et al. (1996); Korkishko et al. (2017); Lefevre et al. (2020); Mead and Mosor (2020). RLG: Honeywell (2018); iMAR (2017b). HRG: Delhaye (2018). CAI: Durfee et al. (2005); Savoie et al. (2018).

currently planned in the AeroQGrav project (BMBF, 2022), in which an integrated solution of an atomic gravimeter, classical accelerometers, LiDAR and GNSS is proposed.

The entirety of the mobile applications were demonstrated for gravimetry only, i.e. the measurement in a single, mainly downward, direction. Also, none of the experiments have seriously demonstrated the hybridization of an actual CAI with classical angular rate sensors so far. For some implementations a Kalman filter for optimal combination of the measurements of both sensors is used which in its many extensions is state of the art in navigation applications since the Apollo missions (Goodman, 2009).

A third category of scientific investigations are the **simulation studies**, with the goal to examine the feasibility and thus pave the way for quantum navigation (Bochkati et al., 2017; Jekeli, 2005; Wang et al., 2023; Wright et al., 2022).

A catalog of open questions remains, that are highly relevant for the final step toward QINS in terrestrial navigation, and have not yet been answered. They include:

- Hybridization of a full six degrees of freedom (6DOF) classical inertial measurement unit (IMU) with CAI. While measurements for single acceleration axes have been demonstrated, no field experiment of a multi-axis CAI has been reported so far. Furthermore, no assessment or serious performance studies about realistic combinations of a complete IMU with a 6DOF CAI have been published so far.
- The hybridization is often based on correlation of the CAI signal with high rate vibration measurements transformed into the CAI observation space by its so-called *sensitivity function* to accelerations (Cheinet et al., 2008). A generalized model for the transformation including systematic effects like the spatial distance and the misalignment between the two sensor systems is essential to allow more insight and to draw meaningful conclusions for future QINS design decisions.
- The drift of the classical sensor's during the measurement cycle of the CAI is seldom discussed. It is mentioned in literature on multiple occasions, that the noise of the classical sensor affects the performance of the combined sensor (Bidel et al., 2018; Geiger et al., 2011; Richardson et al., 2020), but there were no detailed studies about the actual quality requirements for the classical system so far. An analytical description would be highly beneficial for future QINS design decisions.
- A similar important topic is the impact of sensor dead times on the QINS solution. In literature it is often mentioned that the classical sensor helps in bridging the CAI dead times (Bidel et al., 2018; Cheiney et al., 2018; Jekeli, 2005). However, it was never analyzed how long this dead time can actually be, as the drift of the classical sensor might lead to a loss of the CAI fringe-ambiguity solution as well. This is relevant from several points of view. Some multi-axis CAI designs (Gersemann et al., 2020) rely on a subsequent measurement of the three spatial axes which increases the dead time for the measurement on each single axis. Additionally, CAI outages could occur in situations where certain dynamics limits are exceeded, and need to be reckoned with.

The goal of this thesis is to find answers to each of those questions. First and foremost, it is centered around the development of a concept to combine the measurement of CAI and IMU. As extension of the work presented in Tennstedt et al. (2023), the CAI will be applied as a support sensor for a classical IMU, effectively realizing a QINS.

This hybridization concept will be evaluated partly on experimental data which allows to evaluate the scheme in a static lab environment, where a one-axis CAI is combined with a one-axis accelerometer. This allows to derive a noise model of the CAI and to explain some important aspects of the proposed scheme. As the development toward dynamic field

experiments has not progressed far enough at the time of writing, the perspective of an application of the hybridization scheme in kinematic applications is discussed based on few but dedicated simulations.

There are two ways to approach this thesis as a reader. In case one is new to the field of applications of quantum sensors in navigation and keen to understand how the technology works, reading the work from start to end is highly recommended. In case one is interested in concrete solutions to certain challenges of CAI and QINS, Tab. 1.1 directly refers to the corresponding sections. In any case, the road-map in Fig. 1.2 indicates the interaction of the sections, and might help to provide an overview of the material at hand.

The remainder of this thesis is structured as follows: In Chap. 2, the methods of inertial navigation, especially for strapdown navigation systems, are presented. Some state-of-the-art accelerometers and gyroscopes are presented, while a subset that is relevant for the thesis is discussed in more detail. This is followed by a general error model for acceleration and angular rate measurements and typical methods for the assessment of stochastic sensor errors. The chapter is concluded with the effect of the errors on the navigation solution in the terrestrial reference frame.

In Chap. 3, the application of atom interferometry as inertial sensor is developed, starting with a short historical overview and the methods that are used in order to extract inertial information from the sensors. In particular, a model for the interferometric phase shift is presented. The chapter is concluded with the challenges that occur when planning to use atom interferometry for highly dynamic applications. Thus, the methods, equations and major arguments for the hybridization with a classical high-bandwidth sensor are prepared.

Chap. 4 contains the core of this thesis. The chapter starts with a detailed description of the methods used to combine the measurement of both sensor systems. The motion differential equations of the wave packet center of mass is solved by using data of the classical IMU, while the atom interferometer is implemented in a Kalman filter in order to correct the drift of the conventional solution. This filter is analyzed and some aspects like the choice of classical sensors and atom interferometer parameters are discussed, as well as other open questions that regard the implementation of such a QINS. The chapter is concluded with a number of simulation studies in which the theoretical findings are demonstrated and further discussed.

In Chap. 5 a noise model for the atom interferometer is introduced. The aspects and steps needed to parameterize the models based on experimental data are summarized. The hybridization scheme is furthermore applied to data of a single-axis experimental CAI prototype.

A final conclusion is then presented in Chap. 6. The content is summarized and an outlook for future developments is provided.

Challenge	Solution	Section
CAI: systematic errors associated with the response function to accelerations	Assessment of the errors; this opens up further opportunities like avoidance of the measurement or consideration in CAI uncertainty model	3.3
Trade-off: dynamic range vs. sensitivity	Atom Strapdown: trade-off does not occur since the ambiguity is solved by IMU	3.4
CAI: trajectory dynamics exceed the physical limit	Detection and avoidance of measurements in such cases	3.5
Drift of the navigation solution	Hybrid navigation: long-term noise of CAI defines the long-term drift of the hybrid solution, which is largely reduced	4.2
Transformation between IMU and CAI	Included in Atom Strapdown formalism; calibration of misalignment and lever arms possible	4.3.3
Trade-off: IMU quality vs. QINS sensitivity gain	Optimal hybridization for maximum sensitivity gain	4.4.1
Trade-off: atom preparation time vs. dead time	Use of classical accelerometers with sufficiently low drift	4.4.2
Adequate model for the unknown CAI uncertainties	Least squares and/or maximum likelihood estimation	5

Table 1.1: Challenges of CAI navigation and solutions presented in this thesis

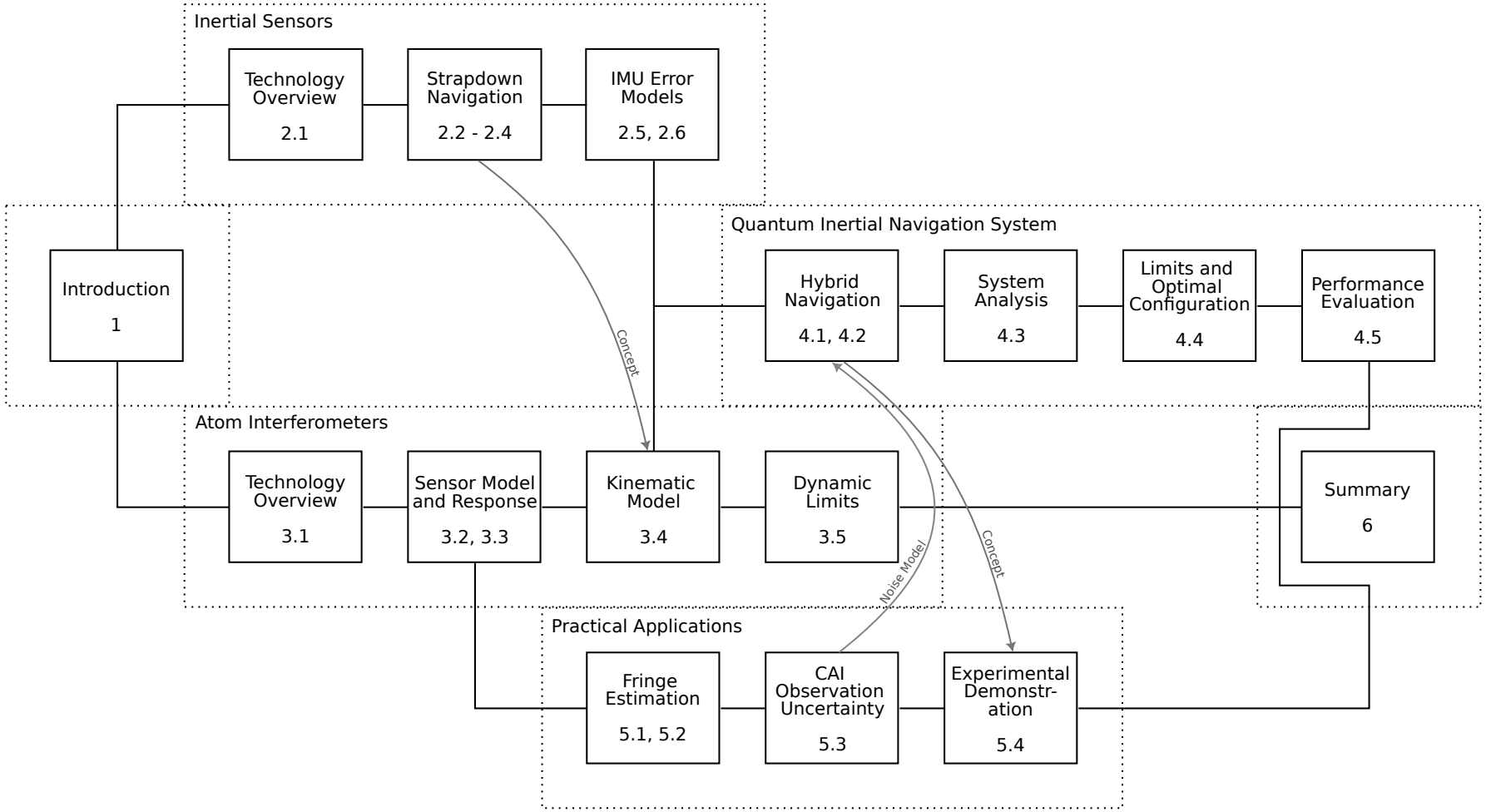

Figure 1.2: Roadmap for the content of this thesis. The general information flow is from left to right. The reader can start with either, the inertial sensors in Chap. 2 or the atom interferometers in Chap. 3. Both are required to understand the QINS concept elaborated in Chap. 4. The practical applications in Chap. 5 mainly require knowledge from Chap. 3.

2

Characteristics of Inertial Sensors

2.1 Introduction to Inertial Navigation and Inertial Sensors

2.1.1 General Overview

Inertial navigation is all about the autonomous estimation of the kinematic state of a moving platform. Early applications of navigation approaches without external references can be found in nautical navigation, where the attitude was determined by magnetic compasses and the velocity by an assumption of the ship's speed. With the time between two measurements as additional information, the navigator was tracking the position of the ship in the ship's log book by updating the last value with the orientation and the relative change of the position due to the velocity. This type of position estimation was highly dependent on the accuracy of the orientation, the knowledge of the velocity, and the precision of the prior estimate. Hence the label **dead reckoning**, the calculation of the relative position without any knowledge of an accurate global position, is often a synonym for inertial navigation.

This basic principle of inertial navigation, the attitude estimation and the velocity/position estimation, has not changed in the past centuries. Even modern ships use combinations of spinning mass or optical gyroscopes, in order to determine the orientation, and sonar for the estimation of the ship velocity. Modern sensors used for inertial navigation can be grouped in two categories, the gyroscopes and the accelerometers. Another sensor often included in low-cost inertial measurement units is the magnetometer. Magnetometers sense orientation with respect to the Earth's magnetic north without measuring inertial quantities. They do not count as inertial sensor in the strict sense and will not be further covered in this work.

With the use of three accelerometers, each one oriented toward one spatial axis, the velocity and position in 3D space can be computed in theory. In practice this only works in case the orientation of the sensors does not change. At that point in the early days of navigation, the gyroscopic effect came into play. A rigid rotor with a certain angular momentum, i.e. mass and angular rate, tends to keep the orientation of its rotation axis with respect to an inertial frame. If such a rotor is placed together with the accelerometers on a platform, and furthermore if this platform is connected to the frame of the vehicle via three independent gimbals, cf. Fig. 2.1, the whole platform keeps its orientation while the vehicle may be changing its direction. If the angles between the gimbals are now measured, for instants, by angle encoders, the orientation of the vehicle with respect to the inertial frame can be measured.

This **gyro-stabilized platform** obviously has the disadvantage of size, weight and the need for maintenance, as a number of mechanical and moving parts are involved. As computation power got more advanced, and better gyroscope technologies were available in the late 1970s (Tazartes, 2014), the stabilized platform was partially replaced by so-called **strapdown**

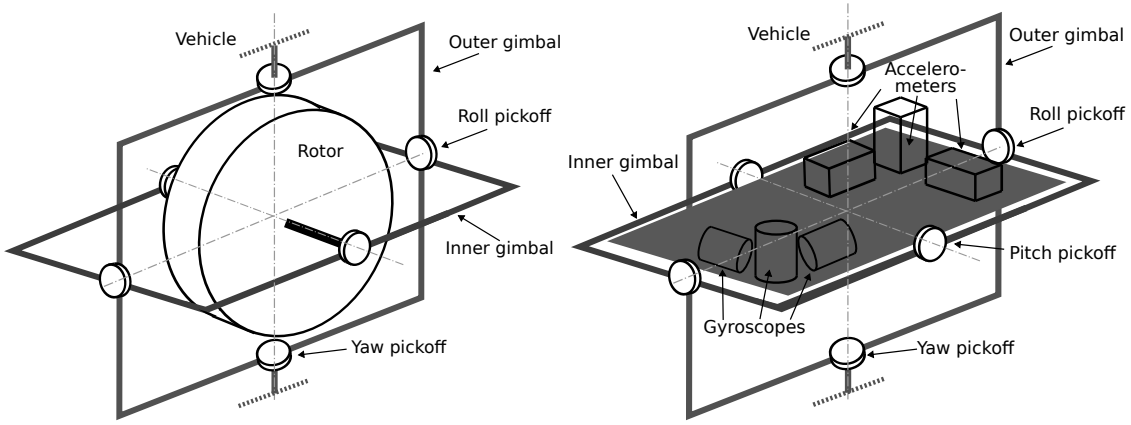

Figure 2.1: Inertial navigation system platforms. Left: mechanical gyro which can be used to stabilize a platform in two directions. The roll and yaw pickoffs yield absolute information about the inclination and the heading of the vehicle. Right: complete inertial navigation system (INS) with three angle pickoffs. If the gimbals were removed and the sensors placed directly on the vehicle frame, the setup would resemble a strapdown inertial navigation system.

systems. Here, the accelerometer triad is placed, i.e. *strapped down*, directly on the vehicle frame, and registers the same dynamics as the vehicle. In addition to the accelerometers, a triad of gyroscopes is involved to realize a complete inertial measurement unit (IMU). The gyroscopes are used to infer about the spatial orientation of the platform with respect to the inertial frame. This can happen, for an example, by integration of the angular rates in an attitude computer. This orientation is then used to transform the accelerations measured by the accelerometer triad and integrate them in order to apply the velocity and position estimation in the required target coordinate system. The general signal flow is illustrated in Fig. 2.2.

Gravity has a large effect on free inertial navigation, i.e. navigation without any supporting systems like GNSS. However, just a single inertial measurement unit alone cannot distinguish between accelerations caused by gravity or non-gravitational effects. As a result, gravity maps or models like latitude-dependent functions are used by a **gravity computer** in order to compensate for those additional acceleration effects. This estimate may lead to errors in the accelerations that accumulate over time. Other drawbacks of this strapdown approach include the drift of the solution, which is directly related to the noise and signal-drift of the sensors that are involved. Also additional effects occur that need to be compensated, such as axis cross-talk due to non-orthogonality of the sensor triads. Finally, the computer needs enough processing power to solve the navigation equations in a sufficiently high data rate.

From a system engineering and control theoretical point of view, the strapdown navigation algorithm has further properties that will be discussed in the frame of the following topics involved in the remainder of this chapter. First, some of the relevant gyroscope and accelerometer technologies that are available today will be presented and shortly evaluated. This is followed by a presentation of the differential equations of the strapdown navigation algorithm in Sec. 2.2. The solution to those equations is presented in Sec. 2.3. The general solution of systems in state space is then discussed in Sec. 2.4, which paves the ground for the discussion of the impact of the IMU errors. The models that are used are presented in Sec. 2.5. The chapter then concludes with a discussion of the long-term navigation performance in Sec. 2.6, including the drift of the kinematic state estimates due to IMU errors, as well as some further aspects of the dynamics that occur due to the feedback loops in the strapdown navigation system.

Before moving on with the technology section, two important sensor characteristics need to be shortly explained.

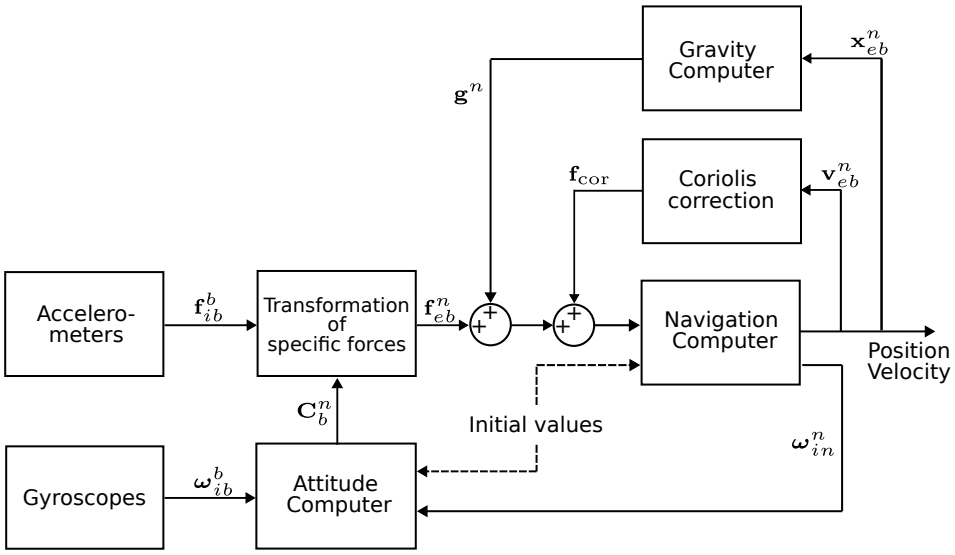

Figure 2.2: Signal flow in a strapdown inertial navigation system. The navigation solution as depicted is computed with respect to a navigation frame (n-frame). Based on the angular rates $\boldsymbol{\omega}^b_{ib}$, the attitude $\mathbf{C}^n_b$ between the b- and n-frame is computed. The specific forces $\mathbf{f}^b_{ib}$ are transformed into the n-frame, corrected by an estimate of the gravity g^n and the Coriolis acceleration $\mathbf{f}_{\mathrm{cor}}$. By double integration, the velocity $\mathbf{v}^n_{eb}$ and position $\mathbf{x}^n_{eb}$ of the platform in the n-frame can be evaluated.

- Sensitivity is related to the level of white noise density in a sensor signal which is often stated in unit/$\sqrt{\mathrm{Hz}}$. The longer a quantity is measured, up to a certain point, the more data can be averaged in order to reduce the deviation from the true value.
- Stability is the minimum level of uncertainty that can be reached by averaging the sensor data. It has the same physical unit as the measured quantity.

This merely verbal introduction should suffice for now, to set the numbers that are going to be stated next for some sensor technologies in relation. A more detailed explanation will follow in Sec. 2.5.

2.1.2 Gyroscope Technology

A simple mechanical gyroscope, like it was illustrated in Fig. 2.1, consists of a spinning mass which is mounted in one or more gimbals (Magnus, 1971, p. 460). By building up a large momentum due to high angular velocity of the mass, the *free rotor* tends to keep its orientation with respect to the inertial frame. If such a sensor is used on the rotating Earth under the effect of gravity, it shows a different behavior. If it is not perfectly aligned with the gravity vector $\mathbf{g}$, it starts rotating toward geographic North as a response to the misalignment. However, as the orientation passes the meridian, the sign of the motion reverses, effectively causing the axis of the rotor to oscillate at a slow pace. This oscillation around the meridian has the angular rate

$$\omega_s = \sqrt{\frac{|\mathbf{g}|}{R}}, \tag{2.1}$$

where R is the radius of the Earth. The period associated with this frequency is often called Schuler period. If the oscillation is dampened by a sophisticated mechanism, the orientation converges to the geographic North after some time. A similar oscillatory effect occurs in strapdown inertial navigation and will be discussed in Sec. 2.6.

The first commercial application of **spinning mass gyroscopes** started 1907 on ships (Lohmeier, 1992, p. 20). They are still used today, as the orientation measurement is absolute

and as such does not inherit any drift. The drawbacks are the moderate accuracy of 0.1 deg and the mechanical wear out, especially of the rotor bearings. Furthermore, the system needs some time to start up and is easily disturbed by external forces, especially when the built-up angular momentum is still low.

The best performance for spinning mass gyroscopes is achieved with electrostatically suspended gyroscopes, where the mechanical parts of the bearings are replaced by electrostatic levitation of the rotor. With such a system, stability levels of 1.7×10^{-12} rad/h are proposed (Bencze et al., 2007), when isolated from any unwanted perturbations.

The next important technology is the **ring laser gyroscope** (RLG) as demonstrated by Macek and Davis (1963). The sensor uses the so-called Sagnac effect (Post, 1967). As depicted in Fig. 2.3, light from a single source is split, reversed by a mirror, and then recombined by another splitter, in order to produce coherent waves at the output port. In case of a rotation of the apparatus, for example due to the Earth rate, the two paths of the laser have a different length. This leads to a phase shift which can be seen in the interference pattern.

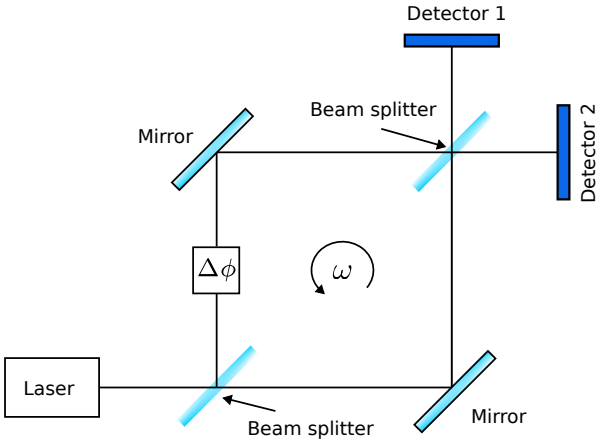

Figure 2.3: Scheme of a Sagnac interferometer. The Sagnac effect describes the occurrence of interference patterns at the detectors. The phase shift $\Delta\phi$ yields information about the angular rate ω of the frame.

With the RLG a frequency difference Δf can be measured, which in turn is related to the rotation rate $\boldsymbol{\omega}$ in the sensor frame. The integrated Δf in a time interval τ yields the phase change $\Delta\phi$ (Jekeli, 2001, p. 76), resulting in the following relationship:

$$\Delta\phi = \frac{4A_r}{L\lambda}\mathbf{n} \cdot \int_0^\tau \boldsymbol{\omega}\, dt. \tag{2.2}$$

Further parameters are the enclosed area A_r with the normal vector $\mathbf{n}$, corresponding to the sensitive direction of this particular sensor axis, the laser wavelength λ and the perimeter L. The beat notes of the difference signal can be measured by a photodetector with sufficiently high bandwidth. The signal thus is directly proportional to the rotation rate of the apparatus.

The scale factor of the RLG mainly depends on the ratio of area and perimeter that the lasers enclose. A large area improves the scale factor, whereas a larger perimeter reduces it. This can sometimes render alternative designs like the square relevant, but at the same time makes it hard to considerably improve the scale factor. One of the largest ring laser gyroscopes is the ROMY (Igel et al., 2021), in which four[1] triangular ring lasers with 12 m side length are assembled in a way that each of them resembles one side of a tetraeder. The sensitivity of this sensor easily reaches sub-nrad/s/$\sqrt{\text{Hz}}$ levels. Another disadvantage is the lock-in effect

[1] For redundancy reasons.

which occurs for low angular rates. In this case the frequencies of the two laser beams tend to "lock together" (Titterton & Weston, 2009, p. 120) and thus cannot be distinguished. As a consequence, no difference signal and thus no measurement of the angular rate can be obtained. The lock-in effect demands additional active compensation like the dither-technique, which in turn adds additional high-frequency noise to the sensor signal.

A few years after the RLG, Vali and Shorthill (1976) presented a slightly different scheme in which the counter-propagating light is guided in a glass fiber. This **fiber optical gyroscope (FOG)** allows to increase the enclosed area by a multitude. They state the following path difference for a laser beam with the velocity of light c enclosing an area A_r which rotates with the angular rate ω:

$$\Delta x = \frac{4A_r}{\lambda c}\omega. \tag{2.3}$$

In practice, the fiber is coiled up, such that the enclosed area A_r is defined by the number of windings n_w of the fiber when one coil is a circle with diameter d,

$$A_r = \frac{\pi}{4}d^2 n_\mathrm{w}. \tag{2.4}$$

Even though the fiber length and thus the sensitivity of the sensor could easily be largely increased, there is a number of effects that prevent an arbitrarily large scale factor. Namely, the coupling efficiency of the light into the fiber, as well as the attenuation factor of the fiber itself. One large advantage of the FOG is that it has no lock-in effect and, as a consequence, no mechanical moving parts are needed. It can thus be seen as a *passive* Sagnac gyroscope. Still, Vali and Shorthill (1976) pointed out that the performance of their FOG is inferior to the ring laser. This was the dominant way of thinking for a long time.

At the end of the 20th century there were some major improvements, namely a better material for the coil fiber, integrated optics and entirely digital signal processing, which lead to the next generation of fiber optical gyroscopes (Lefevre et al., 2020). For current strategic-grade products of companies like Exail (former iXBlue) with the "Marins" and Optolink with the "SRS-5000" (Korkishko et al., 2017), sensitivities and long-term stabilities in an order of magnitude of less than 1×10^{-5} deg/sqrt(h) and deg/h, respectively, at a coil length of 5 km have been reported. Further improvement in order to allow coil lengths of over 10 km might lead to a bias drift of less than 4.7×10^{-6} deg/h, as Paturel et al. (2014) discussed.

The last major category that needs mentioning are the **vibratory gyroscopes**. There is a vast number of different implementations in consumer-grade micro-electromechanical systems (MEMS) up to high performance hemispherical resonator gyroscopes (HRG). They are often based on the Coriolis effect, i.e. a displacement of proof mass m with a well-defined velocity $\mathbf{v}$ due to a force $\mathbf{f}_c$ associated with a rotation $\boldsymbol{\omega}$ of the sensor,

$$\mathbf{f}_c = 2m\boldsymbol{\omega} \times \mathbf{v}. \tag{2.5}$$

The hemispherical resonator gyro uses a feature of resonating structures, which, similar to the spinning mass gyroscopes, tend to keep their orientation even as the support frame rotates (Rozelle, 2009). Such a sensor consists of a hemispheric resonator, which may be made from fused quartz. The rotation rate is related to the nodes of the standing wave of the resonating hemispheric structure which are measured e.g. with a capacitive pickoff (Matthews & Rybak, 1992).

While low-cost and consumer grade designs are certainly possible, the production of high-end devices needs to be highly accurate and is comparably expensive. Main applications are in space (Jerebets, 2007) and for high accuracy inertial navigation. Major manufacturers are Safran and Northrop Grumman. Evaluations of strategic grade HRG indicate a white noise

density of 2×10^{-4} deg/sqrt(h) and a bias stability of 1×10^{-4} deg/sqrt(h) (Delhaye, 2018), which puts it in the same category as FOG and RLG, performance wise (Matthews & Rybak, 1992).

2.1.3 Accelerometer Technology

In the domain of accelerometers, there is a large number of different technologies available. **Mechanical accelerometers** can be understood as a mass-spring system, where a well-defined mass is placed between two spring elements in an enclosed casing, cf. Fig. 2.4. If the system is affected by external forces in direction of the sensitive axis, the mass is accelerated and the displacement can be read out to infer about the actual acceleration by some means of pickoff. This simple design is often called **open loop**, as the displacement of the mass is acquired directly. One special case is the pendulous accelerometer. Here, the mass in the general case can be connected by one hinge made out of spring material. If external forces are affecting the mass, a displacement can be registered.

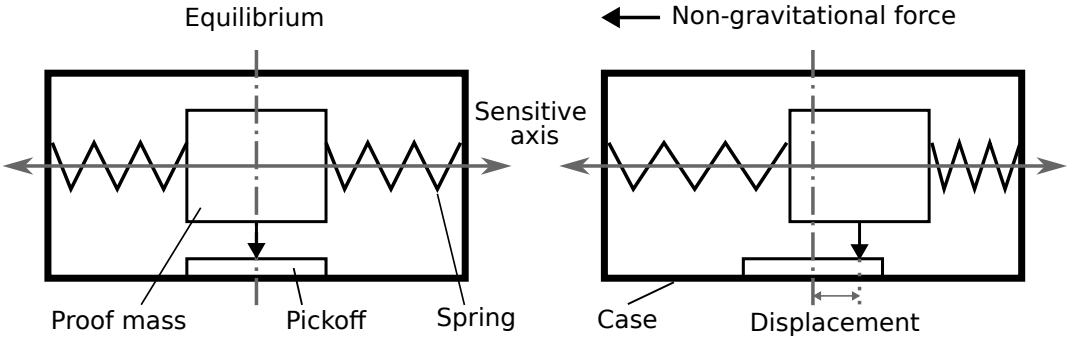

Figure 2.4: Scheme of a force feedback accelerometer. Left: proof mass is in equilibrium. Right: an accelerating force leads to a displacement of the proof mass, which can be related to the acting acceleration.

The drawback of this open loop approach is the comparably low dynamic range, e.g. in case of large accelerations, the mass might reach the end of the casing. Furthermore, non-linearity of the transfer between the displacement and the output of the sensor is a large issue.

In contrast to the open loop design, the spring can be replaced by an actuator of some sorts, which is steered by using information about the displacement of the mass, effectively holding the mass in a state of equilibrium. This way of feeding back the signal to the actuators is called **closed loop** design. To the cost of greater complexity of the system and a dependency of an external power supply, the advantages are an improved dynamic range due to higher stiffness, which is directly related to the gain factor of the force feedback, as well as largely improved linearity due to the controlled equilibrium state. On the other hand, the shock resistance of the closed loop system is generally lower, as a large acceleration far beyond the operating point might damage the sensor.

One specific closed loop pendulous design is the Q-Flex (Q for quartz, Flex for flexure), as depicted in Fig. 2.5. The design was first presented in Jacobs (1972). The main feature is the monolithic structure of the pendulum and the hinge, which are made from a block of fused quartz. The pendulum is provided with coils in order to realize an electromagnet. The proof mass is surrounded by permanent magnets which together with the coils on the mass form the feedback actuator. The pickoff is realized by capacitors. The major manufacturer of the Q-Flex is Honeywell. Typical sensitivity levels are in the order of $1 \times 10^{-5}\,\mathrm{m/s^2/\sqrt{Hz}}$ and below, with a bias floor reached well after several tens of seconds (Roussel et al., 2015). This design currently yields one of the best overall performances that can be achieved with a commercial navigation grade accelerometer.

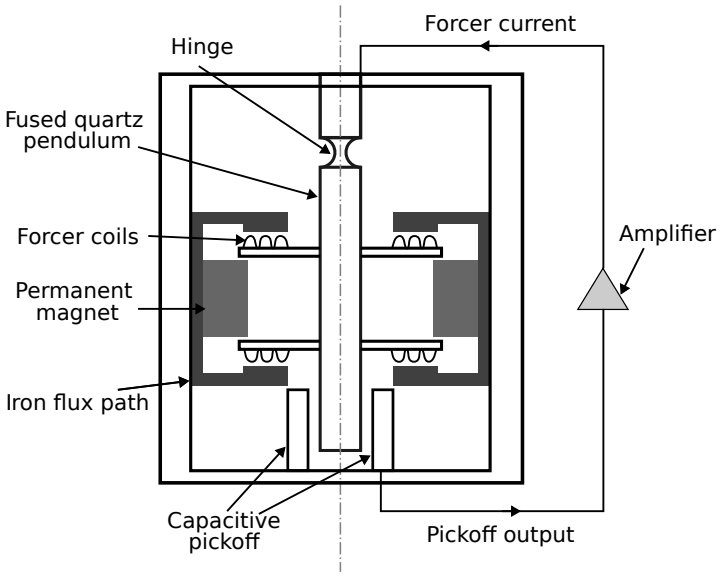

Figure 2.5: Scheme of a Q-Flex accelerometer. The proof mass and the spring hinge are manufactured from one block of fused quartz. A capacitive pickoff signal is amplified and fed back into the system to generate an electromagnetic force through the coils, which holds the pendulum in equilibrium. Sketch based on Lawrence (2001, p. 62).

Another closed loop design without mechanical parts involved is the electrostatic accelerometer (EA), like developed by Christophe et al. (2015). Here, the proof mass is suspended by an electrostatic field which at the same time acts as an actuator. Capacitive pickoffs measure the displacement of the proof mass, enabling inference about the accelerations in 3D. For the highly sensitive devices in the level of $1 \times 10^{-10}\,\mathrm{m/s^2}/\sqrt{\mathrm{Hz}}$, the dynamic range in the sub-$\mathrm{mm/s^2}$ realm is somewhat limited (Krasnov & Rozentsvein, 2022). This is the reason why this sensor is mostly applied in space, like in gravity field recovery missions (Knabe et al., 2022).

Accelerometers can also be based on thermal effects, the magnetic Hall effect, or opto-mechanical principles that will not further be covered. Also, use of the piezoelectric effect can be made in order to create a sensitive element. As this typically exhibits a large drift, this type of sensor in general is better used in consumer electronics or in crash-test applications. Their applicability for navigation purposes is rather limited.

This concludes the inertial sensor technology section. The main takeaways are that in modern sensor design, the trend goes in the direction of having small, monolithic designs that in the ideal case have no moving parts involved. For the gyroscopes, this is the fiber optic and hemispheric resonator design alike. In fact, the highest sensitivities and long-term stabilities have been achieved with fiber optic gyroscopes, and the limit is not yet reached (Paturel et al., 2014). For the accelerometers such a design can be found in shape of the Q-Flex and some optical interferometry based designs, cf. Lawrence (2001, p. 55).

2.2 System Model in Dynamic Environment

2.2.1 Coordinate Frames

A number of different coordinate frames is required in order to include and model the effects that are ultimately measured by an inertial sensor. All systems that will be stated next are right-handed.

The (inertial) **i-frame** spans the mathematical basis in which the motion differential equations are valid. This is typically a frame which is neither accelerating nor rotating. In this thesis, the origin of the inertial frame is the center of mass of the Earth, cf. Fig. 2.6. The axis $\mathbf{i}_3$ aligns with the rotation axis of the Earth. The $\mathbf{i}_1$-axis points toward the vernal equinox. The axis $\mathbf{i}_2$ completes the right-handed system. Subsequently, the frame will be labeled Earth-centered inertial (ECI).

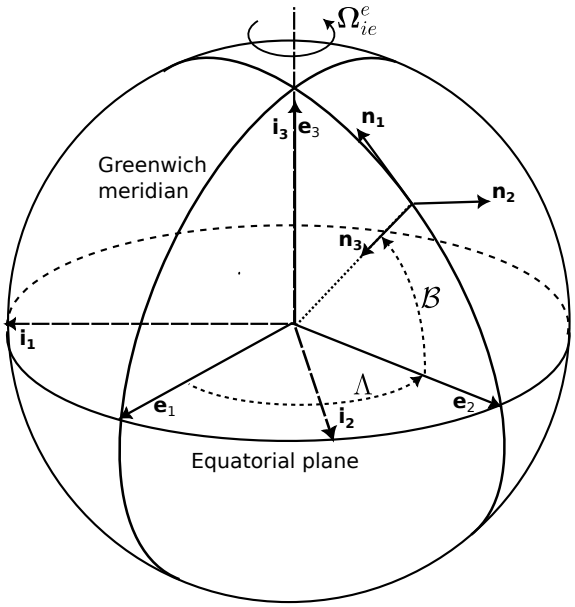

Figure 2.6: Reference frames in a spherical Earth model. The $\mathbf{e}_1$-axis points towards the intersection of the Greenwich meridian with the equatorial plane. The $\mathbf{e}_3$-axis is parallel to the $\mathbf{i}_3$-axis of the star-fixed i-frame. The n-frame origin position corresponds to the latitude $\mathcal{B}$ and longitude Λ, and the distance from the Earth center.

Like the ECI frame, the **e-frame** has its origin at the center of mass of the Earth. The $\mathbf{e}_1$-axis points toward the intersection of the Greenwich meridian with the equatorial plane. It is a rotating frame w.r.t. the axis $\mathbf{e}_3$ with the Earth rotation rate $\boldsymbol{\Omega}^e_{ie}$. The $\mathbf{e}_2$-axis completes the right-handed system. Since the frame is fixed to the rotation of the Earth, this coordinate system is often abbreviated Earth-centered Earth-fixed (ECEF). There is a number of factors like nutation, precession and other tidal effects that have an impact on the magnitude of the Earth rotation rate. However, the amplitude of those effects seldom exceeds 10^{-10} rad/s (Yoder et al., 1981). In the context of this thesis, a constant value of $7.292115 \cdot 10^{-5}$ rad/s (Hofmann-Wellenhof et al., 2001, p. xxiii) is assumed as magnitude for $\boldsymbol{\Omega}^e_{ie}$.

In order to describe motion in a local basis, a tangent (navigation) **n-frame** is introduced. The axes are defined in North-East-Down (NED) convention, where the $\mathbf{n}_1$-axis points towards the geographic North. Unfortunately, the shape of the Earth is not regular and the definition of a position with respect to the surface demands approximations of the actual shape. For this purpose reference ellipsoids are often used. For the tasks addressed in this thesis, a simplified spherical Earth model is sufficient. Here, the $\mathbf{n}_3$-axis is aligned downwards with the local gravity vector, and the $\mathbf{n}_2$-axis is perpendicular to both. The frame origin may be placed at the center of mass of a vehicle. In order to express the orientation of this vehicle however, an additional coordinate system is needed.

The vehicle-fixed **b-frame** shares the origin with the n-frame. The axes are aligned with the main axes of the vehicle, but may have a different orientation with respect to the n-frame. Since this attitude is always well-defined in the tangent frame, the axes can be chosen relatively free. In this thesis the axes are defined according to the *forward-right-down* convention, meaning

that the $\mathbf{b}_1$-axis is pointing in the forward movement direction of the vehicle, while the $\mathbf{b}_3$-axis is pointing parallel to $\mathbf{n}_3$, and $\mathbf{b}_2$ in right direction completes the right-handed system.

In order to model misalignment errors and include the lever arm of single sensor systems w.r.t. the center of the b-frame, the introduction of additional sensor-fixed coordinate frames is useful. Similar to the b-frame, this **s-frame** is usually body-fixed and can be designed depending on the sensor and the respective sensitive elements. The atom interferometer as introduced in Chap. 3 will be equipped with its own s-frame.

Frame Coordinate Rotations and Rotation Expression

The difference between the star-fixed i- and the Earth-bound e-frame consists of the rotation of the Earth around the $\mathbf{e}_3$-axis with magnitude ω_{ie}^e. This results in a time-dependent transformation $\mathbf{C}_i^e$ defined by

$$\mathbf{C}_i^e(t) = \begin{bmatrix} \cos(\omega_{ie}^e t) & \sin(\omega_{ie}^e t) & 0 \\ -\sin(\omega_{ie}^e t) & \cos(\omega_{ie}^e t) & 0 \\ 0 & 0 & 1 \end{bmatrix}. \tag{2.6}$$

The transformation between the e-frame and the tangent n-frame depends on the position on the spherical Earth, latitude $\mathcal{B}$ and longitude Λ. The rotation $\mathbf{C}_n^e$ is given by (Hofmann-Wellenhof et al., 2001, p. 284):

$$\mathbf{C}_n^e = \begin{bmatrix} -\sin\mathcal{B}\cos\Lambda & -\sin\Lambda & -\cos\mathcal{B}\cos\Lambda \\ -\sin\mathcal{B}\sin\Lambda & \cos\Lambda & -\cos\mathcal{B}\sin\Lambda \\ \cos\mathcal{B} & 0 & -\sin\Lambda \end{bmatrix}. \tag{2.7}$$

For the case of the Earth angular rate,

$$\boldsymbol{\omega}_{ie}^n = \mathbf{C}_e^n \begin{bmatrix} 0 \\ 0 \\ \omega_{ie}^e \end{bmatrix} = \omega_{ie}^e \begin{bmatrix} \cos\mathcal{B} \\ 0 \\ -\sin\mathcal{B} \end{bmatrix}. \tag{2.8}$$

The transformation from the b- to the n-frame is a mere rotation, for example expressed as direction cosine matrix (DCM) $\mathbf{C}_b^n$. The matrix can be constructed from Euler angles (Groves, 2013, p. 28):

$$\mathbf{C}_b^n = \begin{bmatrix} \cos\psi\cos\theta & \cos\psi\sin\theta\sin\varphi - \sin\psi\cos\varphi & \cos\psi\sin\theta\cos\varphi + \sin\psi\cos\varphi \\ \sin\psi\cos\theta & \sin\psi\sin\theta\sin\varphi + \cos\psi\cos\varphi & \sin\psi\sin\theta\cos\varphi - \cos\psi\sin\varphi \\ -\sin\theta & \cos\theta\sin\varphi & \cos\theta\cos\varphi \end{bmatrix}. \tag{2.9}$$

The Euler angles are often called roll φ, pitch θ and yaw angle ψ. Alternatively, the rotation matrix $\mathbf{C}_b^n$ can be expressed in terms of a **rotation vector** $\boldsymbol{\delta}$. The formal relation is given by the Rodrigues equation (Savage, 1998a)

$$\mathbf{C}_b^n = \mathbf{I} + \frac{\sin\delta}{\delta}[\boldsymbol{\delta}\times] + \frac{1-\cos\delta}{\delta^2}[\boldsymbol{\delta}\times]^2. \tag{2.10}$$

The rotation vector is expressed by the **Laning-Bortz** notation (Bortz, 1971). Thus, $\|\boldsymbol{\delta}\| = \delta$ equals the rotation angle, where $\frac{\boldsymbol{\delta}}{\delta}$ is a unit vector of the rotation axis. The matrix $[\boldsymbol{\delta}\times]$ is the **skew-symmetric** representation of the vector $\boldsymbol{\delta}$, defined by

$$[\boldsymbol{\delta}\times] = \begin{bmatrix} 0 & -\delta_z & \delta_y \\ \delta_z & 0 & -\delta_x \\ -\delta_y & \delta_x & 0 \end{bmatrix}. \tag{2.11}$$

The direction cosine matrix representation in combination with the rotation vector enables an intuitive and still mathematical versatile tool for the further description. It will be used in the remainder of this thesis in favor of Euler angles and Quaternions. The formulation with Quaternions is a valid and powerful alternative, but less intuitive. Euler angles on the other hand yield the so-called Gimbal Lock problem, a certain constellation which leads to a loss of one degree of freedom and, consequently, ambiguities of the angles. Occasionally the Euler angles are used as a form of graphical display for some of the results. They can be extracted from the direction cosine matrix in Eq. (2.9) in numerous ways. One option is

$$\varphi = \arctan \frac{-c_{3,2}}{c_{3,3}}, \quad \theta = \arcsin c_{3,1}, \quad \psi = \arctan \frac{-c_{2,1}}{c_{1,1}}, \tag{2.12}$$

whereas $c_{i,j}$ represents the entry of the i-th line and j-th column of the DCM. The orientation between a sensor's s- and the b-frame can be similarly expressed with the direction cosine matrix $\mathbf{C}_s^b$. In this case, the angles represent the alignment of the two body-fixed coordinate systems.

2.2.2 Kinematic Differential Equations

In a mere inertial frame, an object is exposed to the gravitation $\mathbf{G}^i$ and (non-gravitational) specific forces $\mathbf{f}^i$. The object acceleration $\ddot{\mathbf{x}}^i$ thus reads

$$\ddot{\mathbf{x}}^i = \mathbf{f}^i + \mathbf{G}^i, \tag{2.13}$$

where the dot operator represents the derivative with respect to time. The accelerometers of an IMU measure specific forces. As an example, if the object is not accelerated, the measurement consists of $\mathbf{f}^i = -\mathbf{G}^i$.

At first, a model for the motion of an object on Earth's surface needs to be described in the inertial frame. For this, $\mathbf{x}_{eb}^e$ will now denote the local vector from the origin of the e-frame to the coordinate center of the b-frame, expressed in the e-frame. This **convention of indices** will be used in the remainder of the thesis, unless defined otherwise.

The transformation of this vector to the i-frame is essentially a rotation, expressed by the matrix $\mathbf{C}_e^i$,

$$\mathbf{x}_{eb}^i = \mathbf{C}_e^i \mathbf{x}_{eb}^e. \tag{2.14}$$

The time derivative of the position yields the velocity $\mathbf{v}_{eb}^i$,

$$\dot{\mathbf{x}}_{eb}^i = \mathbf{v}_{eb}^i = \dot{\mathbf{C}}_e^i \mathbf{x}_{eb}^e + \mathbf{C}_e^i \dot{\mathbf{x}}_{eb}^e. \tag{2.15}$$

Two terms are emerging from the differentiation, according to the product rule. The rate of change of the velocity is:

$$\dot{\mathbf{v}}_{eb}^i = \ddot{\mathbf{C}}_e^i \mathbf{x}_{eb}^e + 2\dot{\mathbf{C}}_e^i \dot{\mathbf{x}}_{eb}^e + \mathbf{C}_e^i \ddot{\mathbf{x}}_{eb}^e. \tag{2.16}$$

The derivatives of the orientation $\mathbf{C}_e^i$ can be expressed by the following attitude differential equation, which will be explained in more detail in Sec. 2.3,

$$\dot{\mathbf{C}}_e^i = \mathbf{C}_e^i \mathbf{\Omega}_{ie}^e. \tag{2.17}$$

After some rearrangement and under extensive use of Eq. (2.17), Eq. (2.16) becomes

$$\dot{\mathbf{v}}_{eb}^i = \mathbf{C}_e^i \ddot{\mathbf{x}}_{eb}^e + 2\mathbf{C}_e^i \mathbf{\Omega}_{ie}^e \dot{\mathbf{x}}_{eb}^e + \mathbf{C}_e^i \left(\mathbf{\Omega}_{ie}^e \mathbf{\Omega}_{ie}^e + \dot{\mathbf{\Omega}}_{ie}^e \right) \mathbf{x}_{eb}^e. \tag{2.18}$$

Note that the Earth angular rate $\mathbf{\Omega}_{ie}^e$ can be considered constant for most applications, in which case the Euler term $\dot{\mathbf{\Omega}}_{ie}^e \mathbf{x}_{eb}^e$ is zero. The term $\mathbf{\Omega}_{ie}^e \mathbf{\Omega}_{ie}^e \mathbf{x}_{eb}^e$ represents the centripetal

acceleration, whereas $\mathbf{x}^e_{eb}$ is the position vector pointing to the b-frame, with a magnitude which is approximately the Earth radius. Inserting into Eq. (2.13) yields

$$\mathbf{f}^i + \mathbf{G}^i = \mathbf{C}^i_e \ddot{\mathbf{x}}^e_{eb} + 2\mathbf{C}^i_e \mathbf{\Omega}^e_{ie} \dot{\mathbf{x}}^e_{eb} + \mathbf{C}^i_e \left(\mathbf{\Omega}^e_{ie} \mathbf{\Omega}^e_{ie} + \dot{\mathbf{\Omega}}^e_{ie} \right) \mathbf{x}^e_{eb}. \tag{2.19}$$

As a next step, the n-frame is introduced in the equation. If a translatory motion is allowed for the n-frame, another rotation occurs with respect to the e-frame, cf. e.g. Groves (2015, p. 132). First, the velocity expressed in the b-frame is rotated to the e-frame,

$$\mathbf{v}^e_{eb} = \mathbf{C}^e_n \mathbf{v}^n_{eb}. \tag{2.20}$$

Differentiation of Eq. (2.20) and application of Eq. (2.17) analogous to before yields

$$\ddot{\mathbf{x}}^e_{eb} = \mathbf{C}^e_n \ddot{\mathbf{x}}^n_{eb} + \mathbf{C}^e_n \mathbf{\Omega}^n_{en} \dot{\mathbf{x}}^n_{eb}. \tag{2.21}$$

This new equation inserted into Eq. (2.19) leads to:

$$\mathbf{f}^i + \mathbf{G}^i = \mathbf{C}^i_e \left(\mathbf{C}^e_n \ddot{\mathbf{x}}^n_{eb} + \mathbf{C}^e_n \mathbf{\Omega}^n_{en} \dot{\mathbf{x}}^n_{eb} \right) + 2\mathbf{C}^i_e \mathbf{\Omega}^e_{ie} \dot{\mathbf{x}}^e_{eb} + \mathbf{C}^i_e \left(\mathbf{\Omega}^e_{ie} \mathbf{\Omega}^e_{ie} + \dot{\mathbf{\Omega}}^e_{ie} \right) \mathbf{x}^e_{eb}. \tag{2.22}$$

Multiplying with $\mathbf{C}^e_i$ from the left side yields

$$\mathbf{C}^e_i \left(\mathbf{f}^i + \mathbf{G}^i \right) = \mathbf{C}^e_n \ddot{\mathbf{x}}^n_{eb} + \mathbf{C}^e_n \mathbf{\Omega}^n_{en} \dot{\mathbf{x}}^n_{eb} + 2\mathbf{\Omega}^e_{ie} \dot{\mathbf{x}}^e_{eb} + \left(\mathbf{\Omega}^e_{ie} \mathbf{\Omega}^e_{ie} + \dot{\mathbf{\Omega}}^e_{ie} \right) \mathbf{x}^e_{eb}. \tag{2.23}$$

The equations should be finally solved in the n-frame, however. By multiplying both sides of the equation with $\mathbf{C}^n_e$ from the left side, the following equation results:

$$\mathbf{C}^n_e \mathbf{C}^e_i \left(\mathbf{f}^i + \mathbf{G}^i \right) = \ddot{\mathbf{x}}^n_{eb} + \mathbf{\Omega}^n_{en} \dot{\mathbf{x}}^n_{eb} + 2\mathbf{\Omega}^n_{ie} \dot{\mathbf{x}}^n_{eb} + \left(\mathbf{\Omega}^n_{ie} \mathbf{\Omega}^n_{ie} + \dot{\mathbf{\Omega}}^n_{ie} \right) \mathbf{x}^n_{eb}. \tag{2.24}$$

Solving everything for $\ddot{\mathbf{x}}^n_{eb}$:

$$\ddot{\mathbf{x}}^n_{eb} = \mathbf{f}^n + \mathbf{G}^n - \mathbf{\Omega}^n_{en} \dot{\mathbf{x}}^n_{eb} - 2\mathbf{\Omega}^n_{ie} \dot{\mathbf{x}}^n_{eb} - \left(\mathbf{\Omega}^n_{ie} \mathbf{\Omega}^n_{ie} + \dot{\mathbf{\Omega}}^n_{ie} \right) \mathbf{x}^n_{eb}. \tag{2.25}$$

Now the centripetal acceleration, Euler term and gravitation can be clustered in gravity $\mathbf{g}^n$,

$$\mathbf{g}^n = \mathbf{G}^n - \left(\mathbf{\Omega}^n_{ie} \mathbf{\Omega}^n_{ie} + \dot{\mathbf{\Omega}}^n_{ie} \right) \mathbf{x}^n_{eb}. \tag{2.26}$$

Furthermore, the IMU data are measured in the b-frame, hence $\mathbf{f}^n = \mathbf{C}^n_b \mathbf{f}^b$. The final navigation equation then reads:

$$\ddot{\mathbf{x}}^n_{eb} = \mathbf{C}^n_b \mathbf{f}^b - \left(\mathbf{\Omega}^n_{en} + 2\mathbf{\Omega}^n_{ie} \right) \dot{\mathbf{x}}^n_{eb} + \mathbf{g}^n. \tag{2.27}$$

This second order differential equation is often reformulated into a system of first order differential equations,

$$\dot{\mathbf{x}}^n_{eb} = \mathbf{v}^n_{eb}, \tag{2.28}$$

$$\dot{\mathbf{v}}^n_{eb} = \mathbf{C}^n_b \mathbf{f}^b - \left(\mathbf{\Omega}^n_{en} + 2\mathbf{\Omega}^n_{ie} \right) \mathbf{v}^n_{eb} + \mathbf{g}^n, \tag{2.29}$$

$$\dot{\mathbf{C}}^n_b = \mathbf{C}^n_b \mathbf{\Omega}^b_{nb}. \tag{2.30}$$

The solution of this system is the main purpose of strapdown inertial navigation computers.

2.3 Solution of the Navigation Equations

Now that the differential navigation equations in the n-frame are established, the next step is the solution. The first part is always the computation of the attitude of the b-frame with respect to the n-frame. With this information, the specific forces measured by the accelerometers can be transformed and integrated in the n-frame, in order to estimate the velocity and position.

Attitude Update

If an arbitrary rotation is expressed as a sequence of rotations relative to an inertial frame via

$$\mathbf{C}_b^n = \mathbf{C}_i^n \mathbf{C}_b^i \tag{2.31}$$

and differentiated in order to get an idea about its change over time, it reads according to the product rule:

$$\dot{\mathbf{C}}_b^n = \mathbf{C}_i^n \dot{\mathbf{C}}_b^i + \dot{\mathbf{C}}_i^n \mathbf{C}_b^i. \tag{2.32}$$

Some reformulation leads to (Savage, 2000, p. 4-40):

$$\dot{\mathbf{C}}_b^n = \mathbf{C}_b^n \boldsymbol{\Omega}_{ib}^b - \boldsymbol{\Omega}_{in}^n \mathbf{C}_b^n, \tag{2.33}$$

with $\boldsymbol{\Omega}_{ib}^b$ in the first term representing the rotation of the b-frame with respect to the i-frame, while the navigation frame rates $\boldsymbol{\Omega}_{in}^n$ in the second term need to be considered as well, as the n-frame rotates relative to the i-frame due to the Earth rate and transportation rates. After some further reformulation, an alternative representation is:

$$\dot{\mathbf{C}}_b^n = \mathbf{C}_b^n \boldsymbol{\Omega}_{nb}^b. \tag{2.34}$$

This is often the basic differential equation for the attitude update. Note that the object rates $\boldsymbol{\Omega}_{nb}^b$ need to be known in order to gain an advantage from this reformulation of Eq. (2.33). For this purpose the addition theorem of angular rates is applied, such that the object rates can be determined by reducing the measured angular rates $\boldsymbol{\Omega}_{ib}^b$ by the Earth rate $\boldsymbol{\Omega}_{ie}^b$ and the transportation rate $\boldsymbol{\Omega}_{en}^b$ in the b-frame,

$$\boldsymbol{\Omega}_{nb}^b = \boldsymbol{\Omega}_{ib}^b - \boldsymbol{\Omega}_{ie}^b - \boldsymbol{\Omega}_{en}^b. \tag{2.35}$$

The transportation rate can be directly related to the velocity in the n-frame, which, in a simplified spherical Earth model, acts tangential to the radius R of the Earth and the height h of the n-frame over the surface. Thus,

$$\boldsymbol{\Omega}_{en}^n = \frac{1}{R+h} \left[\begin{bmatrix} v_{eb,E}^n \\ -v_{eb,N}^n \\ -v_{eb,E}^n \tan \mathcal{B} \end{bmatrix} \times \right]. \tag{2.36}$$

The solution of the attitude update Eq. (2.34) at a time t, based on an initial orientation at time t_0, is given by the matrix exponential (Farrell, 2008, p. 55)

$$\mathbf{C}_b^n(t) = \mathbf{C}_b^n(t_0) \exp^{\int_{t_0}^{t} \boldsymbol{\Omega}_{nb}^b \, dt}. \tag{2.37}$$

The steps that led to Eq. (2.37) followed a mere mathematical derivation. Before the evaluation of the integral and the matrix exponential is discussed, some more background will help to understand the meaning of the equation.

In general, the dynamics of a rotation vector $\boldsymbol{\delta}$ are expressed by the following differential equation (Bortz, 1971),

$$\dot{\boldsymbol{\delta}} = \boldsymbol{\omega} + \dot{\boldsymbol{\sigma}}, \tag{2.38}$$

whereas $\boldsymbol{\omega}$ is the angular rate of the frame. The term $\dot{\boldsymbol{\sigma}}$ is representing the change of the rotation vector which is not[2] "inertially measureable" (Bortz, 1971), with the corresponding differential equation

$$\dot{\boldsymbol{\sigma}} = \frac{1}{2} \boldsymbol{\delta} \times \boldsymbol{\omega} + \frac{1}{\delta^2} \left(1 - \frac{\delta \sin \delta}{2(1 - \cos \delta)} \right) \boldsymbol{\delta} \times (\boldsymbol{\delta} \times \boldsymbol{\omega}). \tag{2.39}$$

[2] The representation of finite rotations around different axes, as needed in strapdown computation, is in general non-commutative and an additional deviation needs to be considered.

This can be approximated by

$$\dot{\boldsymbol{\sigma}} = \frac{1}{2}\boldsymbol{\alpha} \times \boldsymbol{\omega}, \tag{2.40}$$

such that, by combining Eq. (2.38) and (2.40),

$$\dot{\boldsymbol{\delta}} = \boldsymbol{\omega} + \frac{1}{2}\boldsymbol{\alpha} \times \boldsymbol{\omega}. \tag{2.41}$$

Here, $\boldsymbol{\alpha}$ is the integrated angular rate

$$\boldsymbol{\alpha} = \int_{t_1}^{t_2} \boldsymbol{\omega}(t)\, dt. \tag{2.42}$$

The solution of the rotation vector differential equation can be represented as a rotation vector increment $\boldsymbol{\delta}$,

$$\boldsymbol{\delta} = \int_{t_1}^{t_2} \left(\boldsymbol{\omega}(t) + \frac{1}{2}\boldsymbol{\alpha}(t) \times \boldsymbol{\omega}(t) \right) dt. \tag{2.43}$$

As $\boldsymbol{\delta}$ is an increment, the integration constant, i.e. initial value of $\boldsymbol{\delta}$ at t_1, can be set to zero. By using the property of the vector product,

$$\mathbf{a} \times \mathbf{b} = -\mathbf{b} \times \mathbf{a}, \tag{2.44}$$

the equation (2.43) under consideration of the coordinate frame indices can be reformulated:

$$\boldsymbol{\delta} = \int_{t_1}^{t_2} \left(\boldsymbol{\omega}_{nb}^{b}(t) - \frac{1}{2}\boldsymbol{\omega}_{nb}^{b}(t) \times \boldsymbol{\alpha}(t) \right) dt. \tag{2.45}$$

The second term represents the orientation change of the rotation axis during the integration interval, often called coning term. To express the term in dependency of the object rate only, the equation under inclusion of Eq. (2.42) needs to be slightly adapted:

$$\boldsymbol{\delta} = \int_{t_1}^{t_2} \left(\boldsymbol{\omega}_{nb}^{b}(t) - \frac{1}{2}\boldsymbol{\omega}_{nb}^{b}(t) \times \int_{t_1}^{t} \boldsymbol{\omega}_{nb}^{b}(\tau)\, d\tau \right) dt. \tag{2.46}$$

Note that the integral for the rotation axis can be computed with a different frequency, culminating in two-level strapdown computation algorithms like presented in Savage (1998a). A closed solution under the assumption of constant values of $\boldsymbol{\Omega}_{nb}^{b}$ would result in:

$$[\boldsymbol{\delta}\times] = \boldsymbol{\Omega}_{nb}^{b} \Delta t. \tag{2.47}$$

With this information, Eq. (2.37) can be reformulated,

$$\mathbf{C}_b^n(t_2) = \mathbf{C}_b^n(t_1) \exp[\boldsymbol{\delta}\times]. \tag{2.48}$$

This matrix exponential $\exp[\boldsymbol{\delta}\times]$ is defined as an infinite power series

$$\exp[\boldsymbol{\delta}\times] = \sum_{k=0}^{\infty} \frac{1}{k!}[\boldsymbol{\delta}\times]^k. \tag{2.49}$$

For skew-symmetric matrices, like $[\boldsymbol{\delta}\times]$ under neglect of the coning motion, the power series actually has a closed representation in the form of the Rodrigues equation, Eq. (2.10). This, however, holds only true if the value of the matrix is constant. For high data rate, and thus small values of Δt, this requirement can be considered as fulfilled, so that

$$\exp[\boldsymbol{\delta}\times] = \mathbf{I} + \frac{\sin\delta}{\delta}[\boldsymbol{\delta}\times] + \frac{1-\cos\delta}{\delta^2}[\boldsymbol{\delta}\times]^2. \tag{2.50}$$

The solution for the attitude update can thus be formulated:

$$\mathbf{C}_b^n(t_2) = \mathbf{C}_b^n(t_1) \left(\mathbf{I} + \frac{\sin\delta}{\delta}[\boldsymbol{\delta}\times] + \frac{1-\cos\delta}{\delta^2}[\boldsymbol{\delta}\times]^2 \right). \tag{2.51}$$

Velocity and Position Update

The differential equation of the velocity change has been introduced in Eq. (2.29),

$$\dot{\mathbf{v}}_{eb}^{n} = \mathbf{C}_{b}^{n}\mathbf{f}_{ib}^{b} - \left[2\boldsymbol{\Omega}_{ie}^{n} + \boldsymbol{\Omega}_{en}^{n}\right]\mathbf{v}_{eb}^{n} + \mathbf{g}^{n}. \tag{2.52}$$

The velocity increment $\Delta\mathbf{v}^{b}$ is given by a superposition of the integrated specific forces and a term resulting from a change of the quantity during the integration time, resulting from both the change of the acceleration vector and the rotation vector. This term can be combined (Savage, 1998b), so the final equation is:

$$\Delta\mathbf{v}^{b} = \boldsymbol{\nu} + \Delta\mathbf{v}_{\mathrm{rot}} \tag{2.53}$$

whereas $\boldsymbol{\nu}$ are the integrated specific forces during the time interval,

$$\boldsymbol{\nu} = \int_{t_1}^{t_2} \mathbf{f}_{ib}^{b}(t)\, dt, \tag{2.54}$$

and $\Delta\mathbf{v}_{\mathrm{rot}}$ is the term resulting from the change of the rotation vector with respect to the inertial frame, here expressed as $\boldsymbol{\alpha}_{f}$, as well as the specific force during the integration time.

$$\Delta\mathbf{v}_{\mathrm{rot}} = \int_{t_1}^{t_2} \left(\boldsymbol{\alpha}_{f}(t) \times \mathbf{f}_{ib}^{b}(t)\right)\, dt. \tag{2.55}$$

This velocity increment represents the integrated velocity differential equation of the time step $t_1 \rightarrow t_2$ and can be added to the total velocity increment $\Delta\mathbf{v}^{b}$.

In order to describe the equation in dependency of the IMU measurement $\mathbf{f}_{ib}^{b}$ and $\boldsymbol{\omega}_{ib}^{b}$, it needs to be adapted slightly. So the previous equation,

$$\Delta\mathbf{v}^{b} = \int_{t_1}^{t_2} \mathbf{f}_{ib}^{b}(t)\, dt + \int_{t_1}^{t_2} \left(\boldsymbol{\alpha}_{f}(t) \times \mathbf{f}_{ib}^{b}(t)\right)\, dt, \tag{2.56}$$

turns into

$$\Delta\mathbf{v}^{b} = \int_{t_1}^{t_2} \mathbf{f}_{ib}^{b}(t)\, dt + \int_{t_1}^{t_2} \left[\left(\int_{t_1}^{t} \boldsymbol{\Omega}_{ib}^{b}(\tau)\, d\tau\right)\mathbf{f}_{ib}^{b}(t)\right]\, dt. \tag{2.57}$$

In case of constant inertial quantities, again, the result yields:

$$\Delta\mathbf{v}^{b} = \mathbf{f}_{ib}^{b}\Delta t + \frac{1}{2}\boldsymbol{\Omega}_{ib}^{b}\mathbf{f}_{ib}^{b}\Delta t^{2}. \tag{2.58}$$

The velocity in the target n-frame can finally be updated according to the numerical solution to Eq. (2.52):

$$\mathbf{v}_{eb}^{n}(t_2) = \mathbf{v}_{eb}^{n}(t_1) + \mathbf{C}_{b}^{n}\Delta\mathbf{v}^{b} - \left(\boldsymbol{\Omega}_{en}^{n} + 2\boldsymbol{\Omega}_{ie}^{n}\right)\mathbf{v}_{eb}^{n}(t_1)\Delta t + \mathbf{g}^{n}\Delta t. \tag{2.59}$$

For the position update, more sophisticated techniques can be found in Savage (1998b). The change of the velocity and orientation during the integration interval, an effect which is called "scrolling" there, is discussed in detail. In the scope of this thesis, a simple trapezoid rule shall be sufficient,

$$\mathbf{x}_{eb}^{n}(t_2) = \mathbf{x}_{eb}^{n}(t_1) + \Delta\mathbf{x}^{n}, \tag{2.60}$$

where

$$\Delta\mathbf{x}^{n} \approx \frac{1}{2}\left(\mathbf{v}_{eb}^{n}(t_2) + \mathbf{v}_{eb}^{n}(t_1)\right)\Delta t. \tag{2.61}$$

2.4 State Space Representation of a System

An alternative representation of the differential equations are given in state space theory. In order to proceed, a short introduction to the state space formalism is deemed highly useful. This allows for a more compact description of dynamic systems by representing the state of the system, one is interested in modeling, in a state vector $\mathbf{x}$. The system can then be solved and different aspects can be analyzed. The general signal flow is depicted in Fig. 2.7.

Consider the following time-invariant linear (LTI) system of ordinary differential equations (ODE)

$$\begin{aligned} \dot{\mathbf{x}} &= \mathbf{A}\mathbf{x} + \mathbf{B}\mathbf{u} + \mathbf{G}\mathbf{w}, \\ \mathbf{y} &= \mathbf{H}\mathbf{x} + \mathbf{v}. \end{aligned} \tag{2.62}$$

The solution can be achieved in different ways. The first one that is covered here is the solution in complex frequency domain, with the complex frequency s. The system in Eq. (2.62), transformed with the Laplace operator $\mathcal{L}\{...\}$, cf. Appendix A.2, reads

$$\begin{aligned} s\mathbf{X}(s) + \mathbf{x_0} &= \mathbf{A}\mathbf{X}(s) + \mathbf{B}\mathbf{U}(s) + \mathbf{G}\mathbf{W}(s), \\ \mathbf{Y}(s) &= \mathbf{H}\mathbf{X}(s) + \mathbf{V}(s). \end{aligned} \tag{2.63}$$

The solution for $\mathbf{X}$ can be obtained by some rearrangement, with $\mathbf{F} = (s\mathbf{I} - \mathbf{A})^{-1}$:

$$\mathbf{X} = \mathbf{F}\mathbf{x_0} + \mathbf{F}\mathbf{B}\mathbf{U} + \mathbf{F}\mathbf{G}\mathbf{W}. \tag{2.64}$$

$\mathbf{x}, \mathbf{X}$ = state vector in time and frequency domain
$\mathbf{x}_0$ = state vector initial conditions
$\mathbf{u}, \mathbf{U}$ = control vector in time and frequency domain
$\mathbf{w}, \mathbf{W}$ = perturbation vector in time and frequency domain
$\mathbf{y}, \mathbf{Y}$ = observation vector in time and frequency domain
$\mathbf{v}, \mathbf{V}$ = observation noise vector in time and frequency domain
$\mathbf{A}$ = system dynamic matrix
$\mathbf{B}$ = control input matrix
$\mathbf{G}$ = perturbation input matrix
$\mathbf{H}$ = observation matrix
$\mathbf{F}$ = state transition matrix

Transformed back into time domain, the solution reads (Gelb, 2001, p. 66):

$$\mathbf{x}(t) = \mathbf{F}(t - t_0)\mathbf{x}(t_0) + \int_{t_0}^{t} \mathbf{F}(t - \tau)\mathbf{B}(\tau)\mathbf{u}(\tau)\, d\tau + \int_{t_0}^{t} \mathbf{F}(t - \tau)\mathbf{G}(\tau)\mathbf{w}(\tau)\, d\tau. \tag{2.65}$$

One can differentiate between the homogeneous solution $\mathbf{F}(t - t_0)\mathbf{x}(t_0)$ describing the time evolution of the unperturbed system, and the particular solutions $\int_{t_0}^{t} \mathbf{F}(t - \tau)\mathbf{B}(\tau)\mathbf{u}(\tau)\, d\tau$ for control signals and $\int_{t_0}^{t} \mathbf{F}(t - \tau)\mathbf{G}(\tau)\mathbf{w}(\tau)\, d\tau$ for perturbation signals.

In the case that $\mathbf{F}$ is not constant, the equation can also be transformed into a recursive form. Discretization of Eq. (2.65) yields

$$\mathbf{x_k} = \mathbf{F_k}\mathbf{x_{k-1}} + \mathbf{B_k}\mathbf{u_k} + \mathbf{G_k}\mathbf{w_k}, \tag{2.66}$$

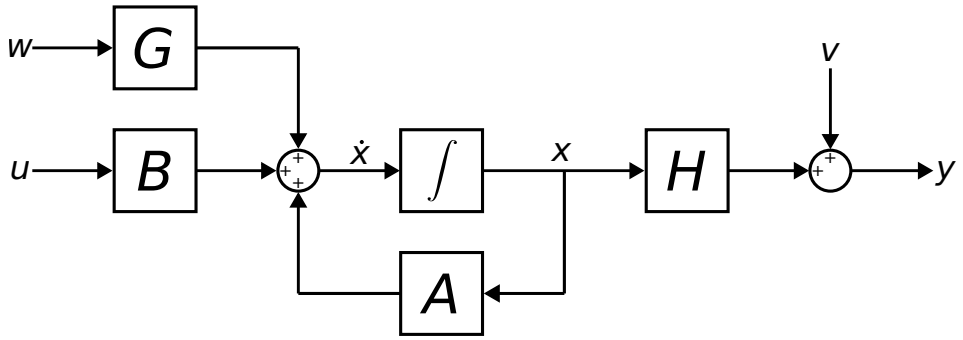

Figure 2.7: State space representation of a system with deterministic input u and stochastic input w to the dynamic system, and v as additive observation noise.

with $\mathbf{x_k}$ as the solution of the system state vector based on its previous value $\mathbf{x_{k-1}}$, as well as $\mathbf{u_k}$ and $\mathbf{w_k}$ as control and perturbation vectors, respectively. The terms $\mathbf{B}_k\mathbf{u}_k$ and $\mathbf{G}_k\mathbf{w_k}$ resemble the solved integrals in Eq. (2.65).

Another method that may be applied in order to represent the transition matrix is by solving the ODE system with the power series of the matrix exponential again,

$$\mathbf{F}(t-t_0) = \mathbf{I} + \mathbf{A}\Delta t + \frac{1}{2}\mathbf{A}^2\Delta t^2 + ... + \frac{1}{n!}\mathbf{A}^n\Delta t^n. \tag{2.67}$$

Unlike the case with the skew-symmetric system dynamic matrix, that allowed the closed solution in Eq. (2.51), this series does not necessarily converge and eventually needs to be truncated. The particular solutions can then be gained analogous according to Eq. (2.65).

Transfer Function

The ratio of the output $\mathbf{Y}(s)$ and the input $\mathbf{U}(s)$ of the system is called transfer function $\mathbf{T}(s)$. After plugging Eq. (2.64) into the system output Eq. (2.63), assuming the initial conditions $\mathbf{x}_0 = \mathbf{0}$ and under neglect of the noise processes $\mathbf{W}(s)$ and $\mathbf{V}(s)$, the transfer function reads in s-domain:

$$\mathbf{T}(s) = \frac{\mathbf{Y}(s)}{\mathbf{U}(s)} = \mathbf{H}(s)\mathbf{F}(s)\mathbf{B}(s). \tag{2.68}$$

This method is mainly used for the propagation of spectral densities in (complex) frequency domain.

Solution to Non-Linear Differential Equation Systems Using Error States

In a general system of nonlinear differential equations,

$$\dot{\mathbf{x}}(t) = \mathbf{f}(\mathbf{x}(t)), \tag{2.69}$$

an error $\boldsymbol{\delta}\mathbf{x}$ is applied to the state vector $\mathbf{x}$,

$$\dot{\mathbf{x}}(t) + \boldsymbol{\delta}\dot{\mathbf{x}}(t) = \mathbf{f}(\mathbf{x}(t) + \boldsymbol{\delta}\mathbf{x}(t)). \tag{2.70}$$

The equations in $\mathbf{f}(\mathbf{x} + \boldsymbol{\delta}\mathbf{x})$ are developed by Taylor series expansion at the operating point $\mathbf{x}$ (Papula, 2007, p. 569),

$$\dot{\mathbf{x}}(t) + \boldsymbol{\delta}\dot{\mathbf{x}}(t) \approx \mathbf{f}(\mathbf{x}) + \frac{\partial \mathbf{f}}{\partial \mathbf{x}}|_x \left(\mathbf{x} + \boldsymbol{\delta}\mathbf{x} - \mathbf{x}\right) + \mathcal{O}\left(t, \mathbf{x}, \boldsymbol{\delta}\mathbf{x}\right), \tag{2.71}$$

with $\mathcal{O}$ denoting higher order terms, which are subsequently neglected.
Replacing $\mathbf{f}(x)$ by Eq. (2.69) and with $\mathbf{A}(\mathbf{x}) = \frac{\partial \mathbf{f}}{\partial \mathbf{x}}(\mathbf{x})|_x$, the following system results

$$\dot{\boldsymbol{\delta}\mathbf{x}} = \mathbf{A}(\mathbf{x})\boldsymbol{\delta}\mathbf{x}. \tag{2.72}$$

With a given operating point, the equation can now be solved analogous to the linear system. This point can be acquired by a prior state estimate, or in the case of the observation equation $\mathbf{H}(\mathbf{x})$ by a prediction based on the dynamic model.

2.5 Modeling Inertial Sensors

2.5.1 Sensor and Error Models

The measurement equation of a generic accelerometer in its specific coordinate frame can be modeled as following, cf. e.g. Farrell et al. (2022), or Lam et al. (2003),

$$\mathbf{f}_{\text{out}} = (\mathbf{I} + \mathbf{S_a} + \mathbf{M_a})\mathbf{f}_{\text{in}} + \mathbf{b_a} + \mathbf{n_a}. \tag{2.73}$$

Here, $\mathbf{f}_{\text{in}}$ is the true specific force, while $\mathbf{f}_{\text{out}}$ is the output of the sensor. $\mathbf{I}$ is the identity matrix, $\mathbf{S_a}$ is a diagonal matrix with its entries representing a scale error. $\mathbf{M_a}$ is a skew symmetric matrix representing correlations and misalignment between the sensor axes, and $\mathbf{b_a}$ is a systematic offset of the signal, i.e. bias. Additional random noise processes are represented by $\mathbf{n_a}$. Depending on the accelerometer technology and the application, extensions of the model are possible. This might include sensitivities to angular accelerations and anisoelastic biases (IEEE, 2019).

For a general gyroscope, the model and the parameters (here with subscript g) are, analogous to Eq. (2.73),

$$\boldsymbol{\omega}_{\text{out}} = (\mathbf{I} + \mathbf{S_g} + \mathbf{M_g})\boldsymbol{\omega}_{\text{in}} + \mathbf{b_g} + \mathbf{n_g}. \tag{2.74}$$

Other error terms like an acceleration sensitive term might be added, depending on the specific gyroscope technology or the application. The Institute of Electrical and Electronics Engineers (IEEE) publishes specifications for different sensors, e.g. IEEE (2021) for FOG based systems, and IEEE (2006) for ring laser gyroscopes. The systematic error models in the context of this thesis are kept general on purpose.

Next to the systematic error, **stochastic errors** are present in the signals of the IMU. For the characterization of the uncertainty in signals, a method proposed by Allan (1966) can be utilized. While this method was initially developed for the characterization of atomic frequency standards, it is usually applied to other time-series like inertial measurement data as well. The method works as follows: the variance $\sigma^2(\tau)$ of averaged data from subsequent chunks with certain window sizes is calculated. The window size is systematically increased and for each size, the variance calculated. This specific variance, which depends on the averaging time, is called Allan variance. In the entirety of this thesis an extended form, the overlapping Allan variance, is used, cf. Appendix A.4.1. The abbreviation AV is used for this extension.

The Allan standard deviation (AD) is the square root of the AV. As a demonstrative example, the AD of static IMU acceleration and angular rate measurements is depicted in Fig. 2.8. In the analyzed acceleration data, three different processes are apparent:

For small sampling times, the white noise is the dominating noise process. This is corresponding to the natural observation, that the variance of a pure white process is decreasing with the amount of data accumulated, i.e. the more data of *something* is collected, the more the uncertainty about this *something* can be reduced. For a continuous time series of data,

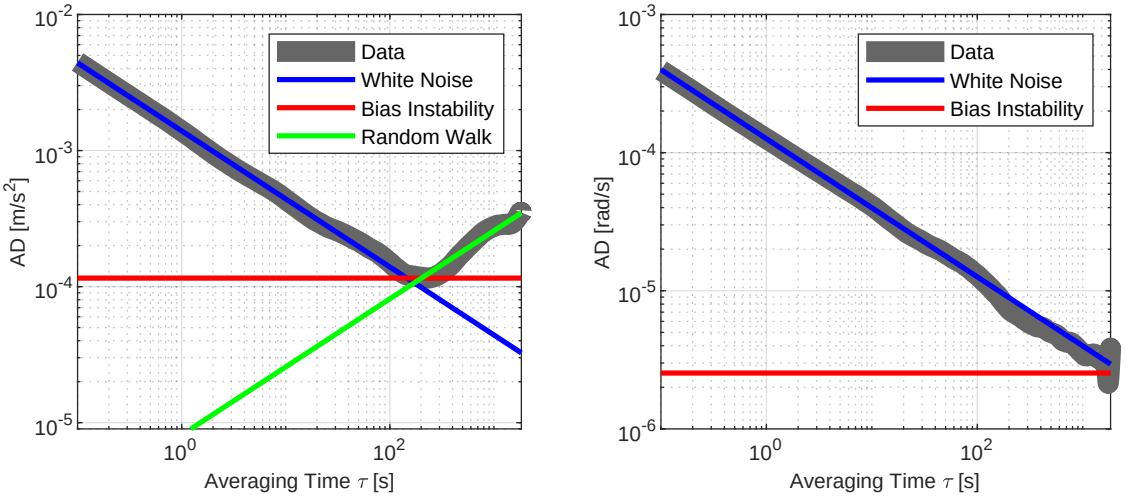

Figure 2.8: Overlapping Allan deviation of data on a horizontal axis gathered from a tactical/navigation grade IMU (iMAR, 2017a). Left: acceleration measurements. Right: angular rate measurements. At low integration times, white noise (indicated by a blue line) with a characteristic slope of -0.5 per decade of τ is the dominating process. At a certain point, the flicker floor (red) is reached. Later, random walk (green line) and other drift effects are occurring. The angular rates do not exhibit any drift in the considered time frame and the flicker floor is barely visible.

the time τ corresponds to the amount of data samples collected, so the resulting variance is proportional to $\sim \frac{1}{\tau}$. In double logarithmic representation this corresponds to a -1 decade reduction of the variance per decade of τ ($-\frac{1}{2}$ for AD). The characteristic technical value is the **white noise density** N^2, with is related to the AV $\sigma_N^2(\tau)$ via

$$\sigma_N^2(\tau) = \frac{N^2}{\tau}. \tag{2.75}$$

This quantity is often provided in sensor data sheets by the manufacturer. For accelerometers it is labeled velocity random walk (VRW), as the white noise in the accelerations can be interpreted as differentiation of the uncertainty of the velocity increments of the accelerometer, following the convention of Itō and McKean (1996). The corresponding term in the case of gyroscope signals is angular random walk (ARW). Typical units are $\mathrm{m/s^2/\sqrt{Hz}}$ for the VRW, and $\mathrm{rad/s/\sqrt{Hz}}$ for the ARW, respectively. In this example, values of $N_a = 1.3951 \times 10^{-3}\,\mathrm{m/s^2/\sqrt{Hz}}$ for the accelerometer, and $N_g = 1.2606 \times 10^{-4}\,\mathrm{rad/s/\sqrt{Hz}}$ for the gyroscope have been determined.

The $\frac{1}{\tau}$ trend is discontinued after a certain time τ_B. The AD reaches a plateau in which no reduction of the variance can be achieved anymore by larger sample window sizes. This **flicker floor** is a result of dominant processes correlated in time. The label is carried over from the flicker noise, an often occurring process in any sensor involving electronic parts. The corresponding technical value is the bias instability B. It is related to the variance σ_B^2 at the flicker floor via

$$\sigma_B^2(\tau) = \frac{2}{\pi} B^2 \ln(2). \tag{2.76}$$

In this example, values of $B_a = 1.7387 \times 10^{-4}\,\mathrm{m/s^2}$ for the accelerometer, and $B_g = 3.8204 \times 10^{-6}\,\mathrm{rad/s}$ for the gyroscope have been determined.

For even longer sampling times, long periodic shifts of the signal are visible. This is often caused by **random walk** processes, but can also result from a systematic change of the signal, e.g. due to tidal effects and similar. The former is characterized by an increase of the variance by 1 decade per decade of τ. A characteristic technical value is often not given in data sheets,

but can be assessed over the AV as well. The connection of the rate random walk K^2 to the corresponding $\sigma_K^2(\tau)$ is (IEEE, 2021)

$$\sigma_K^2(\tau) = \frac{K^2\tau}{3}. \tag{2.77}$$

In practice, the line in Fig. 2.8 which corresponds to the random walk needs to be extended, so the value of $\sigma_K^2(\tau)$ at $\tau = 3\,\mathrm{s}$ can be extracted. In this example, a value of $K_a = 2.6156 \times 10^{-4}\,\mathrm{m/s^3/\sqrt{Hz}}$ has been determined for the accelerometer. The random walk of the gyroscope is not visible even after one hour of integration.

It is also possible to formulate noise processes in frequency domain. The characteristic slopes of the single processes make it reasonable to represent the power spectral density (PSD) S of the complete signal as a weighted sum of power law processes, such that

$$S(f) = \sum_{\alpha} h_\alpha f^\alpha, \tag{2.78}$$

whereas the exponent α of the frequencies f is an integer corresponding to the asymptotic behavior, i.e. slope, of the process in the frequency domain. The coefficients h_α can be related to the results of the AD analysis as following (Farrell et al., 2022),

$$h_0 = N^2, \tag{2.79}$$

$$h_{-1} = \frac{B^2}{2\pi}, \tag{2.80}$$

$$h_{-2} = \frac{K^2}{(2\pi)^2}. \tag{2.81}$$

Notably, the white noise has a constant PSD for all frequencies. This leads to some peculiar attributes for the state space representation of such a process.

2.5.2 Stochastic Input to LTI Systems

There is one point of particular interest, if the system from Eq. (2.62) is affected by random processes $\mathbf{w}$,

$$\dot{\mathbf{x}} = \mathbf{A}\mathbf{x} + \mathbf{G}\mathbf{w}. \tag{2.82}$$

Let $\mathbf{P}(t) = E[\mathbf{x}(t)\mathbf{x}(t)^\mathrm{T}]$ denote the covariance matrix of the state vector, then the homogeneous solution is

$$\mathbf{P}(t) = \mathbf{F}(t - t_0)\mathbf{P}(t_0)\mathbf{F}^\mathrm{T}(t - t_0). \tag{2.83}$$

The propagation of the complete uncertainties is formally

$$\begin{aligned}\mathbf{P}(t) =& \mathbf{F}(t - t_0)\mathbf{P}(t_0)\mathbf{F}^\mathrm{T}(t - t_0) \\ &+ \int_{t_0}^{t} \mathbf{F}(t - \tau)\mathbf{G}(\tau)\mathbf{Q}_{ww}\mathbf{G}^\mathrm{T}(\tau)\mathbf{F}^\mathrm{T}(t - \tau)\, d\tau,\end{aligned} \tag{2.84}$$

with $\mathbf{Q}_{ww}$ being the covariance matrix of the input processes.

One way to model stochastic processes is the white noise process. As introduced before, white noise is uncorrelated in time, and yields a constant spectral density. For a continuous time white noise process $q(t)$, the following mean and variance definitions can be stated, cf. Britting (1971, p. 237), Brown and Hwang (2012, p. 75) or Maybeck (1979, p. 154):

$$\begin{aligned}E\langle q(t)\rangle &= 0, \\ E\langle q(t)q(t_0)\rangle &= N^2\delta(t - t_0).\end{aligned} \tag{2.85}$$

where $E\langle ... \rangle$ denotes the expectation value or ensemble average. This process corresponds to a zero-mean Gaussian function. Furthermore, the Dirac δ function implies that the process is not correlated in time, which is a so-called Markov property. Thus, the class of processes, that are covered by this formalism, are called Gauss-Markov processes.

This white noise model can be used as raw input to the system, or manipulated by another shaping filter in order to produce colored noise signals. A detailed derivation can be found in Appendix A.4.2. The most prominent examples are the following.

Example: White Noise

Assume a simple, one dimensional system with the following differential equations,

$$\begin{aligned} \dot{x} &= v, \\ \dot{v} &= q. \end{aligned} \tag{2.86}$$

which is affected by a velocity random walk process q with power spectral density N^2, acting as input to the system. The state vector reads $\mathbf{x} = [x, v]^{\mathrm{T}}$. The system dynamic and input matrices read

$$\mathbf{A} = \frac{\partial \dot{\mathbf{x}}}{\partial \mathbf{x}} = \begin{bmatrix} 0 & 1 \\ 0 & 0 \end{bmatrix}, \qquad \mathbf{G} = \frac{\partial \dot{\mathbf{x}}}{\partial \mathbf{w}} = \begin{bmatrix} 0 \\ 1 \end{bmatrix}. \tag{2.87}$$

The transition matrix $\mathbf{F}(t) = \mathcal{L}^{-1}\{(s\mathbf{I} - \mathbf{A})^{-1}\}$ results in

$$\mathbf{F}(t) = \begin{bmatrix} 1 & t \\ 0 & 1 \end{bmatrix}. \tag{2.88}$$

By neglecting the initial uncertainty $\mathbf{P}(0)$ of the system, the process noise matrix

$$\mathbf{Q}(t) = \int_0^t \mathbf{F}(t-\tau)\mathbf{G}(\tau)N^2\mathbf{G}(\tau)^{\mathrm{T}}\mathbf{F}(t-\tau)^{\mathrm{T}}\, d\tau \tag{2.89}$$

is equal to the total uncertainty of the state, so that

$$\mathbf{P}(t) = \mathbf{Q}(t) = \begin{bmatrix} \frac{1}{3}N^2t^3 & \frac{1}{2}N^2t^2 \\ \frac{1}{2}N^2t^2 & N^2t \end{bmatrix}. \tag{2.90}$$

Example: Random Walk

Many non-white processes can be modeled as independent systems with white noise as input. To include random walk into the model, the differential equation system is extended,

$$\begin{aligned} \dot{x} &= v, \\ \dot{v} &= a, \\ \dot{a} &= q. \end{aligned} \tag{2.91}$$

This time, the input q is an acceleration random walk process with power spectral density K^2. The computation steps are identical to the white noise example, and the following covariance matrix is resulting,

$$\mathbf{Q}(t) = \begin{bmatrix} \frac{1}{20}K^2t^5 & \frac{1}{8}K^2t^4 & \frac{1}{6}K^2t^3 \\ \frac{1}{8}K^2t^4 & \frac{1}{3}K^2t^3 & \frac{1}{2}K^2t^2 \\ \frac{1}{6}K^2t^3 & \frac{1}{2}K^2t^2 & K^2t \end{bmatrix}. \tag{2.92}$$

If velocity and acceleration random walk are modeled, the two process noise matrices can simply be added, after filling the last line and column of the matrix associated with the VRW with zeroes.

The propagated noise processes can already be applied to estimate the drift of a strapdown navigation solution in Down direction of the n-frame. It occurs that the error is growing unbounded with time. The $\mathbf{n}_1$- and $\mathbf{n}_2$-axis in a terrestrial reference frame, however, yield some interesting aspects. This will now be elaborated in more detail.

2.6 Strapdown Navigation Error Propagation

After models for IMU sensor errors were presented, including the extraction of the parameters from raw static sensor data, the final part of this chapter covers the analysis of the impact of those errors on the strapdown navigation solution. There are a number of feedback loops involved that affect the dynamics of the system. The signal flow in a strapdown inertial navigation system for intermediate durations is depicted in Fig. 2.9. The position errors in

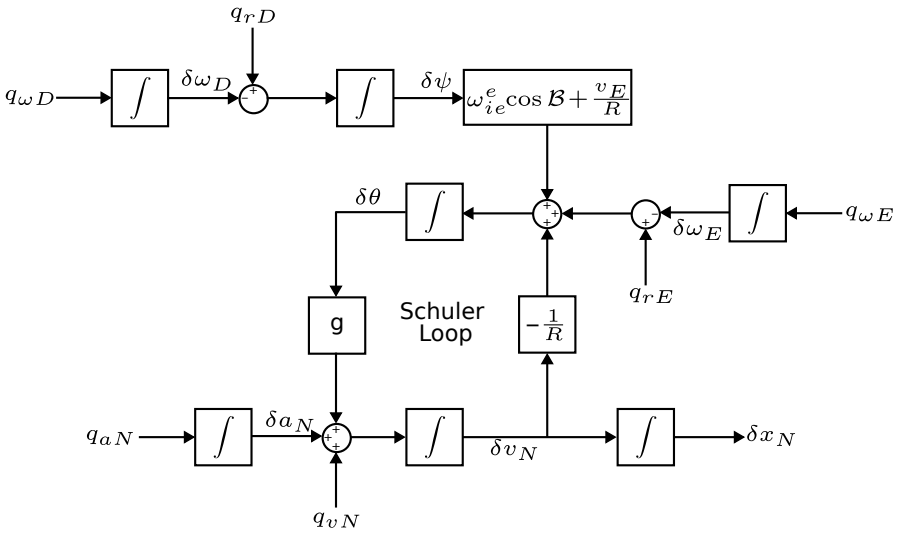

Figure 2.9: Medium-term signal flow in a strapdown inertial navigation system for the North channel. The position errors are modulated by the Schuler loop, resulting from the interaction between the velocity error δv_N and the orientation error $\delta\theta$. The remaining variables and noise processes are explained below Eq. (2.93).

North and East direction are modulated by the **Schuler loop**, resulting from a wrong estimate of the orientation and thus a wrong correction of gravity. In a strapdown navigation system, this loop actually provides an "automatic response" to the error, as pointed out by Tazartes (2014). In the case of a gyro-stabilized platform, the mechanical time constants of the system need to be adapted to this period – a necessity that became known as "Schuler-tuning".

Another long periodic effect which is not visible in Fig. 2.9 is the **Foucault loop**. This effect corresponds to an error in velocity, and further depends on the latitude. The minimum period to be expected is 24 hours at a latitude of 90°. The closer the user is positioned to the equator, the longer the period. Finally, the **Earth rate** itself, with a period of roughly 24 hours, has a periodic impact on the East channel/longitude. For navigation over (very) long periods of time, those oscillations need to be considered as well. In the scope of this thesis, intervals of about an hour are relevant. Thus, a reduced system model, which covers the intermediate time effects, is sufficient.

The differential equations describing the North channel of a strapdown navigation system from Titterton and Weston (2009, p. 350) are extended by the stochastic perturbations,

$$\begin{aligned}
\dot{\delta x}_N &= \delta v_N, \\
\dot{\delta v}_N &= g\delta\theta + \delta a_N + q_{vN}, \\
\dot{\delta a}_N &= q_{aN}, \\
\dot{\delta\theta} &= (\omega_{ie}^e \cos(\mathcal{B}) + \frac{v_E}{R})\delta\psi - \frac{1}{R}\delta v_N - \delta\omega_E + q_{rE}, \\
\dot{\delta\omega}_E &= q_{\omega E}, \\
\dot{\delta\psi} &= -\delta\omega_D + q_{rD}, \\
\dot{\delta\omega}_D &= q_{\omega D}.
\end{aligned} \tag{2.93}$$

δx_N = position error component of $\mathbf{x}_{eb}^n$ in North direction [m]
δv_N = velocity error component of $\mathbf{v}_{eb}^n$ in North direction [m/s]
δa_N = acceleration error in North direction [m/s^2]
$\delta\theta, \delta\psi$ = inclination and yaw angle error components of $\mathbf{C}_b^n$ [rad]
$\delta\omega_E, \delta\omega_D$ = gyroscope bias in East and Down direction [rad/s]
q_{vN} = North velocity random walk process with PSD N_a^2 [m^2/s^3]
q_{aN} = North acceleration random walk process with PSD K_a^2 [m^2/s^5]
q_{rE}, q_{rD} = East and Down angle random walk process with PSD N_g^2 [rad^2/s]
$q_{\omega E}, q_{\omega D}$ = East and Down rate random walk process with PSD K_g^2 [rad^2/s^3]
$\mathcal{B}$ = latitude [rad]
ω_{ie}^e = Earth angular rate magnitude [rad/s]
R = Earth radius [m]
v_E = velocity component of $\mathbf{v}_{eb}^n$ in East direction [m/s]
g = magnitude of the gravity [m/s^2]

It is obvious from the differential equations that this model is based on some conditions like the constant velocity v_E, gravity g, latitude $\mathcal{B}$ and height which is assumed to be part of the Earth radius R. It is mainly useful to get insight into the long-term behavior of the strapdown inertial navigation algorithm. More advanced solutions including all states can be numerically computed, cf. Blankinship (2008); Savage (2000), but the vastly increased complexity does not necessarily give more insight into the system behavior, as Britting (1971) pointed out early. The latter is also an excellent pioneering work regarding an analytical solution and discussion of a number of different inertial navigation systems and state vector configurations.

The system can be formulated as introduced in the error state representation Eq. (2.72). Additionally, a perturbation $\mathbf{Gw}$ is applied which will subsequently be used to include the IMU noise processes,

$$\dot{\delta\mathbf{x}} = \mathbf{A}(\mathbf{x})\delta\mathbf{x} + \mathbf{Gw}. \tag{2.94}$$

The state vector is set to

$$\delta\mathbf{x} = [\delta x_N, \delta v_N, \delta a_N, \delta\theta, \delta\omega_E, \delta\psi, \delta\omega_D]^{\mathrm{T}}. \tag{2.95}$$

The system dynamics matrix reads

$$\mathbf{A} = \begin{bmatrix} 0 & 1 & 0 & 0 & 0 & 1 & 0 \\ 0 & 0 & 1 & g & 0 & 0 & 0 \\ 0 & 0 & 0 & 0 & 0 & 0 & 0 \\ 0 & -\frac{1}{R} & 0 & 0 & -1 & \omega_{ie}^{e}\cos(\mathcal{B}) + \frac{v_E}{R} & 0 \\ 0 & 0 & 0 & 0 & 0 & 0 & 0 \\ 0 & 0 & 0 & 0 & 0 & 0 & -1 \\ 0 & 0 & 0 & 0 & 0 & 0 & 0 \end{bmatrix}. \tag{2.96}$$

The perturbation vector $\mathbf{w}$ consists of the following stochastic processes,

$$\mathbf{w} = [q_{vN}, q_{aN}, q_{rE}, q_{\omega E}, q_{rD}, q_{\omega D}]^{\mathrm{T}}, \tag{2.97}$$

with the corresponding perturbation matrix

$$\mathbf{G} = \begin{bmatrix} 0 & 0 & 0 & 0 & 0 & 0 \\ 1 & 0 & 0 & 0 & 0 & 0 \\ 0 & 1 & 0 & 0 & 0 & 0 \\ 0 & 0 & 1 & 0 & 0 & 0 \\ 0 & 0 & 0 & 1 & 0 & 0 \\ 0 & 0 & 0 & 0 & 1 & 0 \\ 0 & 0 & 0 & 0 & 0 & 1 \end{bmatrix}. \tag{2.98}$$

As a simplification, the stochastic perturbation is modeled as an effect in the n-frame. In a general case, those processes are associated with the axes of the IMU in the b-frame and can be transformed via Eq. (2.9), introducing additional error terms associated with the orientation. It is furthermore assumed that the orientation between b- and n-frame is constant.

In Laplace domain, the following representation of the transition matrix $\mathbf{F}(s)$ can be produced from $\mathbf{F}(s) = (s\mathbf{I} - \mathbf{A})^{-1}$, with $v^* = v_E + \omega_{ie}^{e} R\cos(\mathcal{B})$:

$$\mathbf{F}(s) = \begin{bmatrix} \frac{1}{s} & \frac{R}{Rs^2+g} & \frac{R}{s(Rs^2+g)} & \frac{Rg}{s(Rs^2+g)} & -\frac{Rg}{s^2(Rs^2+g)} & \frac{gv^*}{s^2(Rs^2+g)} & -\frac{gv^*}{s^3(Rs^2+g)} \\ 0 & \frac{Rs}{Rs^2+g} & \frac{R}{Rs^2+g} & \frac{Rg}{Rs^2+g} & -\frac{Rg}{s(Rs^2+g)} & \frac{gv^*}{s(Rs^2+g)} & -\frac{gv^*}{s^2(Rs^2+g)} \\ 0 & 0 & \frac{1}{s} & 0 & 0 & 0 & 0 \\ 0 & -\frac{1}{Rs^2+g} & -\frac{1}{s(Rs^2+g)} & \frac{Rs}{Rs^2+g} & -\frac{R}{Rs^2+g} & \frac{v^*}{Rs^2+g} & -\frac{v^*}{s(Rs^2+g)} \\ 0 & 0 & 0 & 0 & \frac{1}{s} & 0 & 0 \\ 0 & 0 & 0 & 0 & 0 & \frac{1}{s} & -\frac{1}{s^2} \\ 0 & 0 & 0 & 0 & 0 & 0 & \frac{1}{s} \end{bmatrix}. \tag{2.99}$$

Next some important aspects of this system will be elaborated. The first line of the matrix corresponds to the propagation of the state errors to the position error δx_N. The entries 3, 5 and 7 on this first line, notably, are resembling the impact of the acceleration and angular rate errors:

$$\frac{s\,\delta x_N(s)}{\delta a_N(s)} = \frac{R}{Rs^2+g} = \frac{1}{s^2+\frac{g}{R}}, \tag{2.100}$$

$$\frac{s\,\delta x_N(s)}{\delta \omega_E(s)} = -\frac{Rg}{s(Rs^2+g)} = -\frac{g}{s(s^2+\frac{g}{R})}, \tag{2.101}$$

$$\frac{s\,\delta x_N(s)}{\delta \omega_D(s)} = -\frac{g(v_E+\omega_{ie}^{e}R\cos(\mathcal{B}))}{s^2(Rs^2+g)} = -\frac{g(v_E+\omega_{ie}^{e}R\cos(\mathcal{B}))}{Rs^2(s^2+\frac{g}{R})}. \tag{2.102}$$

Note that each of the transitions yields an oscillation with the circular frequency $\omega_s^2 = \frac{g}{R}$. This corresponds to the Schuler loop, which occurs since the differential equation for

the inclination angle $\delta\theta$, i.e. the misalignment with respect to the gravity vector $\mathbf{g}$, has a dependency on the velocity δv_N and vice versa. This leads to the phenomenon that the effect of a constant acceleration bias on the horizontal position is actually bounded by the Schuler oscillation, cf. Fig. 2.10. This unfortunately is not the case for a bias of the gyroscopes, which, although modulated by the Schuler oscillation as well, has an additional integrator (in the case of $\delta\omega_E$) and even two integrators in the case of $\delta\omega_D$.

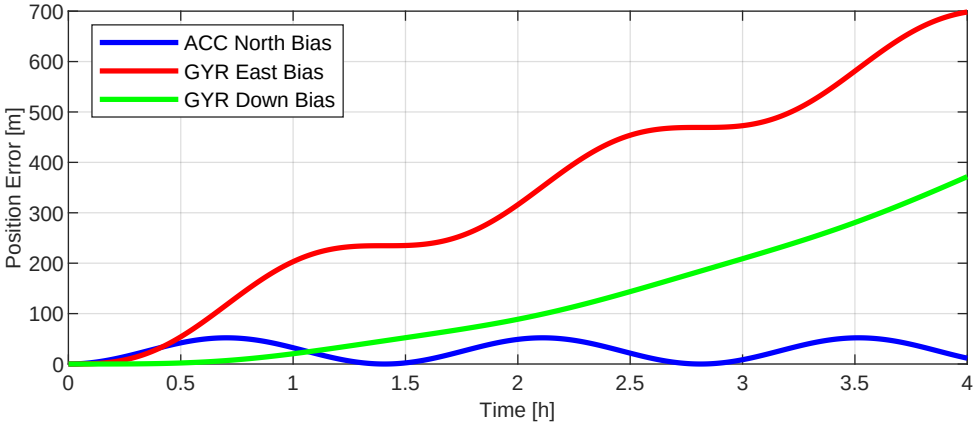

Figure 2.10: Position drift of a navigation grade IMU as a result of constant initial biases in the measurement of accelerations and angular rates. While the error due to an acceleration bias (blue) is bound by the Schuler loop, the error due to the gyroscope bias on the horizontal axis (red) is a superposition of an oscillation and a linear drift. In the case of the gyroscope bias on the vertical axis (green), which mainly corresponds to the yaw angle, the systematic drift of the error is even quadratic in time. The effect of the Schuler oscillation, albeit present, is hardly visible in that case.

The example with the constant biases is a mere academic demonstration of the long-term periodic effects on the navigation solution. In reality this bias is not constant, and rather subject to different noise processes like angular and velocity random walk, respectively.

As before, these processes can be modeled as an input to the system, with the transition matrix $\mathbf{F}(t)$ that was established just before. The state covariance is given by

$$\mathbf{P}(t) = \mathbf{F}(t-t_0)\mathbf{P}(t_0)\mathbf{F}(t-t_0)^{\mathrm{T}} + \int_{t_0}^{t} \mathbf{F}(t-\tau)\mathbf{G}(\tau)\mathbf{Q}_{ww}\mathbf{G}(\tau)^{\mathrm{T}}\mathbf{F}(t-\tau)^{\mathrm{T}}\, d\tau. \tag{2.103}$$

Only processes with zero mean are considered. Hence, the RMS of individual states can directly be assessed on the main diagonal of the matrix. Most prominently, the expected position error can be calculated.

The matrix $\mathbf{Q}_{ww}$ is equipped with the power spectral densities for the VRW N_a^2 and ARW N_g^2, as well as the acceleration K_a^2 and rate random walk K_g^2 as follows,

$$\mathbf{Q}_{ww} = \begin{bmatrix} N_a^2 & 0 & 0 & 0 & 0 & 0 \\ 0 & K_a^2 & 0 & 0 & 0 & 0 \\ 0 & 0 & N_g^2 & 0 & 0 & 0 \\ 0 & 0 & 0 & K_g^2 & 0 & 0 \\ 0 & 0 & 0 & 0 & N_g^2 & 0 \\ 0 & 0 & 0 & 0 & 0 & K_g^2 \end{bmatrix}. \tag{2.104}$$

The bias instability cannot be represented rigorously in state space, and approximations are required like discussed in Kasdin (1995) or Plaszczynski (2007). To keep things simple, it is

included as an initial error of the accelerations B_a^2 and angular rates B_g^2 in $\mathbf{P}(t_0)$ according to

$$\mathbf{P}(t_0) = \begin{bmatrix} 0 & 0 & 0 & 0 & 0 & 0 & 0 \\ 0 & 0 & 0 & 0 & 0 & 0 & 0 \\ 0 & 0 & B_a^2 & 0 & 0 & 0 & 0 \\ 0 & 0 & 0 & 0 & 0 & 0 & 0 \\ 0 & 0 & 0 & 0 & B_g^2 & 0 & 0 \\ 0 & 0 & 0 & 0 & 0 & 0 & 0 \\ 0 & 0 & 0 & 0 & 0 & 0 & B_g^2 \end{bmatrix}. \tag{2.105}$$

The total position error can be assessed by the solution of Eq. (2.103), which is evaluated by using *MATLAB* (R2020b) Symbolic Toolbox. The variances are extracted from the main diagonal of $\mathbf{P}(t)$. Excluding the gyroscope's angular rate random walk, the first entry which corresponds to the position error δx_N reads:

$$\begin{aligned} \sigma_{\delta x_N}^2(t) =& B_a^2 \left[-\frac{\cos(\omega_s t) - 1}{\omega_s^2} \right]^2 \\ &+ B_g^2 \left[R \left(\frac{\sin(\omega_s t)}{\omega_s} - t \right) \right]^2 \\ &+ B_g^2 \left[-v^* \left(\frac{t^2}{2} + \frac{\cos(\omega_s t) - 1}{\omega_s^2} \right) \right]^2 \\ &+ N_a^2 \frac{1}{\omega_s^2} \left(\frac{t}{2} - \frac{1}{4\omega_s} \sin(2\omega_s t) \right) \\ &+ K_a^2 \frac{1}{\omega_s^4} \left(\frac{3}{2} t - \frac{1}{\omega_s} (2 \sin(\omega_s t) - \frac{1}{4} \sin(2\omega_s t)) \right) \\ &+ N_g^2 R^2 \left(\frac{3}{2} t - \frac{1}{\omega_s} (2 \sin(\omega_s t) - \frac{1}{4} \sin(2\omega_s t)) \right) \\ &+ N_g^2 \frac{1}{6\omega_s^3} \left(v^{*2} + 2t^3 \omega_s^3 - \frac{3}{2} \sin(2\omega_s t) - 12 \sin(\omega_s t) + 3\omega_s t + 12 \omega_s t \cos(\omega_s t) \right) \end{aligned} \tag{2.106}$$

The first three terms are representing the propagation of the initial acceleration and angular rate errors, i.e. biases. The remaining terms represent the impact of the white noise and random walk processes.

Fig. 2.11 shows the performance of a navigation grade IMU with the accelerometers characterized by the parameters $N_a = 12 \times 10^{-5}\,\mathrm{m/s^{3/2}}$, $B_a = 4 \times 10^{-5}\,\mathrm{m/s^2}$ and $K_a = 1.1 \times 10^{-5}\,\mathrm{m/s^{5/2}}$, and the gyroscopes by $N_g = 1.45 \times 10^{-6}\,\mathrm{rad/s^{3/2}}$ and $B_g = 7.27 \times 10^{-9}\,\mathrm{rad/s}$. The angular rate random walk of a gyroscope in this quality class is negligible even for long periods of time (El-Sheimy & Youssef, 2020).

The first dominant error source for short term is the white noise of the accelerometer, growing proportional to $\sim t^{1/2}$. The accelerometer random walk and the white noise of the gyroscope at the inclination axis are then becoming more influential and dominate the total error after about one minute of time. The impact of the gyroscope errors in Down direction yields the steepest ascent, but does not exceed the other impact sources even after four hours of inertial navigation. The total position error after one hour is below 1000 m.

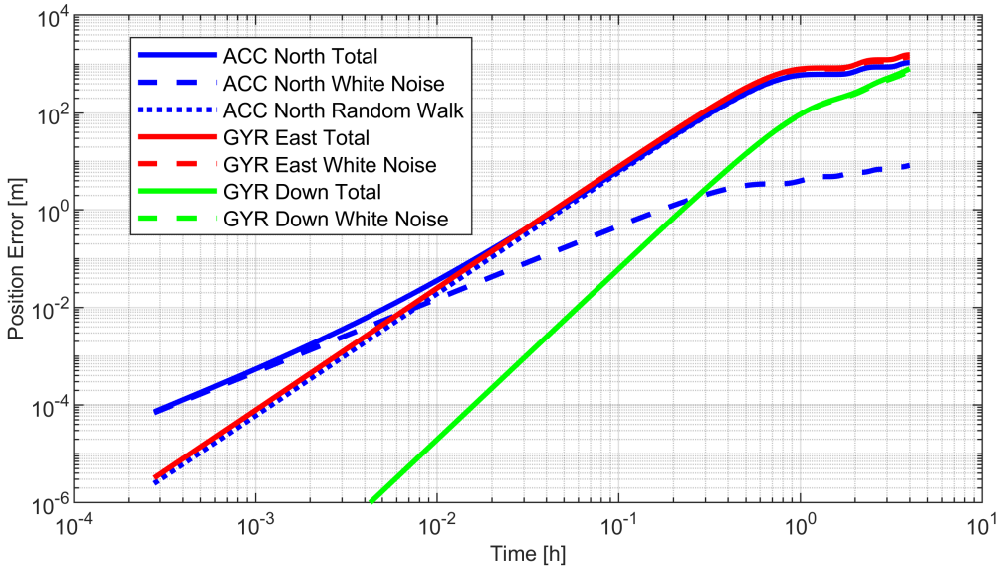

Figure 2.11: Position drift of a navigation grade IMU as a result of noise processes in the measurement of accelerations and angular rates. The individual processes contributing to the total phase shift error are expressed by different line styles. All processes are affected by the Schuler oscillation with a period of 84.4 min.

3

Characteristics of Atom Interferometers

In order to get an impression of the function of a cold atom interferometer (CAI) as inertial sensor, two different pictures can help. The first one is the classical **corner-cube gravimeter** like in Niebauer et al. (1995). By dropping a mass in an enclosed hull and measuring the position of the mass, the acceleration due to gravity can be assessed. The position measurement in this example is realized by using a retro-reflective corner cube as mass, and a laser that is aligned with the direction of gravity and reflected by mirrors. The laser in upward direction is interfering with the reflected light wave in downward direction. A path difference between the incoming and the reflected beam occurs due to the motion of the corner cube, leading to a phase-shifted interference pattern. By counting the interference maxima passing by a specific detector, the phase shift and thus the position of the mass can be measured. This in turn allows to infer about gravity, by using a motion model that connects the position with the acceleration of the mass.

The other picture is that of the classical **Mach-Zehnder experiment** (Zetie et al., 2000) and the Sagnac effect, which was already used to introduce the FOG and ring laser gyroscope technology in Chap. 2, cf. Fig. 2.3. This apparatus may use one laser source. The beam is split, reversed by a mirror, and then recombined by another splitter, in order to produce coherent waves at the output port. In case of a rotation of the apparatus, a phase shift is visible in the resulting interference pattern due to the different length of the two laser paths. The sensitivity of this interferometer can be increased by the distance between the splitter and the two mirrors. The longer the light travels, the higher the sensitivity for a change of their path length, and thus, to rotation.

Atom interferometry with cold atoms can be regarded as a combination of both effects. By releasing and observing a prepared atom wave packet, information about the acceleration of the atoms can be assessed. Contrary to the classical gravimeter it is not the shift of the position of the center of mass of the atoms which is measured directly; the actual measurement rather uses the quantum nature of the atoms. By a certain manipulation, the atoms are set in a superposition of two internal energy levels with different momentum, comparable to the paths of the optical interferometer, and a phase shift is measured in the end which yields information about the inertial quantities like rotations and accelerations.

Equipped with this first impression, a brief history of the discovery of the quantum nature of atoms over the first quantum inertial sensors, leading to quantum optical interferometry with cold atoms, is now summarized.

The discovery of the quantum nature of matter mainly took place over the course of the prior century. It started as a dispute between Max Planck and Ludwig Boltzmann, where the former tried to prove that matter is "continuous" (Baggott, 2020). This was quite the unusual way of thinking in comparison to the probabilistic theory of atoms which was quite common

especially in the field of thermodynamics at that time. His research culminated in the Planck radiation law $E = h\nu$. He discovered that in the case of black body radiation the energy E is composed of discrete "quanta" of energy, characterized by a certain frequency ν and scaled by the Planck constant h.

The next important steps, just to name a few and without claiming completeness, led over Einsteins mass-energy equivalence, the Bohr atom model, and the De Broglie wave length $\lambda_{db} = \frac{h}{\rho}$, which links wave-like properties to particles with momentum ρ. The modern formulation of quantum mechanics was then elaborated by Schrödinger, prominently with the wave equation, Heisenberg and the uncertainty principle, as well as Dirac and Von Neumann (Sakurai, 2011).

The core of this thesis is the experimental side and the application of quantum mechanics in measurements. As such, the historical steps and technologies that allow to use CAI as inertial sensor are now summarized in Sec. 3.1, and the current state of the art of atom interferometry regarding accuracy and performance will be presented. A measurement model is introduced in Sec. 3.2. This is followed by Sec. 3.3 with a detailed discussion of the transfer behavior of CAI on the example of acceleration measurements. In Sec. 3.4 a novel concept is introduced to calculate the CAI phase shift with a classical inertial measurement unit (IMU). A discussion of the limits of CAI in terms of bandwidth in Sec. 3.5 concludes the chapter.

3.1 Introduction to Atom Interferometry

From Stern-Gerlach Experiments to First Inertial Measurements

A first important step toward matter wave interferometric measurement certainly was the Stern-Gerlach experiment in 1921 (French et al., 1979). The experiment is still often used as a model to describe more complex systems involving quantum mechanics (Casimir, 1981) or more prominently in the description of atomic beam splitters (Adams et al., 1993). The experiment is composed as following.

Silver atoms are heated in an oven and reach, collimated via a shutter, a chamber in which they are exposed to a magnetic field. The chamber is equipped with a wedge-shaped upper magnetic pole and an u-shaped lower magnetic pole, effectively leading to a field gradient. This magnetic field supposedly affects the atoms, leading to a deflection. Consequently, the atoms hit different positions on a detector screen. The conception was that if the magnetic moment of the atoms was randomly distributed as expected from a random orientation of the atoms, a vertical line would appear on the screen. However, this was not the case. The actual observation was that only two distinct positions on the screen were reached. Those positions were shown to be dependent on the spin of the electrons on the atoms' outer energy shell, which, as a matter of fact, has exactly two possible states. This was a clear indicator of the quantum nature of atoms.

The effect of potentials like gravity is quite similar to the magnetic field. In this case, the potential difference is causing a phase difference between the two states, which is a mere quantum mechanical property. One of the first matter wave interferometers was revealed in Altshuler and Frantz (1972). Here, a scheme to measure accelerations and rotation rate of the apparatus, as well as magnetic fields, was presented. The general steps are visualized in Fig. 3.1.

The working principle of this comparably basic implementation is very similar to most of the current atom interferometric sensor prototypes. The architecture resembles a classical

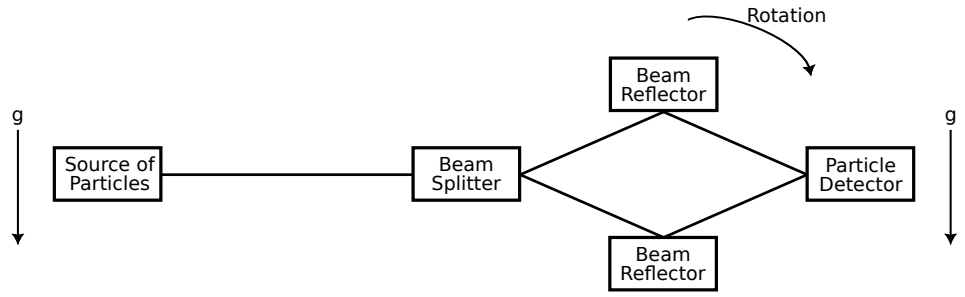

Figure 3.1: Scheme of the first matter wave interferometer, capable of measuring gravity or the Earth rotation (Altshuler & Frantz, 1972).

Mach-Zehnder type configuration, comparable to the optical experiment introduced before. The main components are

1. the source of particles. In this case, it is a continuous matter wave beam. The atoms are heated up and leave the oven in shape of a collimated beam over a shutter;
2. some manipulation devices, namely a beam-splitter and beam reflector. The beam-splitter is realized by a standing electromagnetic wave used for deflecting the particles. This is loosely comparable to the effect of the magnetic field in the Stern-Gerlach experiment described before. The reflectors can be realized again by a standing electromagnetic wave or a crystal lattice;
3. some means to detect the fringe pattern and to infer about the phase difference. A complete fringe pattern can be seen due to the continuous beam of particles that is used. It is assumed that a change of gravity occurs which leads to a shift of the complete fringe pattern. The detector thus counts the number of fringes passing by, allowing to extract the phase shift and thus the acceleration of the frame.

Two Photon and Stimulated Raman Transitions

The next important technology is the light pulse interferometry. Atoms can interact with light waves that are in resonance with the transition between two internal energy levels. For example, an atom in a state $|1, \rho\rangle$[1] with momentum ρ absorbs a photon with momentum $\rho_{ph} = \frac{h}{\lambda}$ and reaches an excited state $|2, \rho + \frac{h}{\lambda}\rangle$. Here, h is the Planck constant and λ the wavelength of the light, which needs to be at the level of the *de Broglie wavelength* of the particles.

A more common form is to express the momentum in terms of the *reduced* Planck constant $\hbar = \frac{h}{2\pi}$, so that the photon momentum is given by $\rho_{ph} = 2\pi\hbar\frac{1}{\lambda}$. The factor $\frac{2\pi}{\lambda} = k$ is labeled the wave number in this context. With those modifications, the excited state reads $|2, \rho + \hbar k\rangle$.

This higher energy state $|2\rangle$ is not stable, and after some time the atom releases its excess energy in shape of a photon in a random direction, while the atom conserves the momentum as recoil velocity in the opposite direction. A mechanism to control the direction of the recoil and the time the atom stays in its exited state would thus be highly beneficial.

In **stimulated Raman state transitions** (Kasevich & Chu, 1991; Kasevich et al., 1991), two counterpropagating standing light waves are used such that an effective wave number

[1] This is the so called "Bra-Ket" notation $|a, b\rangle$, where a indicates a state or energy level of the system, and b a certain property, cf. e.g. Sakurai (2011). In the frame of the thesis (and only in this chapter, in fact), this notation will be used to associate a momentum to a certain internal energy level.

$k_e = k_1 - k_2$ results. The transitions are driven between two hyperfine ground states $|1\rangle$ and $|2\rangle$, cf. Fig. 3.2. At this rate, the atoms first absorb energy of the photons of one beam. Normally the atom would release the excess energy again by spontaneous emission of a photon. If this emission is stimulated (Kasevich & Chu, 1991), i.e., controlled, each atom releases energy in form of another photon into the beam with the opposite direction. The effective momentum transfer is thus $2\hbar k$. In practice, the counter propagating beams can be realized by a retroreflection mirror which reverses the direction of the interrogation laser of a single source. The position of the mirror in particular also resembles the reference frame of the interferometer in that case.

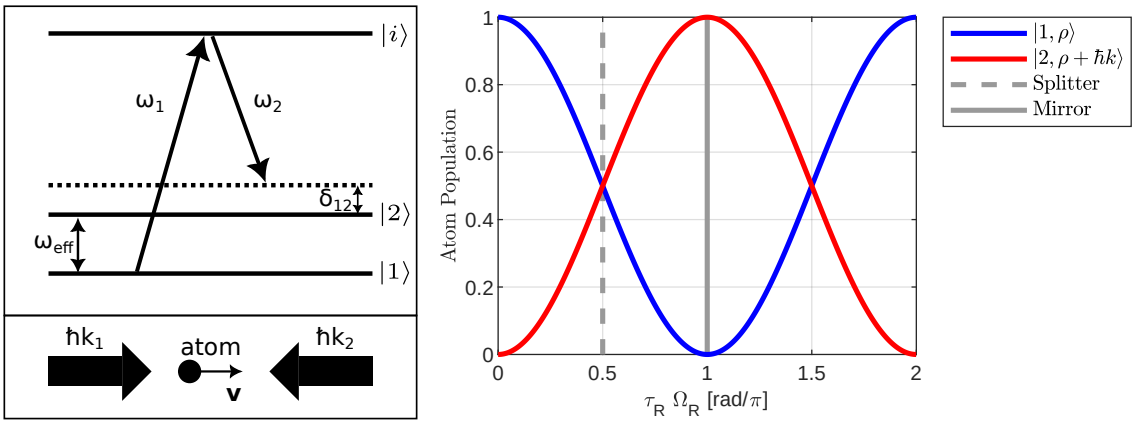

Figure 3.2: Scheme of 2-photon transitions as presented in Kasevich et al. (1991). Left: a certain effective frequency $\omega_{\text{eff}} = \omega_1 - \omega_2$ is needed in order to allow the population to be transferred between the states $|1, \rho\rangle$ and $|2, \rho + \hbar k_e\rangle$. The detuning δ_{12} is needed in order to compensate for the velocity of the atoms in the laser coordinate system. Right: oscillation of the population (normalized by total count) as a function of the interaction with the light field characterized by pulse time τ_R and the Rabi frequency Ω_R.

In order to select the corresponding atoms for the transition, a small detuning $\delta_{1,2}$ from the resonance frequency characteristic for the particular state transition is needed. This corresponds to the velocity of the atoms and the Doppler frequency shift associated with their speed. At this rate, only the atoms moving toward (or away from, respectively) the direction of the beam are affected by the slight shift in frequency. This is the so-called velocity selection.

The technique was applied to measure gravitational acceleration in Kasevich and Chu (1992) and marked the beginning of numerous developments in the field of atom interferometry. Up to date, more than 50 groups worldwide are working on the subject (Geiger et al., 2020). The primary objectives lie in the achievement of higher sensitivities to inertial effects, and more recently, also in developing industrial applications.

Measuring Accelerations and Angular Rates

The stimulated state transitions are a powerful tool to apply in different interferometer architectures. It was visualized in Fig. 3.2 that, depending on the length of the interaction of the laser pulse and the atom wave packet, the internal energy state of the atoms can be manipulated. The phase of the atomic state transition depends on the pulse duration τ_R and is related via

$$\phi_R = \Omega_R \tau_R \tag{3.1}$$

with the effective Rabi frequency Ω_R, a parameter characteristic for the oscillation between certain energy levels. During the interaction of the atoms with the light field, the atom transition probability between the two states oscillates depending on the phase ϕ_R. If all

atoms were in state $|1\rangle$ at the start of the interaction, the transition probability p of finding the atoms in state $|2\rangle$ is

$$p(\phi_R) = \frac{1}{2}\left(1 - \cos(\phi_R)\right). \tag{3.2}$$

Two examples:

- When $\Omega_R \tau_R = \frac{\pi}{2}$ for a given Ω_R, the transition probability is

  $$p(\Omega_R \tau_R) = \frac{1}{2}\left(1 - \cos(\frac{\pi}{2})\right) = \frac{1}{2}.$$

  In this situation, the number of atoms in the two superposed states is equal, and a **beam splitter** pulse is realized.

- A **mirror pulse** can be achieved by twice the pulse duration $2\tau_R$, such that $\Omega_R \tau_R = \pi$. This results in a transition probability of

  $$p(\Omega_R 2\tau_R) = \frac{1}{2}\left(1 - \cos(\pi)\right) = 1.$$

A series of $\frac{\pi}{2} - \pi - \frac{\pi}{2}$ pulses is resembling a **Mach-Zehnder pulse pattern**, comparable to the optical experiment or the matter wave assembly from before. As illustrated in Fig. 3.3, the cycle starts with an atom wave packet in the state $|1, \rho\rangle$. The first splitter pulse creates a superposition of the atoms in the $|1\rangle$ and $|2\rangle$ state by equal numbers. The states are then switched by a π mirror pulse at the time T, before they are finally recombined by another splitter pulse at time $2T$.

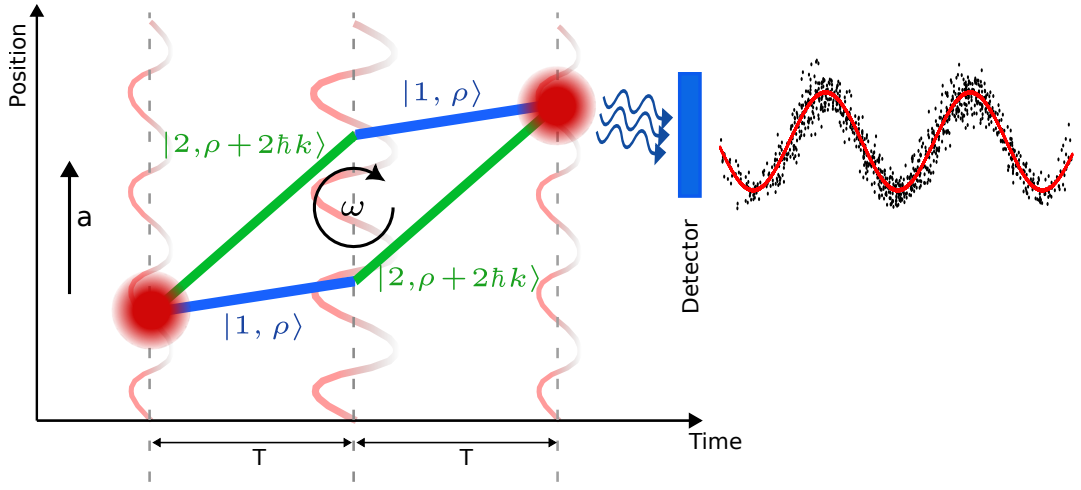

Figure 3.3: Atom interferometry in Mach-Zehnder structure. Right: Qualitative representation of the sinusoidal fringe pattern (red). After each measurement cycle, a single measurement (black dots) can be assessed, which depends on the phase shift between the two interferometer paths.

The interrogation pulse sequence is essentially the effective measurement time of the interferometer, since it resembles the time in which the apparatus is sensitive to inertial effects, like accelerations $\mathbf{a}$, due to the different momentum of the two states. The accelerations result in a measurable phase shift at the end. This will be covered in more detail in Sec. 3.4. Just to convey a first idea about the order of magnitude, let this phase shift for now be denoted by ϕ_a,

$$\phi_a = \mathbf{k}_\mathrm{e} \cdot \mathbf{a} T^2. \tag{3.3}$$

The effective wave vector $\mathbf{k}_\mathrm{e}$ is the spatial representation of the effective wave number k_e. Equation (3.3) shows that the phase shift scales with the square of the interrogation time.

As a general rule of thumb, higher times can be associated with a higher sensitivity of the apparatus to inertial effects.

The apparatus is not only sensitive to linear acceleration, but also to a rotation of the laser field (Riehle et al., 1991). This leads to the challenge of differentiating between the two quantities, as the total phase shift due to inertial effects ϕ_{inertial} is given by a superposition of the phase shift based on linear accelerations and the one resulting from a rotation ϕ_g,

$$\phi_{\text{inertial}} = \phi_a + \phi_g. \tag{3.4}$$

A comparably simple approach to distinguish between those two inertial quantities is the use of two counterpropagating atom wave packets with initial velocity $\pm\mathbf{v}$ that are interrogated at the same time (Canuel et al., 2006; Gersemann et al., 2020; Tackmann et al., 2012). The scheme of this approach is illustrated in Fig. 3.4. After the preparation, an initial separation pulse causes parts of the atom wave packet to move in opposing directions. Both wave packets are then interrogated in parallel. After the measurements, the phase shifts due to acceleration and due to rotation can be assessed via (Gersemann et al., 2020)

$$\phi_a = \frac{1}{2}\left(\phi_1(\mathbf{v}) + \phi_2(-\mathbf{v})\right), \tag{3.5}$$

$$\phi_g = \frac{1}{2}\left(\phi_1(\mathbf{v}) - \phi_2(-\mathbf{v})\right). \tag{3.6}$$

Just like the accelerations, the phase shift due to angular rates $\boldsymbol{\omega}$ scales with $\sim T^2$,

$$\phi_g = 2\mathbf{k}_{\text{e}} \cdot (\boldsymbol{\omega} \times \mathbf{v})T^2. \tag{3.7}$$

This is just a basic outline of the usage of CAI as accelerometer and gyroscope, aiming to put the numbers and state of the art technologies presented in the next section into perspective. A more rigorous definition of the measurement cycle and a formulation of the CAI observation equation will follow.

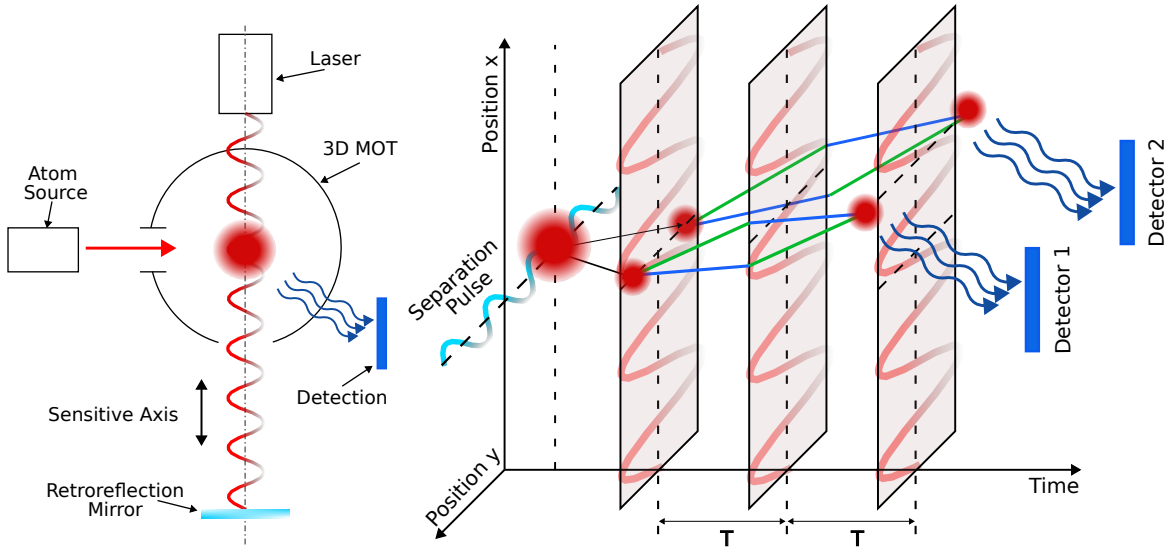

Figure 3.4: Schemes of technical realizations of CAI as accelerometer and gyroscope. Left: CAI sensor with a downward sensitive axis. The retroreflection mirror is used to realize a counterpropagating beam. This is needed in order to allow Raman state transitions. Right: differential scheme like discussed in Gersemann et al. (2020). An initial separation pulse divides an atom wave packet in two parts with opposed momentum in a direction perpendicular to the sensitive axis. They are interrogated in parallel. Thanks to the opposed velocity, a discrimination between phase shifts resulting from linear acceleration and phase shifts based on angular rates is possible.

State of the Art Atom Interferometry Inertial Sensors

To this day, most atom interferometry inertial sensors have only been realized for static lab environment. They have only partially entered commercial stage: the "Absolute Quantum Gravimeter" (AQG) of Muquans (2019) is a commercially available stationary gravity sensor, reaching sensitivity levels of $5 \times 10^{-7}\,\mathrm{m/s^2}/\sqrt{\mathrm{Hz}}$ with a standard deviation of $6 \times 10^{-9}\,\mathrm{m/s^2}$ at 10 hours of integration (Vermeulen et al., 2018). In other experiments, sensitivities of $1.7 \times 10^{-7}\,\mathrm{m/s^2}/\sqrt{\mathrm{Hz}}$ (Peters et al., 2001) or $9.6 \times 10^{-8}\,\mathrm{m/s^2}/\sqrt{\mathrm{Hz}}$ with a long-term stability of $5 \times 10^{-10}\,\mathrm{m/s^2}$ (Freier et al., 2016) have been reported.

The fundamental limitation is often the **quantum projection noise** (Itano et al., 1993). This uncertainty can be seen as the basis for a large number of atom interferometer architectures and directly affects the raw measurement of the interferometer. The value is magnified by the individual scale factor of the interferometer, which depends on the settings, the architecture and the specific type of operation, i.e. whenever the CAI is applied as accelerometer, gyroscope, magnetometer etc., the measured quantity is scaled differently depending on the physical units.

The scale factor in the case of acceleration measurements, cf. Eq. (3.3), is composed of the momentum transfer (effective wave vector), the interrogation time (proportional to the square or even $\sim T^3$), as well as the atom velocity in case of a rotation measurement as stated in Eq. (3.7). Longer atom travel times, or travel distance, respectively, can lead to sensitivites of $3 \times 10^{-8}\,\mathrm{m/s^2}/\sqrt{\mathrm{Hz}}$ at a distance of 70 cm (Biedermann et al., 2015) or $3 \times 10^{-10}\,\mathrm{m/s^2}/\sqrt{\mathrm{Hz}}$ at a distance of 8.7 m (Dickerson et al., 2013). While those travel times are not suitable for terrestrial mobile navigation due to large spurious signals, they might see application in space (Abend et al., 2023).

Large scale factors are especially relevant for the angular rate measurement, as classical gyroscopes like hemispheric resonator gyros, ring laser and fiber optical gyroscopes are a strong competition in terms of sensitivity. Gustavson et al. (1997) demonstrated an atomic gyroscope with $2 \times 10^{-8}\,\mathrm{rad/s}/\sqrt{\mathrm{Hz}}$ with the prospect of a sensitivity of $1 \times 10^{-9}\,\mathrm{rad/s}/\sqrt{\mathrm{Hz}}$ and long-term stability in the 1×10^4 seconds domain. In fact, further development with two counterpropagating thermal beams lead to a sensitivity of down to $6 \times 10^{-10}\,\mathrm{rad/s}/\sqrt{\mathrm{Hz}}$ in a certain spectral range (Gustavson et al., 2000).

Further angular rate sensors based on light pulse interferometry are e.g. Tackmann et al. (2012) with a sensitivity of $6.1 \times 10^{-7}\,\mathrm{rad/s}/\sqrt{\mathrm{Hz}}$ down to a level of $1.2 \times 10^{-7}\,\mathrm{rad/s}/\sqrt{\mathrm{Hz}}$ (Berg et al., 2015). Durfee et al. (2005) reported a stability of $3.2 \times 10^{-10}\,\mathrm{rad/s}$ at 2000 seconds, with a sensitivity close to the shot-noise limit of $8.7 \times 10^{-10}\,\mathrm{rad/s}/\sqrt{\mathrm{Hz}}$ of the apparatus. Altorio et al. (2020) presents an alignment-technique to reduce systematic error effects, reaching stability levels of $1 \times 10^{-10}\,\mathrm{rad/s}$.

Due to the necessity of wave packet preparation and imaging, the data rate is often at the level of about 1 Hz. Additionally, only part of the cycle represents the actual measurement. Full coverage can be achieved by *juggling* several atom wave packets in a series of overlapping cycles (Dutta et al., 2016), whereas each one covers the dead time due to preparation and readout of the others. Here, short-term sensitivities of $100\,\mathrm{nrad/s}/\sqrt{\mathrm{Hz}}$ with a stability of 1 nrad/s have been reported. Further work (Savoie et al., 2018) lead to a long-term stability of $3 \times 10^{-10}\,\mathrm{rad/s}$ at 10^4 seconds. On the other side, by reusing the atoms and thus reducing the preparation time, higher data rates up to 60 Hz have been reported (Rakholia et al., 2014) while still reaching sensitivities at the $\mu\mathrm{rad/s}/\sqrt{\mathrm{Hz}}$ and $\mu\mathrm{m/s^2}/\sqrt{\mathrm{Hz}}$ level, respectively.

The inertial effects affecting the CAI phase shift are manifold. In general, the inertial phase shift is a superposition of the impact of angular rates and linear accelerations. Most of the

prototypes listed above are one-dimensional sensors. One of the assemblies for a multi degree of freedom sensor is presented in Dickerson et al. (2013) with two rotational and one linear acceleration axis. Canuel et al. (2006) and Barrett et al. (2019) present sensor architectures with six degrees of freedom and different pulse schemes to separate the inertial quantities on each axis. X. Wu et al. (2017) propose a multi-axis architecture for two-axis measurement of gravity, rotation and inclination angle using a pyramidal mirror. A sequential measurement scheme with six degrees of freedom (6DOF) based on a Bose-Einstein condensate is presented in Gersemann et al. (2020).

3.2 Atom Interferometry Sensor Model

3.2.1 Measurement Model

There are different modes of operation for CAI. Canuel et al. (2006) present different schemes for a multi-axis CAI, which also includes a four-pulse "butterfly" scheme in order to suppress certain spurious signals. The sensor model in the context of this thesis is elaborated for the Mach-Zehnder pulse sequence, since it resembles a basic, intuitive and comparably easy to implement design. The actual measurement is the transition probability p after the recombination pulse. Theoretically, it is given for the excited state $|2\rangle$ as

$$p_{\text{theory}} = \frac{1}{2}\left(1 - \cos\phi\right). \tag{3.8}$$

In practice it is assessed by the ratio of the atom count $N_{|2\rangle}$ after the readout process, normalized by the total number of atoms:

$$p = \frac{N_{|2\rangle}}{N_{|1\rangle} + N_{|2\rangle}}. \tag{3.9}$$

For a more specific implementation, considering the readout process parameters fringe amplitude A and offset p_0, as well as the phase shift offset $\delta\phi$, the transition probability can also be written as

$$p = A\cos\left(\phi + \delta\phi\right) + p_0 \tag{3.10}$$

with the phase shift ϕ

$$\phi = \phi_{\text{L}} + \phi_{\text{light}} + \phi_{\text{inertial}} + \phi_{\text{sep}} \tag{3.11}$$

consisting of the already introduced phase shift from the interaction of the atoms with the light field ϕ_{light}, the phase shift caused by inertial effects like accelerations of the apparatus ϕ_{inertial}, the laser phase ϕ_{L} which can be manipulated by the control electronics of the laser, as well as an additional ϕ_{sep} which corresponds to the case in which the two atom paths do not exactly overlap at the state recombination pulse.

Fringe Ambiguity and Dynamic Range

In order to extract the inertial effects from a reading of the CAI transition probability, the equation needs to be solved for the phase shift ϕ. On the example of the theoretical model in Eq. (3.8):

$$\phi = \arccos\left(1 - 2p_{\text{theory}}\right). \tag{3.12}$$

The challenge at this point is that the arccos is only defined in the range of $\phi \in [0, \pi]$, which represents one flank of the cosine signal. However, the inertial phase shift, e.g. according to Eq. (3.3), scales via T^2 and can be much larger. In Fig. 3.5 it is visualized, how the phase shift

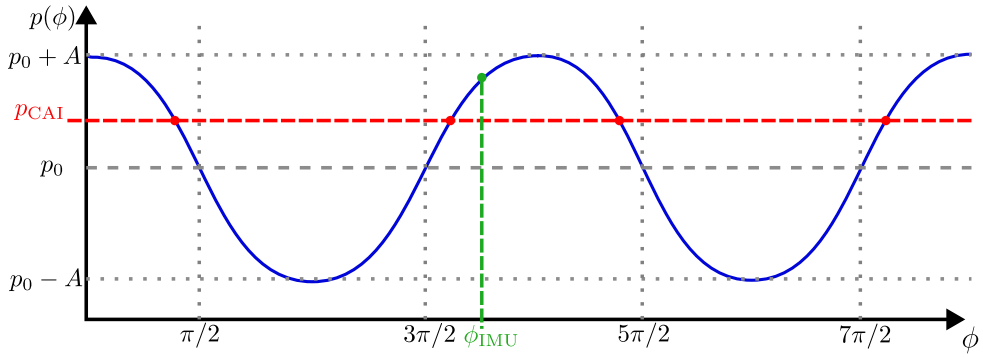

Figure 3.5: Illustration of the fringe ambiguity problem. While the CAI measurement is given as atom count p (red), there is an infinite number of phase shifts ϕ corresponding to the measurement. A classical IMU (green) can be used to find the corresponding flank of the cosine signal.

and the CAI observation are related. The CAI measurement is basically only a number on the y-axis, whereas Eq. (3.12) corresponds to the first falling flank of the measurement equation (blue curve). There are multiple phase shifts that can be associated with the measurement as indicated by the intersections of the curve with the red line. This is essentially the **ambiguity problem**, which affects any signal that is incorporated in the phase shift ϕ. The direct consequence is a limited dynamic range. For an interrogation time of $T = 10\,\mathrm{ms}$ and $k_{\mathrm{e}} = 4\pi/780\,\mathrm{nm}^{-1}$, the range of accelerations that corresponds to the cosine flank is about $4\,\mathrm{mm/s}^2$. A common solution for this ambiguity problem is the usage of high rate acceleration sensors that are used to identify the target flank by a prediction of the expected phase shift. This will be further discussed in Chap. 4.

3.2.2 Timeline of a Measurement

Generally, the timeline of a measurement as illustrated in Fig. 3.6 consists of the following parts,

$$T_{\mathrm{total}} = T_{\mathrm{prep}} + T_{\mathrm{pulses}} + 2T + T_{\mathrm{det}}, \tag{3.13}$$

with the atom preparation time T_{prep}, the manipulation laser pulse time T_{pulses}, the time between beam splitter and mirror pulse T and the detection time T_{det} of the readout process. The total measurement time, in which the atoms are basically in free flight, can be labeled $T_{\mathrm{flight}} = T_{\mathrm{pulses}} + 2T$. The steps are now explained in more detail. Afterwards, they are summarized and their duration quantified by some actual numbers.

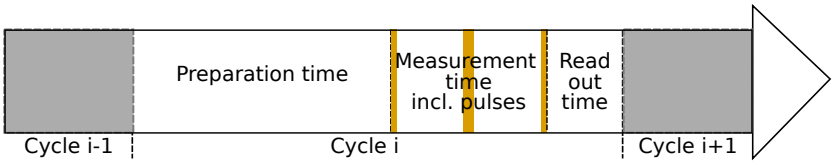

Figure 3.6: Timeline of a CAI measurement cycle. The active measurement happens in the time of the Mach-Zehnder pulse sequence, including the pulse length as indicated qualitatively in dark yellow. During the preparation and readout time, the sensor is essentially blind.

Atom Preparation

The first characteristic section of a measurement is the preparation of the atoms. The atoms are dispensed from their source and guided by a 2D magneto-optical trap (MOT) to their first

target location in a 3D MOT (Raab et al., 1987). In the latter, the atoms are held for a few parts of a second. This is required in order to cool the atoms, which essentially means that their momentum distribution is defined as precise as possible. The corresponding time is T_{prep}. Longer times are allowing for lower atom temperature thanks to longer cooling. Furthermore, higher atom numbers are possible since more atoms can be collected and prepared. This time is typically in the range of several hundred milliseconds in order to reach a temperature of a few nK.

Interrogation Sequence

After the preparation step, the 3D MOT is deactivated and the atoms are released into free spatio-temporal evolution. This is also the time in which the manipulation of the internal states of the atoms by the interrogation laser pulses starts. The classic Mach-Zehnder interferometry pattern by custom starts with the first splitter pulse, followed by the mirror pulse after some time T. The states are then recombined after another time T. The individual pulses duration is bound to the Rabi-Oscillation, e.g. between the two hyperfine ground states $|1\rangle$ and $|2\rangle$. For ^{87}Rb it is $\tau_R = 7.5\,\mu\text{s}$ for the splitter, and $2\tau_R = 15\,\mu\text{s}$ for the mirror pulse, leading to a total T_{pulses} of $4\tau_R = 30\,\mu\text{s}$. The interferometer is only sensitive for any inertial quantities during this interrogation sequence. The time between the release and the first splitter pulse does not necessarily need to be zero. However, as the distribution of the atom wave packet starts to diverge with time due to thermal expansion, small times should be preferred.

Imaging Process

After the interrogation sequence is finished by the recombination pulse, the information about the inertial quantities needs to be extracted from the wave packet. As the population distribution of the atoms in the two hyperfine states oscillates depending on the phase shift, this is realized by measuring the transition probability, i.e. by counting the atoms. One way to do this is by "light induced fluorescence" (Santarelli et al., 1999) where the atoms pass light beams resonant to a particular state transition, and the photons emitted are counted, e.g. by a photo diode. This process takes some time in which the interferometer is not sensitive to inertial effects. The atoms in one state, here: the excited state, are counted first. In a second step, all atoms are counted in order to retrieve the probability $N_{|2\rangle}/(N_{|1\rangle} + N_{|2\rangle})$. Since those numbers might still be affected by residual photons or back light, a third measurement after all atoms have left the light interaction zone is often needed in order to compensate for an offset in the measurements. Another option for the imaging that is mainly applied for Bose-Einstein condensates (BEC) is the use of a charge-coupled device camera (Abend et al., 2016). In this case, the parameters of the wave packet distribution are extracted from the picture.

To sum this section up, the measurement process of an atom interferometer can be divided in three different parts. Each part can be associated with an individual optimization problem. In particular:

- The preparation time is proportional to the number of atoms N active in the interferometer sequence, and thus closely related to the **quantum projection noise** σ_{qpn} one is willing to account for.

$$\sigma_{\text{qpn}} \sim \frac{1}{\sqrt{N}}. \tag{3.14}$$

The reduction of the quantum projection noise is only limited by the laser noise, cf. Fig. 3.7. Some typical preparation times are 50 ms to 155 ms (Gauguet et al., 2009), up to 600 ms for a number of 10^9 atoms (Freier et al., 2016).

- The flight time (including pulse times) squared is directly proportional to the **sensitivity** one is going to achieve with the interferometer. Typical times for terrestrial navigation are 20 ms - 50 ms. For space applications, higher times can be achieved. Note that there is a trade-off between sensitivity and dynamic range.
- The detection time is coupled to the imaging process; higher times can, but not necessarily have to, lead to a more sophisticated and accurate measurement with less signal offset and **technical noise**. A typical sequence can take up to 50 ms (Berg, 2014).

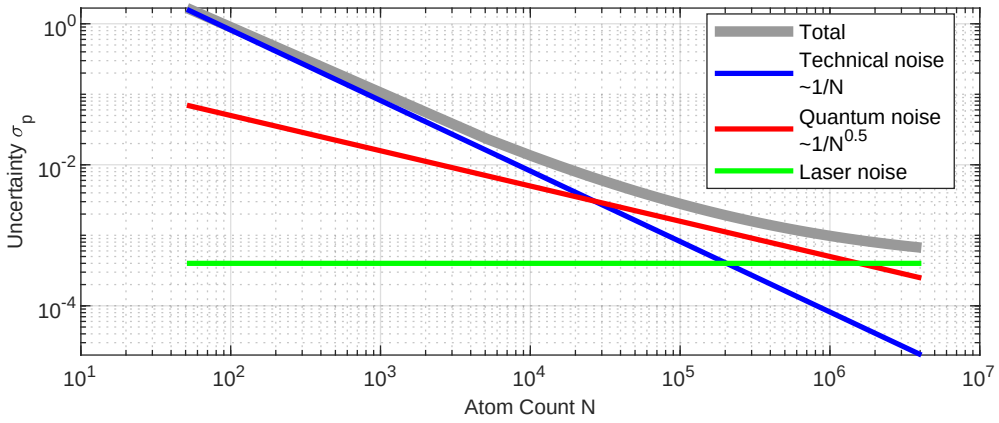

Figure 3.7: CAI observation uncertainty σ_p in relation to the number of observed atoms N. The total process (gray line) is composed of technical noise (blue line), quantum projection noise (red line) and laser phase noise (green line). The underlying parameters are according to Gauguet et al. (2009).

3.3 Response to Inertial Signals

In this section the focus is shifted on the impact of changes in the inertial quantities on the phase shift measured by the interferometer. The main motivation is a better understanding of the atom interferometer's ability to resolve different shaped input signals, i.e. to analyze the transfer behavior and to point out potential systematic error sources. The sensitivity function of an atom interferometer with respect to phase uncertainty via oscillating perturbation signals was analyzed and supported by experimental data in Cheinet et al. (2008). Here, a more general approach by using the Laplace transform is chosen. This enables to analyze the system response to different shaped causal input accelerations, for example, jumps, ramps or more smooth time-depending signals.

3.3.1 Sensitivity Function of the Atom-Light Interaction

The sensitivity function $g(t)$ (Santarelli et al., 1998) describes the change of the interferometer output p with respect to a change of the phase,

$$g(t) = 2 \lim_{\delta\phi \to 0} \frac{\partial p(\delta\phi, t)}{\partial \delta\phi}. \tag{3.15}$$

As such it can be used as a basis to develop the transfer function of the interferometer, making it possible to describe the output of the interferometer based on any input that affects the

interferometer phase. Applications of the sensitivity function are the propagation of laser phase noise or mechanical vibrations and accelerations of the frame to the interferometer readout. If the interferometer laser phase of the second splitter pulse is regulated at $\phi = \frac{\pi}{2}$, Eq. (3.8) is only depending on the time dependent phase fluctuation in $\delta\phi$ and thus can be written as

$$p(\delta\phi, t) = \frac{1}{2}\left(1 - \cos(\frac{\pi}{2} + \delta\phi)\right). \tag{3.16}$$

The sign of the partial derivative in Eq. (3.15) depends on the sign of the phase shift that is applied:

$$\frac{\partial p(\delta\phi, t)}{\partial\delta\phi} = \frac{\partial\left(\frac{1}{2} - \frac{1}{2}\cos(\frac{\pi}{2} \pm \delta\phi)\right)}{\partial\delta\phi} = \pm\frac{1}{2}\sin\left(\frac{\pi}{2} \pm \delta\phi\right). \tag{3.17}$$

By evaluating the limit in order to approximate the derivative,

$$g(t) = \lim_{\delta\phi\to 0} \pm\sin\left(\frac{\pi}{2} \pm \delta\phi\right) = \pm 1, \tag{3.18}$$

the output of the sensitivity function results in one of two possible values:

$$g(t) = \begin{cases} -1 & ,\delta\phi > 0, \\ 1 & ,\delta\phi < 0. \end{cases} \tag{3.19}$$

For the laser-induced phase shifts of the Mach-Zehnder pattern, $\phi_{\text{light}} = \frac{\pi}{2} - \pi + \frac{\pi}{2}$, this means that the sensitivity changes to -1 after the first splitting pulse and stays there until the mirror pulse. Afterwards it yields the value 1 until the recombination pulse.

This simplified description does not include the times of the atom-laser interaction in which the sensitivity changes due to the Rabi oscillation. For a full Mach-Zehnder measurement cycle, the sensitivity function including the effect of the sinusoidal change of the atom states during the laser interaction is described e.g. in Cheinet et al. (2008).

3.3.2 S-Domain Approach

To simplify the analytical solution in the s-domain, or complex frequency domain, it is assumed that the pulse duration τ_R is much smaller than the interrogation time T, $\tau_R << T$. This renders the effect of the pulse time τ_R on the sensitivity function negligible. The function then reads:

$$g(t) = \begin{cases} -1 & ,0 < t \leq T \\ 1 & ,T < t \leq 2T \\ 0 & ,else. \end{cases} \tag{3.20}$$

This function can also be expressed by three unit step functions. A unit step function $\theta(t-T)$ is defined by

$$\theta(t - T) = \begin{cases} 0 & ,t < T, \\ 1 & ,t \geq T. \end{cases} \tag{3.21}$$

Here, the instance T indicates the time in which the step occurs, or in other words, when the function jumps instantly from zero to the value one. The Laplace transform $\Theta(s) = \mathcal{L}\{\theta(t-T)\}$ of the step function delayed by time T is according to the time shift theorem (Weber & Ulrich, 2017),

$$\Theta(s) = \mathcal{L}\{\theta(t - T)\} = \frac{1}{s}e^{-sT}, \tag{3.22}$$

whereas the time delay is expressed as the exponential e^{-sT} the s-domain. The sensitivity function of the interferometer can be interpreted as three step functions with different coefficients, at the times $\tau = 0$, $\tau = T$ and $\tau = 2T$. This reduces the description to a single function with three terms,

$$g(t) = -\theta(t-0) + 2\theta(t-T) - \theta(t-2T). \tag{3.23}$$

The unit step function and the constructed sensitivity function is depicted in Fig. 3.8. At the initial state splitter pulse at $t = 0$, the sensitivity jumps to -1. At the mirror pulse at $t = T$, it jumps to +1. After the final recombination pulse at $t = 2T$ the interferometer is no longer sensitive to any effects. The corresponding representation $G(s) = \mathcal{L}\{g(t)\}$ reads

$$G(s) = -\frac{1}{s} + 2\frac{1}{s}e^{-sT} - \frac{1}{s}e^{-2sT}. \tag{3.24}$$

The weight function for the accelerations reads (Barrett et al., 2014)

$$h_a(t) = -k_\mathrm{e}\int_0^t g(\tau)\,d\tau. \tag{3.25}$$

The integral in s-domain is represented as

$$\mathcal{L}\{\int h_a(t)\,dt\} = -k_\mathrm{e}\frac{1}{s}G(s), \tag{3.26}$$

so that the final $H_a(s) = \mathcal{L}\{h_a(t)\}$ reads

$$\begin{aligned} H_a(s) &= -k_\mathrm{e}\frac{1}{s}\left(-\frac{1}{s} + \frac{2}{s}e^{-sT} - \frac{1}{s}e^{-2sT}\right) \\ &= k_\mathrm{e}\frac{1}{s^2}\left(1 - e^{-sT}\right)^2. \end{aligned} \tag{3.27}$$

Note that Eq. (3.27) is a triangle signal in time domain, as illustrated in Fig. 3.8. The triangle function yields a linear ramp until it reaches its maximum at $t = T$. Afterwards there is a linear descent until the sensitivity to accelerations reaches zero at $t = 2T$. Expressed in s-domain, the triangle function yields an exponential dampening of second order, affecting higher frequencies. The function has two poles at $s = 0$. Additionally, there are two zeroes, which are apparent if the exponential in the bracket has the value one. This happens to be at $s = 0$ as well.

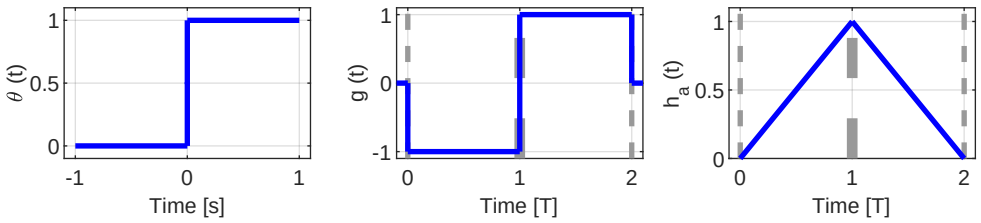

Figure 3.8: CAI phase response. Left: unit step function $\theta(t)$. Middle: CAI sensitivity function $g(t)$ to the phase shift. The three instances of the light pulses are depicted as gray dotted lines. Right: sensitivity function with respect to accelerations.

In the limit $s \to 0$ and after application of L'Hospital's theorem twice, there is still a representation of the maximum of the function, which represents the maximum gain of the transfer function for the three pulse interferometer:

$$\lim_{s\to 0} k_\mathrm{e}\frac{\left(1-e^{-sT}\right)^2}{s^2} = \lim_{s\to 0} k_\mathrm{e}\frac{2Te^{-sT} - 2Te^{-2sT}}{2s} = \lim_{s\to 0} k_\mathrm{e}\frac{-2T^2e^{-sT} + 4T^2e^{-2sT}}{2} = k_\mathrm{e}T^2. \tag{3.28}$$

The phase shift as response to a certain input acceleration signal $A(s)$ can now be evaluated by simple multiplication,

$$\Phi(s) = k_\mathrm{e} H_a(s) A(s). \tag{3.29}$$

Note that the corresponding time-domain representation of this expression is the convolution of the triangular acceleration sensitivity function h_a with the acceleration signal (Geiger et al., 2011),

$$\phi = k_\mathrm{e} \int_{-\infty}^{\infty} h_a(\tau) a(t-\tau)\, d\tau. \tag{3.30}$$

Several different acceleration input signals of different order and shape are now considered, cf. Table 3.1. The factor before the signals a_1 and a_2 is 1, with a unit that ensures the output to be given in $\mathrm{m/s^2}$. For the CAI parameters, an interrogation time of 10 ms and an effective wave number of $4\pi/780\,\mathrm{nm}^{-1}$ are set.

$a(t)$	$A(s)$	$H_a(s) \cdot A(s)$	CAI Response
$a_0(t) = 1$	$\frac{1}{s}$	$\frac{1}{s^3}\left(1 - e^{-sT}\right)^2$	$\hat{a}_0(t)$
$a_1(t) = t$	$\frac{1}{s^2}$	$\frac{1}{s^4}\left(1 - e^{-sT}\right)^2$	$\hat{a}_1(t)$
$a_2(t) = t^2$	$\frac{1}{s^3}$	$\frac{1}{s^5}\left(1 - e^{-sT}\right)^2$	$\hat{a}_2(t)$
$a_3(t) = \sin(ct)$, $c = \frac{\pi}{2T}$	$\frac{c^2}{s^2+c^2}$	$\frac{c^2}{s^2(s^2+c^2)}\left(1 - e^{-sT}\right)^2$	$\hat{a}_3(t)$
$a_4(t) = 1 - \cos(ct)$	$\frac{1}{s} - \frac{s^2}{s^2+c^2}$	$\left(\frac{1}{s^3} - \frac{1}{s^2+c^2}\right)\left(1 - e^{-sT}\right)^2$	$\hat{a}_4(t)$

Table 3.1: CAI response to input acceleration signals of different order and shape. The input signals are stated in the first column. The second and third columns are showing the Laplace space representation $A(s)$ and their product with the sensitivity function $H_a(s)A(s)$. The system response in time domain was computed with the *MATLAB* symbolic toolbox and is not explicitly stated due to its complexity.

The system response is evaluated in the form of the phase shift response function $\Phi(s)$, and additionally as the acceleration output that is produced by the interferometer based on this phase shift. The results are presented in Fig. 3.9. The acceleration sensitivity function H_a is included, in order to emphasize the cutoff frequency at $\frac{1}{T}$. Due to the convolution with the sensitivity function, all of the input acceleration signals are affected by the cutoff frequency. Higher order signals are dampened more in higher frequencies, leading to the effect that the impact of the cutoff lessens with growing signal order. This can clearly be seen in the case of the quadratic input signal.

The time domain system response to the accelerations is computed by the inverse Laplace transform of the respective phase shift response function:

$$\hat{a}(t) = \frac{1}{k_\mathrm{e} T^2} \mathcal{L}^{-1}\{\Phi(s)\}. \tag{3.31}$$

Since the magnitude of the signals differs vastly, the individual acceleration signals are normalized by the average value of the corresponding input signal over the interrogation time interval. The results are illustrated in the right panel of Fig. 3.9. It can be noted that the constant acceleration a_0 as well as the acceleration ramp a_1 coincide with the input signal at the time of the measurement, which means that the output of the CAI at the end of the $2T$ measurement cycle does represent the true acceleration signals correctly. For the signal a_2 which grows quadratic with time, there is an error between the response and the input signal. For highly nonlinear signals like the sine function a_3, this error is quite large. It can be generalized that signals that are point-symmetric in their value around the time T can be resolved without error. In order to demonstrate this, another cosine signal $a_4(t) = 1 - \cos(\frac{2\pi t}{4T})$ with a period of $4T$ is evaluated as well. This period is chosen so that the first half of the cosine is

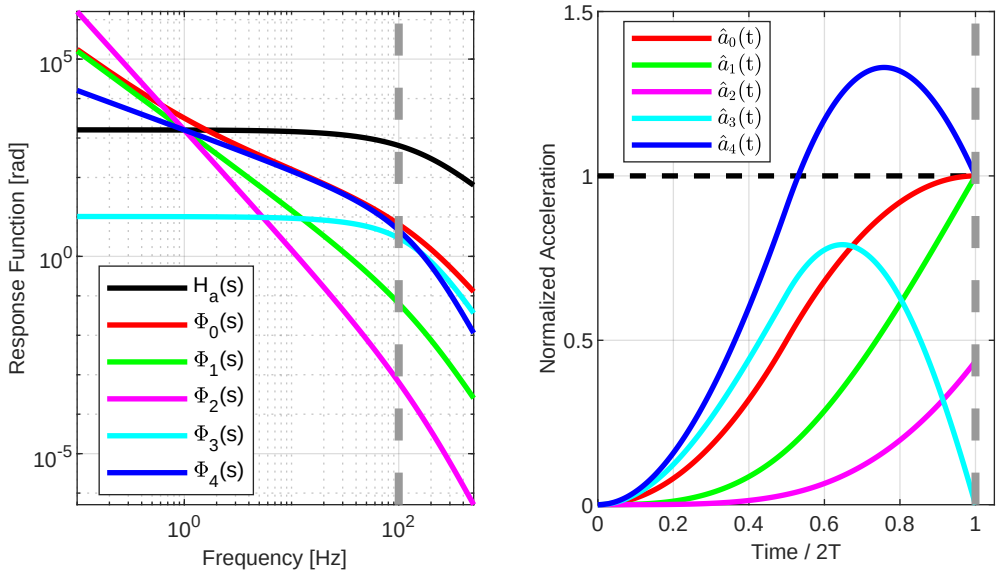

Figure 3.9: CAI response to input acceleration signals of different order and shape. Left: phase responses in the s-domain. The dotted gray line indicates the cutoff frequency at $1/T$. Right: time domain representation of the system acceleration response signals, normalized by the average values of the corresponding input signals. The time of the finished measurement cycle is indicated by a vertical gray dotted line. A value of 1 (dotted black line) at the end of the measurement cycle means that the CAI output represents the actual acceleration signal correctly.

overlapping with the CAI measurement cycle, realizing a smooth sinusoidal transition from 0 to $2\,\mathrm{m/s^2}$. As Fig. 3.9 shows, even though this signal is highly nonlinear as well, the response at the time of the measurement coincides with the average value.

Note that the sine function a_3, while also having a period of $4T$, is symmetric with respect to the time T. As such, the transfer function produces a zero as output. In fact, this behavior can be seen in the frequency domain representation as well, where the system response function of a sinusoidal input has zeros for each sine period length $n \cdot T$, where n is an arbitrary positive integer.

In summary, CAI is only resolving time-depending accelerations correctly when the above mentioned condition, i.e. the point-symmetry with respect to the center pulse, is met. For any other input function, the CAI introduces a systematic error. An extension of this study to reflect the transfer behavior of the complete QINS is discussed in Appendix A.8.2.

3.3.3 Frequency Domain Approach

A similar analysis can be exerted in the frequency domain, which is especially interesting to evaluate the effects of mechanical vibrations and certain high frequency sinusoidal noise processes on the interferometer measurement. The complex frequency s,

$$s = \sigma + j\omega = \sigma + j2\pi f, \tag{3.32}$$

for the case with a real part $\sigma = 0$, only yields a dependency on the (circular) frequency f (ω) in the imaginary term with $j = \sqrt{-1}$. For the transfer of spectral densities it is straight forward to transform the system into frequency domain (Brown & Hwang, 2012),

$$S_\Phi(\omega) = |H_a(\omega)^2| S_a(\omega) = |H_a(s)^2| S_a(s) = S_\Phi(s). \tag{3.33}$$

An alternative is to start from a constructed function of unit steps similar to Eq. (3.23), but at times -T, 0 and T, as the Fourier transform of functions that are not centered around zero is mathematically difficult to handle. The transformation results in:

$$\mathcal{F}\{g(t)\} = G(\omega) = -\frac{4j}{\omega}\sin^2\left(\frac{\omega T}{2}\right). \tag{3.34}$$

If Eq. (3.25) is further applied in the frequency domain, the following transfer function H_a of accelerations to the interferometer phase can be stated

$$H_a(\omega) = 4j\frac{k_\mathrm{e}}{\omega^2}\sin^2\left(\frac{\omega T}{2}\right). \tag{3.35}$$

As an example, a white noise process in the accelerations with spectral density S_a is transferred into the corresponding interferometer phase noise S_Φ via

$$S_\Phi(\omega) = |H_a(\omega)^2| S_a(\omega). \tag{3.36}$$

The complete expression is thus,

$$S_\Phi(\omega) = 16\frac{k_\mathrm{e}^2}{\omega^4}\sin^4\left(\frac{\omega T}{2}\right) S_a(\omega). \tag{3.37}$$

The transfer function is a combination of a sinusoidal modulation and a second order integrator. For large frequencies above the cutoff $f = \frac{1}{T}$, the impact of the integrator is overshadowing the modulation and the transfer function acts a second order low pass filter. However, for frequencies $f_n = n\frac{1}{T}$, $n \in \mathbb{N}^+$, it is zero, and the corresponding signals are consequently blocked.

3.4 Kinematic Model for the Atom Wave Packets

3.4.1 Path Integral and Midpoint Line Model

So far, the impact of accelerations on the phase shift of the interferometer was examined. The basis for the evaluation was the sensitivity function to accelerations stated in Eq. (3.27). In numerous experiments (Barrett et al., 2014; Geiger et al., 2011; Richardson et al., 2020), this function in its frequency domain representation is used to transform the measurement of classical accelerometers, which are attached to the retroreflection mirror, into CAI observation space and correlate the two signals in order to solve the fringe ambiguity in the face of large accelerations and mechanical noise. The circumstance that the mirror vibration directly affects the measurement of the interferometer appears elegant, but somewhat counter-intuitive when it comes to the measurement of uniform accelerations and especially rotations of the interferometer laser frame. Antoine and Bordé (2003) developed a formalism in which the phase shift is expressed in dependence of the position of the atoms in the laser field. By using a proper kinematic motion model for the atoms, a more general description of the phase shift can be derived.

Let's assume that the cloud of atoms can be represented by its center of mass. Following the principle of least action, the action $\mathbf{S}$ along the most likely path of a classical particle is defined by the path integral (Landau & Lifšic, 2011):

$$\mathbf{S} = \int_{t_0}^{t} \mathbf{L}\left[\mathbf{x}(t), \dot{\mathbf{x}}(t)\right]\, dt. \tag{3.38}$$

Here, $\mathbf{L}$ is the Lagrangian and $\mathbf{x}(t)$ and $\dot{\mathbf{x}}(t)$ the time-depending position and velocity, respectively. Storey and Cohen-Tannoudji (1994) pointed out that the space-time evolution of a wave function can be expressed in an equivalent, i.e. classical, fashion if the Lagrangian is at most quadratic with respect to the position and velocity. This includes the cases of free evolution with the kinetic energy $\mathbf{E}_{kin} = \frac{1}{2}m\dot{\mathbf{x}}^2$, the impact of a gravity field leading to the potential $\mathbf{E}_{pot} = m\mathbf{g}\cdot\mathbf{x}$, as well as a particle in a reference frame, rotating at a constant angular rate $\mathbf{\Omega}$, notably the general case

$$\mathbf{L} = \frac{1}{2}m\dot{\mathbf{x}}^2 - m\mathbf{g}\cdot\mathbf{x} + m\mathbf{\Omega}\cdot(\mathbf{x}\times\dot{\mathbf{x}}) + \frac{1}{2}m(\mathbf{\Omega}\times\mathbf{x})^2. \tag{3.39}$$

Now in the atom interferometer there are two states of the wave packet, each with a corresponding center of mass, following one of the two paths of the interferometer. Antoine and Bordé (2003) formulated a closed form representation of the interferometer phase shift between the two paths. They showed that it is sufficient to describe the apparent motion of the wave packet on the "midpoint line", which is essentially the center of mass of both wave packet states, cf. Fig. 3.10. This can be understood as the mean of the two states in terms of position and velocity. Their findings and assumptions can be summarized as following:

- The path of each wave packet can be associated with a corresponding mass, initial position and momentum.
- In the case of the interferometer, and perfect 50/50 splitter pulses, the masses of the atoms on each path can be considered equal.
- The interferometer is further considered as symmetric, meaning that a mid-point line can be defined, and the half-sum of the positions of each path is equal to a midpoint-line position $\mathbf{x}$.
- A change in phase shift between the two paths only occurs during interaction of the wave packet and the light field.

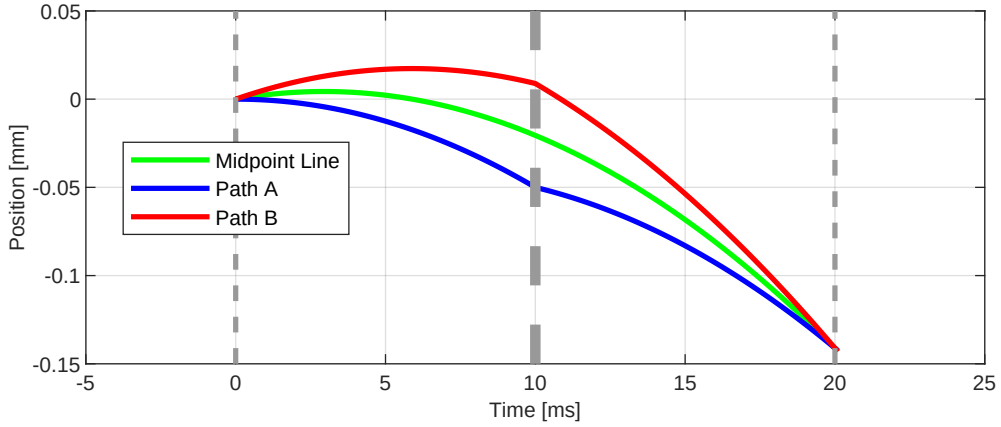

Figure 3.10: Paths of the atom wave packet in a Mach-Zehnder pulse pattern interferometer. An acceleration of $-1\,\mathrm{m/s^2}$ is acting in sensitive direction. The three pulses at 0 ms, 10 ms and 20 ms are depicted as gray dotted lines, the line width used as a qualitative indicator for the pulse length. The two paths A and B are illustrated in blue and red, respectively. The midpoint-line in green represents the mean position of the wave packet center of mass.

Some further assumptions need to be made at this point. The state transition during each interferometer pulse has a dependency on the pulse length itself, the Rabi-oscillation that was already introduced in Sec. 3.1. In order to simplify the further equations, an infinitely short pulse length is assumed, as well as a planar shape of the laser wave front. This can be justified for interrogation times that are considerably larger than the pulse length. The phase shift at

the n-th interaction in a sensitive direction and under the above considerations is then given by:

$$\phi(t_n) = \sum_{i=1}^{n} \left((\mathbf{k}_B(t_i) - \mathbf{k}_A(t_i)) \cdot \mathbf{x}(t_i) + \phi_{\text{light},A}(t_i) - \phi_{\text{light},B}(t_i) \right) \tag{3.40}$$

where $\mathbf{k_e}(t_i) = \mathbf{k}_B(t_i) - \mathbf{k}_A(t_i)$ is the effective wave vector, and $\phi_{\text{light},i} = \phi_{\text{light},A}(t_i) - \phi_{\text{light},B}(t_i)$ the respective differential phase of the counterpropagating lasers at the time t_i.

In a Mach-Zehnder type interferometer with equal pulse separation time T, and an identical effective wave vector $\mathbf{k}_\text{e}$ for each pulse, the phase shift after the second splitter pulse is consequently

$$\phi(2T) = \mathbf{k}_\text{e} \cdot \mathbf{x}(0) - 2\mathbf{k}_\text{e} \cdot \mathbf{x}(T) + \mathbf{k}_\text{e} \cdot \mathbf{x}(2T) + \underbrace{\phi_1 - 2\phi_2 + \phi_3}_{=0}. \tag{3.41}$$

The light induced phase shifts are in sum zero, just as discussed in Sec. 3.3.1.

To wrap this section up, it was pointed out that the evolution of the wave packet state over time can be described with a classical path integral of the Lagrangian of a point mass. Furthermore, in the symmetric atom interferometer it is sufficient to describe the kinematic state of the point mass along the midpoint line. In the next section, this kinematic state will be formalized. This includes the introduction of a coordinate system for the interferometer frame, as well as the solution of the kinematic state differential equations under different dynamic conditions, culminating in the so-called Atom Strapdown (AtoS) method.

3.4.2 Atom Strapdown

First, a new coordinate system for the sensor has to be defined, which is subsequently denoted as **s-frame**. In order to simplify the notation, the origin of the s-frame is placed at the exact location of the atoms at the time of the first splitter pulse. The atom interferometer is assumed to be aligned with the axes of the b-frame appointed to the platform it is placed on. The $\mathbf{s}_1$-axis of the newly introduced s-frame is aligned with the direction of the interrogation laser, cf. Fig. 3.11. The $\mathbf{s}_3$-axis is pointing towards the direction of the gravity vector. The $\mathbf{s}_2$-axis then completes the right-handed system. Any misalignment between the s-frame and the b-frame is neglected for now. They will be further developed in the QINS integration chapter in Sec. 4.2.1.

After preparation in a 3D magneto-optical trap, the atoms are released so they are evolving freely through space and time based on their initial momentum. The s-frame, however, is affected by the accelerations and angular rates. This means that a relative motion occurs between the laser and the atoms. The position vector pointing to the center of the atom cloud in the s-frame is denoted as $\mathbf{x}^s_{sa}$, see Fig. 3.11. As indicated before, it is mandatory to calculate the position of the atoms in the s-frame based on the input dynamics, which are again given by accelerations $\mathbf{f}^s_{is}$ and angular rates $\boldsymbol{\omega}^s_{is}$. The phase shift can then be calculated by Eq. (3.41). It reads:

$$\boldsymbol{\phi}^s = {\mathbf{k}_\text{e}}^s \cdot \mathbf{x}^s_{sa}(t=0) - 2{\mathbf{k}_\text{e}}^s \cdot \mathbf{x}^s_{sa}(t=T) + {\mathbf{k}_\text{e}}^s \cdot \mathbf{x}^s_{sa}(t=2T), \tag{3.42}$$

whereas T is the interrogation time between the Raman laser pulses.

One small hint about the vector representation in this very general equation (3.42). The atom interferometer as introduced so far only has one sensitive axis. This axis is represented by its effective wave vector ${\mathbf{k}_\text{e}}^s$. As an example, if it is only sensitive for the $\mathbf{s}_1$-direction, the wave vector has the form

$${\mathbf{k}_\text{e}}^s = \begin{bmatrix} k_x & 0 & 0 \end{bmatrix}^\text{T} \tag{3.43}$$

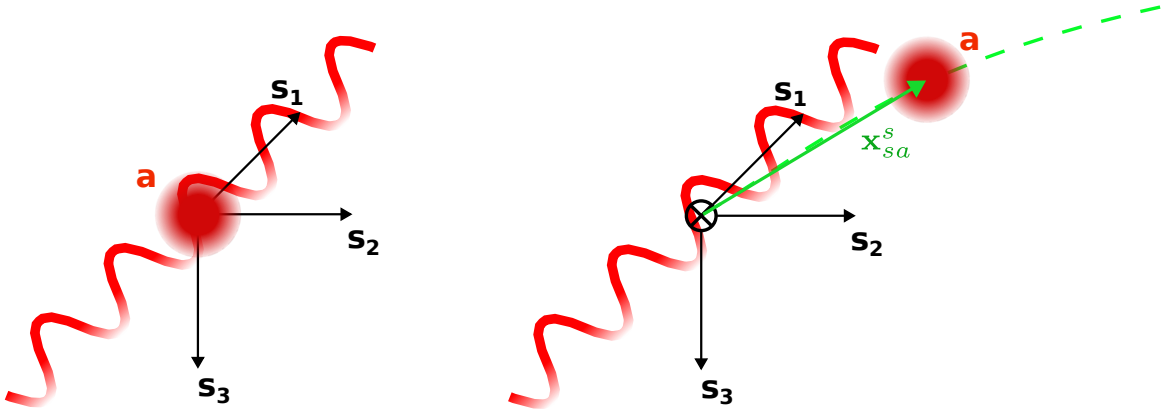

Figure 3.11: Coordinate system of the atom interferometer. Left: initial position of the atom wave packet a at $t = 0$. Right: atom position after some time of evolution. The position vector $\mathbf{x}^s_{sa}$ is pointing onto the center of mass of the atom wave packet a which travels along the midpoint line (dotted green).

and thus there can only be a non-zero phase shift on the respective sensitive axis. The advantage of the general notation is that the question about which axis is covered by an interferometer does not need to be answered now. It will however be important for the specific applications and the system integration of the CAI in Chap. 4.

Accelerating and non-rotating frame

In order to get some intuition about the problem and the new notation, a simple scenario in an inertial non-rotating frame is assumed where only an acceleration in $\mathbf{s}_1$-direction is present. The actual acceleration of the frame, $\mathbf{a}^s$, stands in the following relation with gravity $\mathbf{g}^s$ and the specific force $\mathbf{f}^s_{is}$,

$$\mathbf{f}^s_{is} = \mathbf{a}^s - \mathbf{g}^s. \tag{3.44}$$

The differential equations describing the motion of the atom wave packet in the s-frame are as following

$$\dot{\mathbf{x}}^s_{sa} = \mathbf{v}^s_{sa}, \tag{3.45}$$
$$\dot{\mathbf{v}}^s_{sa} = -\mathbf{f}^s_{is}. \tag{3.46}$$

The indices follow the convention introduced in Sec. 2.2.2. The change of velocity $\dot{\mathbf{v}}^s_{sa}$ of the vector from the center of the s-frame to the atom is opposed to the acceleration $\mathbf{a}^s$ of the frame. This is due to the fact that the frame is accelerated while the atom stays or moves according to the location and momentum it receives from initial manipulation. The equations can be evaluated by numerical integration. The initial atom position is zero, by definition of the s-frame. The initial atom velocity is defined by the recoil velocity $\frac{1}{2}\mathbf{v}_{\mathrm{rec}}$, and potentially by the momentum inherited from the separation pulse which is used for CAI designs sensitive to angular rates like shown in Fig. 3.4.

Under the assumption that the acceleration is constant and the initial atom position is zero, the following closed solution of the phase shift after the CAI measurement can be established:

$$\phi^s = \mathbf{k}^s_e \cdot \left(-2\frac{1}{2}\mathbf{f}^s_{is}T^2 + \frac{1}{2}\mathbf{f}^s_{is}(2T)^2\right),$$
$$\phi^s = -\mathbf{k}^s_e \cdot \mathbf{f}^s_{is}T^2. \tag{3.47}$$

In literature this is a wide-spread equation for atom gravimeters for the special case that $\mathbf{f}^s_{is}$ is entirely caused by gravity and the sensitive axis of the sensor is pointed downwards.

Rotating frame with no acceleration

The next scenario is a rotation of the frame with angular rate $\mathbf{\Omega}^s_{is}$ without any acceleration. This is a rather hypothetical case, and the only purpose is to demonstrate how the sensitivity to rotations is affected by different terms. The differential equations yield:

$$\dot{\mathbf{x}}^s_{sa} = \mathbf{v}^s_{sa}, \tag{3.48}$$

$$\dot{\mathbf{v}}^s_{sa} = 2\mathbf{\Omega}^s_{is}\mathbf{v}^s_{sa} + \mathbf{\Omega}^s_{is}\mathbf{\Omega}^s_{is}\mathbf{x}^s_{sa} + \dot{\mathbf{\Omega}}^s_{is}\mathbf{x}^s_{sa}. \tag{3.49}$$

In this case, there is a number of terms resulting from fictitious forces that occur, namely the Coriolis $2\mathbf{\Omega}^s_{is}\mathbf{v}^s_{sa}$, centrifugal $\mathbf{\Omega}^s_{is}\mathbf{\Omega}^s_{is}\mathbf{x}^s_{sa}$ and Euler term $\dot{\mathbf{\Omega}}^s_{is}\mathbf{x}^s_{sa}$.

Eq. (3.49) implies that in order to get the system evolving, an initial velocity, respectively momentum, is needed. This is the main reason why the atoms in the majority of CAI based gyroscopes are provided with an initial drift velocity perpendicular to the sensitive axis.

The phase shift for the Coriolis term in the rotating frame is the following. Again, a constant value for $\mathbf{\Omega}^s_{is}$ and notably $\mathbf{v}^s_{sa}$ is assumed in order to produce a closed solution:

$$\begin{aligned}\phi^s &= \mathbf{k}^s_e \cdot \left(-2\frac{1}{2}2\mathbf{\Omega}^s_{is}\mathbf{v}^s_{sa}T^2 + \frac{1}{2}2\mathbf{\Omega}^s_{is}\mathbf{v}^s_{sa}(2T)^2\right), \\ \phi^s &= 2\mathbf{k}^s_e \cdot \mathbf{\Omega}^s_{is}\mathbf{v}^s_{sa}T^2. \end{aligned} \tag{3.50}$$

which only includes the effect of the rotation in the Coriolis term, similar to many MEMS gyroscope designs.

Notice that the terms involving the atom position also lead to spurious effects on the phase shift. The implications of this will be further elaborated in Sec. 4.3.3.

Rotating and accelerating frame, general case

Now a more general case with an accelerating and rotating frame is discussed. The differential equations yield

$$\dot{\mathbf{x}}^s_{sa} = \mathbf{v}^s_{sa}, \tag{3.51}$$

$$\dot{\mathbf{v}}^s_{sa} = -\left(\mathbf{f}^s_{is} - 2\mathbf{\Omega}^s_{is}\mathbf{v}^s_{sa} - \mathbf{\Omega}^s_{is}\mathbf{\Omega}^s_{is}\mathbf{x}^s_{sa} - \dot{\mathbf{\Omega}}^s_{is}\mathbf{x}^s_{sa} + \left(\int_{t_1}^{t} \mathbf{\Omega}^s_{is}\, d\tau\right)\mathbf{f}^s_{is}\right). \tag{3.52}$$

The final phase shift in the case of constant signals over 2T is:

$$\phi^s = \mathbf{k}_{\mathrm{e}}{}^s \cdot \left(2\mathbf{\Omega}^s_{is}\mathbf{v}^s_{sa}T^2 - \mathbf{f}^s_{is}T^2 + \mathbf{\Omega}^s_{is}\mathbf{\Omega}^s_{is}\mathbf{x}^s_{sa}T^2 + \dot{\mathbf{\Omega}}^s_{is}\mathbf{x}^s_{sa}T^2 - \mathbf{\Omega}^s_{is}\mathbf{f}^s_{is}T^3\right). \tag{3.53}$$

Note that a higher order phase shift term with T^3 is involved which results from the change of the rotation vector during the velocity integration, comparable to Eq. (2.58).

Sensor Frame Origin

In the frame of discussion in this thesis, the origin of the sensor frame is placed at the location of the initial splitter pulse. Other options are possible, the most prominently one being the position where the interrogation laser interacts with the retroreflection mirror (Zahzam et al., 2022). There is no general solution to this problem, but two hints can be given to the system designer.

First, the placement of the s-frame origin in a location different from the interaction point of the light field with the center of mass of the atom wave packet leads to a non-trivial initial $\mathbf{x}_{sa}^s$, but does not affect the resulting phase shift. To illustrate this, let $\mathbf{x}_{sa}^s$ be an arbitrary non-zero vector $\mathbf{x}_0$. The phase shift reads

$$\phi^s = -\left(\mathbf{k}_\mathrm{e} \cdot \mathbf{x}_0 - 2\mathbf{k}_\mathrm{e} \cdot (\frac{1}{2}\mathbf{f}_{is}^s T^2 + \mathbf{x}_0) + \mathbf{k}_\mathrm{e} \cdot (2\mathbf{f}_{is}^s T^2 + \mathbf{x}_0)\right). \tag{3.54}$$

This equation, after expansion of the inner brackets and some reformulation,

$$\phi^s = -\left(\underbrace{\mathbf{k}_\mathrm{e} \cdot \mathbf{x}_0 - 2\mathbf{k}_\mathrm{e} \cdot \mathbf{x}_0 + \mathbf{k}_\mathrm{e} \cdot \mathbf{x}_0}_{=0} + \mathbf{k}_\mathrm{e} \cdot \mathbf{f}_{is}^s T^2\right) = -\mathbf{k}_\mathrm{e} \cdot \mathbf{f}_{is}^s T^2, \tag{3.55}$$

shows that the initial position is canceled out. This can analogously be shown for rotation induced phase shifts as well.

Second, the s-frame is defined as a rotating frame, meaning that the origin is best placed in the center of rotation of the lasers. It was clarified that the initial position does not affect the phase shift. However, any distance between the center of the frame and the atoms leads to a scaling effect of any rotation-related terms, i.e. centrifugal and Euler. As this depends on the specific implementation of the CAI and the vehicle, it will not be covered in detail.

Gravimetry

A special operation mode needs to be mentioned, which is often applied for pure gravimetric measurements, but is not directly related to the AtoS. This involves cases in which a constant acceleration due to gravity can be expected. In this instance it is possible to apply a phase shift based on a frequency sweep with chirp rate ζ. The frequency sweep can be adjusted, so that the resulting phase shift

$$\phi^s = (\zeta - \mathbf{k}^s \cdot \mathbf{g}^s)T^2 \tag{3.56}$$

is zero. In this occasion the vector of gravity can be reconstructed,

$$\mathbf{g}^s = \zeta {\mathbf{k}_\mathrm{e}}^s / \|{\mathbf{k}_\mathrm{e}}^s\|^2, \tag{3.57}$$

whereas the only non-zero entry of $\mathbf{g}^s$ yields

$$g_z^s = \frac{\zeta}{k_z^s}. \tag{3.58}$$

This result is a scalar and represents the projection of the gravity vector on the sensitive axis as defined by the wave vector and expressed by the scalar product $\mathbf{k}^s \cdot \mathbf{g}^s$. Thus, k_z^s is representing the wave number of the sensitive axis that is supposed to be aligned with the gravity vector.

This technique can be applied for initial calibration of the interferometer. If the same frequency sweep rate is used in subsequent measurements, the impact of the constant gravity vector's magnitude is already compensated. The effect of the Earth rotation rate can be accounted for by turning the retro-reflection mirror to a certain degree in direction of the Coriolis force, cf. Peters et al. (2001). Thereby, the lateral drift due to the Coriolis effect is compensated.

3.4.3 Evaluation and Comparison with the Correlation Approach

The AtoS can be viewed from two different perspectives. First of all, it is a **generalized formalism** for the correlation approach (Barrett et al., 2014; Cheinet et al., 2008; Geiger et al., 2011; Richardson et al., 2020). In the correlation approach the integral in Eq. (3.30) is directly evaluated with accelerometer data as input. Contrary to that, the wave packet position in the sensor frame is calculated explicitly in the AtoS. This enables an arguably more intuitive way of connecting the phase shift of the interferometer with the accelerations and rotations of the sensor frame. Even in the basic configuration, angular rates and accelerations are already included in the mathematical description of the phase shift, in principle enabling the solution of the phase shift with data of a complete IMU under an extended range of dynamic conditions. This renders it even more powerful if the spatial distance and the misalignment between the systems are involved in the formalism. Another advantage of tracking the atom wave packet as position vector is that at this rate, information about the spatial evolution of the atoms in the s-frame is available. Based on this information it is possible to decide, when the atoms will leave the diameter of the interrogation laser field, making fault detection possible. Furthermore, the vacuum chamber and the laser can already be designed early in the production process of a CAI, based on the dynamics that are expected from a specific applications.

The closed solution for the phase shift under the assumption of a constant system that was stated in Eq. (3.47) and Eq. (3.50) also results from the correlation. This was shown experimentally for acceleration data on a single axis (Tennstedt et al., 2023). The advantage of the correlation approach is that it allows to incorporate the laser pulse duration by enhancing the response function $h(t)$. This also makes it easier to compute the noise propagation, especially for uncertainty of the acceleration signal $a(t)$ or phase fluctuations of the laser, cf. Fang et al. (2018).

In the context of noisy IMU data, the **numerical evaluation of the phase shift** based on the computed atom position at the pulse times demands more careful consideration. While in theory the temporal resolution of the phase shift prediction is increased by the numerical solution of the differential equations, the double integration of high rate, noisy IMU data leads to systematic deviations from the variance propagation based on the theoretical model (Thong et al., 2004). This might similarly affect the correlation approach and is open for further investigation which exceeds the frame of this thesis.

3.5 Limits of the Atom Interferometer as Inertial Sensor

The goal of this section is to point out the limits of CAI as inertial sensor. The first issue that was already discussed in Sec. 3.2.1 is the limited dynamic range due to the ambiguity problem. This **soft limit** can be handled by a prediction of the phase shift with classical sensors, e.g. by application of the proposed AtoS method.

Besides the limited dynamic range due to the ambiguity problem, there are other, physical, **hard limits** inherent to the technology. Accelerations and angular rates that are larger than those limits cannot be resolved. Those hard limits will be introduced now. Afterwards, some mitigation techniques will be evaluated that are proposed in literature. The implications of the limits for a terrestrial QINS will finally be summarized.

As indicated in the beginning of the prior section, the classical description and the models for the three-pulse Mach-Zehnder interferometry architecture work quite well for linear and quadratic potentials in position and velocity, see also Heller (1975). For higher order, phase

shift terms associated with the quantum nature of the wave packets need to be considered (Bertoldi et al., 2019). For short interrogation times, the higher order terms are negligible and are not further considered in the frame of this thesis. But even in the cases in which the classical description holds, there are some limitations to the CAI measurement that need to be discussed in order to decide if CAI is applicable to certain navigation tasks. Two major categories of limits can be stated.

The first category, which can mainly be associated with limits for detectable accelerations, is the spatial dimension of the interrogation laser. This can be illustrated with a simple example: assume that a car is in a constant forward acceleration phase. A first CAI axis is measuring in the forward $\mathbf{s}_1$-direction. This yields no limitation, unless the atoms are reaching the inner boundaries of the vacuum chamber. A second CAI axis is measuring in the $\mathbf{s}_2$-direction, perpendicular to the forward direction. Here, the atoms might leave the interaction zone with the laser, if the accelerations are too large. However, Fig. 3.10 indicates that the displacement is often in the order of some mm, while the width of the laser can be as large as 2.5 cm (Abend et al., 2023), so this does not appear to be a severe limitation. Using simple motion equations like $x = \frac{1}{2}at^2$, the dimensions of the vacuum chamber and the width x of the lasers for a certain expected maximum acceleration a, or likewise the maximum acceleration based on the dimensions, can be assessed easily. As an example, an interrogation time of $T = 10\,\mathrm{ms}$ and a laser width of 10 mm yields a maximum lateral acceleration of $25\,\mathrm{m/s^2}$.

Another factor that can be put into this first category is the shape of the laser wavefront. The models introduced so far are based on the assumption, that the laser wave front is planar and the point in time of interaction of the atoms with the lasers is assumed to be identical for each atom. In general, this is not the case. The shape of the laser wave front can vary, and the interaction time of the atoms in one wave packet varies depending on their position in the laser field. This effect is in the order of magnitude of some $\mathrm{nm/s^2}$ (Karcher et al., 2018), and only relevant for very high accuracy measurement with long interrogation times, which, again, is not considered here.

The second category revolves around the issue that the two paths of the interferometer need to be coherent at the time of the recombination pulse, meaning that they need to overlap. This is generally not given in the case of rotations of the laser frame (s-frame). As pointed out in Antoine (2007), a rotation induces "an asymmetric modification of the two main interferometer arms", and might ultimately lead to a nonclosure of the interferometer. See also Fig. 3.12.

Now the shape of the interrogation laser is not too severe in the light of short interrogation times and small spatial expansion of the wave packets. Furthermore, the dimension of the laser beams and the vacuum chamber are mere design parameters which can be handled as well. For those reasons, the focus of this section lies on the impact of rotations on the interferometer readout. The problem will now be further explained, its limits evaluated and possible mitigation strategies will be stated.

3.5.1 Impact of Rotations on the Interferometer Readout

At first, a mere **geometric approach** to understand the impact of rotations is presented. The displacement $\mathbf{x}_{\mathrm{sep}}$ between the two paths at the time of the recombination pulse leads to a separation phase shift ϕ_{sep}. If this phase shift is too large and exceeds a value of $\pm\frac{\pi}{2}$, it might lead to a fringe ambiguity as well. Fig. 3.12 illustrates the impact of rotations on the two paths of the interferometer on the example of an acceleration of $-1\,\mathrm{m/s^2}$ in direction of the sensitive axis and an additional angular rate of 3 rad/s on a perpendicular axis. It is apparent that the two paths do not exactly coincide at the time of the recombination pulse, as the more detailed visualization of the paths and the displacement $\mathbf{x}_{\mathrm{sep}}$ clearly shows.

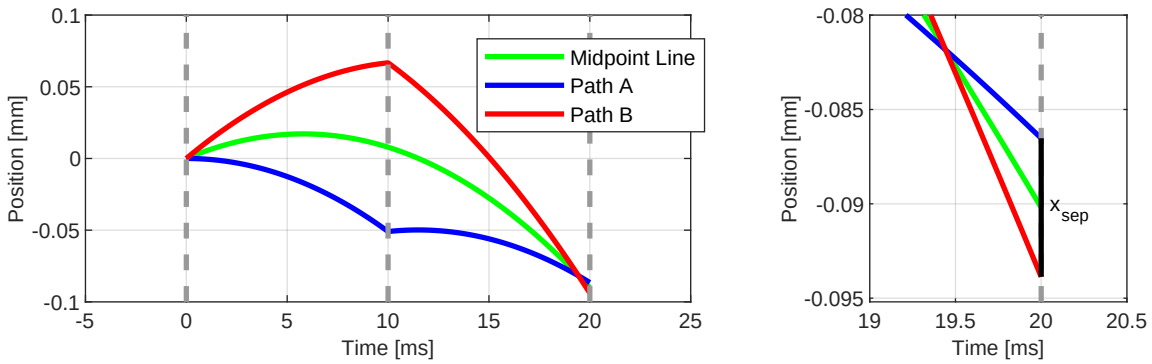

Figure 3.12: Displacement of the CAI interferometer paths under rotation of the frame. The two paths A and B are illustrated in blue and red, respectively. The midpoint-line in green represents the mean position of the wave packet center of mass. A rotation of the s-frame leads to the situation in which the wave packets of the two interferometer paths are not overlapping at the time of the recombination. Note that the midpoint line representation of the mean kinematic state is still valid. The three light pulses are depicted in gray. Right: zoom on the displacement between path A and B during the recombination pulse. The displacement x_{sep} can be related to a separation phase shift ϕ_{sep}, which can surpass the phase ambiguity of $\pi/2$

Note that the position difference at the time of the recombination can also be understood as a direct consequence of the recoil velocity $\mathbf{v}_{\mathrm{rec}}$ (Cadoret et al., 2016). In the case of a rotation with rate $\boldsymbol{\omega}$ only, the position difference is occurring due to the cross-coupling of the rotation and the velocity in the Coriolis term and reads

$$\mathbf{x}_{\mathrm{sep}} = 2\boldsymbol{\omega} \times \mathbf{v}_{\mathrm{rec}} T^2, \tag{3.59}$$

whereas the recoil velocity is given by

$$\mathbf{v}_{\mathrm{rec}} = \frac{\hbar}{m}\mathbf{k}_{\mathrm{e}}, \tag{3.60}$$

with m as the atomic mass.

This spatial separation again leads to a corresponding phase difference ϕ_{sep} (Bongs et al., 2006),

$$\phi_{\mathrm{sep}} = \frac{\rho}{\hbar} x_{\mathrm{sep}}, \tag{3.61}$$

where ρ is the momentum. The expression for three dimensions with the effective wave vector $\mathbf{k}_e$ reads

$$\phi_{\mathrm{sep}} = \mathbf{k}_e \cdot \mathbf{x}_{\mathrm{sep}}. \tag{3.62}$$

For the example of a mean rotation rate of 1 rad/s, this phase shift is in the order of $\phi_{\mathrm{sep}} = 37.94\,\mathrm{rad}$, at $k_{\mathrm{e}} = 4\pi/780\,\mathrm{nm}^{-1}$ and $T = 10\,\mathrm{ms}$. This shows a clear limitation of the interferometer to resolve large rotation rates. For the interferometer with the settings described above, the maximum resolvable rotation rate without correction would thus be about $0.04\,\mathrm{rad/s}$ for a separation phase shift just below $\pi/2$. As a side note, Fig. 3.12 indicates that if the time between the second and the third laser pulse would be reduced by less than 1 ms, the interferometer would still close.

As pointed out in Roura et al. (2014), **another interpretation** of the impact of rotations is that the two distributions of the wave packets in position and momentum do not overlap at the time of the recombination pulse, leading to an *open* interferometer and effectively to a loss of contrast of the interferometer readout. This can be visualized in the phase space of the wave packets, cf. Fig. 3.13.

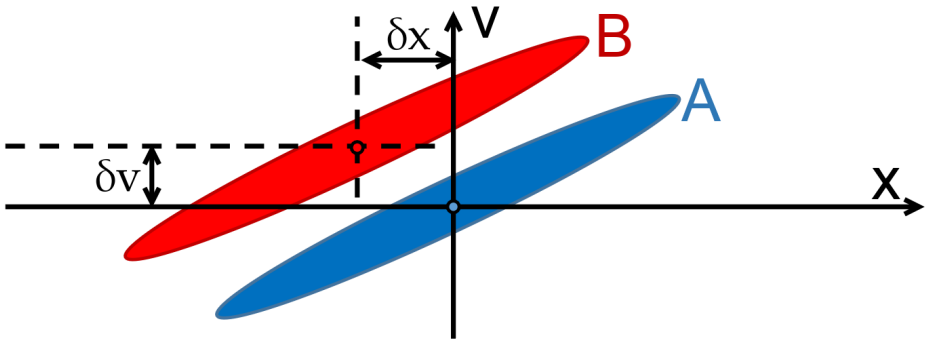

Figure 3.13: Phase space representation of the atom wave packets according to Roura et al. (2014). Depicted is the displacement of the two interferometer paths A (blue) and B (red) in momentum (velocity δv) and position (δx). The values are related to the distance between the centers of mass of the wave packets.

Note that this representation can be gained by an alternative approach to model the phase shift of the atom interferometer. Namely, the formulation of the atom states via probability distribution (Wigner-function, cf. Dubetsky and Kasevich (2006)). Contrary to the path integral approach used for the midpoint line model this representation is much more helpful in modeling the distributions of the atoms in momentum and position. This allows to get an actual quantitative measure of the overlap of the two states, simply by spatial correlation of the two probability densities. This model is often essential to describe the behavior of BEC, but is not further considered in the frame of this thesis as the path integral approach is sufficient and arguably easier to analyze and implement in simulations.

In order to get an idea about the impact of the actual distribution on the interferometer readout, the uncertainties in velocity $\sigma^2_{v^s_{sa}}$ and position $\sigma^2_{x^s_{sa}}$ can be propagated by the phase shift equation (3.53) as a simplification. Note that this representation is equivalent to the first geometric interpretation of the separation phase shift for the case that the propagated uncertainties on the displacement are equal to the actual displacement of the wave packets $\mathbf{x}_{\text{sep}}$. This seems reasonable, as the distance between the wave packets centers of mass can be interpreted as the standard deviation of the spread of the atom wave packets, assuming they share the same distribution.

For example, the effect of the Coriolis acceleration is the following, whereas $\mathbf{\Sigma}_{v^s_{sa}}$ is a covariance matrix representing the spatial velocity dispersion of the wave packet,

$$\phi^2_{\text{sep}} = \sigma^2_\phi = 4T^4 \mathbf{k}_\text{e}{}^\text{T} [\boldsymbol{\omega}^s_{is}\times] \mathbf{\Sigma}_{v^s_{sa}} [\boldsymbol{\omega}^s_{is}\times]^\text{T} \mathbf{k}_\text{e}, \tag{3.63}$$

which, often expressed for the sensitive direction, can also be found in literature (Narducci et al., 2022; Zahzam et al., 2022). For continuous matter wave beam interferometers the same formulation can be applied (Black et al., 2020; Gustavson et al., 1997).

For the remaining dynamics that correspond to the position of the atom wave packet in the rotating s-frame, the centrifugal term reads

$$\phi^2_{\text{sep}} = T^4 \mathbf{k}_\text{e}{}^\text{T} \left([\boldsymbol{\omega}^s_{is}\times][\boldsymbol{\omega}^s_{is}\times]\right) \mathbf{\Sigma}_{x^s_{sa}} \left([\boldsymbol{\omega}^s_{is}\times][\boldsymbol{\omega}^s_{is}\times]\right)^\text{T} \mathbf{k}_\text{e}, \tag{3.64}$$

and the Euler term

$$\phi^2_{\text{sep}} = T^4 \mathbf{k}_\text{e}{}^\text{T} [\dot{\boldsymbol{\omega}}^s_{is}\times] \mathbf{\Sigma}_{x^s_{sa}} [\dot{\boldsymbol{\omega}}^s_{is}\times]^\text{T} \mathbf{k}_\text{e}. \tag{3.65}$$

Here, $\mathbf{\Sigma}_{x^s_{sa}}$ resembles the spatial spread of the wave packet. The propagation of the uncertainty variances according to Eqs. (3.63) - (3.65) demands constant values of $\boldsymbol{\omega}^s_{is}$.

The contrast C_0 can be related to the amplitude A and offset p_0 of the interferometer observation equation (3.10) by

$$C_0 = \frac{A}{p_0}. \tag{3.66}$$

The contrast loss C/C_0 with respect to the unperturbed contrast C_0 can finally be expressed in terms of the separation phase shift ϕ_{sep}, which is directly related to the displacement of the wave packets (Cronin et al., 2009),

$$\frac{C}{C_0} = e^{-\frac{1}{2}\phi_{\text{sep}}^2}. \tag{3.67}$$

The more difficult part is to model the uncertainties $\sigma^2_{v^s_{sa}}$ and $\sigma^2_{x^s_{sa}}$. This is not covered in detail in this thesis, but a few numbers are now summarized to convey the order of magnitude. One way to assess the distribution of the ensemble is by the velocity selection of the Raman pulses, as described in Kasevich et al. (1991) and Moler et al. (1992). They pointed out the following relation for the spread of the atom velocity, depending on the recoil velocity v_{rec},

$$\sigma_{v^s_{sa}} = 3.6 v_{\text{rec}} \frac{1}{\sqrt{2}}. \tag{3.68}$$

For a recoil velocity of 11.8 mm/s this results in a dispersion of $\sigma_{v^s_{sa}} = 30$ mm/s for a single atom.

Recent research for the application in future space gravity missions (Zahzam et al., 2022) uses the following assumptions for the uncertainties in their simulations, $\sigma_{x^s_{sa}} = 2$ mm, $\sigma_{v^s_{sa}} = 2.5\,\text{mm/s}$ for a cloud of 100 atoms. While the authors do not further comment on their assessment of the value of $\sigma_{x^s_{sa}}$, the order of magnitude of $\sigma_{v^s_{sa}}$ can be explained by Eq. (3.68), divided by the square root of the number of atoms.

One more theoretical approach is discussed in Lan et al. (2012), where the size of the wave packet is related to the thermal de Broglie wavelength. The latter is mainly depending on the atom temperature. On the example of Caesium atoms, a typical value of $\sigma_{x^s_{sa}} = 13\,\text{nm}$ is named. This rather small value can be explained by the connection between the uncertainty of position and momentum which is given by the Heisenberg uncertainty principle (Kennard, 1927),

$$\sigma_{x^s_{sa}} \sigma_{v^s_{sa}} m \geq \frac{\hbar}{2}. \tag{3.69}$$

By reformulating Eq. (3.69), the uncertainty of the position can be approximated,

$$\sigma_{x^s_{sa}} \approx \frac{\hbar}{2\sigma_{v^s_{sa}} m}. \tag{3.70}$$

Using the ^{87}Rb example, the position uncertainty is in fact in the order of magnitude of a few nm. The combination of Eq. (3.68) and Eq. (3.70) thus appears to be a good basis to approximate the initial uncertainty of the wave packets.

As a demonstration, the uncertainty is modeled for an atom cloud consisting of 5×10^5 ^{87}Rb atoms. An angular rate of 0.05 rad/s and an angular acceleration of $0.01\,\text{rad/s}^2$ is simulated on one of the axes perpendicular to $\mathbf{k}_e$. The initial uncertainties $\sigma_{v^s_{sa}} = 9.5 \times 10^{-5}\,\text{m/s}$ and $\sigma_{x^s_{sa}} = 3.9 \times 10^{-6}\,\text{m}$ as gained from Eq. (3.68) and Eq. (3.70) are propagated according to Eqs. (3.63)-(3.65). The contrast loss is then computed with Eq. (3.67). The results are presented in Fig. 3.14. Out of the three dynamic terms, the Coriolis term clearly has the largest effect since it scales linearly with the magnitude of the rotation. In case of large rotation rates $> 1\,\text{rad/s}$ (centrifugal term), or in the case of large angular acceleration (Euler term), the impact of the remaining terms can potentially surpass the impact of the Coriolis

term. This example further illustrates that the impact of the initial uncertainty on the contrast loss is mainly relevant for larger interrogation times. Even for $T = 25\,\mathrm{ms}$, there is almost no reduction apparent.

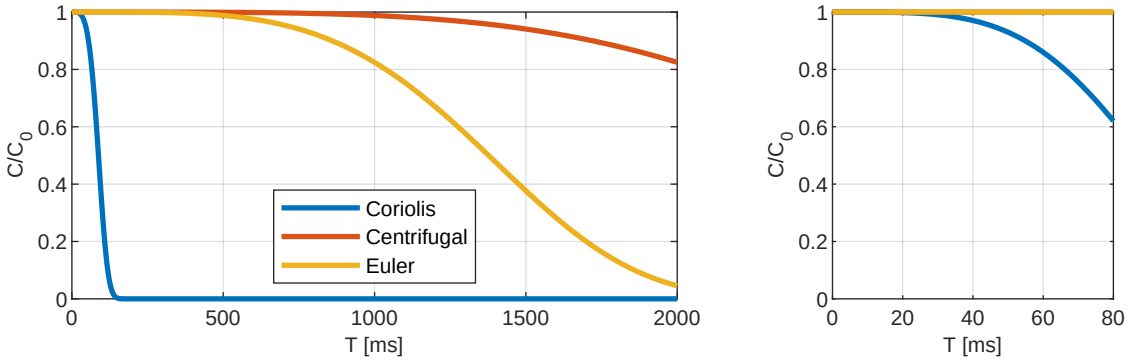

Figure 3.14: Impact of rotations on the CAI contrast for different pulse separation times T. Left: the contrast loss due to the occurrence of dynamic terms associated with a rotation of the sensor frame is illustrated. Right: detail view on small values of T up to 80 ms.

3.5.2 Mitigation Techniques

In the previous section, it was shown that rotations yield a strong limitation for the dynamics that an atom interferometer can resolve. Rotations of the sensor frame might lead to situations in which the atoms leave the diameter of the interrogation lasers. Additionally, rotations lead to a spatial separation of the atomic paths at the time of the recombination pulse, which results in a separation phase shift. Next to the centrifugal and Euler effect, it is especially the Coriolis effect that has the largest impact on the separation phase shift, and thus yields the strongest reduction in contrast. Interestingly, it is the very same dynamic term which in turn enables the interferometer to be sensitive to rotations and thus measure angular rates. As a consequence, the compensation of the effects that lead to a loss of contrast is highly important.

A straight forward approach to compensate for a separation phase shift is to counter act the rotation itself. This could be realized by applying a tilt angle on the retroreflection mirror which spans the reference frame for the interferometer measurement. This was realized in terrestrial gravimetry, see for instants Peters et al. (2001), in order to compensate for the Coriolis effect with a magnitude of $\sim$0.07 mrad/s. Furthermore, this method is proposed for the satellite scenario, e.g. in Beaufils et al. (2023), in order to handle rotations in the 1 mrad/s realm.

However, the drawback of this approach is that the uncertainty of the correction measure is propagated to the uncertainty of the CAI measurement itself. Thus, the accuracy of the compensation needs to be at least at the level as, or preferably an order of magnitude better than, the accuracy of the rotation measurement with the CAI. This means that the control of the rotation, or the sensors that measure the tip angle, need to be precise enough in order to qualify for the rotation compensation, as pointed out in Beaufils et al. (2023) as well. Furthermore, both examples that were stated are compensating for small rotations up to 1 mrad/s, which is quite small compared to the rotation rates that can be expected in terrestrial navigation, i.e. several orders of magnitude larger.

A different approach tackles the problem that the two interferometer paths are not directly overlapping at the time of the recombination pulse, cf. Fig. 3.12, but about a millisecond earlier. As a consequence, Roura et al. (2014) proposed to apply the recombination pulse

not after the interrogation time T after the mirror pulse, but at a time T' that is adapted exactly to the point in time that the two paths intersect. In their experiment, the contrast was reproduced after the adaption. This compensation requires knowledge about the actual rotation.

A different approach is to not compensate for the rotations directly, but to avoid them. This is especially interesting for applications with large rotation rates that cannot be compensated for by any means. A car trajectory might include rotations with up to 3 rad/s angular velocity. Even trains with the lower angular rates by design can still achieve rates up to 0.025 rad/s and more. Thus, the tendency should be to avoid CAI measurement in maneuvers that exceed the dynamic limit, rather than to compensate for them. This requires sensors to measure the dynamics, and some decision logic to detect the maneuvers in order to avoid, or at least discard the CAI measurement. Contrary to most classical accelerometers which are physically damaged in case of crossing the dynamic range limit, the atom interferometer, aside from the measurement being cancelled, is unaffected by atoms which are getting in touch with the internal frame of the vacuum chamber.

Some additional options for a compensation or handling cases of large rotations might include

- Different interferometer schemes that compensate for the rotation phase shift by design (Barrett et al., 2019; Canuel et al., 2006). Pulse schemes can be designed specifically to make the interferometer sensitive to distinct physical quantities, and cancel other effects (Cadoret et al., 2016).
- Usage of a stabilized platform which covers the corresponding degree of freedom. The actuators and the control introduce additional vibrations and noise in the measurement and need to be precise enough.
- Use of continuous matter wave beams (Black et al., 2020; Gustavson et al., 2000). For specific axes of rotation the dynamics can far surpass the values that can be achieved by light pulse interferometers, but come to the cost of larger bias instability.
- Optimization of the control of the laser pulses is another option that is at least partially applicable to counteract the effect of small rotations. The cost function that needs to be maximized is the overlap of the wave packets (Saywell et al., 2020). Rather than having the standard $\frac{\pi}{2}$ or π pulses characterized by the Rabi frequency, pulse compounds of small phase shift increments have lots of potential and can improve the fidelity of the atom state transition in highly dynamic applications.

Discussion

The **hard limits** of a CAI have been presented. It was stated that the acceleration hard limit is comparably unproblematic. For certain, high dynamic applications, the necessary width of the laser and the dimensions of the vacuum chamber can be assessed by simple kinematic models. The more severe limit comes in the form of rotations. Here, a geometric and a stochastic approach to model the effects and the boundaries have been presented. Both indicate that the limit for angular rates is quite low; well below 0.1 rad/s, already for short interrogation times of 10 ms.

Furthermore, different approaches to increase the dynamic range of the CAI measurement were evaluated. Every single one of them demand the measurement of the motion, or some highly precise actuator. Regarding the question, how precise such an actuator should be, no concrete numbers can be stated at this point, since the parameters depend on the dynamics as

well as on the CAI settings. However, the propagation of systematic errors and uncertainties to the CAI measurement is discussed in detail in Sec. 4.3.2, and can be used as a starting point for such evaluations.

For the remainder of the thesis, the hard limits will be considered as actual boundaries of the sensor, and no attempt will be made to include any stabilization platform or other means of compensation in the simulation or discussion. Regarding the soft limits, the QINS is the proposed solution and will be covered in the next chapter.

4

Formulation of a Quantum Inertial Navigation System

4.1 Introduction

So far, models were introduced for the inertial measurement unit (IMU) in Chap. 2 and the cold atom interferometer (CAI) in Chap. 3. It was pointed out that in order to compute the kinematic state of a vehicle, the angular rates are integrated as a means to update the attitude of the platform w.r.t. a defined target coordinate system, while the accelerations are integrated twice in order to compute the velocity and the position. Furthermore, it was made clear that this method of computing the kinematic state has inherent error characteristics. Prominently, the drift of the solution due to integrated uncertainties of the base signals.

The CAI measurement on the other hand is practically drift-free, in a sense that with each measurement, a new independent wave packet is interrogated. The observation is essentially a position measurement of the atoms in the s-frame. The flicker noise floor due to laser phase noise is reached well after three hours or later (Gouët et al., 2008). This affects the acceleration as well as angular rate measurement. Also the sensitivity of the CAI to accelerations is, in theory, superior, but bound to the dynamic range. The major tweaking parameter of this trade-off is, besides the momentum transfer characterized by k_e, the interrogation time T.

As a simple example, in order to measure a variation of acceleration $\Delta a = 1\,\mathrm{m/s^2}$ the interrogation time would be required to be as low as

$$T = \sqrt{\frac{\pi}{2\Delta a k_\mathrm{e}}} \approx 0.3\,\mathrm{ms}. \tag{4.1}$$

The uncertainty of the produced acceleration measurement in this case, provided an uncertainty of the CAI observation of $\sigma_p^2 = 10^{-3}$, is

$$\sigma_a = \frac{\sqrt{10^{-3}}}{k_\mathrm{e} T^2} \approx 0.022\,\mathrm{m/s^2}, \tag{4.2}$$

which is a consumer-grade accuracy level. This obviously does not yield any gain.

In order to fully make use of the sensitivity of a CAI, hybridization with high rate accelerometers is often proposed in literature in order to enhance the dynamic range of the interferometer:

- Gouët et al. (2008) examined the limits of the sensitivity of an atomic gravimeter. One of the sources is the signal of a classical seismometer which they transferred into the phase space of the interferometer. They also discussed a feedback loop in which the seismometer signal is directly translated into the corresponding phase correction.

- Merlet et al. (2009) extended that research and compared the fringe fitting technique from Gouët et al. (2008) with a new non-linear estimation technique. A low noise seismometer has been applied as classical accelerometer. The impact of the accelerometer sensor noise was not further evaluated.
- A similar strategy is presented in Lautier et al. (2014). The authors state that this combination would allow for an accelerometer-bias induced position error of one meter after four hours of navigation.
- Fang et al. (2016) presented a continuous cold atom gyroscope in a static setting, in which perturbing vibrations are measured by classical accelerometers.
- Cheiney et al. (2018) applied a Kalman filter (KF) for the fusion of the measurement of a classical accelerometer and a one-axis CAI in lab-environment. They demonstrated that it is possible to track the acceleration bias phase.
- Zhang et al. (2019) presented a monitoring navigation method for the combination of an atomic gyroscope with classical sensors. In simulation they showed that the misalignment and the gyroscope bias between the systems can be estimated. Using two classical fiber optical gyroscopes, they successfully demonstrated the method in kinematic experiments. The limit of an *actual* CAI in presence of large dynamics is mentioned, but not further specified.
- Richardson et al. (2020) presented a combination of a one-axis CAI with an optomechanical resonator OMR in order to increase the dynamic range of the sensor. An improved long-term stability of the combined solution was demonstrated. Due to high short-term drift of the OMR, the data had to be high-pass filtered which makes this approach inapplicable to changing inertial signals of a trajectory.

The experiments listed so far were performed in a static environment. The following mobile applications have been demonstrated.

- Parabolic flight experiments were performed by Geiger et al. (2011). Here, CAI was used to measure the gravity in zero-g conditions. Furthermore, a hybrid solution with a classical accelerometer was demonstrated in accelerated maneuvers. The authors pointed out a relationship between the accelerometer noise and the achievable sensitivity of the CAI.
- Staying in the regime of parabolic flights, Battelier et al. (2016) demonstrated the measurement of accelerations along a horizontal axis using their 1-axis CAI and a classical accelerometer. They also pointed out the theoretical sensitivity limit of the combined solution, which is defined by the noise of the mechanical accelerometer.
- Bidel et al. (2018) presented a marine matter wave gravimeter on a gyro-stabilized platform. The accelerations in sensitive direction were additionally measured with a classical force-feedback accelerometer in order to increase the dynamic range of the gravimeter. They noted that the sensitivity of the combined sensor is limited by the classical accelerometer as well.
- The same gravimeter was then utilized for an airborne scenario (Bidel et al., 2020). Further effort has been applied by the empirical estimation of the transfer function between the classical accelerometer and the matter wave gravimeter. For the two experiments a gyro-stabilized platform was used.
- In Templier et al. (2022) a three-axis hybrid accelerometer is presented and tested on a rotation platform. Accelerations in the range of ± 5 m/s^2 were emulated by the changing orientation of the platform w.r.t. the gravity vector. Notably, the combined solution

in the closed-loop mode works even during the small rotation steps. The interrogation time and the speed of rotation are small enough so the correct fringe information due to the phase shift ambiguity is not lost.

Furthermore, evaluations based on simulations are required to examine the feasibility of quantum navigation and to point out promising future applications.

- One of the first studies was done in Jekeli (2005). Here it was proposed that it is possible to achieve a position solution with an error of below five meters after one hour of navigation. The author included dead times in the discussion in a sense that the dynamics in times that are not covered by CAI must be resolved by a classical sensor. This sensor however needed to be 20 times more precise than commercially available navigation grade accelerometers, in order to considerably improve the positioning accuracy.
- Bochkati et al. (2017) discussed several CAI architectures with different sensitivity levels and used an integration scheme adapted for the low data rate. However, the CAI was simulated as acceleration and angular rate sensor affected by white noise only, and the dynamic range limit and dead times were neglected.
- Wright et al. (2022) performed a quite comprehensive simulation covering different error sources as well as systematic effects of the classical sensor. It is assumed that the biases of the classical IMU are estimated by the CAI. The correction of the classical sensor is realized by subtracting the estimated bias. No lever arm between the sensors is considered.
- Wang et al. (2023) presented a scheme in which the ambiguity of the CAI is solved explicitly with the help of a classical sensor on one axis. The measurements are then fused in the acceleration domain. Systematic effects between the two sensors are not considered.

In all of the mentioned references for mobile applications, CAI was used in conjunction with high rate accelerometers. Most of the studies agree that there is a limit for the sensitivity of the hybridized solution which is related to the quality of the classical sensor. This is mostly tackled by a reduction of the interrogation time to a range where operating the CAI is possible, or by high-pass filtering of the classical sensor's signals. The hybridization can generally be realized in one of two ways:

1. **High pass filtering** the data of the classical system, predicting the phase shift and solving the fringe ambiguity.
2. Predicting the phase shift and solving the fringe ambiguity and **correcting the errors of the classical system**.

In the first option, the atom interferometer is used as the main sensor, supported by accelerometers in order to improve its dynamic range and enable the CAI to work in the face of large mechanical vibrations. The signals of the conventional accelerometers are basically correlated with the CAI sensitivity function to accelerations. This approach is applied mainly in the field of atomic gravimetry (Fang et al., 2016; Gouët et al., 2008; Lautier et al., 2014; Richardson et al., 2020) as it allows to hybridize one accelerometer with a single CAI axis. There is no further need to mention that this is inapplicable to most dynamic scenarios without enormous effort to compensate for any unwanted inertial quantities, as pointed out in Sec. 3.5.

The second approach is to use a complete IMU as main sensor, so that the navigation solution can be computed as presented in Sec. 2.3. This allows to transfer most of the algorithms already developed by the navigation community, and it also solves most of the issues associated

with the low data rate of the CAI in the face of changing dynamics. During the measurement cycles of the CAI, the IMU data is filtered together with the CAI data to increase the dynamic range of the CAI and to infer about the IMU errors. While it is often mentioned in literature that the CAI can be used to correct for the drift of the classical sensor (Cheiney et al., 2018; HosseiniArani et al., 2023; Zahzam et al., 2022), this approach, and the expected performance of the navigation solution, is seldom discussed in detail.

In this chapter, a specific hybridization technique of the second kind is presented, cf. Fig. 4.1, which makes use of a conventional IMU to compute the kinematic state of the moving platform. Whenever a CAI measurement is available, the bias of the conventional sensors are estimated by using an extended Kalman filter (EKF). Thus, the overall performance of the IMU strapdown navigation solution is improved. The prediction can be done by applying the Atom Strapdown (AtoS) method that was presented in Sec. 3.4. The phase shift equations are solved by using the conventional IMU in order to resolve the ambiguity of the CAI, realizing a quantum inertial navigation system (QINS). This includes an extension of the model to consider the spatial distance and relative orientation between the s-frame and the IMU b-frame.

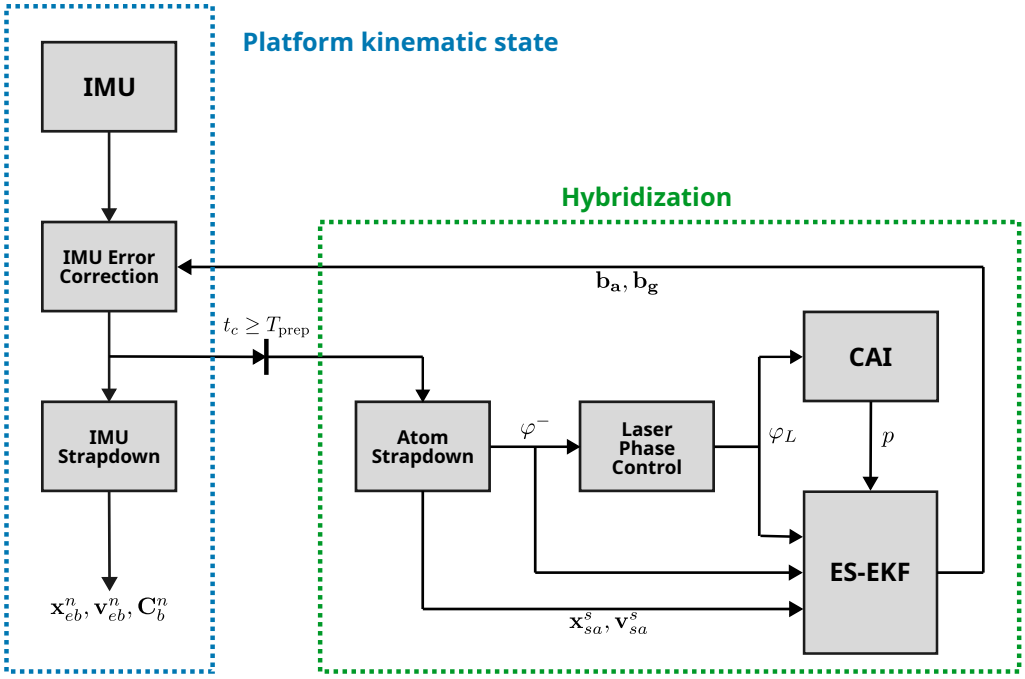

Figure 4.1: Signal flow in the QINS simulation and navigation framework. The CAI phase shift is predicted by the conventional IMU data and fused with the actual CAI observation in order to estimate the bias of the IMU sensors.

In the upcoming Sec. 4.2, the QINS filter framework is introduced and explained. The presented scheme has a number of implications that will be elaborated, including a stability analysis of the hybrid system in Sec. 4.3. This stability analysis covers the derivation of the steady state variance of the filtered accelerations, which in turn allows the discussion of some additional topics like the optimal choice of sensor parameters for the hybridization in Sec. 4.4. Furthermore, the impact of CAI dead times will be discussed, as well as the limitations of the steady state formalism. The findings are discussed in Sec. 4.5 with the help of short but dedicated low level simulation studies, including the complete error models and numerical solution of the navigation equations. Some hints on the long-term performance will then be elaborated in high level simulation studies.

4.2 Hybrid Navigation

The proposed algorithm consists of two major levels. In the **outer level**, the kinematic state of the vehicle, $\mathbf{x}_{eb}^{n}$, $\mathbf{v}_{eb}^{n}$ and $\mathbf{C}_{b}^{n}$ is computed by using the classical IMU based on the equations presented in Sec. 2.3. This dead reckoning computation of the kinematic state is continuously possible at the rate of the IMU. The differential equations are solved by numerical integration with a data rate Δt according to the IMU. This ensures that systematic effects due to low data rate are kept small.

The algorithms in the **inner level** are executed when the CAI measurement interval starts. The following steps are processed:

1. The CAI phase shift is predicted. This can be realized by the correlation according to Eq. (3.30), or with the solution of the AtoS differential equations in the s-frame. For this step, the IMU data is used as input again. The atom position $\mathbf{x}_{sa}^{s}$ and velocity $\mathbf{v}_{sa}^{s}$ is calculated.

2. The predicted phase shift serves several purposes. First, it solves the CAI ambiguity. Thanks to this first *rough* guess of the phase shift, the correct fringe can be identified. Second, it is used as an offset for the laser controller for mid fringe operation.

3. When the observation p of the CAI is available, the filter step is processed. Here, the predicted phase shift, the laser phase and the atom position and velocity are used for the observation model. The bias estimates $\mathbf{b_a}$ and $\mathbf{b_g}$ are updated.

4. With the estimated $\mathbf{b_a}$ and $\mathbf{b_g}$, the IMU data are corrected and the navigation solution subsequently improved.

This was a brief summary for a first impression of the proposed algorithm. A detailed description follows next.

4.2.1 QINS Navigation Framework

The QINS filter framework is now described. For the IMU, a classical 6DOF assembly with orthogonal triads of accelerometers and gyroscopes is implemented. The CAI is realized by a quite general assembly with three sensitive axes according to the three principal axes of the s-frame. It is assumed that all three CAI sensors use a single atomic source as displayed in Fig. 4.2, see also Gersemann et al. (2020). Thus, a single sensor frame $\mathbf{s}$ is sufficient. For the remainder of this section, the effective wave vector will simply be denoted by $\mathbf{k}_e$, as it is always associated with the s-frame. This multi-axis CAI model has three sensitive axes, which are considered in the model by their respective $\mathbf{k}_e$-vector. For example, for the interferometer sequence in x-direction the vector reads $\mathbf{k}_e = [k_x, 0, 0]^{\mathrm{T}}$ with k_x as respective effective wave number. The coordinate center and the starting position of the atoms in each direction are identical. Note that in this multi-axis CAI, an initial splitter pulse is applied right before the Mach-Zehnder sequence, which divides the initial wave packet into two counter-propagating ensembles with opposed initial velocity $\pm\mathbf{v}_{sa}^{s}(0)$. This is applied in order to differentiate between phase shifts based on linear acceleration and those based on rotations. This also means that there are always two measurements per axis at the same time.

A detailed description of the hybrid navigation algorithm is now provided. The processing steps are explained in the order of their occurrence in the simulation framework.

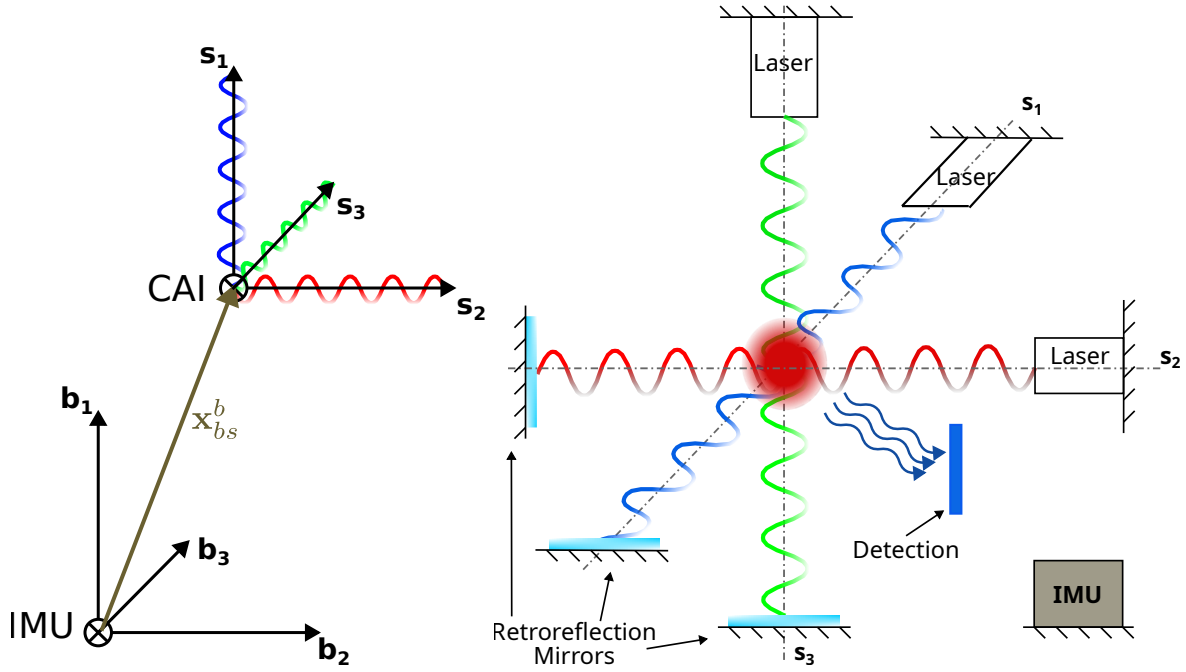

Figure 4.2: Sensor frames as defined in the QINS. Left: the b-frame embodies the platform and corresponds to the system in which the IMU is measuring. The sensitive axes of the CAI sensor frame are expressed as colored wavy lines corresponding to the respective spatial direction. Right: multi-axis scheme for the QINS. The six degrees of freedom (6DOF) CAI scheme was proposed by Gersemann et al. (2020). By using a single atom source and three orthogonal interrogation lasers, accelerations on all three spatial dimensions are covered by a single device. In the QINS scheme the retroreflection mirrors are assumed to be rigidly connected to a common platform with the IMU.

IMU Signal Generator (Simulation only)

In the frame of the simulation, the data of the IMU are generated based on a given simulated **reference** time-series of $\check{\mathbf{f}}_{ib}^{b}$ and $\check{\boldsymbol{\omega}}_{ib}^{b}$ in the b-frame. Errors are added according to Sec. 2.5. The output is $\tilde{\mathbf{f}}_{ib}^{b}$ and $\tilde{\boldsymbol{\omega}}_{ib}^{b}$.

IMU Error Correction

The data of the IMU, $\tilde{\mathbf{f}}_{ib}^{b}$ and $\tilde{\boldsymbol{\omega}}_{ib}^{b}$, are affected by errors. These data are corrected based on the biases $\mathbf{b_a}$ and $\mathbf{b_g}$, which are estimated by the EKF,

$$\mathbf{f}_{ib}^{b} = \tilde{\mathbf{f}}_{ib}^{b} - \mathbf{b_a}, \tag{4.3}$$

$$\boldsymbol{\omega}_{ib}^{b} = \tilde{\boldsymbol{\omega}}_{ib}^{b} - \mathbf{b_g}. \tag{4.4}$$

Kinematic State Computation

The corrected IMU data $\mathbf{f}_{ib}^{b}$ and $\boldsymbol{\omega}_{ib}^{b}$ are used in the strapdown navigation solution of the ODE system Eqs. (2.28) - (2.30) which is explained in Sec. 2.3. The quantities $\mathbf{x}_{eb}^{n}$, $\mathbf{v}_{eb}^{n}$ and $\mathbf{C}_{b}^{n}$ are computed.

Atom Strapdown with Spatial Distance between IMU and CAI

Recall the differential equations Eq. (3.51) and Eq. (3.52) describing the velocity and position of the wave packet in the s-frame,

$$\begin{aligned}\dot{\mathbf{x}}^s_{sa} &= \mathbf{v}^s_{sa},\\ \dot{\mathbf{v}}^s_{sa} &= -\left(\mathbf{f}^s_{is} - 2\boldsymbol{\Omega}^s_{is}\mathbf{v}^s_{sa} - \boldsymbol{\Omega}^s_{is}\boldsymbol{\Omega}^s_{is}\mathbf{x}^s_{sa} - \dot{\boldsymbol{\Omega}}^s_{is}\mathbf{x}^s_{sa} + \left(\int_{t_1}^{t}\boldsymbol{\Omega}^s_{is}\,d\tau\right)\mathbf{f}^s_{is}\right).\end{aligned} \tag{4.5}$$

All quantities are time dependent, unless stated otherwise. The inertial quantities are measured with an IMU in the b-frame, cf. Sec. 2.2.1. The b-frame's origin in this section is defined in a way that its coordinate center is assigned to the intersection point of the sensitive axes of the IMU. The b- and s-frame are separated in space by a distance $\mathbf{x}^b_{bs}$, subsequently labeled **lever arm**. The specific forces $\mathbf{f}^b_{ib}$ measured by the IMU are transformed according to

$$\mathbf{f}^s_{is} = \mathbf{f}^s_{ib} + \mathbf{f}^s_{bs} = \mathbf{C}^s_b\mathbf{f}^b_{ib} - \mathbf{C}^s_b\boldsymbol{\Omega}^b_{ib}(\boldsymbol{\Omega}^b_{ib}\mathbf{x}^b_{bs}) - \mathbf{C}^s_b\dot{\boldsymbol{\Omega}}^b_{ib}\mathbf{x}^b_{bs} - 2\mathbf{C}^s_b\boldsymbol{\Omega}^b_{ib}\dot{\mathbf{x}}^b_{bs}. \tag{4.6}$$

The transformation introduces an additional centrifugal term $\boldsymbol{\Omega}^b_{ib}(\boldsymbol{\Omega}^b_{ib}\mathbf{x}^b_{bs})$ and Euler term $\dot{\boldsymbol{\Omega}}^b_{ib}\mathbf{x}^b_{bs}$, depending on the lever arm $\mathbf{x}^b_{bs}$. The Coriolis term $2\boldsymbol{\Omega}^b_{ib}\dot{\mathbf{x}}^b_{bs}$ can have an impact in the case that the distance $\mathbf{x}^b_{bs}$ is varying. Often, one can assume a rigid connection between the systems and thus $\dot{\mathbf{x}}^b_{bs} = \mathbf{0}$. This then further leads to $\mathbf{f}^b_{bs} = \mathbf{0}$, as no accelerations between the systems occur.

The transformation of the angular rates $\boldsymbol{\Omega}^b_{ib}$ is straight forward,

$$\boldsymbol{\Omega}^s_{is} = \boldsymbol{\Omega}^s_{ib} + \boldsymbol{\Omega}^s_{bs} = \mathbf{C}^s_b\boldsymbol{\Omega}^b_{ib}. \tag{4.7}$$

The direction cosine matrix $\mathbf{C}^s_b$ resembles the relative orientation between the systems. However, no change of this orientation in time is expected, hence $\boldsymbol{\Omega}^s_{bs} = \mathbf{0}$. The position of the wave packet can be predicted by solving $\ddot{\mathbf{x}}^s_{sa}(t) = \dot{\mathbf{v}}^s_{sa}(t)$ from Eq. (4.5), hence

$$\mathbf{x}^s_{sa}(t) = \iint_0^t \left[-\mathbf{f}^s_{is} + 2\boldsymbol{\Omega}^s_{is}\mathbf{v}^s_{sa} + \boldsymbol{\Omega}^s_{is}\boldsymbol{\Omega}^s_{is}\mathbf{x}^s_{sa} + \dot{\boldsymbol{\Omega}}^s_{is}\mathbf{x}^s_{sa} - \left(\int_{t_1}^{t}\boldsymbol{\Omega}^s_{is}\,d\tau\right)\mathbf{f}^s_{is}\right] dt^2 \tag{4.8}$$

with Eq. (4.6) for $\mathbf{f}^s_{is}$ and (4.7) for $\boldsymbol{\Omega}^s_{is}$ applied, respectively. The predicted phase shift is then given by

$$\phi^- = \mathbf{k}_\mathrm{e}\cdot\mathbf{x}^s_{sa}(0) - 2\mathbf{k}_\mathrm{e}\cdot\mathbf{x}^s_{sa}(T) + \mathbf{k}_\mathrm{e}\cdot\mathbf{x}^s_{sa}(2T). \tag{4.9}$$

A closed solution can be stated under the assumption that $\mathbf{f}^b_{ib}$ and $\boldsymbol{\omega}^b_{ib}$ are constant during the interrogation time. As the equation will be needed for the derivation of the measurement sensitivity matrix, the solution is stated here in full,

$$\begin{aligned}\phi^- = {}& 2\mathbf{k}_e\cdot\mathbf{C}^s_b\boldsymbol{\Omega}^b_{ib}\mathbf{v}^s_{sa}T^2 - \mathbf{k}_e\cdot\left(\mathbf{C}^s_b\mathbf{f}^b_{ib} - \mathbf{C}^s_b\boldsymbol{\Omega}^b_{ib}(\boldsymbol{\Omega}^b_{ib}\mathbf{x}^b_{bs}) - \mathbf{C}^s_b\dot{\boldsymbol{\Omega}}^b_{ib}\mathbf{x}^b_{bs}\right)T^2 + \mathbf{k}_e\cdot\mathbf{C}^s_b\boldsymbol{\Omega}^b_{ib}(\boldsymbol{\Omega}^b_{ib}\mathbf{x}^s_{sa})T^2\\ &+ \mathbf{k}_e\cdot(\mathbf{C}^s_b\dot{\boldsymbol{\Omega}}^b_{ib})\mathbf{x}^s_{sa}T^2 - \mathbf{k}_e\cdot\mathbf{C}^s_b\boldsymbol{\Omega}^b_{ib}\left(\mathbf{f}^b_{ib} - \boldsymbol{\Omega}^b_{ib}(\boldsymbol{\Omega}^b_{ib}\mathbf{x}^b_{bs}) - \dot{\boldsymbol{\Omega}}^b_{ib}\mathbf{x}^b_{bs}\right)T^3.\end{aligned} \tag{4.10}$$

Laser Phase Controller

The main task of the laser controller is to steer the laser phase ϕ_L at the time of the recombination pulse in order to operate the CAI at mid fringe, i.e. reference the observation to a value of $\phi_0 = \frac{\pi}{2}$. In turn this means that, after wrapping up ϕ^-,

$$\phi_\mathrm{L} = \frac{\pi}{2} - \mathrm{mod}(\phi^-, 2\pi). \tag{4.11}$$

This mid fringe operation enables the CAI to achieve the highest sensitivity to changes of the inertial phase shift. The controlled laser phase affects the measurement of the CAI. While laser phase noise is added to the CAI observation, the uncertainty of the predicted phase shift is not propagated to the laser phase. That is because the predicted ϕ^- acts as a reference for the setting of the laser phase, including all potential deviations due to IMU errors, and only the additional uncertainty of the laser phase is added in the process.

A special case of the filter operation occurs if the laser phase is not controlled. In this case, the operating point for the EKF update is arbitrary and unfavorable sensitivities as low as zero might result. As the phases are randomly scattered in this mode of operation as a result of ambient vibrations, the analytical studies and performance assessment are more complicated. For those reasons this case is not considered in frame of this chapter.

CAI Signal Generator (Simulation only)

The CAI measurement is generated based on a given time-series of $\check{\mathbf{f}}_{ib}^{b}$ and $\check{\boldsymbol{\omega}}_{ib}^{b}$ (true values) which are acting as input to the AtoS according to Sec. 3.4. The phase shift $\check{\phi}$ is produced. The generated CAI observation p is then related to the phase shift via

$$p = A\cos(\phi_{\mathrm{L}} + \check{\phi}) + (p_0 + \delta p). \tag{4.12}$$

The laser phase ϕ_{L} is given by Eq. (4.11). Additional parameters are the amplitude A of the fringe signal and the offset p_0. In the frame of this thesis, additive observation noise is applied via the parameter δp. A theoretical treatment about the sources of impact on the observation uncertainty was given in Sec. 3.2.2. The practical assessment of the noise is covered in Chap. 5.

4.2.2 Extended Kalman Filter

The extended Kalman filter implemented here follows the **feedback form** definition as explained and discussed in Farrell (2008, p. 209). The general signal flow from a high level perspective is visualized in Fig. 4.3. The prediction of the nominal state $\tilde{\mathbf{x}}^-$ and the nominal output $\tilde{\mathbf{y}}^-$ is computed by a classical IMU. The error $\mathbf{z}$ between $\tilde{\mathbf{y}}^-$ and the observation $\mathbf{y}$ is weighted by a so-called Kalman gain $\mathbf{K}$ and used to compute an estimate of the error state $\delta\mathbf{x}$. The estimate of the total state is then computed by

$$\tilde{\mathbf{x}}^+ = \tilde{\mathbf{x}}^- + \mathbf{K}\mathbf{z}. \tag{4.13}$$

It is beneficial that both, the IMU and the CAI, are inertial sensors that measure in a body-mounted system. As such, no complicated transformations besides the one from the b- to the s-frame are needed. The minimum configuration of the state vector $\mathbf{x}$ consists of the 3-dimensional vectors of acceleration and angular rate biases $\mathbf{b_a}$ and $\mathbf{b_g}$,

$$\mathbf{x} = \begin{bmatrix} \mathbf{b_a} & \mathbf{b_g} \end{bmatrix}^{\mathrm{T}}. \tag{4.14}$$

Some augmentation options will be discussed later. Let the biases be exited by the noise processes $\mathbf{w_a}$ and $\mathbf{w_g}$. The differential equation system in this basic configuration is quite simple,

$$\begin{aligned} \dot{\mathbf{b}}_{\mathbf{a}} &= \mathbf{w_a} \\ \dot{\mathbf{b}}_{\mathbf{g}} &= \mathbf{w_g}. \end{aligned} \tag{4.15}$$

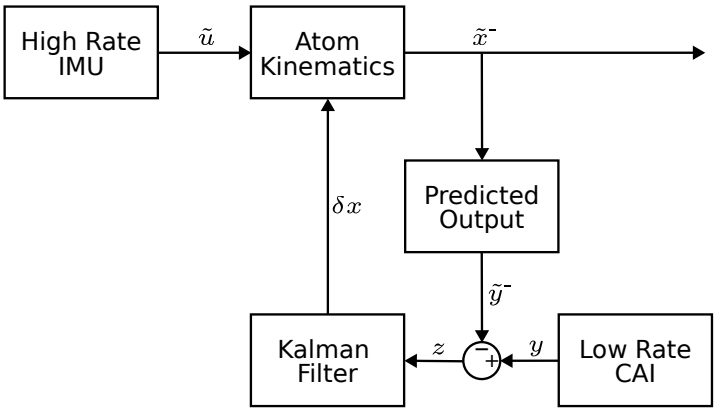

Figure 4.3: Schematic of an extended Kalman filter. Based on the high rate IMU data, the atom wave packet velocity and position is estimated. Subsequently, the phase shift and the CAI observation are predicted based on the position estimate. The predicted and actual observation are then fused in the EKF, and an update of the state vector is produced.

They are additionally expressed in the system perturbation vector

$$\mathbf{u} = \begin{bmatrix} \mathbf{w_a} & \mathbf{w_g} \end{bmatrix}^{\mathrm{T}}. \tag{4.16}$$

The system dynamic matrix $\mathbf{A}$ is

$$\mathbf{A} = \mathbf{0}_6. \tag{4.17}$$

The corresponding transition matrix $\mathbf{F}$ can be accurately represented by

$$\mathbf{F} = \begin{bmatrix} \mathbf{I}_3 & \mathbf{0}_3 \\ \mathbf{0}_3 & \mathbf{I}_3 \end{bmatrix}. \tag{4.18}$$

The perturbation input matrix $\mathbf{B}$ is similar,

$$\mathbf{B} = \begin{bmatrix} \mathbf{I}_3 & \mathbf{0}_3 \\ \mathbf{0}_3 & \mathbf{I}_3 \end{bmatrix}. \tag{4.19}$$

The EKF is a recursive algorithm. A subscript k is now introduced which corresponds to the discrete filter time step $t \to t + T_\mathrm{f}$, where T_f is the time of the active CAI measurement cycle excluding dead times. The prediction of the error state follows formally

$$\delta\mathbf{x}_k^- = \mathbf{F}(\tilde{\mathbf{x}}_{k-1}^+)\delta\mathbf{x}_{k-1}^+ + \mathbf{u}_k. \tag{4.20}$$

The superscript $-$ denotes a predicted state, while $+$ denotes a filtered state. The error state $\delta\mathbf{x}_{k-1}^+$ is typically not carried over from one filter step to the next. The prediction expressed as total state $\tilde{\mathbf{x}}_k^-$ reads

$$\tilde{\mathbf{x}}_k^- = \tilde{\mathbf{x}}_{k-1}^+ + \mathbf{u}_k. \tag{4.21}$$

The covariances are propagated according to

$$\mathbf{P}_k^- = \mathbf{F}\mathbf{P}_{k-1}^+\mathbf{F}^{\mathrm{T}} + \mathbf{Q}_k. \tag{4.22}$$

The discrete time process noise matrix $\mathbf{Q}_k$, cf. Appendix A.4.3, can be assembled as following:

$$\mathbf{Q}_k = \begin{bmatrix} \boldsymbol{\sigma}_a^2\mathbf{I}_3 & \mathbf{0}_3 \\ \mathbf{0}_3 & \boldsymbol{\sigma}_g^2\mathbf{I}_3 \end{bmatrix} = \begin{bmatrix} (\frac{N_a^2}{T_\mathrm{f}} + K_a^2 T_\mathrm{f})\mathbf{I}_3 & \mathbf{0}_3 \\ \mathbf{0}_3 & (\frac{N_g^2}{T_\mathrm{f}} + K_g^2 T_\mathrm{f})\mathbf{I}_3 \end{bmatrix}, \tag{4.23}$$

with the noise densities N_a^2 and N_g^2 associated with a white noise process, as well as the noise densities K_a^2 and K_g^2 characterizing a random walk according to Sec. 2.5. The adaption of the

model including dead times of the CAI is discussed in Sec. 4.4.2. The remaining equations follow that of a regular extended Kalman Filter with error states. This means that at the filter step at time step k, the total state $\tilde{\mathbf{x}}_k$ is updated with the estimated error state $\delta\mathbf{x}_k$,

$$\tilde{\mathbf{x}}_k^+ = \tilde{\mathbf{x}}_k^- + \delta\mathbf{x}_k^+. \tag{4.24}$$

At each filter update, the error state is always initialized as zero, hence the filtered error state is essentially the difference between the observation $\mathbf{y}_k$ and the predicted observation $\tilde{\mathbf{y}}^- = \mathbf{h}(\tilde{\mathbf{x}}_k^-)$, weighted by the Kalman gain $\mathbf{K}_k$,

$$\delta\mathbf{x}_k^+ = \mathbf{K}_k \cdot (\mathbf{y}_k - \mathbf{h}(\tilde{\mathbf{x}}_k^-)). \tag{4.25}$$

The Kalman gain $\mathbf{K}_k$ is representing a ratio of the noise covariances $\mathbf{P}_k^-\mathbf{H}_k^{\mathrm{T}}$, which express the uncertainty of the state estimate, and the sum of the observation uncertainty $\mathbf{R}_k$ and the uncertainty of the predicted observation $\mathbf{H}_k\mathbf{P}_k^-\mathbf{H}_k^{\mathrm{T}}$,

$$\mathbf{K}_k = \mathbf{P}_k^-\mathbf{H}_k^{\mathrm{T}} \left(\mathbf{R}_k + \mathbf{H}_k\mathbf{P}_k^-\mathbf{H}_k^{\mathrm{T}}\right)^{-1}. \tag{4.26}$$

The observation covariance matrix $\mathbf{R}_k$ is filled with the variances σ_p^2 of the CAI observations on the main diagonal. The filtered covariances $\mathbf{P}_k^+$ can be formulated in the so-called Joseph-Form assuring symmetry (Farrell, 2008, p. 196) as follows,

$$\mathbf{P}_k^+ = (\mathbf{I} - \mathbf{K}_k\mathbf{H}_k)\mathbf{P}_k^-(\mathbf{I} - \mathbf{K}_k\mathbf{H}_k)^{\mathrm{T}} + \mathbf{K}_k\mathbf{R}_k\mathbf{K}^{\mathrm{T}}. \tag{4.27}$$

The prediction of the state and its covariances is rather a formality. The true complexity of the system, which has been avoided so far, is introduced with the predicted observations. A single CAI observation $h(\tilde{\mathbf{x}}_k^-)$ is a scalar which depends on the phase shift predicted with the nominal IMU data from Eq. (4.10),

$$h(\tilde{\mathbf{x}}_k^-) = A\cos(\phi^- + \phi_{\mathrm{L}}) + p_0. \tag{4.28}$$

The observation matrix $\mathbf{H}$ per single predicted observation h is computed based on the following chain of derivatives:

$$\mathbf{H} = \frac{\partial h}{\partial \tilde{\mathbf{x}}_k^-} = \frac{\partial h}{\partial \phi^-}\frac{\partial \phi^-}{\partial \tilde{\mathbf{x}}_k^-}\frac{\partial \tilde{\mathbf{x}}_k^-}{\partial \delta\mathbf{x}_k^-} \tag{4.29}$$

The **outer derivative** with respect to the predicted phase shift yields

$$\frac{\partial h}{\partial \phi^-}\Big|_{\phi^-+\phi_{\mathrm{L}}=\frac{\pi}{2}} = -A\sin(\frac{\pi}{2}) = -A. \tag{4.30}$$

In order to approach the remaining **inner derivatives** of the predicted phase shift ϕ^- to the state vector and to the error states, the connection between the true values, the nominal variables and the error states has to be clarified. The inertial quantities are given by

$$\tilde{\mathbf{f}}_{ib}^b = \mathbf{f}_{ib}^b + \tilde{\mathbf{b}_{\mathbf{a}}}, \qquad \tilde{\mathbf{\Omega}}^b = \mathbf{\Omega}^b + [\tilde{\mathbf{b}_{\mathbf{g}}}\times], \tag{4.31}$$

where

$$\tilde{\mathbf{b}_{\mathbf{a}}} = \mathbf{b}_{\mathbf{a}} - \delta\mathbf{b}_{\mathbf{a}}, \qquad [\tilde{\mathbf{b}_{\mathbf{g}}}\times] = [\mathbf{b}_{\mathbf{g}}\times] - [\delta\mathbf{b}_{\mathbf{g}}\times]. \tag{4.32}$$

For simplicity reasons, aligned systems are assumed such that $\mathbf{C}_b^s = \mathbf{I}$. The impact of a misalignment is discussed later in Sec. 4.3. The derivation of Eq. (4.10) w.r.t. the accelerometer bias reads

$$\frac{\partial \phi^-}{\partial \tilde{\mathbf{b}_{\mathbf{a}}}} = -(\mathbf{k}_{\mathbf{e}})^{\mathrm{T}}T^2 - (\mathbf{k}_{\mathbf{e}})^{\mathrm{T}}\mathbf{\Omega}_{ib}^b T^3. \tag{4.33}$$

The derivation of the accelerometer bias w.r.t. the bias error reads

$$\frac{\partial \tilde{\mathbf{b}_\mathbf{a}}}{\partial \delta \mathbf{b}_\mathbf{a}} = -\mathbf{I}. \tag{4.34}$$

The observation matrix $\mathbf{H_a}$ for the acceleration bias error is therefore

$$\mathbf{H_a} = \frac{\partial h}{\partial \delta \mathbf{b_a}} = -A(\mathbf{k_e})^{\mathrm{T}} T^2 - A(\mathbf{k_e})^{\mathrm{T}} \mathbf{\Omega}_{ib}^b T^3. \tag{4.35}$$

The acceleration and the mixed term yield a sensitivity to the acceleration bias. The skew-symmetric matrix $\mathbf{\Omega}_{ib}^b$ leads to the second term being only non-zero if a rate of change of the orientation in direction of the respective perpendicular axes is present.

The derivation of the observation matrix $\mathbf{H_g}$ for the gyroscope bias error follows a similar pattern. A mathematical treatment of the derivatives of the involved cross products is provided in Appendix A.3. The observation matrix $\mathbf{H_g}$ results in the rather extensive expression

$$\begin{aligned}\mathbf{H_g} = \frac{\partial h}{\partial \delta \mathbf{b_g}} = {} & A(\mathbf{k_e})^{\mathrm{T}}[(\mathbf{\Omega}_{ib}^b \mathbf{x}_{bs}^b)\times] T^2 + A(\mathbf{k_e})^{\mathrm{T}} \mathbf{\Omega}_{ib}^b [\mathbf{x}_{bs}^b \times] T^2 \\ & + 2A(\mathbf{k_e})^{\mathrm{T}}[\mathbf{v}_{sa}^s \times] T^2 + A(\mathbf{k_e})^{\mathrm{T}}[\mathbf{f}_{ib}^b \times] T^3 \\ & + A(\mathbf{k_e})^{\mathrm{T}}[\mathbf{\Omega}_{ib}^b (\mathbf{\Omega}_{ib}^b \mathbf{x}_{bs}^b)\times] T^3 + A(\mathbf{k_e})^{\mathrm{T}} \mathbf{\Omega}_{ib}^b [(\mathbf{\Omega}_{ib}^b \mathbf{x}_{bs}^b)\times] T^3 + A(\mathbf{k_e})^{\mathrm{T}} \mathbf{\Omega}_{ib}^b (\mathbf{\Omega}_{ib}^b [\mathbf{x}_{bs}^b \times]) T^3 \\ & + A(\mathbf{k_e})^{\mathrm{T}}[(\dot{\mathbf{\Omega}}_{ib}^b \mathbf{x}_{bs}^b)\times] T^3 + A(\mathbf{k_e})^{\mathrm{T}}[(\mathbf{\Omega}_{ib}^b \mathbf{x}_{sa}^s)\times] T^2 + A(\mathbf{k_e})^{\mathrm{T}} \mathbf{\Omega}_{ib}^b [\mathbf{x}_{sa}^s \times] T^2.\end{aligned} \tag{4.36}$$

The first two terms come from the derivation of the centrifugal term w.r.t. the gyroscope bias. The term $2A(\mathbf{k_e})^{\mathrm{T}}[\mathbf{v}_{sa}^s \times] T^2$ resembles the Coriolis term seen by the atoms in a rotating s-frame. This term scales with the atom velocity. The fourth term $A(\mathbf{k_e})^{\mathrm{T}}[\mathbf{f}_{ib}^b \times] T^3$ results from the partial derivative of the mix term, which scales with the linear accelerations. The terms five to seven arise from differentiating the centrifugal term between the b- and s-frame according to the product rule. The final line consists of the Euler term including the angular acceleration $\dot{\mathbf{\Omega}}_{ib}^b$ and the two terms resulting from the differentiation of the centrifugal term w.r.t. the atom wave packet position $\mathbf{x}_{sa}^s$.

Formal Expression for a 6DOF CAI Model

The observation equation and matrices in the s-frame are stated so far for an arbitrary CAI observation on a single sensitive axis as defined by the wave vector $\mathbf{k_e}$. In the six degree of freedom case, there are now two measurements per spatial axis at a time in order to differentiate between angular rates and linear accelerations. This differential measurement is available for the three axes that span the sensor frame. For the complete description, the index j is introduced with $j \in \{x\uparrow, y\uparrow, z\uparrow, x\downarrow, y\downarrow, z\downarrow\}$, whereas CAI can produce one of the six observations in p_j. The indices $\uparrow$ and $\downarrow$ represent the two observations that are covered by the initially split propagating wave packets due to different sign of the initial velocity. This also means that there is a total of six predicted observations that need to be evaluated with the AtoS. The general observation equations are

$$h_j = A\cos(\phi_{\mathrm{L}j} + \phi_j^-) + p_{0j}. \tag{4.37}$$

The wave vector $\mathbf{k_e}_j$ is only dependent on the axis of the s-frame, but not on the direction of the initial split velocity, e.g.

$$\mathbf{k_e}_{x\uparrow} = \mathbf{k_e}_{x\downarrow} = \begin{bmatrix} k_x & 0 & 0 \end{bmatrix}^{\mathrm{T}}.$$

The complete observation matrix $\mathbf{H}$ reads

$$\mathbf{H} = \begin{bmatrix} \sum_j \mathbf{H_a}_j & \sum_j \mathbf{H_g}_j \end{bmatrix}. \tag{4.38}$$

4.3 QINS System Analysis

In this section, some specific aspects of the system are discussed. This includes the *stability* of the system for different state vector augmentations. Stability is concerning the question about how a system behaves in the face of different dynamics. One can define stability based on the Eigenvalues of the dynamic matrix $\mathbf{A}$, or transition matrix $\mathbf{F}$, respectively (Lunze, 2008, p. 476). This kind of stability analysis can only give information about the stability of the homogeneous part of the system.

In a feedback system the stability analysis needs to be enhanced, since the control input affects the system dynamics. This leads to the question of *controllability*. Furthermore, feeding information back to the system also means that the corresponding state has to be measured in the first place. Hence, the *observability* needs to be granted.

In a Kalman filter, a system that is both, observable and controllable, eventually converges to a *steady state*, in a sense that the state covariance $\mathbf{P}$ converges to a certain value, and thus a stationary condition is reached (Schweppe, 1973, p. 142). In the context of the QINS, this steady state enables several options for an in-depth analysis. Namely, the accuracy of the hybrid navigation solution for different settings and the sensitivity of the EKF for different states can be assessed, while additional topics like the choice of classical sensors for the hybridization can be discussed analytically.

4.3.1 Error State Dynamic System and Stability

The system state vector as introduced before only inherited the biases of the classical accelerometers and gyroscopes. In the frame of this section, some further state vector augmentations are discussed. Namely, the misalignment $\boldsymbol{\gamma}_b^s$ and the lever arm $\mathbf{x}_{bs}^b$ between the b- and the s-frame. The CAI's sensitivity to those parameters will be examined in order to see how precise they need to be defined in the system integration.

Further augmented states are the error of the position and velocity of the atom wave packet center of mass in the s-frame, $\delta\mathbf{x}_{sa}^s$ and $\delta\mathbf{v}_{sa}^s$. The platform kinematic states $\mathbf{x}_{eb}^n$ and $\mathbf{v}_{eb}^n$, like included in Tennstedt et al. (2023), are not considered here in order to limit the discussion to the platform-bound coordinate frames used by the hybrid sensor system, i.e. the b- and s-frame. Beyond the scope of this *sensor unit*, the sensor behaves like an arbitrary inertial measurement unit and analysis as shown in Sec. 2.6 can be applied as demanded.

The error state vector is given by

$$\delta\mathbf{x} = \begin{bmatrix} \delta\mathbf{x}_{sa}^s & \delta\mathbf{v}_{sa}^s & \delta\mathbf{b}_\mathbf{a} & \delta\mathbf{b}_\mathbf{g} & \boldsymbol{\gamma}_b^s & \delta\mathbf{x}_{bs}^b \end{bmatrix}^\mathrm{T}. \tag{4.39}$$

As extension to Eqs. (4.31) and (4.32), the additional nominal states and error states stand in the following relation:

$$\tilde{\mathbf{v}}_{sa}^s = \mathbf{v}_{sa}^s - \delta\mathbf{v}_{sa}^s, \qquad \tilde{\mathbf{b}_\mathbf{a}} = \mathbf{b}_\mathbf{a} - \delta\mathbf{b}_\mathbf{a}, \qquad \tilde{\mathbf{b}_\mathbf{g}} = \mathbf{b}_\mathbf{g} - \delta\mathbf{b}_\mathbf{g}.$$

$$\tilde{\mathbf{x}}_{sa}^s = \mathbf{x}_{sa}^s - \delta\mathbf{x}_{sa}^s, \qquad \tilde{\mathbf{x}}_{bs}^b = \mathbf{x}_{bs}^b - \delta\mathbf{x}_{bs}^b, \qquad \tilde{\mathbf{C}}_b^s = (\mathbf{I} - [\boldsymbol{\gamma}_b^s\times])\mathbf{C}_b^s.$$

The alignment is defined as $\mathbf{C}_b^s = \mathbf{I}$. Furthermore, the misalignment $\boldsymbol{\gamma}_b^s$ is assumed to be small in order to avoid complicated description of the orientation, so that the nominal alignment is given by $\tilde{\mathbf{C}}_b^s = \mathbf{I} - [\boldsymbol{\gamma}_b^s\times]$. The specific forces and angular rates are represented by $\mathbf{f}^b$ and $\boldsymbol{\omega}^b$ in the scope of this section in order to improve the readability. The adaptions and the derivation of the error state kinematic equations are further explained in Appendix A.5.

The differential equations for the velocities in nominal $\tilde{\mathbf{v}}^s_{sa}$ and true state $\mathbf{v}^s_{sa}$ read

$$\dot{\mathbf{v}}^s_{sa} = -\left((\mathbf{f}^b + \mathbf{b_a}) - 2(\boldsymbol{\omega}^b + \mathbf{b_g}) \times \mathbf{v}^s_{sa} - (\boldsymbol{\omega}^b + \mathbf{b_g}) \times [(\boldsymbol{\omega}^b + \mathbf{b_g}) \times \mathbf{x}^b_{bs}]\right), \tag{4.40}$$

$$\begin{aligned}\dot{\tilde{\mathbf{v}}}^s_{sa} = &-\Big((\mathbf{I} - [\boldsymbol{\gamma}^s_b\times])(\mathbf{f}^b + \tilde{\mathbf{b}_\mathbf{a}}) - 2((\mathbf{I} - [\boldsymbol{\gamma}^s_b\times])(\boldsymbol{\omega}^b + \tilde{\mathbf{b}_\mathbf{g}})) \times \tilde{\mathbf{v}}^s_{sa} \\ &-(\mathbf{I} - [\boldsymbol{\gamma}^s_b\times])(\boldsymbol{\omega}^b + \tilde{\mathbf{b}_\mathbf{g}}) \times [(\boldsymbol{\omega}^b + \tilde{\mathbf{b}_\mathbf{g}}) \times \tilde{\mathbf{x}}^b_{bs}]\Big).\end{aligned} \tag{4.41}$$

The error state differential equation system including the additional states is:

$$\dot{\delta\mathbf{x}}^s_{sa} = \delta\mathbf{v}^s_{sa}, \tag{4.42}$$

$$\begin{aligned}\dot{\delta\mathbf{v}}^s_{sa} = &-\delta\mathbf{b_a} - \boldsymbol{\gamma}^s_b \times (\mathbf{f}^b + \mathbf{b_a}) \\ &+ 2(\boldsymbol{\omega}^b + \mathbf{b_g}) \times \delta\mathbf{v}^s_{sa} + 2\delta\mathbf{b_g} \times \mathbf{v}^s_{sa} \\ &+ 2\mathbf{v}^s_{sa} \times (\boldsymbol{\omega}^b + \mathbf{b_g}) \times \boldsymbol{\gamma}^s_b \\ &+ \boldsymbol{\omega}^b \times \delta\mathbf{b_g} \times \mathbf{x}^b_{bs} + \delta\mathbf{b_g} \times \boldsymbol{\omega}^b \times \mathbf{x}^b_{bs} \\ &+ \mathbf{b_g} \times \delta\mathbf{b_g} \times \mathbf{x}^b_{bs} + \delta\mathbf{b_g} \times \mathbf{b_g} \times \mathbf{x}^b_{bs} \\ &+ \boldsymbol{\gamma}^s_b \times \boldsymbol{\omega}^b \times \boldsymbol{\omega}^b \times \mathbf{x}^b_{bs} + \boldsymbol{\gamma}^s_b \times \boldsymbol{\omega}^b \times \mathbf{b_g} \times \mathbf{x}^b_{bs} \\ &+ \boldsymbol{\gamma}^s_b \times \mathbf{b_g} \times \boldsymbol{\omega}^b \times \mathbf{x}^b_{bs} + \boldsymbol{\gamma}^s_b \times \mathbf{b_g} \times \mathbf{b_g} \times \mathbf{x}^b_{bs} \\ &+ \boldsymbol{\omega}^b \times \boldsymbol{\omega}^b \times \delta\mathbf{x}^b_{bs} + \boldsymbol{\omega}^b \times \mathbf{b_g} \times \delta\mathbf{x}^b_{bs} \\ &+ \mathbf{b_g} \times \boldsymbol{\omega}^b \times \delta\mathbf{x}^b_{bs} + \mathbf{b_g} \times \mathbf{b_g} \times \delta\mathbf{x}^b_{bs},\end{aligned} \tag{4.43}$$

$$\dot{\delta\mathbf{x}}^b_{bs} = \mathbf{0}, \tag{4.44}$$

$$\dot{\boldsymbol{\gamma}}^s_b = \mathbf{0}, \tag{4.45}$$

$$\dot{\delta\mathbf{b_a}} = \mathbf{w_a}, \tag{4.46}$$

$$\dot{\delta\mathbf{b_g}} = \mathbf{w_g}. \tag{4.47}$$

Any products of error terms are neglected in the analysis because of their low impact and in order to reduce the complexity of the already rather inflated system. An input to the system exists in shape of the yet to be defined processes $\mathbf{w_a}$ and $\mathbf{w_g}$ affecting the bias states. The input matrix reads

$$\mathbf{B} = \begin{bmatrix}\mathbf{0} & \mathbf{0} \\ \mathbf{0} & \mathbf{0} \\ \mathbf{I} & \mathbf{0} \\ \mathbf{0} & \mathbf{I} \\ \mathbf{0} & \mathbf{0} \\ \mathbf{0} & \mathbf{0}\end{bmatrix}. \tag{4.48}$$

The system dynamic matrix reads

$$\mathbf{A} = \begin{bmatrix}\mathbf{0} & \mathbf{I} & \mathbf{0} & \mathbf{0} & \mathbf{0} & \mathbf{0} \\ \frac{\partial\dot{\delta\mathbf{v}}^s_{sa}}{\partial\delta\mathbf{x}^s_{sa}} & \frac{\partial\dot{\delta\mathbf{v}}^s_{sa}}{\partial\delta\mathbf{v}^s_{sa}} & -\mathbf{I} & \frac{\partial\dot{\delta\mathbf{v}}^s_{sa}}{\partial\delta\mathbf{b_g}} & \frac{\partial\dot{\delta\mathbf{v}}^s_{sa}}{\partial\boldsymbol{\gamma}^s_b} & \frac{\partial\dot{\delta\mathbf{v}}^s_{sa}}{\partial\delta\mathbf{x}^b_{bs}} \\ \mathbf{0} & \mathbf{0} & \mathbf{0} & \mathbf{0} & \mathbf{0} & \mathbf{0} \\ \mathbf{0} & \mathbf{0} & \mathbf{0} & \mathbf{0} & \mathbf{0} & \mathbf{0} \\ \mathbf{0} & \mathbf{0} & \mathbf{0} & \mathbf{0} & \mathbf{0} & \mathbf{0} \\ \mathbf{0} & \mathbf{0} & \mathbf{0} & \mathbf{0} & \mathbf{0} & \mathbf{0}\end{bmatrix}, \tag{4.49}$$

where

$$\frac{\partial\dot{\delta\mathbf{v}}^s_{sa}}{\partial\delta\mathbf{v}^s_{sa}} = 2[(\boldsymbol{\omega}^b + \mathbf{b_g})\times], \tag{4.50}$$

$$\frac{\partial\dot{\delta\mathbf{v}}^s_{sa}}{\partial\delta\mathbf{b_a}} = -\mathbf{I}, \tag{4.51}$$

$$\frac{\partial \dot{\delta \mathbf{v}}^s_{sa}}{\partial \delta \mathbf{b_g}} = -2[\mathbf{v}^s_{sa}\times] - [\boldsymbol{\omega}^b\times][\mathbf{x}^b_{bs}\times] - [(\mathbf{b_g}\times\mathbf{x}^b_{bs})\times], \tag{4.52}$$

$$\begin{aligned}\frac{\partial \dot{\delta \mathbf{v}}^s_{sa}}{\partial \boldsymbol{\gamma}^s_b} &= [(\mathbf{f}^b + \mathbf{b_a})\times] - 2[\mathbf{v}^s_{sa}\times][(\boldsymbol{\omega}^b + \mathbf{b_g})\times] \\ &\quad - [(\boldsymbol{\omega}^b \times (\boldsymbol{\omega}^b \times \mathbf{x}^b_{bs}))\times] - [(\boldsymbol{\omega}^b \times (\mathbf{b_g}\times\mathbf{x}^b_{bs}))\times] \\ &\quad - [(\mathbf{b_g} \times (\boldsymbol{\omega}^b \times \mathbf{x}^b_{bs}))\times] - [(\mathbf{b_g} \times (\mathbf{b_g}\times\mathbf{x}^b_{bs}))\times],\end{aligned} \tag{4.53}$$

$$\frac{\partial \dot{\delta \mathbf{v}}^s_{sa}}{\partial \delta \mathbf{x}^b_{bs}} = [\boldsymbol{\omega}^b\times][\boldsymbol{\omega}^b\times] + [\boldsymbol{\omega}^b\times][\mathbf{b_g}\times] + [\mathbf{b_g}\times][\boldsymbol{\omega}^b\times] + [\mathbf{b_g}\times][\mathbf{b_g}\times]. \tag{4.54}$$

The terms that involve the lever arm $\mathbf{x}^b_{bs}$ and its error state can be stated for the initial atom position $\mathbf{x}^s_{sa}$ and error state $\delta\mathbf{x}^s_{sa}$ in an analogous fashion. The following properties are worth noting from the equations (4.50)-(4.54):

- The velocity error $\delta\mathbf{v}^s_{sa}$ is always affected by an acceleration bias error in the corresponding direction.
- It is affected by the angular rate bias error if the atoms move perpendicular to the sensitive axis, or if an rotation *and* a lever arm or atom displacement perpendicular to the axis is present.
- On a specific axis it is affected by an error in the calibrated lever arm on that axis, if a rotation or initial angular rate bias is present in any direction perpendicular to the sensitive axis.
- The misalignment on a specific axis will affect the phase shift in the same direction if it forms an orthogonal system with a rotation or initial angular rate bias and a lever arm or atom displacement.

A closed solution of the system is not possible since the velocity error state grows unbounded due to the dependency on its own state. However, in the light of small interrogation times the impact of this autoregression of $\delta\mathbf{v}^s_{sa}$ is rather small. As a simplification, the derivatives $\partial\dot{\delta\mathbf{v}}^s_{sa}/\partial\delta\mathbf{v}^s_{sa}$ and $\partial\dot{\delta\mathbf{v}}^s_{sa}/\partial\delta\mathbf{x}^s_{sa}$ are set to zero and the following closed solution of the system can be produced.

$$\mathbf{F}(t) = \begin{bmatrix} \mathbf{I} & \mathbf{I}t & -\frac{1}{2}\mathbf{I}t^2 & \frac{1}{2}\frac{\partial\dot{\delta\mathbf{v}}^s_{sa}}{\partial\delta\mathbf{b_g}}t^2 & \frac{1}{2}\frac{\partial\dot{\delta\mathbf{v}}^s_{sa}}{\partial\boldsymbol{\gamma}^s_b}t^2 & \frac{1}{2}\frac{\partial\dot{\delta\mathbf{v}}^s_{sa}}{\partial\delta\mathbf{x}^b_{bs}}t^2 \\ \mathbf{0} & \mathbf{I} & -\mathbf{I}t & \frac{\partial\dot{\delta\mathbf{v}}^s_{sa}}{\partial\delta\mathbf{b_g}}t & \frac{\partial\dot{\delta\mathbf{v}}^s_{sa}}{\partial\boldsymbol{\gamma}^s_b}t & \frac{\partial\dot{\delta\mathbf{v}}^s_{sa}}{\partial\delta\mathbf{x}^b_{bs}}t \\ \mathbf{0} & \mathbf{0} & \mathbf{I} & \mathbf{0} & \mathbf{0} & \mathbf{0} \\ \mathbf{0} & \mathbf{0} & \mathbf{0} & \mathbf{I} & \mathbf{0} & \mathbf{0} \\ \mathbf{0} & \mathbf{0} & \mathbf{0} & \mathbf{0} & \mathbf{I} & \mathbf{0} \\ \mathbf{0} & \mathbf{0} & \mathbf{0} & \mathbf{0} & \mathbf{0} & \mathbf{I} \end{bmatrix}. \tag{4.55}$$

Because of its triangular structure it is easy to see that the transition matrix $\mathbf{F}(t)$ in Eq. (4.55) is unipotent, and thus all Eigenvalues are equal to one. As such, the dynamic system itself, even with the simplifications, can never be stable regardless of the remaining entries in the upper triangle part. The observability and controllability thus need to be evaluated.

4.3.2 Impact of Error Sources on the Phase Shift

Before the observability and controllability are being discussed, the error state kinematics of the atom wave packet will be analyzed by means of Monte Carlo (MC) simulation. This will

help to gain some first impression of the interaction of the different parameters, and reveals how the phase shift error is affected. The terms which yield the largest impact on the phase shift error are then discussed in detail, and parameter assessment models for system design are derived. Using the simplified transition matrix in Eq. (4.55), the atom position error can be stated as closed solution,

$$\begin{aligned}\delta\mathbf{x}^s_{sa}(t_0+\Delta t) = \delta\mathbf{x}^s_{sa}(t_0) + \Delta t\delta\mathbf{v}^s_{sa}(t_0) \\ - \frac{1}{2}\Delta t^2\delta\mathbf{b}_\mathbf{a}(t_0) + \frac{1}{2}\Delta t^2\frac{\partial\delta\dot{\mathbf{v}}^s_{sa}}{\partial\delta\mathbf{b}_\mathbf{g}}\delta\mathbf{b}_\mathbf{g}(t_0) \\ + \frac{1}{2}\Delta t^2\frac{\partial\delta\dot{\mathbf{v}}^s_{sa}}{\partial\boldsymbol{\gamma}^s_b}\boldsymbol{\gamma}^s_b(t_0) + \frac{1}{2}\Delta t^2\frac{\partial\delta\dot{\mathbf{v}}^s_{sa}}{\partial\delta\mathbf{x}^b_{bs}}\delta\mathbf{x}^b_{bs}(t_0).\end{aligned} \tag{4.56}$$

For the position error $\delta\mathbf{x}^s_{sa}$, a corresponding phase shift error $\delta\phi$ can be associated, which is similar to the total state phase shift,

$$\delta\phi = \mathbf{k_e}\cdot\delta\mathbf{x}^s_{sa}(t_0) - 2\mathbf{k_e}\cdot\delta\mathbf{x}^s_{sa}(t_0+T) + \mathbf{k_e}\cdot\delta\mathbf{x}^s_{sa}(t_0+2T). \tag{4.57}$$

Interestingly, if Eq. (4.56) is inserted into Eq. (4.57), the first two terms, namely the dependency of $\delta\mathbf{x}^s_{sa}$ on the initial atom position error as well as the atom velocity error, are compensated due to their linear growth,

$$\begin{aligned}\mathbf{k_e}\cdot\delta\mathbf{x}^s_{sa}(0) - 2\mathbf{k_e}\cdot\delta\mathbf{x}^s_{sa}(T) + \mathbf{k_e}\cdot\delta\mathbf{x}^s_{sa}(2T) = 0, \\ \mathbf{k_e}\cdot\delta\mathbf{v}^s_{sa}(0)\cdot 0 - 2\mathbf{k_e}\cdot\delta\mathbf{v}^s_{sa}(T)\cdot T + \mathbf{k_e}\cdot\delta\mathbf{v}^s_{sa}(2T)\cdot 2T = 0.\end{aligned} \tag{4.58}$$

Of course this is only valid if their values do not change over time, i.e. the scatter of the wave packet stays constant. Since the focus is on the impact of systematic and calibration errors like misalignment and lever arm errors, their initial values are set to zero. More sophisticated approaches could include modeling the evolution of the errors according to Sec. 3.5.1. The final phase shift error can be stated as

$$\delta\phi = -\mathbf{k_e}\cdot T^2\left(\delta\mathbf{b}_\mathbf{a}(t_0) + \frac{\partial\delta\dot{\mathbf{v}}^s_{sa}}{\partial\delta\mathbf{b}_\mathbf{g}}\delta\mathbf{b}_\mathbf{g}(t_0) + \frac{\partial\delta\dot{\mathbf{v}}^s_{sa}}{\partial\boldsymbol{\gamma}^s_b}\boldsymbol{\gamma}^s_b(t_0) + \frac{\partial\delta\dot{\mathbf{v}}^s_{sa}}{\partial\delta\mathbf{x}^b_{bs}}\delta\mathbf{x}^b_{bs}(t_0)\right). \tag{4.59}$$

A total of 1×10^4 MC samples are generated. The CAI is configured with the following properties: an interrogation time of $T = 0.025\,\mathrm{s}$, an effective wave number of $k_\mathrm{e} = 4\pi/780\ \mathrm{nm}^{-1}$ for the respective sensitive axis, as well as an initial atom velocity of $\mathbf{v}^s_{sa} = [5.5, 100, 5.5]^\mathrm{T}$ mm/s. Furthermore, the following accelerations and angular rates are applied, $\mathbf{f}^b_{ib} = [-1, 1, 9.81]^\mathrm{T}\ \mathrm{m/s^2}$, $\boldsymbol{\omega}^b_{ib} = -[0.01, 0.01, 0.05]^\mathrm{T}$ rad/s. An initial lever arm with the dimension $\mathbf{x}^b_{bs} = [0.1, 0.1, 0.5]^\mathrm{T}$ m length is applied. The lever arm error $\delta\mathbf{x}^b_{bs}$ is varied in all three spatial directions, sampled uniformly from a range of zero to 10 cm. Likewise, the misalignment between the systems is sampled uniformly from 0 to 10 µrad. This makes a total of six MC variables. In addition, deterministic initial bias errors of $\delta\mathbf{b_g} = 2\cdot10^{-4}\cdot[1,1,1]^\mathrm{T}$ rad/s and $\delta\mathbf{b_a} = 4\cdot10^{-5}\cdot[1,1,1]^\mathrm{T}\ \mathrm{m/s^2}$ are applied. For now they are chosen to resemble a *reasonable* classical IMU that is used for the hybridization. The origin of those values will be elaborated in another dedicated study in Sec. 4.4.1.

The phase shifts $\delta\phi$ for all three axes of the s-frame are depicted in Fig. 4.4. Here, the solutions based on the linearized model are compared with the difference between the numerically integrated true and nominal solution of the differential equations. Both methods are in good agreement. The deviation is in the order of 20 mrad.

Fig. 4.5 reveals additional correlation effects, which are further quantified in Tab. 4.1. The letters x, y and z are referring to the sensor frame's respective axis.

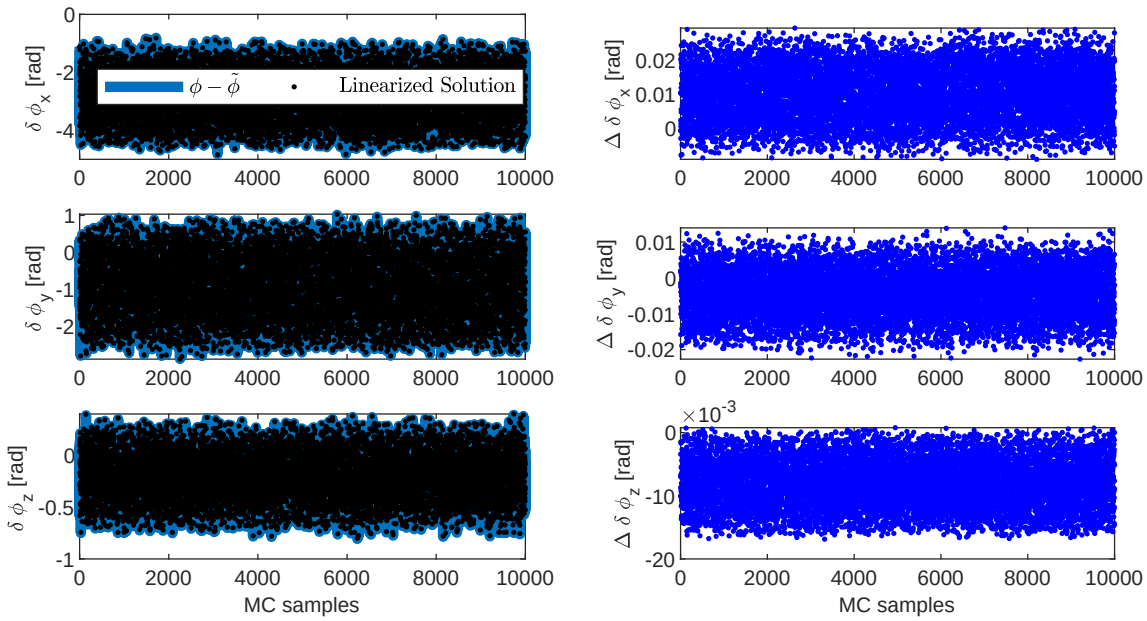

Figure 4.4: Comparison of QINS error state solutions. Left: phase shift error as computed from the difference between the true and nominal phase shift as gained from numerical integration (blue) and the analytical linearized solution with the simplified transition matrix (black dots). Right: difference of the numerical and the linearized solution.

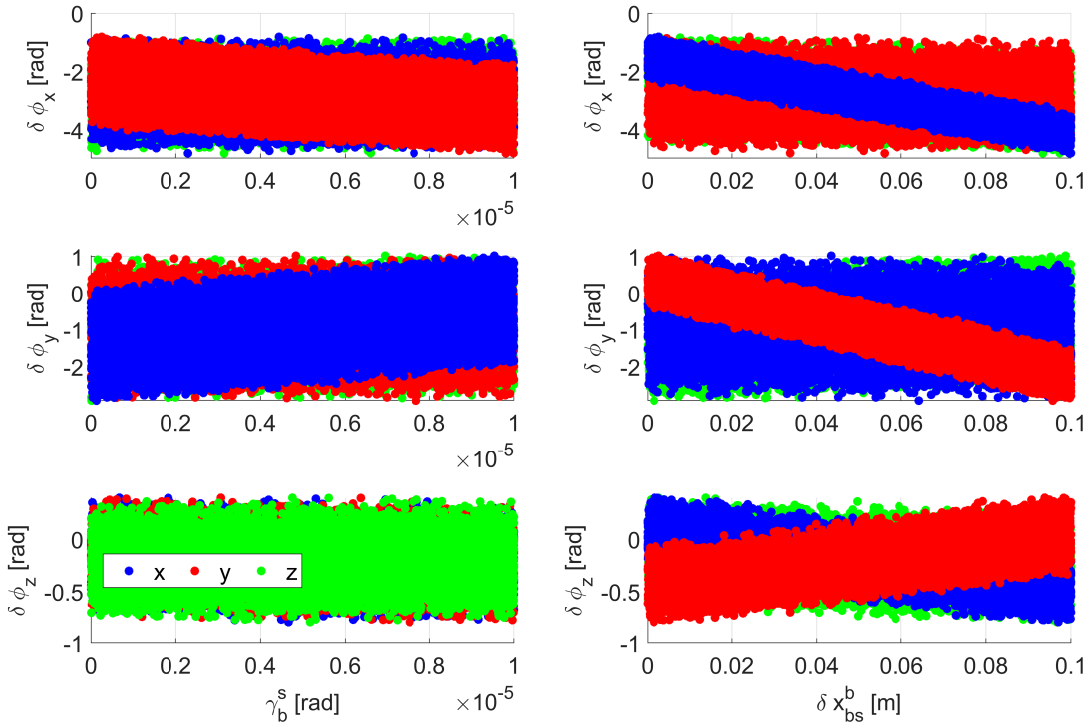

Figure 4.5: CAI phase shift errors resulting from calibration uncertainty. Left panels: misalignment. Right panels: lever arm error. The color code indicates the coordinate component of the error source ($\boldsymbol{\gamma}_b^s$ or $\delta\mathbf{x}_{bs}^b$). The plots are partially overlapped. The pairings with the strongest correlations are shown in the front. The pairings in the back show no particular interesting behavior.

- Phase shift error in x-direction (top row): The lever arm in x-direction has the largest impact, which is further amplified by the initial atom velocity and the misalignment in y-direction. A weaker effect of the lever arm error in y- and z-direction is visible as well.
- Phase shift error in y-direction (middle row): In analogy to the phase error in x-direction the y-axis corresponds to the lever arm error in y- and the misalignment in x-direction. An increased effect of the lever arm error in z-direction is visible as well.
- Phase shift error in z-direction (bottom row): The lever arm error in y-direction has the largest impact, mainly because of the initial atom velocity in this direction, while the lever arm error in x-direction has slightly less impact. The lever arm error in z-direction, just like all three misalignment axes, has almost no effect.

	$\delta\phi_x$	$\delta\phi_y$	$\delta\phi_z$
$\gamma^s_{b,x}$	-0.0054	**0.4461**	-0.0718
$\gamma^s_{b,y}$	**-0.3508**	0.0252	-0.0956
$\gamma^s_{b,z}$	0.0407	0.0301	0.0075
$\delta x^b_{bs,x}$	**-0.9220**	-0.0373	**-0.6710**
$\delta x^b_{bs,y}$	-0.0326	**-0.9186**	**0.6658**
$\delta x^b_{bs,z}$	-0.1756	0.1733	-0.2655

Table 4.1: Pearson correlation coefficients of the error state kinematic system.

The correlations between the phase shift errors and the parameters in Tab. 4.1 give a first qualitative idea about the effects of the parameters on the phase shift errors. A more quantitative and design oriented analysis demands full evaluation of the kinematic equations, which of course depends on the dynamics of the trajectory. Just to convey a very rough idea, simple equations based on the knowledge of the correlations can be stated for the lever arm error as well as for the misalignment. The respective strongest correlation to any of the phase shift errors is focused. Taking the phase shift error in x-direction as an example, the strongest correlation with the lever arm error can be found in the x-component $\delta x^b_{bs,x}$ with a correlation coefficient of -0.9220, while for the misalignment it is the y-component with a correlation coefficient of -0.3508.

Dominant Systematic Effects

The correlations in Tab. 4.1 show that there are some impact factors that clearly outweigh the others. To further examine the relations, the resulting phase shift error in x-direction $\delta\phi_x$ is now taken as an example. The strong impact of the misalignment in y-direction, $\gamma^s_{b,y}$, on the phase shift error $\delta\phi_x$ is mainly caused by the large effect of gravity. A simplified formulation for the phase shift error caused by misalignment, gained by inserting Eq. (4.53) into Eq. (4.59) and reduced to this particular term and parameter pair, clearly supports this finding:

$$\delta\phi_x = k_\mathrm{e} T^2 g_z \gamma^s_{b,y}. \tag{4.60}$$

The misalignment $\gamma^s_{b,x}$ has a similar effect on the phase shift error $\delta\phi_y$.

Consulting Tab. 4.1 again, the lever arm error term with the largest influence on any phase shift error can be found in the x-direction, where the corresponding lever arm error that causes the phase shift error is the one aligned in x-direction. In Eq. (4.54), the major impact factor appears to be the angular rates. For this particular pair of phase shift error and lever arm error, the following approximation can be formulated,

$$\delta\phi_x = -k_\mathrm{e} T^2 (\omega_z^2 + \omega_y^2) \delta x^b_{bs,x}. \tag{4.61}$$

Clearly, the angular rates on the axes perpendicular to the errors of phase shift and lever arm lead to a scaling of $\delta x^b_{bs,x}$.

A similar assessment can be done for the impact of the total state of the lever arm, which might resemble a serious design limitation for the QINS. The corresponding derivative reads

$$\begin{aligned}\frac{\partial \delta \dot{\mathbf{v}}^s_{sa}}{\partial \mathbf{x}^b_{bs}} &= [\boldsymbol{\omega}^b\times][\delta\mathbf{b_g}\times] + [\delta\mathbf{b_g}\times][\boldsymbol{\omega}^b\times] + [\mathbf{b_g}\times][\delta\mathbf{b_g}\times] + [\delta\mathbf{b_g}\times][\mathbf{b_g}\times] \\ &+ [\boldsymbol{\gamma}^s_b\times][\boldsymbol{\omega}^b\times][\boldsymbol{\omega}^b\times] + [\boldsymbol{\gamma}^s_b\times][\boldsymbol{\omega}^b\times][\mathbf{b_g}\times] + [\boldsymbol{\gamma}^s_b\times][\mathbf{b_g}\times][\boldsymbol{\omega}^b\times] + [\boldsymbol{\gamma}^s_b\times][\mathbf{b_g}\times][\mathbf{b_g}\times].\end{aligned} \tag{4.62}$$

The term with the largest impact of the x-axis lever arm on the phase shift error $\delta\phi_x$ in the given scenario can be simplified to

$$\delta\phi_x = -2k_\mathrm{e}T^2(\omega_z\delta b_{g,z} + \omega_y\delta b_{g,y})x^b_{bs,x}, \tag{4.63}$$

which shows that the largest scaling effect in conjunction with the lever arm is resulting from the angular rate of the heading ω_z and the bias error $\delta b_{g,z}$, which represents the uncertainty of the classical gyroscope.

Fig. 4.6 shows the impact of different parameters on the phase shift according to the most dominant terms in Eqs. (4.60), (4.61) and (4.63). The total lever arm is less problematic, which is mainly thanks to the low angular rates that are allowed for the CAI to work. Despite of this, in practice the lever arm should be kept as small as possible in any case, as such large distances need more sophisticated modeling (Wagner, 2003), since the structures cannot be considered rigid anymore.

The lever arm error mainly scales with the angular rates on the perpendicular axes. It can be slightly larger than 5 cm for the given scenario. Again, this value is not problematic, as calibration procedures based on laser trackers reach an accuracy level of well below 1 mm. The critical value of the misalignment is about 15 µrad. This value could cause problems for larger CAI scale factors like the one in the simulated scenario, as values of up to 50 µrad of intrinsic misalignment are typical (iMAR, 2017b). As this large impact is mainly caused by gravity on Earth, applications in space would not suffer as much from this specific effect and other phase shift error terms might become dominant.

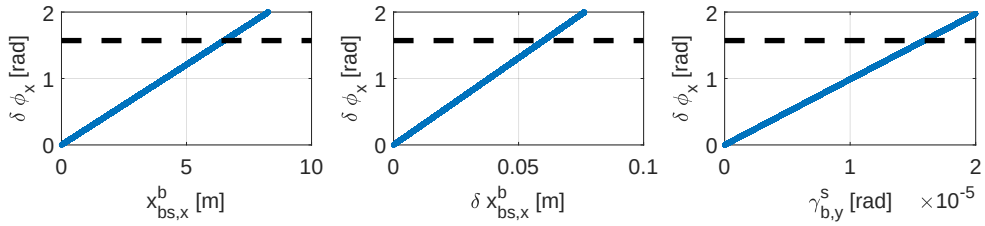

Figure 4.6: Impact of misalignment and lever arm on the phase shift error. The lever arm can be quite large and only surpasses a phase shift error of $\pi/2$ (dotted black line) after a horizontal distance of 6 m. The lever arm error is critical for values larger than 5 cm. The misalignment yields the largest impact which is mainly caused by the vertical acceleration due to gravity. The critical value for the chosen scenario is about 15 µrad.

Once more it has to be stressed that the impact of the initial uncertainty of the atom wave packet position and velocity has not been considered in this study in order to allow a closed solution as approximation for the interaction of the calibration errors and the phase shift error. Larger initial values of $\delta\mathbf{x}^s_{sa}$ and $\delta\mathbf{v}^s_{sa}$ do scale larger with time due to the autoregression over the Coriolis and centrifugal terms. Those two effects however are associated with the s-frame. The only way they interact with the other error states of the QINS is by the misalignment affecting the angular rates, including gyroscope bias and $\delta\mathbf{b_g}$. Here it can be argued that

$\delta\mathbf{x}_{sa}^{s}$ has a similar effect on the phase shift as the lever arm error. It was shown in Sec. 3.5.1 that the initial atom position uncertainty is in the order of some µm, as compared to the cm that are allowed for the lever arm error. Consequently, the contrast loss due to the spread of the wave packet over time is reached long before any of the just mentioned effects have a meaningful impact.

4.3.3 Observability

Method

Observability answers the question if a state in $\mathbf{x}$ is observable, i.e. if it can be *reached* by at least one observation in the vector $\mathbf{y}$ via

$$\mathbf{y} = \mathbf{H}\mathbf{x}.$$

It is quite apparent that this question is directly related to the observation sensitivity described by the matrix $\mathbf{H}$. Assume that each state can be reached by an observation. The next question that subsequently needs to be asked is, if there are several states that are reached by this particular observation. If this is the case, this might lead to an underdetermined system. An approach to answer both questions is the observability matrix $\mathbf{O}_{\text{obs}}$ (Lunze, 2008, p. 95),

$$\mathbf{O}_{\text{obs}} = \begin{bmatrix} \mathbf{H} \\ \mathbf{H}\cdot\mathbf{F} \\ \mathbf{H}\cdot\mathbf{F}^{2} \\ \dots \\ \mathbf{H}\cdot\mathbf{F}^{n-1} \end{bmatrix}. \tag{4.64}$$

For n states, the observability of the system is given if $\mathbf{O}_{\text{obs}}$ yields full column rank,

$$\text{rank}(\mathbf{O}_{\text{obs}}) = n. \tag{4.65}$$

As Eq. (4.64) indicates, observability can also be granted via the system model expressed in the transition matrix $\mathbf{F}$. This multiplication in each line of the matrix $\mathbf{O}_{\text{obs}}$ can be interpreted in a way that the system model *generates* additional observations with each new prediction step. If no dynamic model connects the states and hence $\mathbf{F} = \mathbf{I}_n$, then it is sufficient to evaluate the observation matrix $\mathbf{H}$. Obviously, this is a mere qualitative method, as the matrix $\mathbf{O}_{\text{obs}}$ in principle compares the number of linear independent observation equations with the number of states and gives a *yes or no* answer to the observability question.

The presented approach requires a constant $\mathbf{H}$ for the time frame that is considered. There are other approaches like the observability analysis for piecewise constant systems (Goshen-Meskin & Bar-Itzhack, 1990) to tackle nonlinear problems. Another interesting method for a more quantitative approach, including the effect of the noise variances, is the computation of observability coefficients via the modal values of the steady state transition matrix (Becker et al., 2010). This section's goal is to examine the qualitative observability of different state vector settings. For this task, the presented approach is deemed sufficient.

Application to QINS State Vector

The observation model according to Eq. (4.28) has already been presented for acceleration and angular rate biases. The derivative is now revisited with closer attention to the implications for the observability. Furthermore, the observation model h and the matrix $\mathbf{H}$ are now extended by lever arm and misalignment.

The chain of derivatives for the CAI observation update was expressed in Eq. (4.29). The *outer* derivative which was evaluated in Eq. (4.30) is independent from the state vector. It says that, in order to produce an observation, the amplitude A needs to be different from zero. This is the first general condition.

The derivative $\frac{\partial \tilde{\mathbf{x}}}{\partial \delta \mathbf{x}}$ is essentially -1 for the biases and the lever arm. This means that the observability properties of state and error state, besides a change of sign, are not altered. The only exception is the alignment error $\boldsymbol{\gamma}_b^s$, which is related to the nominal alignment $\tilde{\mathbf{C}}_b^s$ by

$$\tilde{\mathbf{C}}_b^s = (\mathbf{I} - [\boldsymbol{\gamma}_b^s \times])\mathbf{C}_b^s. \tag{4.66}$$

Apart from that, the attributes of relevance to the observability lie in the middle term of Eq. (4.29), the derivative $\frac{\partial \phi}{\partial \tilde{\mathbf{x}}}$. As simplification the frames are assumed to be aligned, $\mathbf{C}_b^s = \mathbf{I}_3$. Some error in form of a misalignment is still present, so that $\tilde{\mathbf{C}}_b^s = (\mathbf{I} - [\boldsymbol{\gamma}_b^s \times])$. The predicted phase shift which is based on the nominal IMU data then reads

$$\begin{aligned}\phi^- = \mathbf{k_e} \cdot \Big(& 2(\tilde{\mathbf{C}}_b^s \tilde{\boldsymbol{\Omega}}_{ib}^b)\tilde{\mathbf{v}}_{sa}^s T^2 - \tilde{\mathbf{C}}_b^s \tilde{\mathbf{f}}_{ib}^b T^2 + \tilde{\mathbf{C}}_b^s \tilde{\boldsymbol{\Omega}}_{ib}^b (\tilde{\boldsymbol{\Omega}}_{ib}^b \tilde{\mathbf{x}}_{bs}^b) T^2 + \tilde{\mathbf{C}}_b^s \dot{\boldsymbol{\Omega}}_{ib}^b \tilde{\mathbf{x}}_{bs}^b T^2 + (\tilde{\mathbf{C}}_b^s \dot{\boldsymbol{\Omega}}_{ib}^b)\tilde{\mathbf{x}}_{sa}^s T^2 \\ & + (\tilde{\mathbf{C}}_b^s \tilde{\boldsymbol{\Omega}}_{ib}^b)((\tilde{\mathbf{C}}_b^s \tilde{\boldsymbol{\Omega}}_{ib}^b)\tilde{\mathbf{x}}_{sa}^s) T^2 - \tilde{\boldsymbol{\Omega}}_{ib}^b (\tilde{\mathbf{f}}_{ib}^b - \tilde{\boldsymbol{\Omega}}_{ib}^b (\tilde{\boldsymbol{\Omega}}_{ib}^b \tilde{\mathbf{x}}_{bs}^b) - \dot{\boldsymbol{\Omega}}_{ib}^b \tilde{\mathbf{x}}_{bs}^b) T^3 \Big).\end{aligned} \tag{4.67}$$

This rather extensive equation requires some detailed discussion. First, every term involves the nominal orientation $\tilde{\mathbf{C}}_b^s$, which yields the alignment error $(\mathbf{I} - [\boldsymbol{\gamma}_b^s \times])$. As $[\boldsymbol{\gamma}_b^s \times]$ is in general a small value, the observability properties of the remaining equation are not qualitatively different from the terms that are multiplied by the identity $\mathbf{I}$. The study will thus first concentrate on the terms that are **not** multiplied by $[\boldsymbol{\gamma}_b^s \times]$. The only exception is the discussion of the observability of the misalignment itself, which focuses on the remaining terms.

A number of different terms can be found in Eq. (4.67) that contribute to the observation sensitivity. For simplicity reasons they are grouped into:

- *Principal* terms with major impact on the phase shift, such as

  $$\mathbf{k_e} \cdot \tilde{\mathbf{f}}_{ib}^b T^2, \qquad 2\mathbf{k_e} \cdot \tilde{\boldsymbol{\Omega}}_{is}^s \tilde{\mathbf{v}}_{sa}^s T^2, \qquad \mathbf{k_e} \cdot \tilde{\boldsymbol{\Omega}}_{ib}^b \tilde{\mathbf{f}}_{ib}^b T^3.$$

  These terms are the ones that qualify the interferometer as an inertial sensor and will be the focus of the discussion.

- Terms that are associated with the *lever arm* $\tilde{\mathbf{x}}_{bs}^b$ between the systems. A lever arm can greatly improve the observability of certain terms in turn maneuvers, but at the same time it scales uncertainties of the IMU data by the transformation to the s-frame and generally needs to be kept small.

- Terms that are associated with the position of the wave packet $\tilde{\mathbf{x}}_{sa}^s$. The displacement of the wave packet raises fictitious force terms that make the interferometer sensitive to a rotation as well. The effect for the observability is similar to that of the lever arm, but on a much smaller scale.

The mixed term has additional dependencies that arise with the transformation of the specific forces, namely $\mathbf{k_e} \cdot \tilde{\boldsymbol{\Omega}}_{ib}^b \tilde{\boldsymbol{\Omega}}_{ib}^b (\tilde{\boldsymbol{\Omega}}_{ib}^b \tilde{\mathbf{x}}_{bs}^b) T^3$ and $\mathbf{k_e} \cdot \tilde{\boldsymbol{\Omega}}_{ib}^b \dot{\boldsymbol{\Omega}}_{ib}^b \tilde{\mathbf{x}}_{bs}^b T^3$. They are neglected for two reasons: First, from a qualitative perspective, they have the same properties as the terms resulting from the transformation of $\mathbf{f}_{ib}^b$ itself, safe from an additional factor of T and $\tilde{\boldsymbol{\Omega}}_{ib}^b$. Second, those additional factors drastically reduce the magnitude of the impact for the observability in most cases, which does not justify the added complexity of the model.

The observability of the states $\delta \mathbf{b_a}$, $\delta \mathbf{b_g}$, $\boldsymbol{\gamma}_b^s$ and $\delta \mathbf{x}_{bs}^b$ on the basis of the principal terms in the observation equation is now discussed in detail.

Acceleration Bias

For the discussion, the index j indicating the axes of the 6DOF CAI is included again. The derivative of the phase shift to the acceleration bias reads

$$\frac{\partial \phi_j^-}{\partial \mathbf{b_a}} = -(\mathbf{k_e}_j)^{\mathrm{T}}\mathbf{I}T^2 - (\mathbf{k_e}_j)^{\mathrm{T}}[\tilde{\boldsymbol{\omega}}_{ib}^b\times]T^3. \tag{4.68}$$

Two terms are resulting. Depending on the vector $\mathbf{k_e}_j$, the first term can always assure the observability of the corresponding acceleration bias. As an example, in order to observe $b_{a,x}$, the first entry of $\mathbf{k_e}_j$ has to be non-zero, e.g. $j = x\uparrow$ or $j = x\downarrow$.

The second term, however, also yields a small observability to the biases perpendicular to the sensitive axis, whenever an angular rate is present on either one of those axes. The derivative of this second term reads in detail,

$$-\begin{bmatrix} k_x & 0 & 0 \end{bmatrix} T^2 - \begin{bmatrix} k_x & 0 & 0 \end{bmatrix} \cdot \begin{bmatrix} 0 & -\omega_z & \omega_y \\ \omega_z & 0 & -\omega_x \\ -\omega_y & \omega_z & 0 \end{bmatrix} T^3 = -\begin{bmatrix} k_x T^2 & -k_x\omega_z T^3 & k_x\omega_y T^3 \end{bmatrix}. \tag{4.69}$$

The indices are reduced to improve readability, such that $f_{ib,x}^b = f_x$, $\omega_{ib,x}^b = \omega_x$, $v_{sa,x}^s = v_x$, $\gamma_{b,x}^s = \gamma_x$, etc. It is obvious that the system is unstable if an angular rate on either perpendicular axis is present. For this case, three perpendicular CAI observations are required,

$$\begin{bmatrix} \frac{\partial \phi_x^-}{\partial \mathbf{b_a}} \\ \frac{\partial \phi_y^-}{\partial \mathbf{b_a}} \\ \frac{\partial \phi_z^-}{\partial \mathbf{b_a}} \end{bmatrix} = -\begin{bmatrix} k_x T^2 & -k_x\omega_z T^3 & k_x\omega_y T^3 \\ k_y\omega_z T^3 & k_y T^2 & -k_y\omega_x T^3 \\ -k_z\omega_y T^3 & k_z\omega_x T^3 & k_z T^2 \end{bmatrix}, \tag{4.70}$$

in order to achieve a full rank($\mathbf{H}$) = 3 of the observation matrix according to the dimension of the acceleration bias states.

Gyroscope Bias

Displaying only the principal terms, the derivative of the phase shift to the gyroscope bias is

$$\frac{\partial \phi_j^-}{\partial \mathbf{b_g}} = 2(\mathbf{k_e}_j)^{\mathrm{T}}[\tilde{\mathbf{v}}_{sa,j}^s\times]T^2 + (\mathbf{k_e}_j)^{\mathrm{T}}[\tilde{\mathbf{f}}_{ib}^b\times]T^3. \tag{4.71}$$

Two terms with large impact result, both involving a skew-symmetric matrix. This means that, contrary to the accelerometer bias, the gyroscope bias is not always observable. In order to observe the gyroscope bias on a particular axis, e.g. $j = x\uparrow$, a velocity or acceleration on one of the perpendicular axes needs to be present. For this reason, many CAI gyroscope designs are providing an initial momentum to the atom wave packet in a direction perpendicular to the sensitive axis.

For the sake of further discussion of the case with $j = x\uparrow$, let $\mathbf{v}_{sa,j}^s = [0, v_y, 0]^{\mathrm{T}}$ be applied in y-direction. The derivative of the Coriolis term w.r.t. the bias reads in detail

$$2\begin{bmatrix} k_x & 0 & 0 \end{bmatrix} \cdot \begin{bmatrix} 0 & 0 & v_y \\ 0 & 0 & 0 \\ -v_y & 0 & 0 \end{bmatrix} T^2 = \begin{bmatrix} 0 & 0 & 2k_x v_y T^2 \end{bmatrix}. \tag{4.72}$$

This shows that it is possible for the system to be sensitive to the gyroscope bias in z-direction only. However, as the velocity of the atoms evolves with time, a sensitivity on a much smaller

scale is also present for the bias on the y-axis[1]. Furthermore, the mixed term adds additional sensitivity with the gyroscope bias in the x-direction being the only exception. For terrestrial applications the most notable parameter in this term is the gravitational acceleration, which adds a huge sensitivity to the gyroscope bias in x- and y-direction and cannot be neglected.

According to the observability analysis, the system is theoretically unstable in any case if only the observation of one CAI axis is used. The full observation sensitivity matrix with three perpendicular observations reads

$$\begin{bmatrix} \frac{\partial \phi_x^-}{\partial \mathbf{b_g}} \\ \frac{\partial \phi_y^-}{\partial \mathbf{b_g}} \\ \frac{\partial \phi_z^-}{\partial \mathbf{b_g}} \end{bmatrix} = \begin{bmatrix} 0 & -2k_x v_z T^2 - k_x f_z T^3 & 2k_x v_y T^2 + k_x f_y T^3 \\ 2k_y v_z T^2 + k_y f_z T^3 & 0 & -2k_y v_x T^2 - k_y f_x T^3 \\ -2k_z v_y T^2 - k_z f_y T^3 & 2k_z v_x T^2 + k_z f_x T^3 & 0 \end{bmatrix}, \tag{4.73}$$

which has full rank of 3 again, according to the three gyroscope bias states.

Misalignment

For the misalignment, three terms of Eq. (4.67) are of interest,

$$\phi_j^- = -\mathbf{k}_{\mathbf{e}j} \cdot (\mathbf{I} - [\boldsymbol{\gamma}_b^s \times]) \tilde{\mathbf{f}}_{ib}^b T^2 + 2\mathbf{k}_{\mathbf{e}j} \cdot ((\mathbf{I} - [\boldsymbol{\gamma}_b^s \times]) \tilde{\boldsymbol{\Omega}}_{ib}^b) \tilde{\mathbf{v}}_{sa,j}^s T^2 - \mathbf{k}_{\mathbf{e}j} \cdot (\mathbf{I} - [\boldsymbol{\gamma}_b^s \times]) \tilde{\boldsymbol{\Omega}}_{ib}^b \tilde{\mathbf{f}}_{ib}^b T^3. \tag{4.74}$$

The derivative with respect to the misalignment $\boldsymbol{\gamma}_b^s$ yields the following result:

$$\frac{\partial \phi_j^-}{\partial \boldsymbol{\gamma}_b^s} = -(\mathbf{k}_{\mathbf{e}j})^{\mathrm{T}} [\tilde{\mathbf{f}}_{ib}^b \times] T^2 - 2(\mathbf{k}_{\mathbf{e}j})^{\mathrm{T}} [\tilde{\boldsymbol{\omega}}_{ib}^b \times] [\tilde{\mathbf{v}}_{sa,j}^s \times] T^2 - (\mathbf{k}_{\mathbf{e}j})^{\mathrm{T}} [(\tilde{\boldsymbol{\omega}}_{ib}^b \times \tilde{\mathbf{f}}_{ib}^b) \times] T^3. \tag{4.75}$$

Three terms are emerging. The first one indicates that in order to observe the misalignment on one axis, an acceleration on an axis perpendicular to it needs to be present. Once again, the index $j = x \uparrow$ is taken as an example:

$$-[k_x, 0, 0] \cdot \begin{bmatrix} 0 & -f_z & f_y \\ f_z & 0 & -f_x \\ -f_y & f_x & 0 \end{bmatrix} T^2. \tag{4.76}$$

The remaining terms are comparable, but not as intuitive. Taking the same example as developed for the gyroscope bias, with an initial atom velocity in y-direction, the second term in detail reads

$$\begin{aligned} &-2 \begin{bmatrix} k_x & 0 & 0 \end{bmatrix} \cdot \begin{bmatrix} -\omega_z v_z - \omega_y v_y & \omega_y v_x & \omega_z v_x \\ \omega_x v_y & -\omega_z v_z - \omega_x v_x & \omega_z v_y \\ \omega_x v_z & \omega_y v_z & -\omega_y v_y - \omega_x v_x \end{bmatrix} T^2 \\ &= \begin{bmatrix} 2k_x(\omega_z v_z + \omega_y v_y) T^2 & -2k_x \omega_y v_x T^2 & -2k_x \omega_z v_x T^2 \end{bmatrix}. \end{aligned} \tag{4.77}$$

The first entry corresponds to the observability of the misalignment in x-direction. This term requires an atom velocity and an angular rate on a common axis perpendicular to the observation to be different from zero. The observation on the x-axis can also reach the remaining two misalignments $\gamma_{b,y}^s$ and $\gamma_{b,z}^s$. For this purpose, an angular rate on the respective axis needs to be present in addition, as well as an atom velocity on the axis of the observation.

[1] For this reason it is more suitable to use the mean velocity as parameter in the equation rather than the initial velocity. The same applies to the terms depending on the wave packet position, if they need to be included in the model.

The third term is evaluated now, resulting in

$$-[k_x,0,0]\cdot\begin{bmatrix}0 & \omega_z f_y & 0\\ -\omega_z f_y & 0 & -\omega_x f_y\\ 0 & \omega_x f_y & 0\end{bmatrix} T^3 = \begin{bmatrix}0 & -k_x\omega_z f_y T^3 & 0\end{bmatrix}. \tag{4.78}$$

The result shows that with this observation term the misalignment on a perpendicular axis, here: γ_y, can be reached by an acceleration acting on the atoms in direction of this axis. However, in that case an angular rate has to be present that is perpendicular to the acting force and the axis of the observation.

Lever Arm

For the lever arm, two terms of Eq. (4.67) are relevant:

$$\phi_j^- = \mathbf{k}_{\mathbf{e}j}\cdot(\tilde{\mathbf{\Omega}}_{ib}^b(\tilde{\mathbf{\Omega}}_{ib}^b\tilde{\mathbf{x}}_{bs}^b)T^2 + \dot{\mathbf{\Omega}}_{ib}^b\tilde{\mathbf{x}}_{bs}^b T^2). \tag{4.79}$$

The derivative w.r.t. the lever arm is

$$\frac{\partial\phi_j^-}{\partial\mathbf{x}_{bs}^b} = (\mathbf{k}_{\mathbf{e}j})^{\mathrm{T}}[\tilde{\boldsymbol{\omega}}_{ib}^b\times][\tilde{\boldsymbol{\omega}}_{ib}^b\times]T^2 + (\mathbf{k}_{\mathbf{e}j})^{\mathrm{T}}[\dot{\boldsymbol{\omega}}_{ib}^b\times]T^2. \tag{4.80}$$

Taking the example with $j = x$ again, the second term shows that an angular acceleration around the y- or z-axis leads to the lever arm in x-direction to be observable. The first term associated with the centrifugal acceleration is not that intuitive. In detail it reads:

$$\begin{aligned}&\begin{bmatrix}k_x & 0 & 0\end{bmatrix}\cdot\begin{bmatrix}-\omega_z^2-\omega_y^2 & \omega_y\omega_x & \omega_z\omega_x\\ \omega_y\omega_x & -\omega_z^2-\omega_x^2 & \omega_z\omega_y\\ \omega_z\omega_x & \omega_z\omega_y & -\omega_x^2-\omega_y^2\end{bmatrix}T^2\\ &= \begin{bmatrix}-k_x(\omega_z^2+\omega_y^2)T^2 & k_x\omega_y\omega_x T^2 & k_x\omega_x\omega_z T^2\end{bmatrix}.\end{aligned} \tag{4.81}$$

Here it can be seen that the lever arm in sensitive direction is observable, as long as angular rates on the perpendicular axes are present. Furthermore, observability is given for the y- and z-direction, when additionally an angular rate on the x-axis is present. Thus the system is only stable with one CAI observation, when no rotation on the sensitive axis occurs. Since only small rotations are allowed for the CAI, and furthermore all angular rates are quadratic in the matrix, the lever arm is expected to be only weakly observable.

Conclusion

The observability of the different states has been discussed individually. Altogether there is a maximum of six observations available at a time for a total of 12 independent states. An overview is given in Tab. 4.2, where the major dynamic requirements, which connect the observations and the states, are pointed out. The terms proportional to T^3, as well as products of different conditions, e.g. $v_y\omega_z$, are not included.

The states are not correlated over a dynamic model and hence the system cannot produce any additional observations via $\mathbf{H}\cdot\mathbf{F}$ in Eq. (4.64). This indicates that the system is not fully observable at any time. Hence, and this is the first conclusion, a **reduced state vector** augmentation with only angular rate and acceleration bias is proposed for the QINS.

For this augmentation with the bias states, it was shown that the acceleration bias can be distinguished from the angular rate bias thanks to the interrogation of two parts of an atomic

	$h_{x\uparrow}$	$h_{y\uparrow}$	$h_{z\uparrow}$	$h_{x\downarrow}$	$h_{y\downarrow}$	$h_{z\downarrow}$
$\delta b_{a,x}$	1	0	0	1	0	0
$\delta b_{a,y}$	0	1	0	0	1	0
$\delta b_{a,z}$	0	0	1	0	0	1
$\delta b_{g,x}$	0	v_z	v_y	0	v_z	v_y
$\delta b_{g,y}$	v_z	0	v_x	v_z	0	v_x
$\delta b_{g,z}$	v_y	v_x	0	v_y	v_x	0
$\gamma^s_{b,x}$	ω_z, ω_y	f_z	f_y	ω_z, ω_y	f_z	f_y
$\gamma^s_{b,y}$	f_z	ω_z, ω_x	f_x	f_z	ω_z, ω_x	f_x
$\gamma^s_{b,z}$	f_y	f_x	ω_y, ω_x	f_y	f_x	ω_y, ω_x
$\delta x^b_{bs,x}$	ω_z^2, ω_y^2	$\dot{\omega}_z$	$\dot{\omega}_y$	ω_z^2, ω_y^2	$\dot{\omega}_z$	$\dot{\omega}_y$
$\delta x^b_{bs,y}$	$\dot{\omega}_z$	ω_z^2, ω_x^2	$\dot{\omega}_x$	$\dot{\omega}_z$	ω_z^2, ω_x^2	$\dot{\omega}_x$
$\delta x^b_{bs,z}$	$\dot{\omega}_y$	$\dot{\omega}_x$	ω_y^2, ω_x^2	$\dot{\omega}_y$	$\dot{\omega}_x$	ω_y^2, ω_x^2

Table 4.2: QINS observability requirements.

wave packet after the initial momentum split. However, the observation is sensitive to up to two perpendicular angular rate biases, leading to the situation that two observations per axis are present for three observable states. Something similar occurs for the acceleration bias, where additional sensitivities arise from the mixed term. Hence, the only way to guarantee full observability is by using all six CAI observations. This was shown in Eq. (4.70) and (4.73). This means that any reduced CAI configuration with less than six linear independent observations would lead to an unstable system. Consequently, the proposal for **using a full 6DOF CAI** is the second conclusion.

4.3.4 Controllability

Controllability in a control-theory sense measures whether a state can be *reached* by control input. In other words, the goal of a controllability study is to find out if one can control a certain state by external input. In a Kalman filter the interpretation is slightly different. In the prediction step, the state is driven by the data that are modeled as control input. In the frame of the QINS, it is an IMU that is used to propagate the motion model of the kinematic state. Consequently, the core of the controllability analysis in the Kalman filter is to evaluate if the dynamic model is sufficient in order to have a prediction for each state. If no prediction model for a particular state exists, the corresponding system is unstable. Similarly to the observability matrix, a controllability matrix $\mathcal{C}$ (Lunze, 2008, p. 66) can be defined such that

$$\mathcal{C} = \begin{bmatrix} \mathbf{B} & \mathbf{FB} & \mathbf{F}^2\mathbf{B} & \dots & \mathbf{F}^{n-1}\mathbf{B} \end{bmatrix}. \tag{4.82}$$

For n states, the controllability of the system is given if,

$$\operatorname{rank}(\mathcal{C}) = n. \tag{4.83}$$

The input is given by $\mathbf{u} = [\mathbf{w_a}, \mathbf{w_g}]^{\mathrm{T}}$, with the two processes $\mathbf{w_a}$ associated with the acceleration input, and $\mathbf{w_g}$ associated with the angular rates. The input matrix was already stated before in Eq. (4.48),

$$\mathbf{B} = \begin{bmatrix} \mathbf{0} & \mathbf{0} \\ \mathbf{0} & \mathbf{0} \\ \mathbf{I} & \mathbf{0} \\ \mathbf{0} & \mathbf{I} \\ \mathbf{0} & \mathbf{0} \\ \mathbf{0} & \mathbf{0} \end{bmatrix}.$$

Using the simplified transition matrix from Eq. (4.55), the powers $\mathbf{F}^n$ of the matrix can be represented as a closed solution,

$$\mathbf{F}^n = \begin{bmatrix} \mathbf{I} & n\mathbf{I}\Delta t & -\frac{n^2}{2}\mathbf{I}\Delta t^2 & \frac{n^2}{2}\Delta t^2 \frac{\partial \delta \dot{\mathbf{v}}^s_{sa}}{\partial \delta \mathbf{b_g}} & \frac{n^2}{2}\Delta t^2 \frac{\partial \delta \dot{\mathbf{v}}^s_{sa}}{\partial \delta \boldsymbol{\gamma}^s_b} & \frac{n^2}{2}\Delta t^2 \frac{\partial \delta \dot{\mathbf{v}}^s_{sa}}{\partial \delta \mathbf{x}^b_{bs}} \\ \mathbf{0} & \mathbf{I} & -n\mathbf{I}\Delta t & n\Delta t \frac{\partial \delta \dot{\mathbf{v}}^s_{sa}}{\partial \delta \mathbf{b_g}} & n\Delta t \frac{\partial \delta \dot{\mathbf{v}}^s_{sa}}{\partial \delta \boldsymbol{\gamma}^s_b} & n\Delta t \frac{\partial \delta \dot{\mathbf{v}}^s_{sa}}{\partial \delta \mathbf{x}^b_{bs}} \\ \mathbf{0} & \mathbf{0} & \mathbf{I} & \mathbf{0} & \mathbf{0} & \mathbf{0} \\ \mathbf{0} & \mathbf{0} & \mathbf{0} & \mathbf{I} & \mathbf{0} & \mathbf{0} \\ \mathbf{0} & \mathbf{0} & \mathbf{0} & \mathbf{0} & \mathbf{I} & \mathbf{0} \\ \mathbf{0} & \mathbf{0} & \mathbf{0} & \mathbf{0} & \mathbf{0} & \mathbf{I} \end{bmatrix}. \tag{4.84}$$

The complete controllability matrix $\mathcal{C}$ reads

$$\mathcal{C} = \begin{bmatrix} \mathbf{0} & \mathbf{0} & ... & -\frac{1}{2}(n-1)^2\Delta t^2\mathbf{I} & \frac{1}{2}(n-1)^2\Delta t^2 \frac{\partial \delta \dot{\mathbf{v}}^s_{sa}}{\partial \delta \mathbf{b_g}} \\ \mathbf{0} & \mathbf{0} & ... & -(n-1)\Delta t\mathbf{I} & (n-1)\Delta t \frac{\partial \delta \dot{\mathbf{v}}^s_{sa}}{\partial \delta \mathbf{b_g}} \\ \mathbf{I} & \mathbf{0} & ... & \mathbf{I} & \mathbf{0} \\ \mathbf{0} & \mathbf{I} & ... & \mathbf{0} & \mathbf{I} \\ \mathbf{0} & \mathbf{0} & ... & \mathbf{0} & \mathbf{0} \\ \mathbf{0} & \mathbf{0} & ... & \mathbf{0} & \mathbf{0} \end{bmatrix}. \tag{4.85}$$

While for $n = 1$ only the bias error states $\delta\mathbf{b_a}$ and $\delta\mathbf{b_g}$ can be reached by the input, it is only possible to extend the controllability to $\delta\mathbf{x}^s_{sa}$ and $\delta\mathbf{v}^s_{sa}$, even with an arbitrary number of $n > 1$. The impact of $\mathbf{w_g}$ further depends on the derivative

$$\frac{\partial \delta \dot{\mathbf{v}}^s_{sa}}{\partial \delta \mathbf{b_g}} = -2[\mathbf{v}^s_{sa}\times] - [\boldsymbol{\omega}^s\times][\mathbf{x}^b_{bs}\times] - [(\mathbf{b_g} \times \mathbf{x}^b_{bs})\times],$$

which was already discussed in Sec. 4.3.1. The misalignment and lever arm error stay unaffected by the input at all times.

4.3.5 Steady State Formulation

If the state of a Kalman filter is both controllable and observable, it will eventually reach a **steady state**, in which the covariances of the predicted observation and the actual observation are in equilibrium, i.e. the Kalman gain $\mathbf{K}$ does not change anymore. This steady state Kalman gain, denoted by $\mathbf{K}_\infty$, is given by

$$\mathbf{K}_\infty = \mathbf{P}_\infty \mathbf{H}^\mathrm{T} \mathbf{R}^{-1}, \tag{4.86}$$

with the measurement noise matrix $\mathbf{R}$. The steady state covariance matrix $\mathbf{P}_\infty$ still needs to be derived. An alternative representation of the filtered covariance matrix $\mathbf{P}^+_k$ is the following,

$$\mathbf{P}^+_k = \left[\mathbf{H}^\mathrm{T}_k \mathbf{R}^{-1}_k \mathbf{H}_k + (\mathbf{P}^-_k)^{-1}\right]^{-1}, \tag{4.87}$$

which can be established based on the so-called information filter formulation of the KF (Simon, 2006, p. 156), allowing for an arguably simpler representation of the update step. The time propagation of the covariance matrix is given by

$$\mathbf{P}^-_k = \mathbf{F}_{k-1}\mathbf{P}^+_{k-1}\mathbf{F}^\mathrm{T}_{k-1} + \mathbf{Q}_{k-1}. \tag{4.88}$$

In a steady state situation, the covariance matrix converges to its steady state value, $\mathbf{P}^+_k = \mathbf{P}^+_{k-1} = \mathbf{P}_\infty$. Further assume, that the matrices $\mathbf{F}$, $\mathbf{H}$, $\mathbf{Q}$ and $\mathbf{R}$ are time invariant. The

equations (4.88) and (4.87) can then be reformulated and included in a single expression (Schweppe, 1973, p. 142), which is a discrete algebraic matrix Riccati equation:

$$\mathbf{P}_\infty = \left[\mathbf{H}^\mathrm{T}\mathbf{R}^{-1}\mathbf{H} + (\mathbf{F}\mathbf{P}_\infty\mathbf{F}^\mathrm{T} + \mathbf{Q})^{-1}\right]^{-1}. \tag{4.89}$$

The next step would be the solution of Eq. (4.89). This can be done with numerical approaches like discussed in Bittanti et al. (1991), or the so-called Hamiltonian approach (Simon, 2006, p. 207), which further allows to test the feasibility of the solution. Analytical solutions are generally not possible, but can be developed under certain circumstances. As the analytical solution is an important topic for several aspects of the QINS system design, it will be discussed next.

Analytical Solution of the Steady State Variances

The analytical solution of the Riccati equation is driven by the objective to derive a closed solution for the accuracy of the output that is produced by the QINS. In order to allow an analytical solution, the following characteristics of the system are assumed:

- A single state on a single axis is considered.
- There are no correlations between individual states.
- All noise processes are considered stationary.

Those assumptions appear strongly limiting at first, but they can be justified for certain cases:

- Only inertial quantities given in the b-frame are considered. Thus, no transient transformations between the systems are required. The kinematic states of the moving platform are excluded from the analysis.
- Only the reduced state vector with $\delta\mathbf{b_a}$ and $\delta\mathbf{b_g}$ is discussed. With the reduced state vector of degree n, the transition matrix from Eq. (4.55) is the unity matrix, $\mathbf{F} = \mathbf{I}_{nxn}$.
- CAI yields high long-term stability of several thousand seconds. In contrast, the time of a measurement cycle is below one second. The noise in the measurement over the course of one cycle can therefore be regarded as white noise only. The variance is stationary and thus $\mathbf{R}$ is constant.
- The process noise $\mathbf{Q}$ for the respective IMU measurement is considered as constant over the course of a measurement cycle. This can be justified for IMUs of tactical grade or better, as the white noise is dominant for several seconds, before the flicker floor is reached.

Note that those requirements are provided for the analytical description of the steady state of $\delta\mathbf{b_a}$ and, to a degree, $\delta\mathbf{b_g}$. For the latter, a constant atom velocity is assumed.

The analysis is now simplified according to the items listed above, and only a single state is considered. The matrices $\mathbf{P}$, $\mathbf{F}$, $\mathbf{H}$, $\mathbf{Q}$ and $\mathbf{R}$ will not be displayed in **bold** style anymore for the remainder of this section, since they are of dimension 1×1. Still, the label matrix will be used.

Starting from Eq. (4.89), the system matrix F for a single bias state can be simplified to assume a value of one, thus

$$P_\infty = \frac{1}{\frac{H^2}{R} + \frac{1}{P_\infty + Q}}. \tag{4.90}$$

Some reformulation leads to:

$$0 = P_\infty^2 + QP_\infty - \frac{QR}{H^2}, \tag{4.91}$$

which has the two solutions,

$$P_{\infty,1,2} = -\frac{Q}{2} \pm \sqrt{\frac{Q^2}{4} + \frac{QR}{H^2}}. \tag{4.92}$$

Only the first solution is needed, since no negative variances exist and P_∞ will only be greater or equal zero if the square root is added to the first term. The final equation for the steady state variance reads

$$P_\infty = -\frac{Q}{2} + \sqrt{\frac{Q^2}{4} + \frac{QR}{H^2}}. \tag{4.93}$$

Some interesting properties of Eq. (4.93) can be observed:

- If $R = 0$, the equation yields the trivial solution $P_\infty = 0$.
- If $Q = 0$, the steady state solution would be zero, independent from R.
- If $H = 0$, the state is not observable, and the solution of P_∞ approximates ∞ in the limit. A similar outcome is achieved by $R \to \infty$.
- For $Q \gg R$, the solution converges to $P_\infty = \frac{R}{H^2}$, cf. Fig. 4.7.
- For $R \gg Q$, the solution can be approximated[2] by $P_\infty \approx \sqrt{QR}/H$.

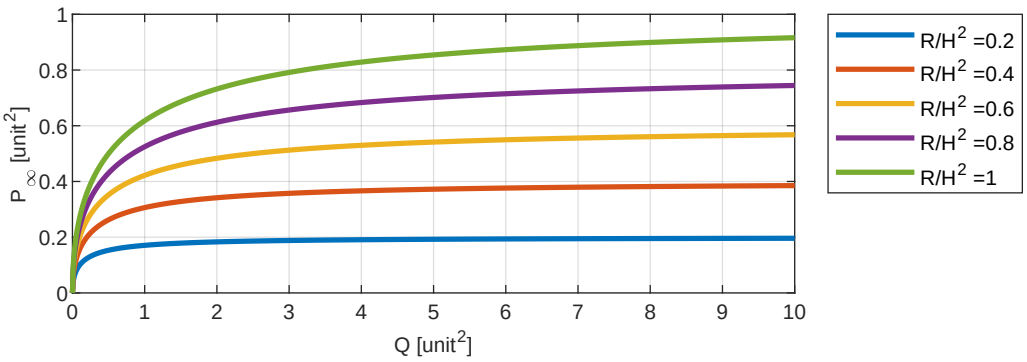

Figure 4.7: Steady state variance in a Kalman filter. For different process noise values Q (x-axis) and different observation variances R (colored lines) the resulting P_∞ is expressed. Large values of $Q \gg R$ cause the steady state variance to converge to $P_\infty = \frac{R}{H^2}$.

In summary it can be stated that individual solutions for P_∞ other than zero are only possible if

$$R > 0, \qquad Q > 0.$$

For the accelerometer bias with the discrete input white noise variance Q_a and observation matrix $H_a = Ak_eT^2$, the following steady state variance results

$$P_{a,\infty} = -\frac{Q_a}{2} + \sqrt{\frac{Q_a^2}{4} + \frac{Q_aR}{(Ak_eT^2)^2}}. \tag{4.94}$$

The steady state expression for the gyroscope bias variance only works under the assumption that only an atom velocity v_y perpendicular to the observed state and the laser wave vector

[2] This rough approximation can be derived by setting R/H^2 to ηQ, where η is a large factor. E.g. $P_\infty \approx 30Q$, when $\eta = 900$.

is present according to Eq. (4.72). In this particular case it can be formulated as

$$P_{g,\infty} = -\frac{Q_g}{2} + \sqrt{\frac{Q_g^2}{4} + \frac{Q_g R}{(2Ak_e v_{sa}^s T^2)^2}}. \tag{4.95}$$

Obviously the applicability of $P_{g,\infty}$ is highly problematic, and the equation can only be regarded as a rough estimate for the resulting variance on a specific sensor axis. The atom velocity v_{sa}^s is subject to accelerations, notably the component in z-direction due to gravity, which causes it to be a non-constant value. Additionally, components of the velocity in several directions are almost inevitable, in which case $\mathbf{H}$ is not a scalar anymore.

4.4 Limits of Hybrid Navigation

By developing the error state kinematics of the wave packet time evolution it was shown that different errors affect the predicted phase shift, resulting in a phase shift error $\delta\phi$ of the prediction. As a first example, the phase shift error is assumed to be caused entirely by the accelerometer bias. By assuming constant values of $\mathbf{f}_{is}^s$, a closed form to approximate the phase shift can be stated. The true value of ϕ and the nominal value $\tilde{\phi}$ are given by

$$\phi = -\mathbf{k_e}(\mathbf{f}_{is}^s + \mathbf{b_a})T^2, \qquad \tilde{\phi} = -\mathbf{k_e}(\mathbf{f}_{is}^s + \tilde{\mathbf{b_a}})T^2, \qquad \tilde{\mathbf{b_a}} = \mathbf{b_a} - \delta\mathbf{b_a},$$

so that the error phase shift $\delta\phi = \phi - \tilde{\phi}$ results in

$$\delta\phi = -\mathbf{k_e}\delta\mathbf{b_a}T^2. \tag{4.96}$$

This $\delta\phi$ can be troublesome for two major reasons:

- Similarly to the ambiguity of the CAI phase shift due to large variations of the dynamic input, the phase shift error is not allowed to be larger than the interval which defines the dynamic range of the sensor. This can be a problem if the dead time of the CAI is too large, i.e. the time in which the bias can grow without correction due to systematic and long-periodic effects so that the accumulated $\delta\phi$ grows beyond the reciprocal region of the cosine signal.
- Even if the accumulated $\delta\phi$ is still on the corresponding flank of the cosine signal, the sensitivity for the bias is smaller, the further away the observation is from the mid fringe operating point.

The second point is the focus of the following section.

4.4.1 Optimal Hybridization

Motivation

Assume a static case with no external dynamics. An accelerometer is used to measure the accelerations of the interferometer frame on a single axis. The data of the classical accelerometer a_{acc} and the CAI observations are sampled from a zero-mean normal distribution with variance Q and R, respectively. This is done for a total of 10^4 MC instances. The filtered accelerations are given by

$$a_{\mathrm{fil}} = \bar{a}_{\mathrm{acc}} + b_a. \tag{4.97}$$

The bar represents the mean of the accelerations during the atom flight time $T_{\mathrm{f}} = 2T$. This step is necessary, as the values of b_a can only be produced at the rate of the EKF, which is given by T_{f}.

To simplify the analysis and actually allow a closed analytical representation of the solution, the following linearized model can be used to calculate the phase shift for this static case,

$$\phi = -k_e \bar{a}_{\mathrm{acc}} T^2. \tag{4.98}$$

Let σ^2_{acc} and σ^2_{fil} denote the variances as computed from the acceleration samples a_{acc} and a_{fil}, respectively. A ratio $\mathcal{R} = \frac{\sigma_{\mathrm{acc}}}{\sigma_{\mathrm{fil}}}$ can be defined, resembling the **gain of sensitivity** thanks to the EKF.

This simulation is now processed for different values of Q which defines the variance of the normal distribution from which the accelerometer data values are sampled. The corresponding $\mathcal{R}$ is calculated for each simulation, allowing to illustrate the relationship between Q and the filter sensitivity gain. The results are depicted in Fig. 4.8. Clearly, there is a large increase of $\mathcal{R}$ for growing uncertainty of the accelerometer, thanks to the superior accuracy of the CAI and, at a certain value of σ_a, a maximum of the sensitivity gain is reached. After that point, $\mathcal{R}$ begins to drop until it approximates a value of one again, which represents a situation in which no improvement can be achieved anymore. This drop is explained by the phase shift

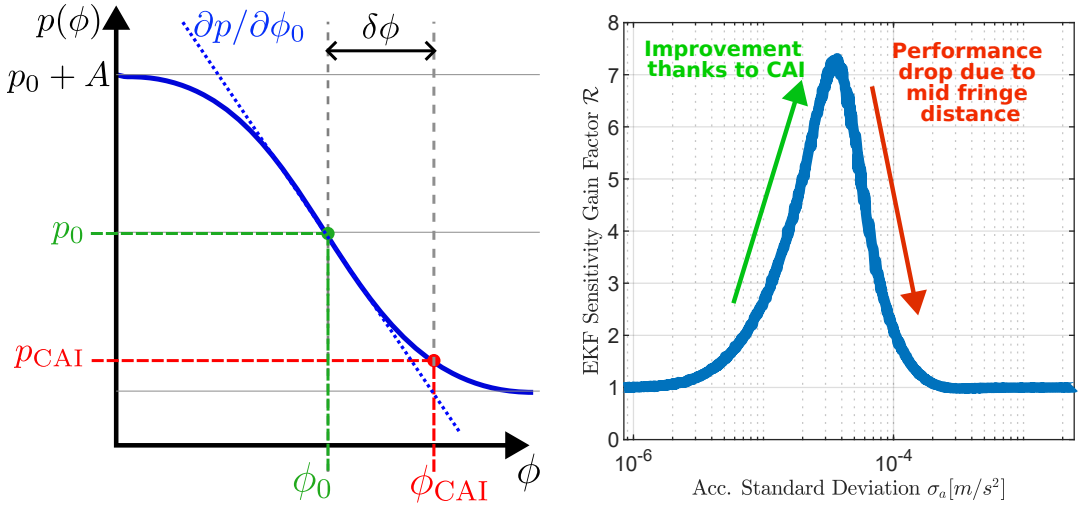

Figure 4.8: Limit of the QINS performance gain. Left: the conventional IMU is used to predict the phase shift of the target interval and the laser phase is adjusted so that the sum of both terms equals $\phi_0 = \pi/2$ (green). The further away the actual observation p_{CAI} (red) is from the mid fringe point, the larger is the error of the linear model assumption $H = \partial p/\partial\phi_0$ in the stochastic model used for the Kalman filter update. Right: the larger the error of the IMU is, the better the sensitivity gain thanks to the EKF. Further increase of the error leads to a drop of sensitivity gain until the target fringe interval is left and no improvement can be achieved anymore.

error $\delta\phi$ approaching the top or bottom of the cosine fringe flank. The distinct performance peak indicates that there is an optimal setting of parameters of the CAI and the uncertainty of the classical sensor. It is highly relevant to understand this behavior in detail, and derive an analytical description of $\mathcal{R}$: It would allow an assessment of the ideal interrogation time of the interferometer for a given accelerometer. Likewise, if the scale factor of the CAI is fixed, maybe due to sensitivity requirements, the ideal classical accelerometer can be identified. The latter might also be interesting from an economical point of view, since a QINS with a lower quality accelerometer can have a similar performance as if a higher quality and perhaps more expensive accelerometer is used which is *too good* for the CAI.

The task at hand can be addressed by finding models for two sub-problems:

1. Model for the improvement of the EKF estimates. The sensitivity gain of the filtered solution for a scalar state can be assessed with the use of the respective steady state

variance P_∞. The following relationship is proposed,

$$\mathcal{R}^2 = \frac{Q}{P_\infty}. \tag{4.99}$$

where Q is the discrete noise variance of the input process affecting that particular state.

2. Model to penalize the accuracy of CAI observations close to top/bottom fringe. For this part, a model is developed which is based on the linearization error occurring close to the top or bottom region of the cosine flank. For this, the measurement uncertainty R is adapted by an additional variance R_{pen},

$$R = \sigma_p^2 + R_{\text{pen}} \tag{4.100}$$

Both models are subsequently applied and discussed for the accelerometer and gyroscope hybridization. The derivation of the penalty model is elaborated in Appendix A.6 extensively. The general steps are the following:

- Derivation of the linearization model of the CAI observation, cf. Appendix A.6.1.
- Propagation of the IMU uncertainty in order to associate an additional observation variance to the distance to the mid fringe operating point due to the RMS of the IMU bias error, cf. Appendix A.6.2.
- Determination of the optimal IMU uncertainty by evaluating the intersection point of the variances of CAI and penalty model.
- Evaluation of the performance gain at the optimal IMU uncertainty.

Optimal Accelerometer Hybridization

For the accelerometer a discrete time white noise variance of σ_a^2 is the input. This can be justified for short interrogation times in which the white noise behavior is clearly dominant, and the process noise Q can be assumed to be consisting of white noise only, so that

$$Q = \sigma_a^2. \tag{4.101}$$

More sophisticated models which include random walk are discussed later on in Sec. 4.4.2. The steady state variance of the filtered accelerations Eq. (4.94) including the penalty model R_{pen} reads

$$P_{a,\infty} = -\frac{1}{2}\sigma_a^2 + \sqrt{\frac{\sigma_a^4}{4} + \frac{\sigma_a^2(\sigma_p^2 + R_{\text{pen}})}{H_a^2}}, \tag{4.102}$$

where

$$H_a = -Ak_{\text{e}}T^2.$$

The derivation of the model for R_{pen} is described in Appendix A.6.3, cf. Eq. (A.75). It is given by,

$$R_{\text{pen}} = \frac{5}{12}A^2(k_{\text{e}}T^2)^6\sigma_a^6. \tag{4.103}$$

The model of the sensitivity gain $\mathcal{R}$ can be stated as

$$\mathcal{R}^2 = \frac{Q_a}{P_{a,\infty}}. \tag{4.104}$$

In order to find the optimal σ_a^* corresponding to the peak of the improvement $\mathcal{R}$, one option is to maximize Eq. (4.104) with respect to σ_a,

$$\max\left\{\mathcal{R}^2 = \frac{\sigma_a^2}{-\frac{1}{2}\sigma_a^2 + \sqrt{\frac{\sigma_a^4}{4} + \frac{\sigma_a^2(R+\frac{5}{12}A^2(k_\mathrm{e}T^2)^6\sigma_a^6)}{H_a^2}}}\right\}. \tag{4.105}$$

As this is analytically cumbersome, a good alternative approximation is to find the intersection point of the CAI variance with the variance of the penalty model in acceleration space, see Fig. 4.9 to get a clearer picture. The optimum appears to coincide with the intersection, which in fact makes sense, as the point in which the uncertainty due to the linearization error is larger than the variance of the CAI observation marks the moment at which the solution should degrade. By setting $R_\mathrm{pen} = \sigma_p^2$, and solving for σ_a, the following optimum σ_a^* can be retrieved,

$$\sigma_a^* = \frac{1}{k_\mathrm{e}T^2}\sqrt[3]{\sqrt{\frac{12}{5}}\frac{\sigma_p}{A}}. \tag{4.106}$$

The empirical results, the model and the optimum are visualized in Fig. 4.10. The detail plot shows that the approximation only leads to a rather small offset from the actual peak.

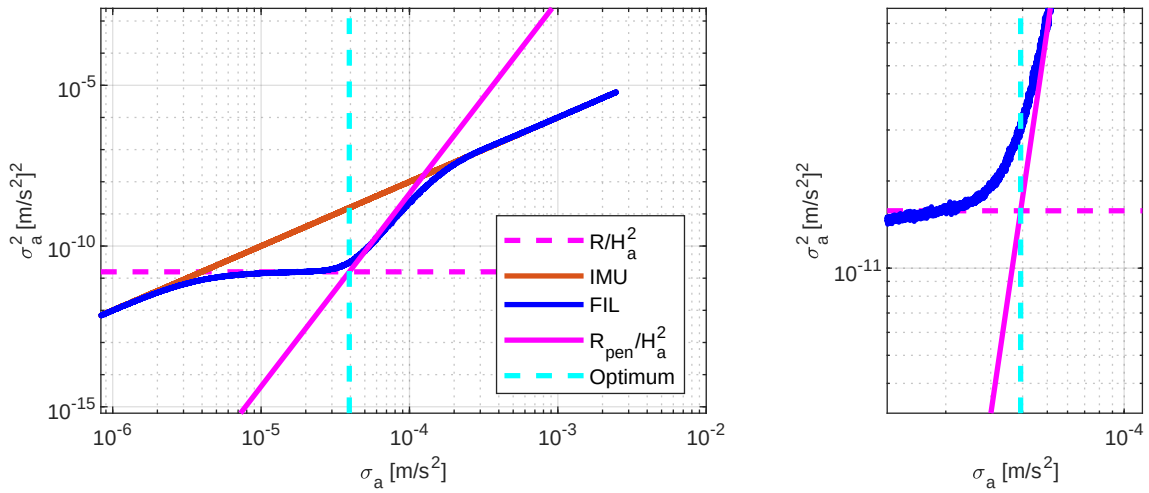

Figure 4.9: Uncertainty of the different QINS components expressed as acceleration variance. CAI parameters: $\sigma_p^2 = 4 \times 10^{-4}$, $T = 25\,\mathrm{ms}$. Red: empirical variance of the accelerations of the MC instances, which directly corresponds to the input standard deviation of the acceleration signal. Blue line: empirical variance of the filtered accelerations. After an initial improvement, the variance converges to the input noise process again due to the distance to the mid fringe operating point. The latter is expressed by the penalty model R_pen (solid magenta line). The CAI variance expressed in acceleration space (dotted magenta line) represents a limit to which the steady state variance of the filtered accelerations (blue line) is converging until the linearization error grows too large. For large values of σ_a, the variance of the filtered state converges to the variance of the input signal again. The optimal accelerometer quality (dotted cyan line) is evaluated at the intersection of the CAI variance and the penalty model. Right: detailed view on the intersection of R_pen and σ_p^2.

Equation (4.106) shows, that all parameters of the interferometer have an impact on the value σ_a^*. The impact of k_e and T^2 is much larger than that of the parameters σ_p and A under the cubic root, which are related to the detection and imaging process of the interferometer. More specifically, the ratio of A/σ_p can also be interpreted as the signal-to-noise ratio (Geiger et al., 2011).

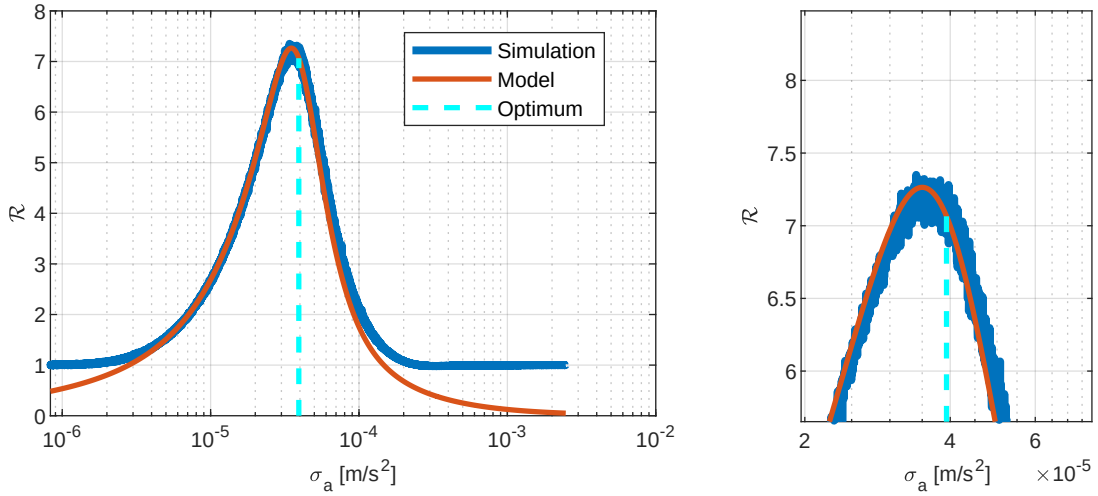

Figure 4.10: QINS sensitivity gain as a function of the accelerometer uncertainty. CAI parameters: $\sigma_p^2 = 4 \times 10^{-4}$, $T = 25\,\text{ms}$. The empirical gain $\mathcal{R}$ is illustrated as blue line, the model as red line. The larger the error of the IMU is, the better the sensitivity gain thanks to the EKF. Further increase of the error leads to a drop of sensitivity gain until the target fringe interval is left and no improvement can be achieved anymore. Right: detailed view on the section around the maximum.

In turn, if one has an accelerometer with noise variance σ_a^2 and momentum transfer defined in k_e, and is interested in a feasible interrogation time T^*, the equation (4.106) can be rearranged,

$$T^* = \sqrt{\frac{1}{k_\text{e}\sigma_a}\sqrt[3]{\sqrt{\frac{12}{5}}\frac{\sigma_p}{A}}}. \tag{4.107}$$

Or, if only the velocity random walk/acceleration white noise density N_a^2 as stated in data sheets is considered,

$$T^* = \left(\frac{\sqrt{2}}{k_\text{e}N_a}\sqrt[3]{\sqrt{\frac{12}{5}}\frac{\sigma_p}{A}}\right)^{2/3}. \tag{4.108}$$

The iNAT-RQT-4003 (iMAR, 2017b), as one example of a navigation grade sensor, yields a white noise density $N_a^2 = (12\frac{\mu g}{\sqrt{Hz}})^2$. Thus, the optimal CAI interrogation time would be as large as $T^* = 4.4\,\text{ms}$, if rotational induced phase shifts and other cross-coupling effects are neglected.

The theoretical improvement of the EKF sensitivity for the optimal value σ_a^* can be assessed by inserting the value into Eq. (4.104). The derivation leads to the following solution for $\mathcal{R}$:

$$\mathcal{R}^2 = \frac{1}{-\frac{1}{2} + \sqrt{\frac{1}{4} + \sqrt[3]{\frac{10}{3}\left(\frac{\sigma_p}{A}\right)^4}}}. \tag{4.109}$$

Or after further McLaurin series expansion and truncation as discussed in Appendix A.6.4,

$$\mathcal{R}^2 \approx 1 + \sqrt[3]{\frac{3}{10}\left(\frac{A}{\sigma_p}\right)^4}. \tag{4.110}$$

The level of improvement is solely defined by the amplitude A and the detection noise σ_p of the interferometer. This is a very important result, as it implies that the length of the interrogation time as well as the momentum transfer are not relevant for the relative improvement of the hybrid solution over the conventional accelerometer. To point out two examples, for an

amplitude of $A = 0.5$ and a CAI noise variance of 4×10^{-4}, the value for the improvement is $\mathcal{R} \approx 7$. This is the improvement that was already illustrated in Fig. 4.10. This value is not affected by a lower interrogation time of $T = 5\,\mathrm{ms}$, as demonstrated in Fig. 4.11. With a sufficiently large preparation time and number of atoms, the uncertainty level of the laser noise with a variance of 1.6×10^{-7} could be reached in a static application, cf. Fig. 4.12. This corresponds to $\mathcal{R} \approx 95$.

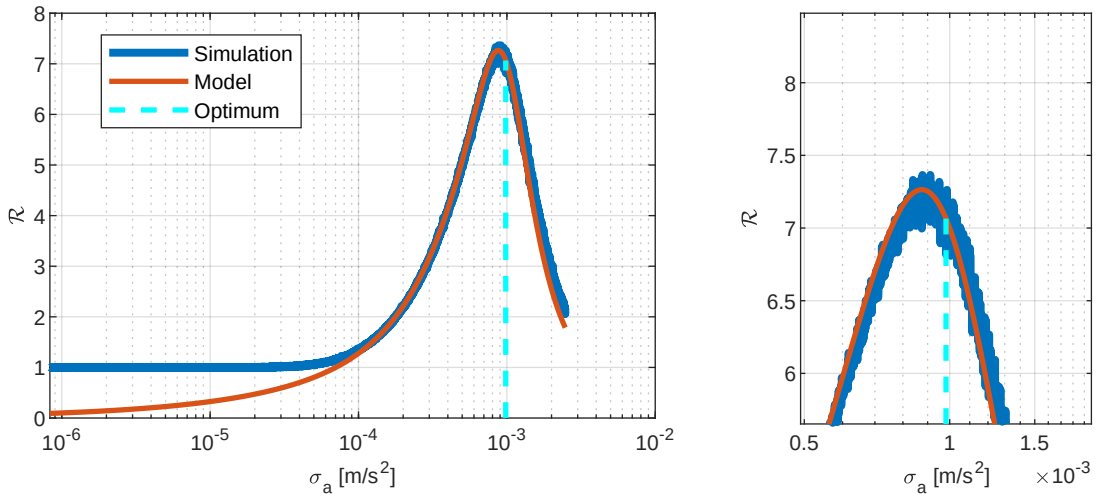

Figure 4.11: Comparison of the empirical sensitivity gain $\mathcal{R}$ (blue) as compared to the model (red). CAI parameters: $\sigma_p^2 = 4 \times 10^{-4}$, $T = 5\,\mathrm{ms}$. Right: detailed view on the section around the maximum.

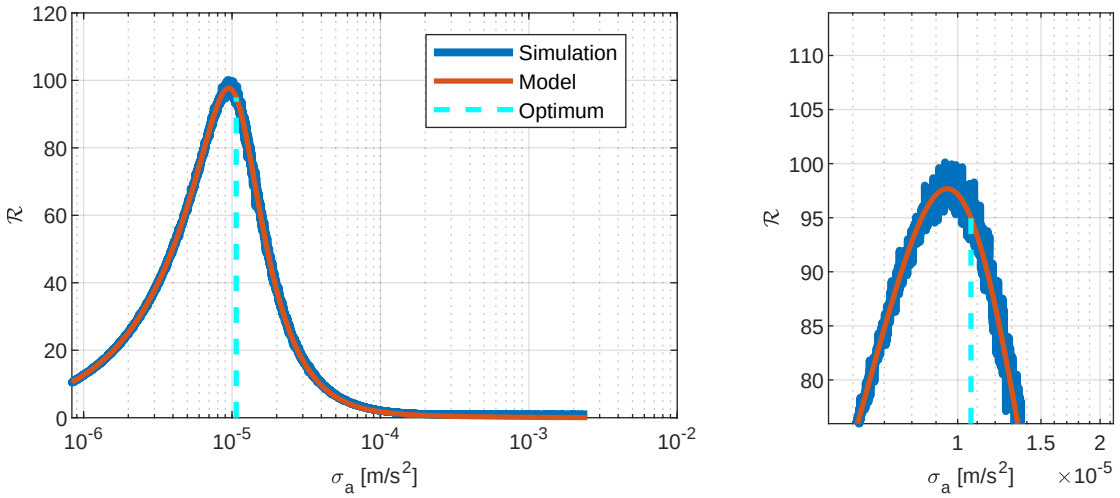

Figure 4.12: Comparison of the empirical sensitivity gain $\mathcal{R}$ (blue) as compared to the model (red). CAI parameters: $\sigma_p^2 = 1.6 \times 10^{-7}$, $T = 25\,\mathrm{ms}$. Right: detailed view on the section around the maximum.

The result in Eq. (4.110) can be used for a quick assessment of the accuracy of the QINS acceleration output. By reformulating Eq. (4.104),

$$P_{a,\infty} = \frac{Q_a}{\mathcal{R}^2}. \tag{4.111}$$

Optimal Gyroscope Hybridization

For the optimization of the gyroscope solution the equations from before can be applied, with the major difference being the scale factor. The observation sensitivity in this case reads

$$H_g = 2Av_{sa}^s k_e T^2. \tag{4.112}$$

The values for the optimal angular rate noise variance σ_g^* of the gyroscope is straightforward, as only the scale factors are changing,

$$\sigma_g^* = \frac{1}{2v_{sa}^s k_e T^2} \sqrt[3]{\sqrt{\frac{12}{5}} \frac{\sigma_p}{A}}, \tag{4.113}$$

which for the chosen parameters of $v_{sa}^s = 94\,\mathrm{mm/s}$ and $T = 25\,\mathrm{ms}$ results in a variance of $2.09 \times 10^{-4}\,\mathrm{rad/s}$, which equals a white noise density of $0.0027\,\mathrm{deg/s/\sqrt{Hz}}$. This corresponds to a typical tactical grade gyroscope.

The corresponding improvement is calculated just as in the acceleration hybridization case,

$$\mathcal{R}^2 = \frac{Q_g}{P_{g,\infty}}. \tag{4.114}$$

After including σ_g^* in Eq. (4.95) and subsequently in Eq. (4.114), the scale factors $2v_{sa}^s k_e T^2$ are canceled out. This results in the same expression as for the accelerations in Eq. (4.109). The interaction between the different components of the model in angular rate space are illustrated in Fig. 4.13. The comparison of the model with the empirical results is expressed in Fig. 4.14.

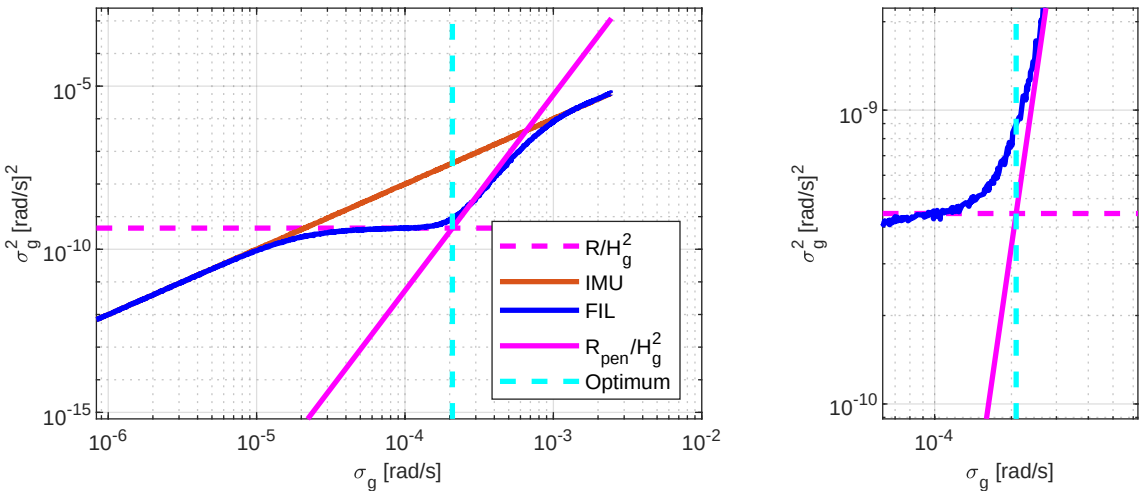

Figure 4.13: Uncertainty of the different QINS components expressed as angular rate variance. CAI parameters: $\sigma_p^2 = 4 \times 10^{-4}$, $T = 25\,\mathrm{ms}$. Red: Empirical variance of the angular rates of the MC instances, which directly corresponds to the input standard deviation of the gyroscope signal. Blue line: empirical variance of the filtered angular rates. After an initial improvement the variance converges to the input noise process again due to the distance to the mid fringe operating point. The latter is expressed by the penalty model R_{pen} (solid magenta line). The CAI variance expressed in angular rate space (dotted magenta line) represents a limit to which the steady state variance of the filtered angular rates (blue line) is converging until the linearization error grows too large. For large values of σ_g, the variance of the filtered state converges to the variance of the input signal again. The optimal gyroscope quality (dotted cyan line) is evaluated at the intersection of the CAI variance and the penalty model. Right: detailed view on the intersection of R_{pen} and σ_p^2.

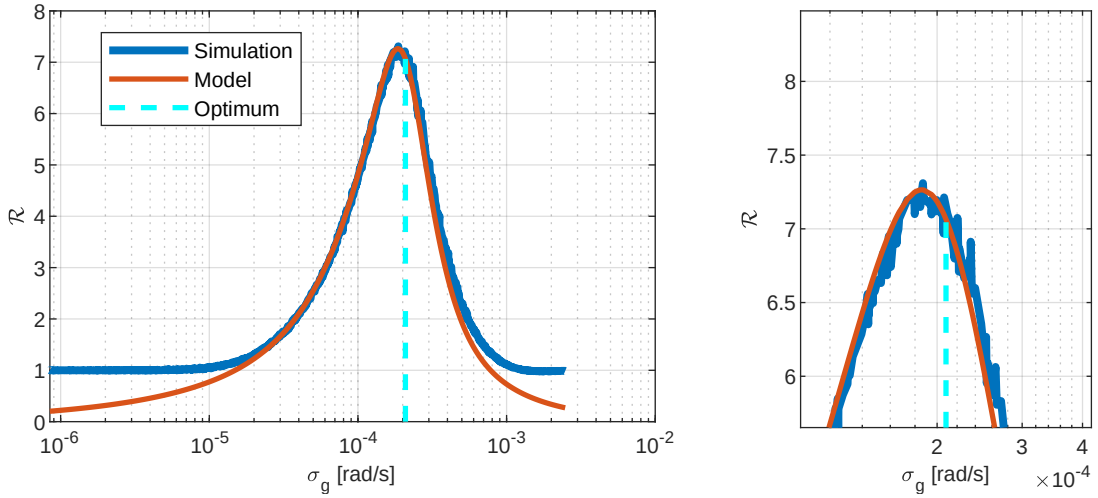

Figure 4.14: QINS sensitivity gain as a function of the gyroscope uncertainty. CAI parameters: $\sigma_p^2 = 4 \times 10^{-4}$, $T = 25\,\text{ms}$, $v_{sa}^s = 94\,\text{mm/s}$. Comparison of the empirical sensitivity gain $\mathcal{R}$ (blue) as compared to the model (red). The larger the error of the IMU is, the better the sensitivity gain thanks to the EKF. Further increase of the error leads to a drop of sensitivity gain until the target fringe interval is left and no improvement can be achieved anymore. Right: detailed view on the section around the maximum.

One open question is how the filtered QINS variance in the optimal configuration is related to the observation noise variance of the CAI. This is relevant for situations in which one is interested in the quality of the QINS in terms of angular rate measurements, if it is only coupled with accelerometers. Let R_a denote the observation variance in acceleration space,

$$R_a = \frac{R}{H_a^2}. \tag{4.115}$$

Then, another ratio $\mathcal{R}_{\text{obs}}^2$ can be defined which relates the steady state variance with the CAI observation variance,

$$\mathcal{R}_{\text{obs}}^2 = \frac{P_{a,\infty}}{R_a} = \frac{Q_a}{\mathcal{R}^2 R_a}. \tag{4.116}$$

This ratio is a mere placeholder. It is the same for accelerations and angular rates, consequently it can be stated that

$$\mathcal{R}_{\text{obs}}^2 = \frac{P_{a,\infty}}{R_a} = \frac{P_{g,\infty}}{R_g}, \tag{4.117}$$

where R_g is the CAI observation variance expressed in angular rate space. The performance of the angular rate output of the QINS is given by

$$P_{g,\infty} = \frac{R_g}{R_a} P_{a,\infty} = \frac{H_a^2}{H_g^2} P_{a,\infty} = \frac{1}{4(v_{sa}^s)^2} P_{a,\infty}. \tag{4.118}$$

Discussion

This section leaves several important implications: First, the level of noise that a classical accelerometer and/or gyroscope can have in order to work with an atom interferometer with certain settings. The parameters k_e and T have the largest impact on that. Second, the order of magnitude of the improvement can be assessed. Here, the amplitude A and the observation noise σ_p of the CAI are the defining factors.

The observation noise could theoretically be reduced with a larger number of atoms. In a static setting without perturbations it could be as low as the quantum projection noise limit of

the CAI. This means, that with a larger number of atoms and thus longer preparation times, the relative improvement can be enhanced until the technical noise floor due to laser phase fluctuations is reached. In the experiment of Gouët et al. (2008), the observation noise of the CAI was limited by the laser phase noise with a variance at a level of 1.6×10^{-7}.

The requirements for the quality of classical sensors that were derived can be seen as a foundation for future QINS designs. It has to be stressed that the model was developed on the base of an acceleration on a single axis. Applications to a three dimensional case might introduce axis cross-coupling and similar effects that were not considered. Also, the averaging of the input acceleration signal in Eq. (4.98), which was applied in order to enable an analytical solution, could stand in conflict with the actual trajectory, as averaging or any other means of filtering the data comes with a loss of certain information about the actual dynamics. Thus, the model for the improvement of sensitivity is representing the ideal case scenario, providing a general idea about the potential sensitivity of the QINS.

4.4.2 Impact of Dead Times

The real acceleration data as gained from an IMU including the uncertainties are a continuous process. The CAI on the other hand does in general need some time per measurement cycle to prepare the atoms, in which the interferometer is not sensitive, while the readout process covers some time as well in which the interferometer is blind. As the error of the IMU with respect to the latest bias estimate is growing during this dead times, and the latter can be as large as 10 times the interrogation time, this raises two important questions:

1. How long can the dead time between CAI measurements last, before the phase shift error induced by bias errors grows beyond the reciprocal region of the cosine flank;
2. How does the dead time affect the sensitivity of the CAI and the QINS?

Maximum Dead Time

The timeline of a CAI measurement cycle as introduced in Eq. (3.13) is extended by an additional time T_{inactive} which resembles a systematic, but potentially varying time between the CAI cycles as due to dynamic maneuvers in which the measurement needs to be discarded, or due to a sequential 6DOF operation mode. The total time T_{total} between the ends of two subsequent CAI measurement cycles is

$$T_{\text{total}} = T_{\text{prep}} + T_{\text{f}} + T_{\text{det}} + T_{\text{inactive}}, \tag{4.119}$$

where $T_{\text{f}} = 2T$ is the duration of the atom travel including the individual interrogation pulses.

The evaluation of the optimum solution for the noise densities in the sections before can be enhanced by the knowledge of the complete noise processes. Inertial measurement units are often characterized by power law noise processes. In order to keep the degree of freedom reasonably low, let the time discrete process noise Q be composed of a white noise process with power spectral density (PSD) N^2, an acceleration random walk with PSD K^2, as well as a bias fluctuation with variance B^2. The variance of the white noise process, resembling the mere measurement accuracy of the IMU, can be reduced during the interrogation interval, since it scales with $\sim 1/t$ over the active measuring time. Thus, the time frame $t \in [0; 2T]$ of the corresponding CAI measurement is relevant here. On the other hand, let the acceleration random walk process result from external factors like a change of temperature. This causes

the difference between both systems to grow over the course of T_{total}. Q then reads

$$Q = \frac{N^2}{2T} + K^2 T_{\text{total}} + B^2, \tag{4.120}$$

where $\frac{N^2}{2T}$ is the white noise variance corresponding to a band-limitation of the white noise PSD N^2 for the course of a measurement, $K^2 T_{\text{total}}$ is the white noise variance of the integrated random walk process, and B^2 the variance corresponding to the flicker noise floor.

The dead time $T_{\text{d}} = T_{\text{prep}} + T_{\text{det}} + T_{\text{inactive}}$ is the interesting quantity now. During this time, an error in the acceleration of the IMU is accumulated, driven mainly by the random walk process. The acceleration difference leads to a phase uncertainty with variance $\sigma_\phi^2 = \sigma_a^2 (k_{\text{e}} T^2)^2$, which can be expressed as

$$\sigma_\phi^2 = \left(N^2 \frac{1}{2T} + K^2 T_{\text{total}} + B^2 \right) (k_{\text{e}} T^2)^2. \tag{4.121}$$

By demanding that $\sigma_\phi \leq \frac{\pi}{2}$, the equation can be solved for the time T_{total}:

$$T_{\text{total}} \leq \frac{\frac{\pi^2}{4} - (N^2 \frac{1}{2T} + B^2)(k_{\text{e}} T^2)^2}{K^2 (k_{\text{e}} T^2)^2}. \tag{4.122}$$

Note that the value computed by Eq. (4.122) is based on the 1-σ value of the accumulated phase uncertainty. For a more robust assessment, the value could be divided by a safety factor.

Two inertial measurement unit accelerometers of different quality are considered: A navigation grade sensor with the noise characteristics $N_{\text{nav}} = 12 \times 10^{-5}\,\text{m/s}^{3/2}$, $B_{\text{nav}} = 4 \times 10^{-5}\,\text{m/s}^2$ and $K_{\text{nav}} = 1.1 \times 10^{-5}\,\text{m/s}^{5/2}$, as well as a tactical grade MEMS sensor with $N_{\text{tac}} = 50 \times 10^{-5}\,\text{m/s}^{3/2}$, $B_{\text{tac}} = 2 \times 10^{-4}\,\text{m/s}^2$ and $K_{\text{tac}} = 6.7 \times 10^{-5}\,\text{m/s}^{5/2}$. The CAI interrogation time is $T = 10\,\text{ms}$. In Fig. 4.15 the phase shift error resulting from the noise processes is illustrated. It is differentiated between the total error, the impact of the white noise processes and the impact of the random walk processes.

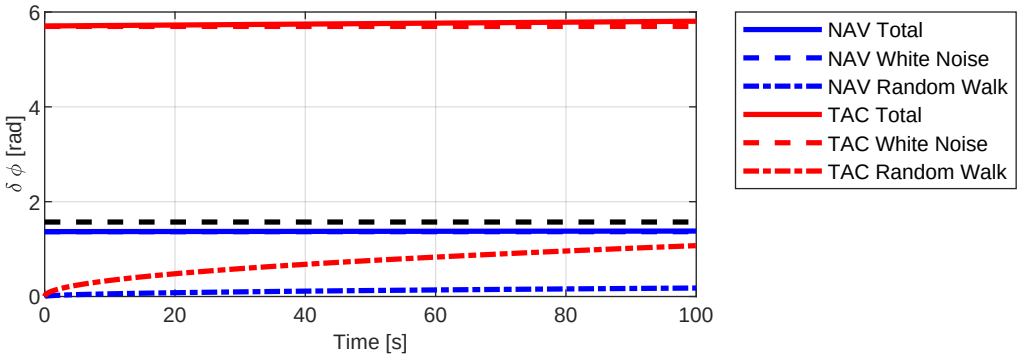

Figure 4.15: Impact of integrated noise on the phase shift error $\delta\phi$ during CAI dead time for tactical grade (TAC, red lines) and navigation grade IMU (NAV, blue lines). The individual processes contributing to the total phase shift error are expressed by different line styles.

The first observation is that the white noise clearly has the largest impact on the resulting phase shift error. The phase shift error resulting from the white noise of the navigation grade accelerometer is just below the $\pi/2$ threshold, while the corresponding phase shift error of the tactical grade accelerometer is far beyond the limit. The phase shift error caused by random walk only slowly grows over time. While the drift of the navigation grade accelerometers is small enough, the phase shift error due to the MEMS approaches the $\pi/2$ line comparably fast. It still does not transgress the limit in the time of 100 s that is considered, here.

This study shows that in the frame of hybridization, the consideration of dead times is mostly relevant for high drift sensors like OMR or piezoelectric devices. For most conventional IMU, the white noise density yields the larger limitation. Limiting the analysis to the noise characteristics of single axis acceleration data, even if it is the major impact source for a single sensitive axis, only conveys a rough idea about the increase of the phase shift error during the dead times. Additional systematic effects and axis cross coupling depend on the specific implementation of the QINS and need to be carefully considered in applications where longer outages of CAI are to be expected.

QINS Long-Term Noise Characteristics

It was mentioned before that the steady state variance in Eq. (4.94) is only valid for stationary noise processes, meaning that neither the observation noise variance R nor the accelerometer noise Q_a is allowed to be time-varying. However, it is an interesting question, how the hybrid solution behaves for longer time periods. Recall the steady state solution $P_{a,\infty}$, stated for (very) large values of $Q_a \gg R$,

$$\lim_{Q_a \to \infty} P_{a,\infty} = \lim_{Q_a \to \infty} -\frac{Q_a}{2} + \sqrt{\frac{Q_a^2}{4} + \frac{Q_a R}{H_a^2}} = \frac{R}{H_a^2}. \tag{4.123}$$

This result is apparent in Fig. 4.9, where the value for $P_{a,\infty}$ converges to $\frac{R}{H_a^2}$ before the linearization error is taking effect. This fraction resembles the variance of the CAI observation, expressed in accelerometer space. However, it was demonstrated that the variance of the filtered acceleration does not exactly reach this limit and is rather represented by the sensitivity gain $\mathcal{R}$ from Eq. (4.110).

One further aspect that needs clarification is the impact T_d has on the resulting variance of the QINS. In the presence of dead times, the following approximation for the accuracy on a certain axis can be used,

$$Q_\mathrm{QINS} = \alpha P_\infty + \beta Q_\mathrm{IMU}. \tag{4.124}$$

The weight factors α and β are based on the ratio of dead time T_d and active measurement time T_f,

$$\alpha = \frac{T_\mathrm{f}}{T_\mathrm{d} + T_\mathrm{f}}, \qquad \beta = \frac{T_\mathrm{d}}{T_\mathrm{d} + T_\mathrm{f}}. \tag{4.125}$$

In order to avoid the explicit computation of P_∞, the equation can also be reformulated, if $\mathcal{R}$ is solved for P_∞,

$$P_\infty = \frac{Q_a}{\mathcal{R}^2}, \tag{4.126}$$

and inserted in Eq. (4.124):

$$Q_\mathrm{QINS} = Q_\mathrm{IMU} \left(\frac{\alpha}{\mathcal{R}^2} + \beta \right). \tag{4.127}$$

This equation can be used to assess the long-term uncertainty of the QINS. As $\mathcal{R}$ is a function of the CAI observation uncertainty, also model extensions like random walk could be included in the latter. Note that Eq. (4.127) applies to either accelerometer or gyroscope data, as the sensitivity gain factor in the optimal configuration is independent of the sensor type.

4.4.3 Conclusion

In the previous sections, models have been introduced to assess the optimal configuration of CAI and classical sensors on the example of accelerometer and gyroscope hybridization. It

was demonstrated that several degrees of freedom are present in form of different parameters of the CAI and the noise processes of the classical sensors. Concerning the question how an optimal configuration of classical accelerometers and gyroscopes in conjunction with the CAI parameters should look like, it is safe to say: it depends.

The situation gets even more complicated in real world applications, because the spatial distance between the sensors needs additional consideration. This introduces several effects that are depending on the dynamics of the trajectory. The studies using the error state kinematics of the atom wave packet in the sensor frame already included a bias error that corresponds to the standard deviation of the VRW and ARW according to Eqs. (4.106) and (4.113). There it was shown that, at least for the trajectories discussed in the frame of this thesis, the lever arm has a minor impact.

As a major takeaway it can be stated that accelerometers constitute the more severe limitation. The requirements for gyroscopes are comparably relaxed. Here, the effects due to lever arms are negligible and the accuracy requirements are low enough so even some tactical grade gyroscopes are valid for hybridization. In turn, this even means that in order to achieve a noticeable reduction in noise level of the hybrid angular rate measurement of high-quality classical gyroscopes, the required CAI scale factor would exceed the level of any classical accelerometer that is available up to date.

Consequently, the search for the optimal CAI/IMU configuration can be reduced to the accelerometers alone. After the optimal configuration of accelerometers and CAI parameters is found, the gyroscopes of the chosen IMU need to be *good enough*, i.e. the white noise variance due to ARW has to be well below the value of Eq. (4.113). This value was already declared problematic before, because of the non-constant atom velocity. Thus, it should only be used as a rough guess of the upper limit, rather than a sound recommendation.

4.5 Performance Evaluation and Discussion

So far, the theory behind the hybridization concept has been presented. The AtoS as a method for the prediction step, as well as the EKF for the bias correction were introduced and some further aspects like stability and state vector augmentations were elaborated in detail. Furthermore, the choice of optimal parameters for the hybridization was discussed.

In this section, some dedicated simulation results are presented which are used to verify the hybridization concept and some of the hypotheses that have been stated. Since the Monte Carlo simulations are computationally rather demanding, the simulated maneuvers are designed as long and simple as needed.

The goals of the upcoming, first group of low level performance studies are:

- Transfer of the findings from the studies for the optimal configuration to the 6-DOF case.
- Validation of the extended model for the EKF CAI observation variance, including the linearization error.
- Discussion of the impact of a present lever arm and misalignment in the basic state vector configuration of the EKF.
- Evaluating the impact of dead times on the solution.

Ultimately, a set of statements about the accuracy of the QINS solution under stationary conditions will be formulated, which will further help to create a base of understanding for

a final dynamic scenario. In the latter, the focus lies on further aspects like cross-coupling between different sensor axes, which is mainly caused by the addition of a lever arm and misalignment between the classical IMU and the CAI. This will further underline the effects that have already been laid out in Sec. 4.3.2. Additionally, the working procedure of the EKF in the basic state vector configuration, i.e. when only acceleration and angular rate biases are included, is demonstrated.

An additional intention of these **low level** performance studies is to justify some of the assumptions that are made for the second group of **high level** simulation studies. Those are based on the error state navigation differential equations from Sec. 2.6 and allow a comparison and discussion of different QINS sensor settings.

4.5.1 Low Level Performance Studies

The first part of the simulation studies is based on *MATLAB* scripts in which the IMU navigation computer, CAI signal generator and EKF according to the equations in the prior Chaps. 2 - 4 are implemented. This allows for detailed studies on the behavior of the QINS in the light of different maneuvers and sensor settings. The reference trajectories are given as time series of specific forces $\mathbf{f}_{ib}^{b}$ and angular rates $\boldsymbol{\omega}_{ib}^{b}$ in the b-frame.

The single processing steps follow the pattern as illustrated in Fig. 4.1. The kinematic state is computed by the navigation solution from Sec. 2.3. The prediction of the atomic states and the phase shift is based on Sec. 3.4, and the EKF is applied as described in Sec. 4.2. The initial conditions and settings for IMU and CAI are stated in the beginning of the individual scenario.

Static Scenario

As a first step, the findings of the optimal combination of CAI and IMU from Sec. 4.4.1 are now tested in the simulation framework. The scenario, labeled NoMotion, is generated which includes roughly four seconds of IMU noise only. The white noise density of the accelerometers is always set according to the optimum defined by the CAI parameters. Additionally, a random walk process is included, which raises the phase shift error into the region above the optimal operation point. For a fair comparison with the analytical study in Sec. 4.4.1, the acceleration and angular rate signals are averaged for each observation interval before the phase shift is evaluated for each axis individually according to the first two terms of Eq. (3.53).

Two different cases are now considered. The first one without dead times, the second one including a dead time of $T_{\mathrm{d}} = 200\,\mathrm{ms}$. The atom flight time of the CAI measurements yields $T_{\mathrm{f}} = 0.05\,\mathrm{s}$, the IMU data rate is equal to $200\,\mathrm{Hz}$. The variance of the CAI observation yields $\sigma_p^2 = 4 \times 10^{-4}$. The white noise variance σ_a^2 of the acceleration noise is set according to the optimum as in Eq. (4.106) and corresponds to a noise density of $N_a = 8.9 \times 10^{-6}\,\mathrm{m/s^{3/2}}$. The noise density of the gyroscopes is set equal to $N_g = 1.45 \times 10^{-6}\,\mathrm{rad/s^{1/2}}$. An additional random walk process is added to the accelerometers and gyroscopes, with input white noise amplitude spectral density of $K_a = 2 \times 10^{-5}\,\mathrm{m/s^{5/2}}$ and $K_g = 2 \times 10^{-5}\,\mathrm{rad/s^{3/2}}$, respectively, on all axes. A total number of 200 MC samples are processed.

Fig. 4.16 shows the results of the empirical standard deviation (STD) for all six sensor axes, as computed from the scatter of the single MC solutions. First to notice is the reduction of the overall uncertainty by a factor of above five for the acceleration uncertainty on all three axes. This is in accordance with the theoretical sensitivity gain that was assessed in Sec. 4.4.1. The IMU acceleration uncertainty is furthermore affected by an increase in time caused by

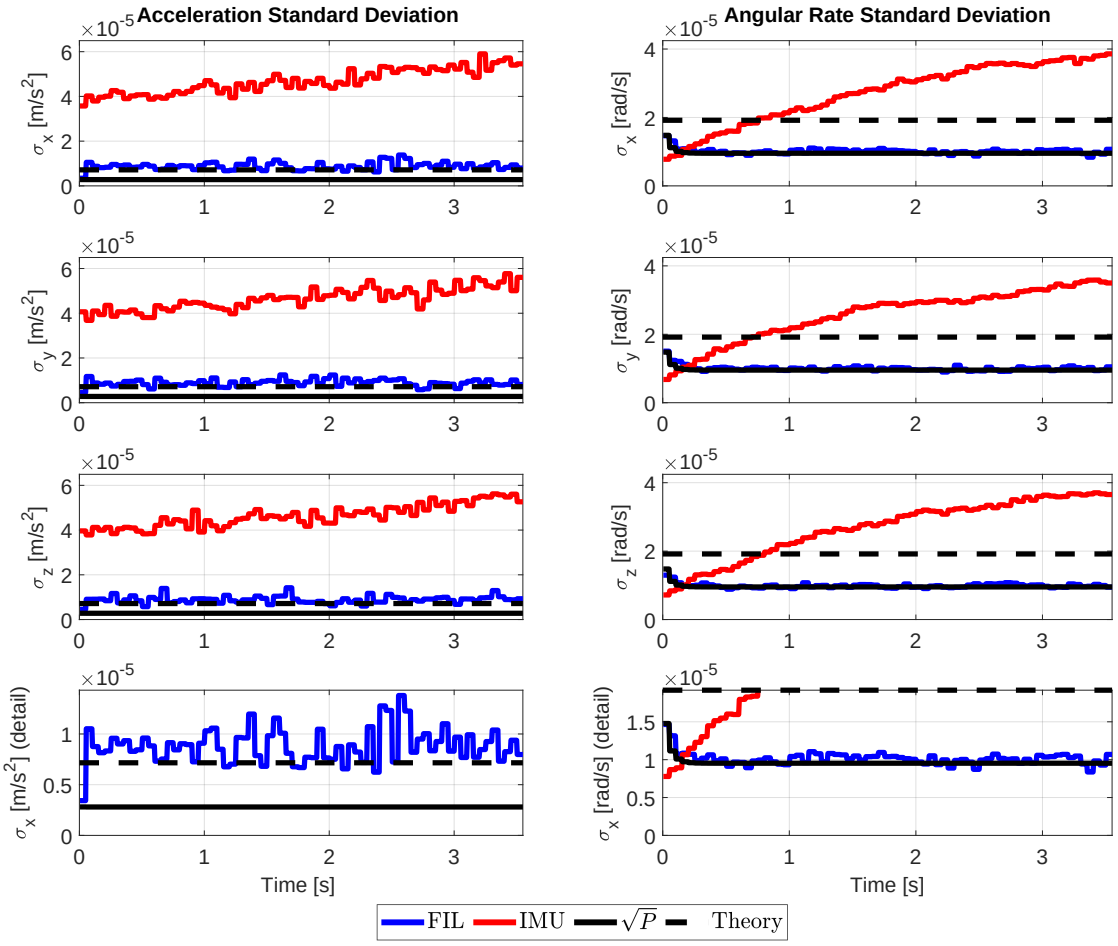

Figure 4.16: Standard deviation of the estimated acceleration and angular rate bias in the NoMotion scenario. The phase shift is predicted with the correlation method. Blue and red represent the scatter of the QINS and IMU signals, respectively. Black is the standard deviation as assessed from the square root of the respective state covariance matrix entry. Dotted black is the theoretical QINS signal standard deviation including the penalty model.

the random walk process. This drift is successfully compensated with the help of the CAI, which causes the uncertainty of the filtered signal to stay at a constant magnitude over the course of the scenario.

The growing uncertainty of the gyroscope signal caused by the random walk is suppressed as well. The filtered solution assumes the accuracy level of the CAI and the standard deviation estimate of the EKF coincides with the empirical standard deviation. In this case, the estimate including the penalty model is larger than the empirical variance. The reason for this rather pessimistic assessment is that the model for the observation variances,

$$\tilde{R} = R + R_{\text{pen}},$$

can only be applied to the CAI observation itself, which is of course used for both the observation of the gyroscope biases as well as the accelerometer biases. It will always be dominated by the sensor with the largest uncertainty, and thus it represents a worst case scenario. In this case, the gyroscope uncertainty is far below the level of the acceleration uncertainty, expressed in CAI observation space.

Fig. 4.17 shows the results for a dead time of 200 ms. During the preparation time there is no obvious difference between the IMU signal and the filtered signal for both, the accelerations

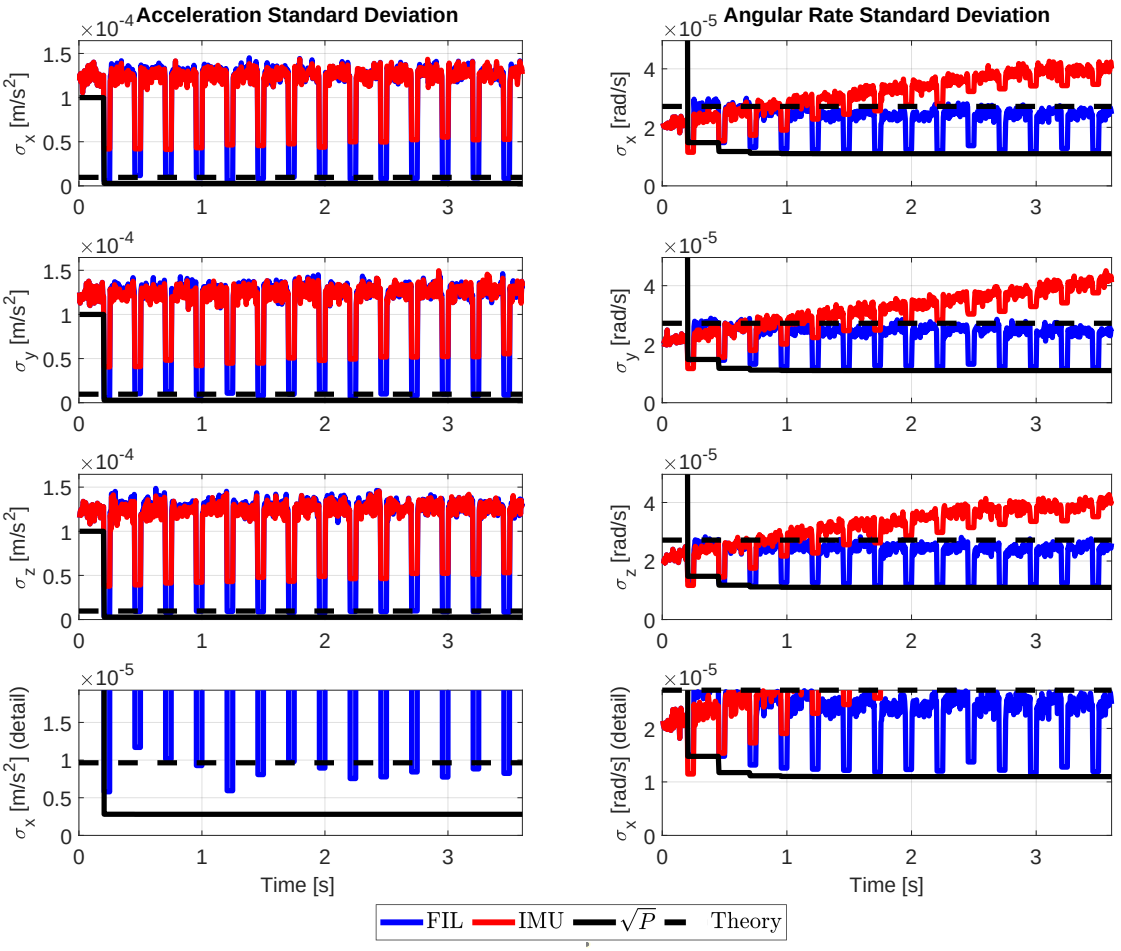

Figure 4.17: Estimated acceleration and angular rate bias in the NoMotion scenario with a dead time of 200 ms between CAI measurements. Blue and red represent the scatter of the QINS and IMU signals, respectively. Black is the standard deviation as assessed from the square root of the respective state covariance matrix entry. Dotted black is the theoretical QINS signal standard deviation including the penalty model.

and angular rates. The CAI measurement intervals that cover a time of 50 ms every 200 ms are illustrated by the empirical standard deviation according to the length of the CAI measurement interval, which explains the systematic ditches in the STD at those times. The IMU is treated in the same way in order to allow comparison of the results. The filtered signal yields a largely reduced uncertainty compared with the IMU signal. For the accelerations it is at the level of the analytically assessed theoretical sensitivity value, as can be seen in the *detail* plot of Fig. 4.17. The empirical STD of the angular rates, like in the scenario without dead times, comply with the STD from the state covariances produced by the EKF. Note that after some time when the long periodic drift of the IMU signal is apparent, the EKF is able to remove those parts of the signal. This shows that the filtered signal is improved during the preparation time intervals as well, which is in line with the discussions about the dead times in Sec. 4.4.2, where it was stated that the QINS works as long as the drift between the signals does not exceed the ambiguity limit posed by the CAI fringe pattern period.

It is further worth to mention that the question whether the IMU data should be averaged before being used for the phase shift prediction in order to improve the sensitivity gain, is losing its importance in the light of longer dead times, as the improvement in shot-by-shot sensitivity is only achieved for a fraction of the total time.

Dynamic Scenario

This second scenario is motivated by the question about how the QINS would behave when applied in a realistic, dynamic trajectory. The simulated trajectory is based on actual dynamic measurements recorded by different inertial measurement units in experiments where a car was used as platform (Weddig et al., 2022). The angular rates and accelerations are depicted in Fig. 4.18. The trajectory features an initial phase in almost stationary conditions with minor vibrations during the first ten seconds, followed by larger vibrations on all axes with a forward acceleration from second 10 to 15 and a deceleration on the same axis from second 15 to 20. The trajectory is concluded with an s-shaped curve between second 20 and 30, with a large spike of the signals on multiple axes occurring right after second 25.

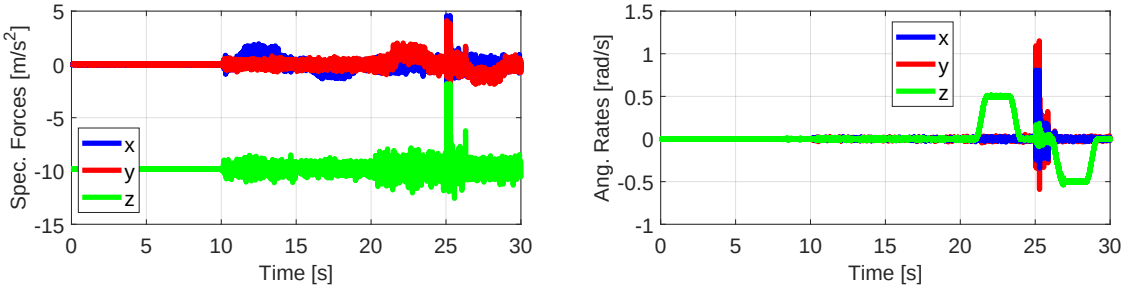

Figure 4.18: Simulated dynamic scenario. Left: simulated specific forces. Right: simulated angular rates.

Regarding the sensor settings, the same parameters of IMU and CAI are applied as in the NoMotion scenario from before. The dead time of CAI is 100 ms. The random walk in the accelerations and angular rates measured by the IMU is kept at a high level in order to illustrate the ability of the QINS to remove long-term drifts and systematic error effects better. Additionally, a lever arm between the CAI and the IMU body frame is applied in $\mathbf{b}_1$-direction, $x_{bs}^b = [3, 0, 0]$ m. The phase shift is evaluated with the AtoS method, meaning that the QINS is expected to be able to resolve the changing dynamics with the data rate of the IMU. A certain degree of cross-talk between the sensor axes due to noise and the dynamics is to be expected. This time, the stochastic model for the CAI observation in the EKF, and thus the standard deviation as gained from the main diagonal of $\mathbf{P}$, already includes the penalty model from Sec. 4.4.1, so that no further differentiation is needed. The scenario is evaluated for two different cases: with and without a misalignment between CAI and IMU.

The first setting illuminates the impact of a lever arm on the QINS solution. In Fig. 4.19, the empirical standard deviation of the accelerations and angular rates for this setting are depicted. Starting with the angular rates first, the empirical STD of the filtered solution is in good agreement with the STD gained from the EKF. Besides the jumps between the dead times and the CAI update, which are not visible because of the density of data in time, it stays at a constant magnitude while the STD of the IMU is growing over time as caused by the random walk process. There is no visible effect of the lever arm, which stands in line with the theoretical model. The transformation of angular rates on rigid body-fixed systems is not depending on the position of the sensing element on the rotating frame, any location on the same rigid rotating platform experiences the same angular rate. This is fully embodied in Eq. (4.7), where the angular rates are only transformed by the multiplication with $\mathbf{C}_b^s$.

Regarding the accelerations, there is a number of different interesting effects visible. First of all, the STD of the filtered accelerations is considerably larger than the one produced by the EKF, even with the penalty model included. This can be explained by a violation of the requirements that were stated for the closed solution of the steady state variances in Sec. 4.4.1. More specifically: the assumption that there are no correlations between individual

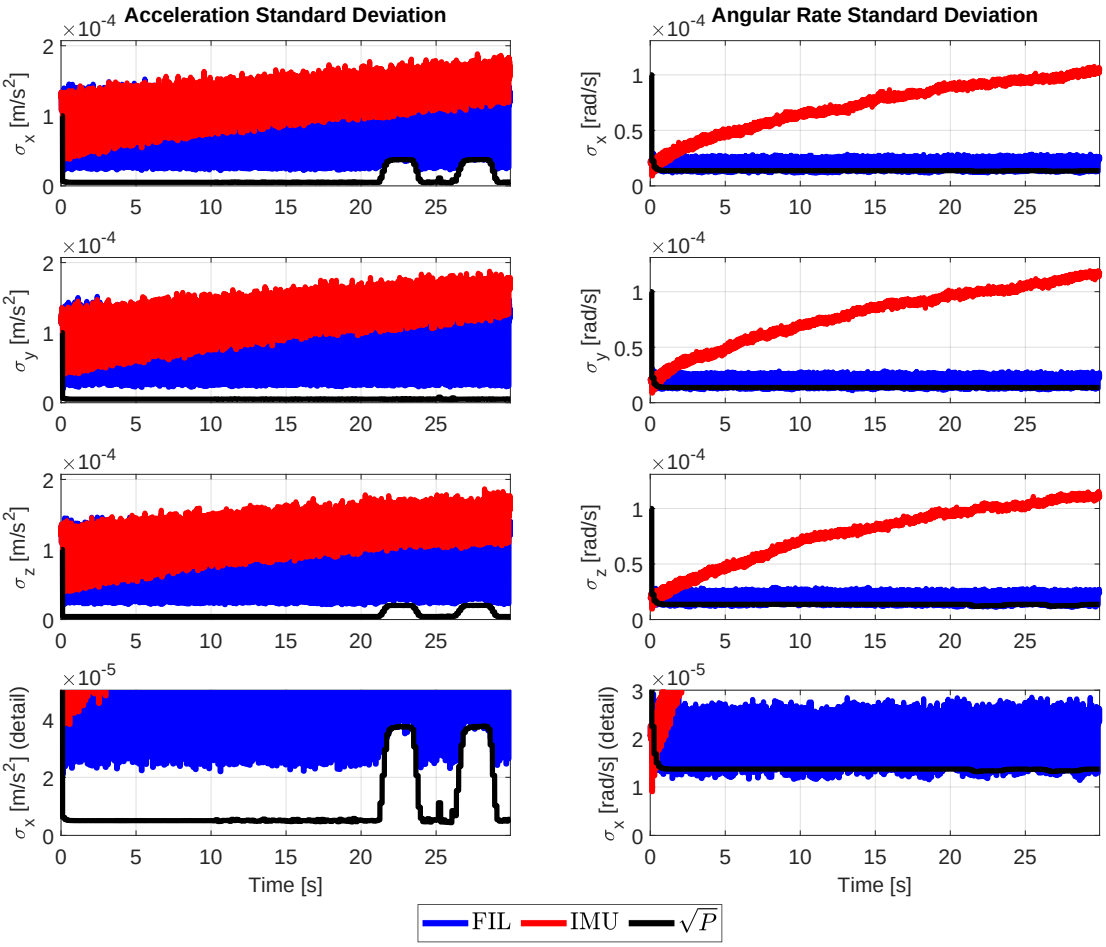

Figure 4.19: Standard deviation of the estimated bias in a dynamic scenario without misalignment. Depicted are the standard deviations of the IMU signals (red) and the filtered signals (blue). The black line indicates the QINS standard deviation including the penalty model.

states. Since the AtoS uses data from all sensor axes in order to predict the phase shift on a single CAI axis, there are clearly correlations present. The comparably large empirical STD of the filtered accelerations is the result of noise processes of essentially *all* IMU sensor axes, culminating in a phase shift error that is very likely exceeding the optimum stated in Sec. 4.4.1, ultimately leading to a sub-optimal EKF update. This problem could be tackled by a numerical solution of the complete Riccati equation from Eq. (4.89). It is, however, an open question whether analytical solutions exist.

At the S-curve between seconds 20 and 25 there is a clear systematic effect visible which is caused by the lever arm. Just like discussed in Sec. 4.3.2, the lever arm in x-direction mainly affects the phase shift error in x-direction, and to a less degree in z-direction. Subsequently this impacts the acceleration bias estimate on those two axes and consequently the filtered acceleration signal. The detail view in Fig. 4.19 furthermore shows that the STD produced by the EKF represents the empirical STD of the filtered signal quite well again during the time of the maneuver, which shows that the magnitude of the uncertainties overshadows the effect of the combined stationary white noise processes of the single IMU axes on the corresponding phase shift error. Interestingly, the spike in the trajectory signals at 25 s has only a very small effect on the uncertainty. It is mainly visible in the filtered accelerations in x-direction, caused

by the increase of the angular rates in z-direction. The y- and z-direction are barely sensitive to this effect.

In Fig. 4.20, the velocity and attitude errors of the mean process of the MC samples w.r.t. the reference trajectory in the n-frame are illustrated. After initial convergence of the EKF, the velocity error of each single axis of the QINS solution is reduced by about an order of magnitude, as compared to the IMU solution. The velocity errors in x- and y-direction are considerably larger than in z-direction for IMU and QINS alike, resulting from the trajectory being mostly planar. The final velocity error of the QINS yields 1×10^{-2} m/s horizontally and 1×10^{-4} m/s vertically at 30 s.

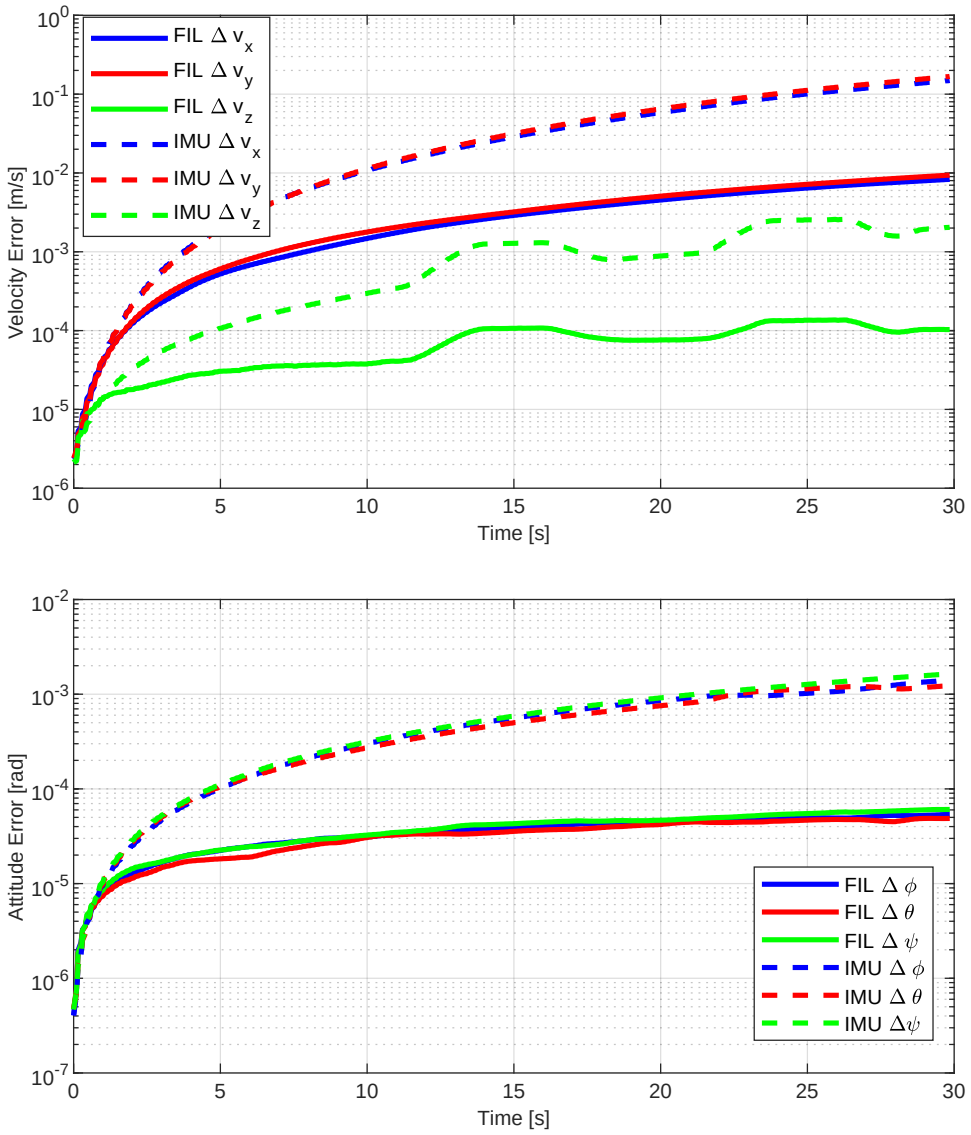

Figure 4.20: Dynamic scenario: mean velocity and attitude errors of the MC samples w.r.t. the reference trajectory in the n-frame. Bold lines: QINS filtered solution. Dotted lines: classical IMU solution.

Systematic effects caused by the lever arm are not really visible. The small systematic changes of the filtered velocity error in z-direction after 12 s coincide with the accelerations on the x- and y-axis and can be related to the computation scheme for the platform kinematic state. They are independent from the lever arm and the QINS. This result complies with the discussion in Sec. 4.3.2, where the limit for the lever arm for the given settings was determined

at 7 m. Note that the 3 m that are set in this scenario are already unrealistically large, as most implementations will see the IMU placed right next to the CAI sensor frame. Consequently, the lever arm is not a particular limitation for QINS design. The attitude error shows a similar improvement of over an order of magnitude as the velocity. At 30 s, the error is about 5×10^{-5} rad on all three axes. As expected, no impact of the lever arm is visible.

The second setting includes an additional, presumably unknown, misalignment γ_b^s of 30 µrad on all three axes. This value is notably larger than the 15 µrad that were stated as the limit in the first theoretical assessment in Sec. 4.3.2. Looking at the STD of the filtered acceleration in Fig. 4.21, the solution seems to be unaffected by the misalignment.

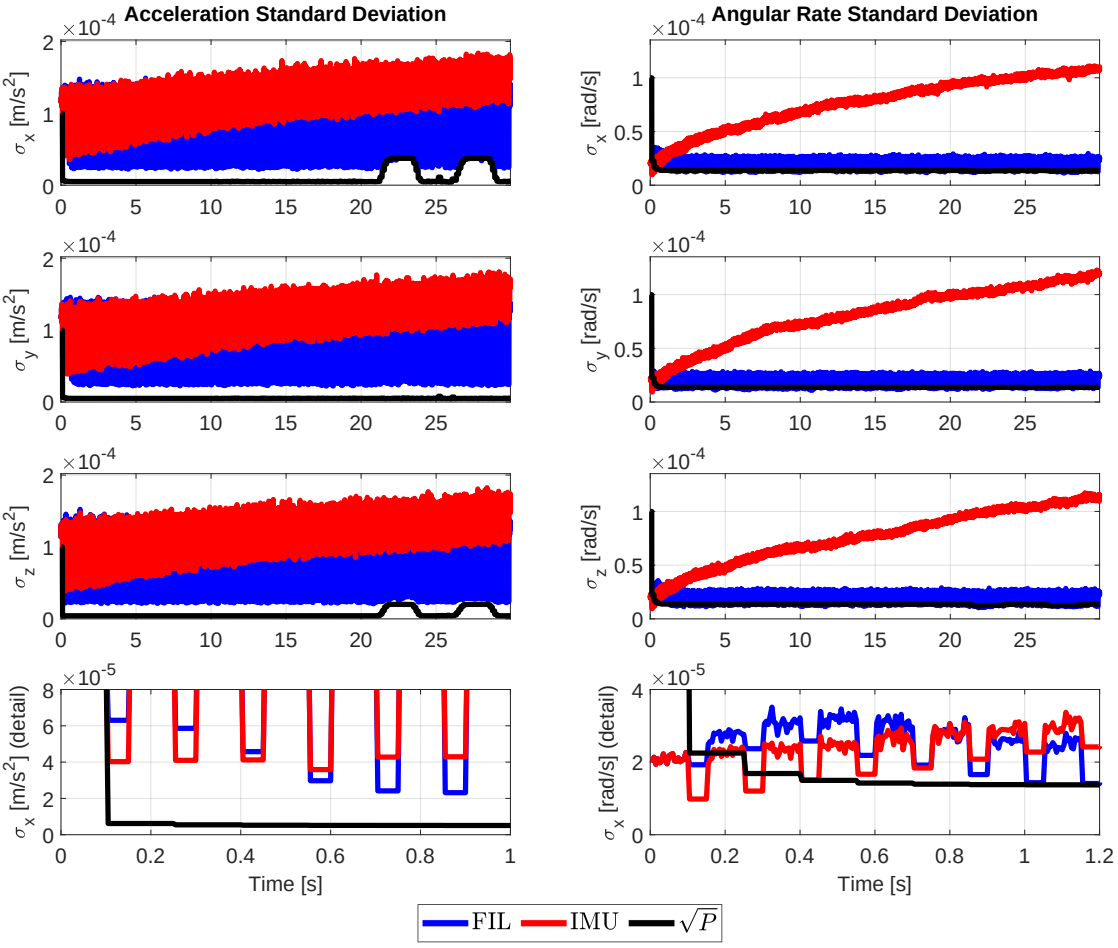

Figure 4.21: Standard deviation of the estimated bias in a dynamic scenario with misalignment. Depicted are the standard deviations of the IMU signals (red) and the filtered signals (blue). The black line indicates the QINS standard deviation including the penalty model. While the peaks in the acceleration bias at 22.5 and 27.5 seconds are similar to the case without misalignment, a large decline of the accuracy in the gyroscope biases in x- and z-direction during the first few filter steps at less than one second is visible.

This is not entirely true, as the detailed view in x-direction clearly shows. During the first few EKF updates, there is a large decline in accuracy of the filtered signals. The solution stabilizes after about 0.8 s, when the STD reaches a level that compares to the scenario without the misalignment. The same effect can be seen in the filtered accelerations on the y-axis as well. Both can be explained by the large magnitude of the gravity vector which stands perpendicular to both axes. The inclination angles due to the misalignment are projecting the gravity vector on those two axes, introducing a phase shift error. Following the observability results from

Sec. 4.3.3, the phase shift error on a specific axis is directly related to the estimated acceleration bias on the same axis. Consequently, the filtered accelerations in x- and y-direction are directly affected. A similar effect can be seen in the STD of the filtered angular rates. Here, the phase shift errors $\delta\phi_x$ and $\delta\phi_y$ are directly affecting the observations of the angular rate bias in z- and x-direction. This is, again, right according to the observability analysis. The initial decline in accuracy can also be seen in the velocity and attitude errors in Fig. 4.22, where the velocity error of the filtered solution in x- and y-direction jumps to about 1×10^{-4} m/s before it stabilizes and follows the same pattern as in the setting without the misalignment. This applies to the attitude errors as well which, aside from the initial increase in the roll φ and pitch angle θ, show the same behavior as in the case without misalignment.

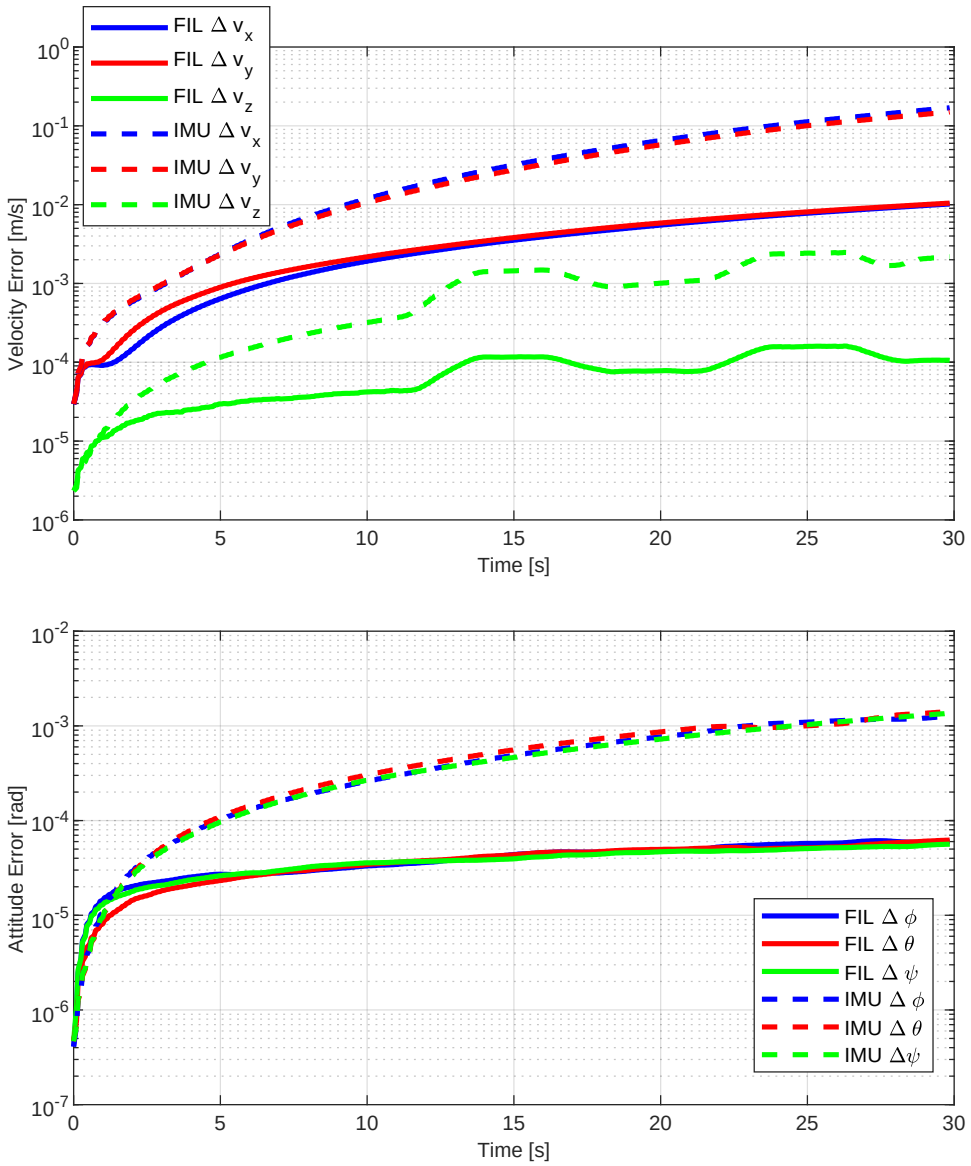

Figure 4.22: Dynamic scenario: mean velocity and attitude errors of the MC samples w.r.t. the reference trajectory in the n-frame with misalignment between CAI and IMU. Bold lines: QINS filtered solution. Dotted lines: classical IMU solution.

This example demonstrates that the basic configuration of the EKF works quite well even for unknown systematic error sources like the misalignment. The reason the system converges is that the parts of the gravity vector that are projected to the observable axes are essentially treated as a bias, partially in the angular rates and partially in the accelerations. The mis-

alignment is thus effectively compensated by the bias states. One word of caution has to be stated: in this leveled scenario with almost zero inclination with respect to the n-frame this works quite well, as the error introduced by the projection of the gravity vector to the horizontal axes stays nearly constant over the course of the whole trajectory. In cases of very large changes of acceleration, or a considerable larger roll or pitch angle, this particular error term is not constant anymore and might lead to a loss of the tracked phase shift error. As in this scenario it was already demonstrated that for accelerations as large as 1 g the compensation works well, it can be expected that the largest problem for QINS design is still the magnitude of the unknown misalignment.

4.5.2 High Level QINS Performance

The studies before showed that if all the necessary conditions are met, i.e.

- CAI is able to physically resolve the dynamics of the trajectory, meaning that rotations and accelerations are not too large according to the requirements in Sec. 3.5,
- CAI and IMU parameters are designed or chosen according to the requirements stated in Sec. 4.4.1, i.e. the integrated noise of the classical sensors does not exceed the limits posed by the CAI fringe ambiguity,
- the dead time of CAI can be bridged by the IMU without losing track of the phase shift error which might occur at $|\delta\phi| \geq \pi/2$, or ultimately will occur at $|\delta\phi| \geq \pi$,

the EKF in the minimum configuration converges well, and the hybrid quantum navigation system is fully functional. Furthermore, the corrected accelerations and angular rates essentially allow to treat the QINS just as any other classical IMU for higher level navigation systems or performance studies. From this high level system integration perspective, the QINS as combination of IMU and CAI can thus be considered as a single entity, producing inertial measurements at the data rate of the classical sensors that are used for the hybridization.

The simplified model for strapdown navigation error kinematics as presented in Chap. 2 is used again here, meaning that the impact of an acceleration error in the North channel, as well as the angular rate error in the East and Down channel is defined as perturbation input to the system, and their respective impact on the total position error on the $\mathbf{n}_1$-axis is computed. As before, all sensors as well as the body frame are assumed to be aligned with the n-frame. This is done in order to exclude additional and particular nasty effects from the attitude representation, to clearly point out the differences between the sensors and to focus the discussion on those aspects. The resulting positioning accuracy can be seen as a benchmark to compare the different QINS designs. They might give a hint about the order of magnitude of the accuracy of a QINS, but should by no means be taken as reliable indicators for actual performance.

The input noise processes for the accelerations and angular rates are composed of white noise of the respective sensor of the classical IMU. An additional bias stability is added which corresponds to the CAI standard deviation limit of $\sigma^2_{lpn} = 1.6 \times 10^{-7}$, as defined by the laser phase noise (Gouët et al., 2008), expressed as acceleration and angular rate by the corresponding scale factor.

Comparison between IMU and CAI

As a first step, the navigation solution based on an entirely CAI-based sensor, assuming it is able to resolve the dynamics of the trajectory, is compared to a classical navigation grade

IMU (iMAR, 2017b) equipped with force-feedback accelerometers and RLG. The CAI has an effective wave number of $k_\mathrm{e} = 4\pi/780\,\mathrm{nm}^{-1}$, an interrogation time of $T = 10\,\mathrm{ms}$, as well as an initial atomic drift velocity of $v_{sa}^s = 94\,\mathrm{mm/s}$. The sensor is assumed to be measuring on all axes at the same time. The preparation and readout times are combined in a dead time of $T_\mathrm{d} = 100\,\mathrm{ms}$. The observation uncertainty per shot is $\sigma_p^2 = 4 \times 10^{-4}$. Those settings are also applied to any upcoming CAI in this section, unless stated otherwise.

In Fig. 4.23 the North position error is visualized based on the different error sources, namely the accelerometer in $\mathbf{n}_1$-direction, as well as the gyroscopes in $\mathbf{n}_2$- and $\mathbf{n}_3$-direction. For the accelerometer, velocity random walk, initial bias uncertainty and an acceleration random walk process is included. The angular rates are modeled with an angular random walk and an initial bias uncertainty. That being said, the performance of the IMU is essentially the same as in the example shown in Fig. 2.11, but in double logarithmic representation. The modulation of the Schuler loop is clearly visible especially in the portions of the position error caused by the East angular rate uncertainty and North acceleration uncertainty. The latter is in fact mostly bounded and only a long-term increase that scales with $\sim t^{0.5}$ is visible, as discussed in Sec. 2.6. The CAI on the other hand shows some interesting properties. The

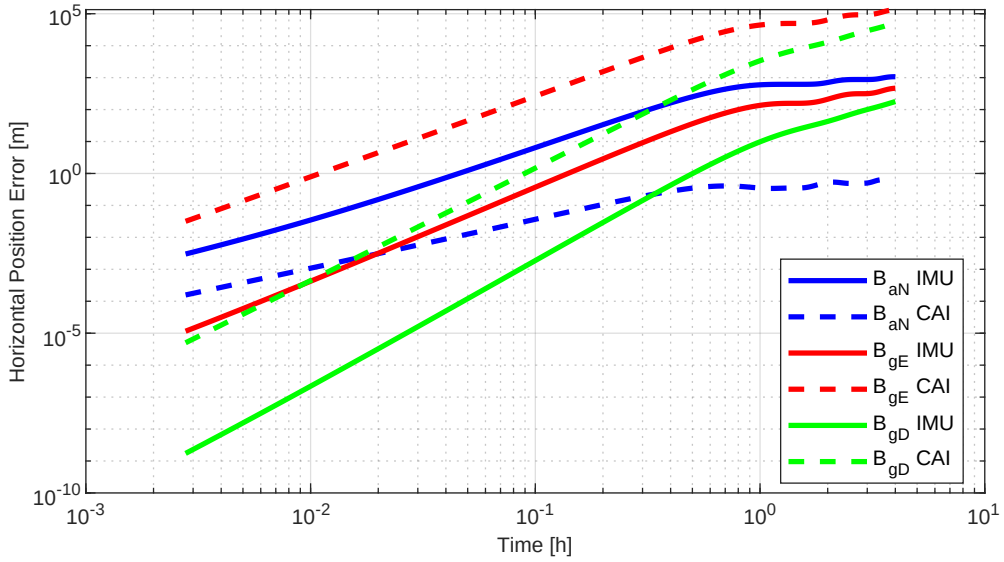

Figure 4.23: Position drift of a navigation grade IMU compared to a CAI. The position errors (here: North) of a strapdown navigation solution in a terrestrial setting based on a classical navigation grade IMU (bold lines) and CAI only (dotted lines) are compared. The impact of the acceleration error on the position error is depicted in blue. The impact of an inclination (red) and heading (green) gyroscope error is shown as well.

position error caused by the acceleration uncertainty is largely reduced. In fact, even after one hour of navigation, the error is well below one meter. Contrary to that, the comparably lower sensitivity of the CAI to angular rates leads to a degradation of the performance as compared to the classical RLG. Long before the CAI solution profits from the improved long-term stability, the horizontal position error already reaches a level of several tens of thousands of meters, which renders the overall solution inferior to that of the navigation grade IMU. This comparison demonstrates that the CAI could be a superior inertial sensor, but its sensitivity to angular rates is a bottleneck that prevents it from being utilized as *complete* inertial measurement unit. The major adjustment parameter that is independent from the acceleration sensitivity and the trade-offs that were already widely discussed, is the initial drift velocity of the atoms. Larger values would improve the sensitivity in a direct proportional manner, and thus reduce the position error caused by the integrated angular rate uncertainty.

On the other hand, higher velocities would demand larger space in the vacuum chamber, so this is another design discussion that would exceed the frame of this thesis.

Comparison of different QINS Designs

In order to design a complete QINS, a long list of different decisions has to be tackled. While the most important topics have been covered in the previous chapters, they all have been stated under the premise that a QINS consists of a 6DOF classical IMU and a 6DOF CAI. There is another option especially relevant for gravimetry, where only accelerometers (seismometers, OMR) are used for the ambiguity solution in order to enable the CAI measurement. Most of the algorithms developed so far can also be applied here, but there is a difference in the assessment of the sensitivity of the QINS, since no continuous measurement is available. In order to include the CAI dead time for a case in which hybridization is only used to make the CAI measurement work, the measurement is only covering a fraction of the time. The resulting variance $Q_{\text{QINS-C}}$ under consideration of the dead time T_d and flight time T_f reads:

$$Q_{\text{QINS-C}} = \frac{T_\text{d} + T_\text{f}}{T_\text{f}} Q_{\text{CAI}}. \tag{4.128}$$

The schematics of the two QINS designs are illustrated in Fig. 4.24. Each follows a different objective:

- **QINS-C (1)**: **C**AI based with classical sensor support. This is a design that is mainly proposed by the physics community. The goal is to apply conventional accelerometers to measure high frequency vibrations of the retroreflective mirror which defines the inertial reference of the frame. The scatter of this vibration spans several fringe intervals, so a complete pattern can be assessed by measuring the vibrations with the accelerometer. For this reason, small high sensitivity sensors like piezoelectric accelerometers or OMR (Gerberding et al., 2015) are very convenient and easy to be implemented directly on the mirror. The downside is the large drift of this type of classical sensor, which consequently needs to be reduced, e.g. by applying bandpass filters. This has the additional advantage of drastically reducing the systematic errors like misalignment and initial bias between the systems, but leads to a limited bandwidth of the QINS, as systematic changes of the accelerations lead to an additional offset between the null-fringe and the predicted phase shift. Consequently, this sensor design is mainly supposed to work for stationary maneuvers, in conjunction with canceling any unwanted effects, either by a stabilized platform or rotation compensation.
- **QINS-I (2)**: **I**MU based with CAI support. This is the combination of three classical accelerometers and gyroscopes with the CAI, proposed as a solution to navigation problems in this thesis. The mirror is assumed to be fixed to the sensor frame, and the accelerations and rotations of the frame are measured by a classical IMU. For the accelerometers, navigation grade high accuracy force-feedback sensors with sufficient long-term stability are chosen. The gyroscopes are FOG in the upper end of the navigation grade spectrum. For actual performance values please refer to Honeywell (2020) and Cordova et al. (1996), respectively. This design is an all-rounder and can be applied to most scenarios, as long as the dynamics do not exceed the hard-limit of the CAI. It has to be stressed that the combination of IMU with CAI demands very precise calibration in terms of lever arm and sensor alignment, as a small misalignment in the face of gravity can already cause a loss of the target fringe.

For the two different QINS designs, the following computation steps are necessary in order to derive the parameters as they are stated in Tab. 4.3:

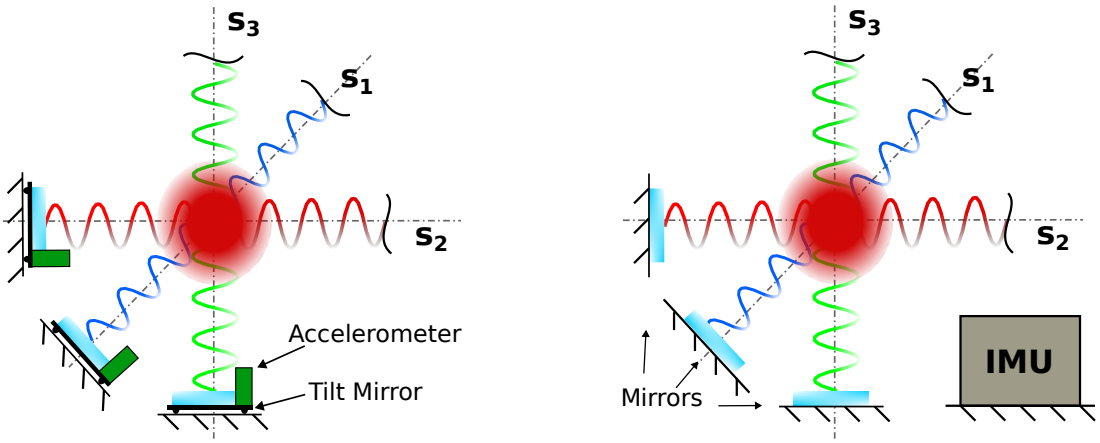

Figure 4.24: Schematics of different QINS designs. Left: QINS-C with tilt mirrors and accelerometers attached. Right: QINS-I with fixed mirrors and a complete inertial measurement unit. The axes of the sensor frame are indicated by $\mathbf{s}_1, \mathbf{s}_2$ and $\mathbf{s}_3$. The laser systems are not depicted.

1. Definition of the CAI parameters (not including T) and the noise density of the classical accelerometer.
2. Computation of the optimal T for the chosen parameters according to Eq. (4.108).
3. Computation of the sensitivity gain factor $\mathcal{R}^2$ according to Eq. (4.110).
4. Computation of the steady state variances for accelerations and angular rates based on Eqs. (4.111) and (4.118).
5. Inclusion of dead times in the assessed values. Two different cases occur, depending on the QINS design:
   - QINS-C: Computation based on Eq. (4.128).
   - QINS-I: Computation based on Eq. (4.124).
6. Expression of the QINS variances as noise densities under the knowledge of T from step 2.

The bias stabilities of QINS-C are assessed by transforming the laser phase noise variance 1.6×10^{-7} with the corresponding scale factors into the respective acceleration and angular rate representation. The noise values of the gyroscope of QINS-I are based on the classical gyroscope, as the noise of the CAI in that combination is an order of magnitude larger.

The performance of those two settings, in terms of horizontal position error, is shown in Fig. 4.25. The impact of the acceleration error on the position error is visualized secluded from the total error. The following should be noted from the classical IMU, first. The position error due to the accelerometer uncertainty dominates the solution up to the point where the Schuler oscillation reaches its maximum at exactly 42.2 minutes. Afterwards, the error due to acceleration bias does only marginally grow in magnitude since it is bounded by the oscillation. The total error after that point in time mainly grows due to the impact of the gyroscope uncertainty. It is apparent that the gyroscopes and accelerometers that are integrated in this IMU are optimally adapted to each other, and a well-rounded sensor system is the result. A gyroscope of better quality would not improve the solution in the initial time frame at all.

The QINS design 1 yields the best sensitivity to accelerations. However, the comparably lower scale factor for rotations leads to the result that the overall performance cannot profit

Design	(1) QINS-C	(2) QINS-I
Continuous Solution	no	yes
Data Rate	low, defined by CAI	high, defined by IMU
Bandwidth	limited	large
System Calibration	easy	complex
Classical Acc	OMR (Gerberding et al., 2015)	Q-Flex (Honeywell, 2020)
White Noise N [m/s^2/$\sqrt{\text{Hz}}$]	$1 \cdot 10^{-6}$	$7 \cdot 10^{-6}$
Bias B [m/s^2]	≈ 0 (high pass filtered)	$2 \cdot 10^{-6}$
Classical Gyro	none	IFOG (Cordova et al., 1996)
White Noise N [rad/s/$\sqrt{\text{Hz}}$]	-	$2.618 \cdot 10^{-7}$
Bias B [rad/s]	-	$4.363 \cdot 10^{-9}$
CAI Parameters		
k_e	$32\pi/780\,\text{nm}$	$4\pi/780\,\text{nm}$
T	26.6 ms	29.1 ms
v_{sa}^s	94 mm/s	94 mm/s
T_d	100 ms	100 ms
QINS Acc		
White Noise N [m/s^2/$\sqrt{\text{Hz}}$]	$2.401 \cdot 10^{-7}$	$5.598 \cdot 10^{-6}$
Bias B [m/s^2]	$8.762 \cdot 10^{-9}$	$5.867 \cdot 10^{-8}$
QINS Gyro		
White Noise N [rad/s/$\sqrt{\text{Hz}}$]	$1.277 \cdot 10^{-6}$	$2.618 \cdot 10^{-7}$
Bias B [rad/s]	$4.661 \cdot 10^{-8}$	$4.363 \cdot 10^{-9}$

Table 4.3: Parameters and attributes of two different QINS design approaches.

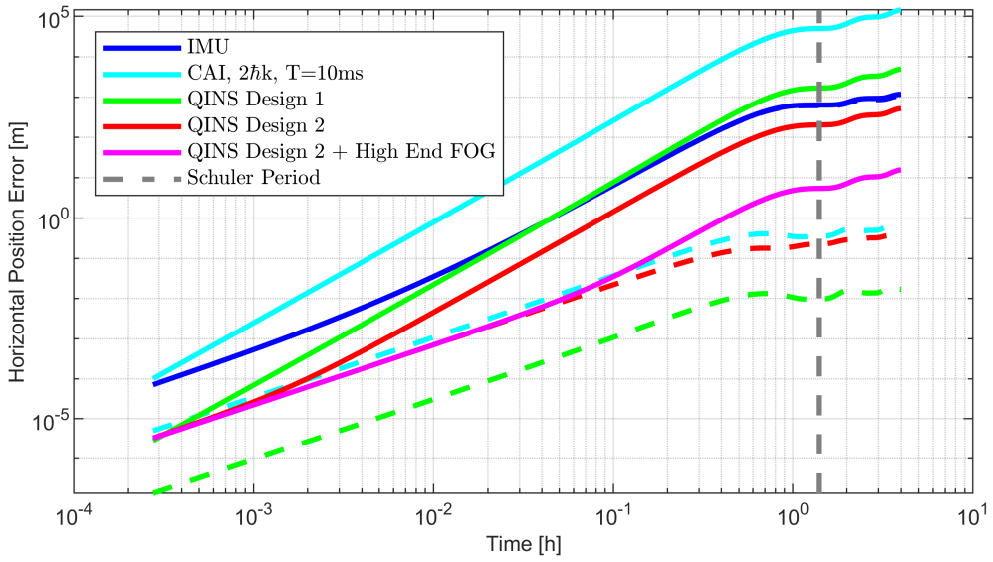

Figure 4.25: Position drift of different QINS implementations. The position error in North direction is compared for different QINS designs in double logarithmic representation. The impact of the acceleration errors on the position error is depicted as dotted line, while the total error is depicted as bold line. For a comparison, the iNAT RQT as navigation grade IMU (blue) is included again, as well as the CAI from Fig. 4.23 (cyan). Magenta is representing the performance of design 2 with a current high end gyroscope replacing the navigation grade FOG.

from the high accuracy of the accelerations at all. In the end, design 1 reaches a positioning accuracy roughly at the same order of magnitude as the classical IMU. The QINS design 2 is already closer in its core to a well-rounded integrated sensor system. The sensitivity

to accelerations is lower than that of design 1 by a factor of almost 10, but thanks to the navigation grade FOG, the overall performance is much better. As it is visible in the first few seconds, the overall solution can even profit from the improved acceleration sensitivity. The horizontal position error after an hour of navigation is well below 200 meters. If the gyroscope in this configuration is replaced by one of the current high end strategic grade gadgets (Mead & Mosor, 2020) with $N_g = 4.654 \times 10^{-9}\,\mathrm{rad/s}/\sqrt{\mathrm{Hz}}$ and $B_g = 1.454 \times 10^{-10}\,\mathrm{rad/s}$, the error can be further reduced. Horizontal position errors of below 10 meters after one hour of navigation could be possible.

5
Experimental Applications

In Chap. 3 the atom interferometer was presented as an inertial sensor, with its advantages and special characteristics. The measurement of the cold atom interferometer (CAI) was introduced as a transition probability of an atom wave packet between two entangled momentum states, or rather, paths. This transition probability depends on the phase difference between the paths, and can be modeled by a sinusoidal function with amplitude A and offset p_0, which were, so far, assumed to be known and constant.

The goals of this chapter are twofold: After shortly summarizing the data set that was used, a method to estimate the parameters of the fringe pattern is presented first. This method is based on a least-squares method (Koch, 1999), which allows a parametrization of the observation model. The second goal is a demonstration of the hybridization method. For both purposes, a data set from an actual CAI prototype (Richardson et al., 2020) is used.

5.1 Introduction

5.1.1 ATLAS Data Set

The *ATLAS* data set (Richardson et al., 2020) in use was kindly provided by the IQO Quantum Sensing group of Ernst Rasel. For the duration of almost one full day, data of a single-axis atom interferometer were recorded in a static laboratory environment. The data set was recorded with the goal in mind to validate the coupling of the interferometer with a novel prototype of an opto-mechanical resonator (OMR). The classical accelerometer (Nanometrics inc., 2023) was merely a reference for the accelerations. The use of this data set has several implications that need to be stated. Namely:

- The data recording of all three sensors was triggered by an automatic script. The timestamps however were not recorded. For the CAI shots, timestamps of the time of creation of the files in the Windows file system are available. This allows for sorting the CAI measurement shots, but accurate variance propagation *between* subsequent CAI measurements is not possible. The raw data of the Titan is available in chunks of 60.03 ms each, sampled around the center pulse of the interferometer. Since the CAI measurement time is 20.03 ms, a subset of 2003 data values is corresponding to each CAI shot.
- CAI has a single sensitive axis and acceleration data were only recorded for this one axis, cf. Fig. 5.1.
- No calibration of the distance or alignment between the accelerometer and CAI exists.

- No offset in the laser phase is applied, meaning that a mid fringe feedback control is not possible.

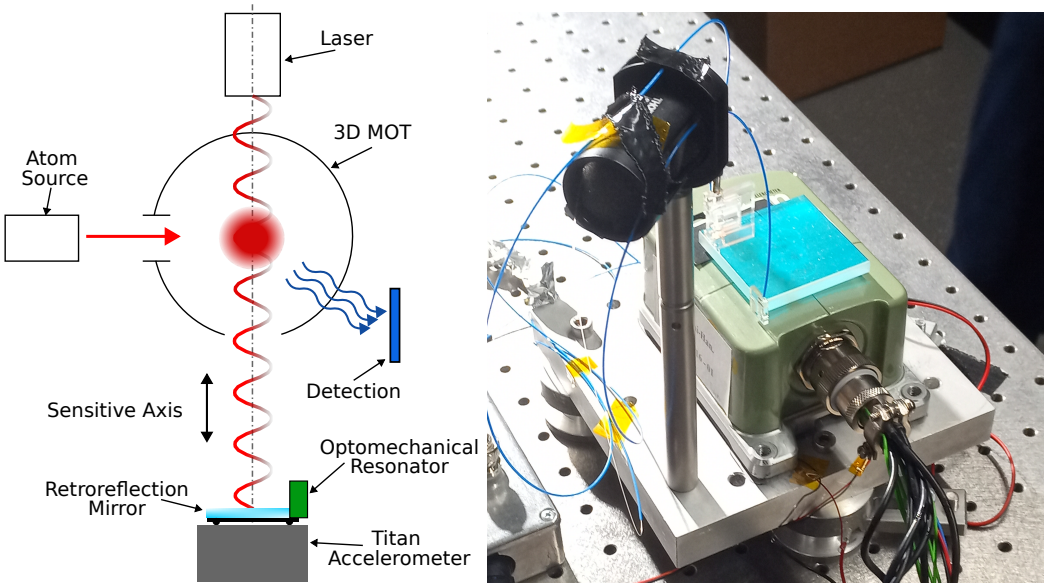

Figure 5.1: ATLAS experimental assembly. Left: sketch of the schematics. The Titan accelerometer is placed directly under the retroreflection mirror. The detection of the photons after the interferometer sequence is realized by a photo diode (blue box). No seismic attenuation is applied. Right: remaining parts of the assembly without vacuum system, atomic source and interrogation laser. Visible are the mirror and OMR placed on the Titan accelerometer, as well as parts of the detection opto-electronics.

For these reasons, a full 6DOF experimental verification of the extended Kalman filter (EKF) presented in Chap. 4 is not possible. However, the data set will serve three purposes in the frame of this thesis.

1. Estimation of the CAI measurement uncertainty. The data set provides an excellent basis for an evaluation of the CAI uncertainty processes, and thus to derive a basic observation uncertainty estimate for the EKF and to understand some aspects of the measurement. For the first step of parameterizing the fringe pattern, least-squares estimation (LSE) is applied.

2. The residuals of the estimate and the data will further be analyzed by a maximum likelihood estimation (MLE) method in order to derive the uncertainties of the parameters in a more differentiated way, opening the possibility to distinguish between technical noise and phase noise, and enabling the identification of the true error source.

3. The parameters and their uncertainties are saved after the identification. A reduced form of the EKF is applied, in which the acceleration bias on the one axis available is estimated. Instead of a mid fringe operation as introduced in Sec. 4.2.1, the operating point is defined by the predicted phase shift. This means that the sensitivity can vary largely.

Especially the last point is of high interest, because the operation without the laser feedback control to the mid fringe point is easier to implement both from a hardware and software point of view. The main drawbacks are an expected lower sensitivity of the EKF update and the increased complexity for an analytical solution like presented in Sec. 4.2.

5.1.2 CAI and Titan Parameters

The atom interferometer is of Kasevich-Chu type (Kasevich & Chu, 1992). The interrogation time is 10 ms, the pulse time τ is 7.5 µs. The sensitive time interval of the interferometer, consistent of beamsplitter pulse (τ), mirror pulse (2τ) and a final beamsplitter pulse, spans a total of 20.03 ms. The effective wave number k_e is $4\pi/780\,\mathrm{nm}^{-1}$.

The CAI measurement was done in sets of ten subsequent measurements. After one set, the direction of the sensitive axis, as expressed by the effective wave vector $\mathbf{k_e}$, was reversed by changing the orientation of the momentum transfer. This *k-reversal* technique (Snadden et al., 1998) is mainly used in order to suppress systematic errors of the CAI itself. Each direction has different fringe pattern parameters. In the frame of this thesis only the *k-minus* direction is considered, as the data in *k-plus* direction have additional leakages. The timestamps are reproduced by taking the time of the first and the last CAI measurement and dividing this by the number of samples, which results in an estimate of the total cycle time T_{total} of 1.8157653 seconds.

The classical accelerometer considered here is a Nanometrics Titan TACCL-N1 (Nanometrics inc., 2023). The data is not continuously available. The recording was triggered for each CAI measurement shot, so that there are slices of 60.03 ms of data available at a rate of T_{total}. During post-processing the data were high-pass filtered with a cutoff frequency at 50 Hz, and each data slice reduced to a length of 20.03 ms which corresponds to the CAI measurement interval. The corresponding data are visualized in Fig. 5.2.

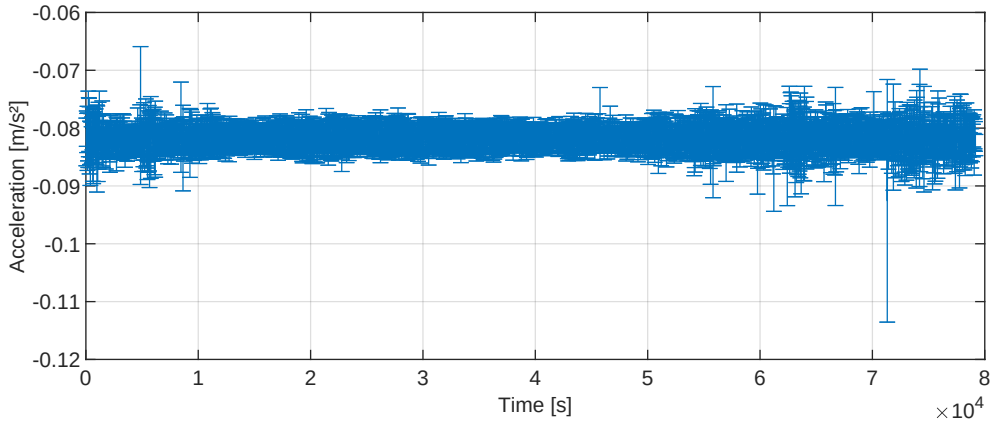

Figure 5.2: Ambient accelerations as measured by the Titan accelerometer over time. Since the measurement is not continuous, the data have been averaged for ten subsequent CAI measurements, and the mean and standard deviation were computed as depicted. This gives a general idea about the magnitude of the offset and the vibrations for different times.

5.2 Fringe Parameter Estimation

5.2.1 Approach

As the data set was recorded in a static laboratory environment, the contrast is not subject to varying rotations or other systematic deviations caused by dynamics (apart from ambient vibrations). For the theoretical and the concept studies in the prior chapter it was assumed that the amplitude $A = 0.5$ and the zero offset $p_0 = 0.5$ were known and constant. On the basis of the prototype data set some aspects of the real observations will now be elaborated.

This is done in two steps: the estimation of the fringe parameters, followed by an estimation of the observation uncertainty.

For the fringe parameter estimation a least-squares adjustment is applied. The method consists of the following equations. The model for a single observation is

$$h(\mathbf{x}) = A\cos(\phi + \phi_0) + p_0. \tag{5.1}$$

The parameter vector reads

$$\mathbf{x} = \begin{bmatrix} A & \phi_0 & p_0 \end{bmatrix}^{\mathrm{T}}, \tag{5.2}$$

with amplitude A, offset p_0 and phase offset ϕ_0, which resembles a shift of the fringe pattern with respect to its *null-fringe*, i.e. the intersection of the fringe pattern with the y-axis at $\phi = 0$. This null-fringe is realized by a frequency sweep at about 25 MHz, which is applied in each measurement in order to compensate for the acceleration due to gravity[1], cf. Eq. (3.56).

The phase shift ϕ in this context is produced from the correlation of the accelerations with the CAI acceleration sensitivity function, cf. Fig. 5.3. Actual changes of the acceleration with respect to gravity, for which the CAI is calibrated thanks to the null-fringe sweep rate, are measured by the Titan. Those changes, which lead to a scatter of the phase shift over several periods of the sinusoidal fringe pattern, mainly result from ambient vibrations. The offset ϕ_0 from the null-fringe is resulting from systematic errors between the Titan and the CAI.

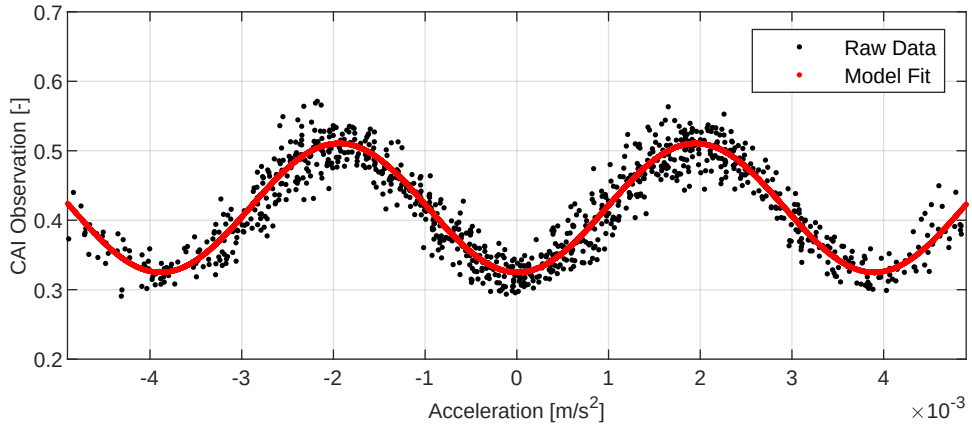

Figure 5.3: Fringe pattern as reconstructed from the accelerometer data. The accelerations represent the x-axis and the CAI data the y-axis. The black dots represent the raw data. The red dots which look like a line are generated by the model based on the estimated fringe parameters.

For the adjustment a number of n observations is available. In the case of a general linear system, the actual observation vector $\mathbf{y}$ and the observation model, as gained by the product of the Jacobian $\mathbf{H}$ and the parameter vector $\mathbf{x}$, reads

$$\mathbf{y} + \mathbf{v} = \mathbf{H}\mathbf{x}. \tag{5.3}$$

The adjustment is done by minimizing the residuals $\mathbf{v}$, or more specifically (Niemeier, 2008),

$$\mathbf{v}^{\mathrm{T}}\mathbf{R}^{-1}\mathbf{v} \rightarrow \min. \tag{5.4}$$

The estimated parameter vector $\hat{\mathbf{x}}$ associated with this minimal error is

$$\hat{\mathbf{x}} = \left(\mathbf{H}^{\mathrm{T}}\mathbf{R}^{-1}\mathbf{H}\right)^{-1}\mathbf{H}^{\mathrm{T}}\mathbf{R}^{-1}\mathbf{y}. \tag{5.5}$$

[1] Based on correspondence with the authors of Richardson et al. (2020).

Note, that in this model there is no discrimination between co-factor matrix and covariance matrix as it is often used in geodesy, e.g. Niemeier (2008), in order to avoid the introduction of additional symbols. As the observation noise $\mathbf{R}$ is unknown, it is for now defined as the identity matrix, $\mathbf{R} = \mathbf{I}$.

Since the observation model is non-linear, the equation is solved in several iterations indexed by the superscript i, with error parameters $\delta\hat{\mathbf{x}}^{(i)}$ with respect to an operation point $\hat{\mathbf{x}}^{(i-1)}$,

$$\delta\hat{\mathbf{x}}^{(i)} = \left((\mathbf{H}^{(i-1)})^{\mathrm{T}}\mathbf{R}^{-1}\mathbf{H}^{(i-1)}\right)^{-1}(\mathbf{H}^{(i-1)})^{\mathrm{T}}\mathbf{R}^{-1}\hat{\mathbf{v}}^{(i-1)}, \tag{5.6}$$

where

$$\hat{\mathbf{v}}^{(i-1)} = \mathbf{y} - \mathbf{h}(\hat{\mathbf{x}}^{(i-1)}). \tag{5.7}$$

The Jacobian $\mathbf{H}^{(i-1)}$ is given by

$$\mathbf{H}^{(i-1)} = \frac{\partial\mathbf{h}(\hat{\mathbf{x}}^{(i-1)})}{\partial\hat{\mathbf{x}}^{(i-1)}} = \begin{bmatrix} \cos(\phi_1 + \hat{\phi_0}^{(i-1)}) & -\hat{A}^{(i-1)}\sin(\phi_1 + \hat{\phi_0}^{(i-1)}) & 1 \\ \cos(\phi_2 + \hat{\phi_0}^{(i-1)}) & -\hat{A}^{(i-1)}\sin(\phi_2 + \hat{\phi_0}^{(i-1)}) & 1 \\ & \dots & \\ \cos(\phi_n + \hat{\phi_0}^{(i-1)}) & -\hat{A}^{(i-1)}\sin(\phi_n + \hat{\phi_0}^{(i-1)}) & 1 \end{bmatrix}. \tag{5.8}$$

The parameter vector is updated after each iteration,

$$\hat{\mathbf{x}}^{(i)} = \delta\hat{\mathbf{x}}^{(i)} + \hat{\mathbf{x}}^{(i-1)}. \tag{5.9}$$

The computation is aborted, if the update $\delta\hat{\mathbf{x}}^{(i)}$ is below a certain threshold ϵ. All parameters that were indexed by i before assume the value after the final iteration for the upcoming equations. As an indicator for the accuracy of the least-squares adjustment, the a posteriori variance factor $\hat{\sigma}_0^2$ can be estimated

$$\hat{\sigma}_0^2 = \frac{\hat{\mathbf{v}}^{\mathrm{T}}\mathbf{R}^{-1}\hat{\mathbf{v}}}{n_{\mathrm{DOF}}}, \tag{5.10}$$

where n_{DOF} is the degree of freedom of the system, i.e. the number of observations n_{obs} minus the number of parameters n_{par},

$$n_{\mathrm{DOF}} = n_{\mathrm{obs}} - n_{\mathrm{par}}. \tag{5.11}$$

This n_{DOF} acts as a weight, or rather correction factor, for the initially unknown $\mathbf{R}$. Furthermore, with the help of this weight coefficient, an estimate of the parameter covariances $\mathbf{P}$ can be computed,

$$\mathbf{P}_{\mathrm{total}} = \hat{\sigma}_0^2\left(\mathbf{H}^{\mathrm{T}}\mathbf{R}^{-1}\mathbf{H}\right)^{-1}. \tag{5.12}$$

Note that this variance resembles the accuracy of the estimate for a number of n samples. The shot by shot variance which is required for the EKF can be assessed by

$$\mathbf{P} = n_{\mathrm{DOF}}\mathbf{P}_{\mathrm{total}}. \tag{5.13}$$

This iterative method requires adequate initial values $\hat{\mathbf{x}}_0$. They can generally be initialized as $A = 0.5$, $p_0 = 0.5$ and $\phi_0 = 0$. Two other options for A and p_0 are:

- The mean of the sample set in order to assess p_0, followed by a histogram fit which yields information about the amplitude A.
- For subsequent estimations, the prior estimate $\hat{\mathbf{x}}$ can be used as initial parameter vector.

In case the phase shift offset ϕ_0 is not known at all, it can be acquired by a cross-correlation of the data set with a template fringe model based on the initial estimates of A and p_0, after the data set is ordered with respect to the phase shifts, and possibly interpolated as required. The data array resulting from the correlation, in theory, yields its maximum at the location of the phase shift ϕ_0.

5.2.2 Application and Discussion

The application of the method to the experimental data set is done in two steps. First, the fringe parameters are estimated for sets of ten subsequent measurements in order to get a first idea about the order of magnitude of the fringe parameters, cf. Fig. 5.4. Besides the uncertainty due to low sample size, all estimates reveal a drift of the parameters over time. The value of ϕ_0, besides the initial offset of about $-132\,\mathrm{rad}$, varies over a range of $0.5\,\mathrm{rad}$ over the course of this stationary data set. The amplitude A and the offset p_0 show similar changes, especially in the beginning.

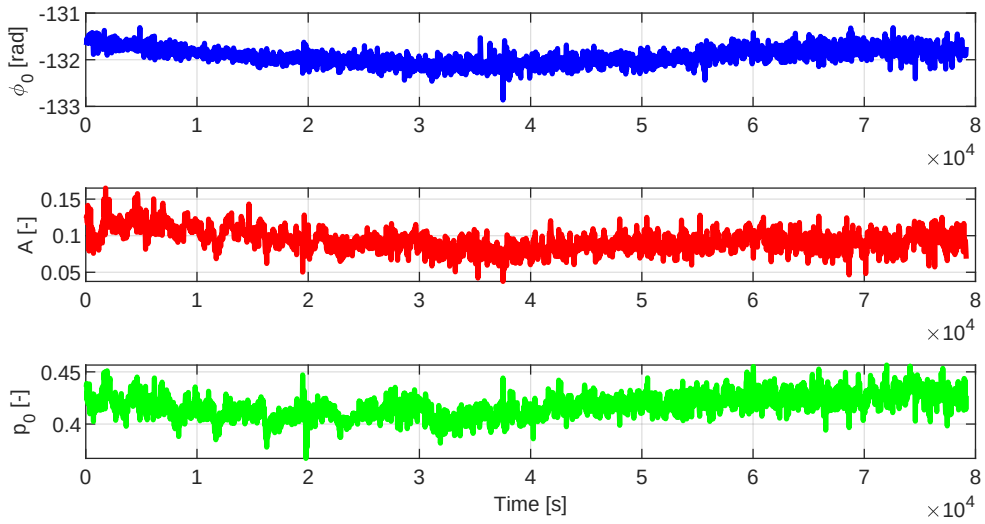

Figure 5.4: Fringe parameters estimated by a least-squares method with a window size of ten subsequent samples. From top to bottom: phase shift in blue, amplitude A in red and the offset p_0 in green.

Furthermore, a rough idea about the change over time of the parameters is gained by applying the Allan variance computation method to the estimated parameters. This step needs further explanation, since the main application of the method is to analyze the stability of oscillators. The interpretation in this case is different. Here, the Allan variance method does not allow to extract any noise processes, but it gives an idea about how the estimated parameters scatter for different averaging intervals. If this scatter is uncorrelated in time and follows a normal distribution, the variance will decrease by a $\frac{1}{n_{\mathrm{obs}}}$ rule. For systematic changes of the parameters, different behavior will occur. Ultimately, and this leads to the second step of the analysis, there is a plateau in which the scatter between the estimated parameters is minimal. The corresponding averaging time can then be used as window size for the parameter estimation process. This reduces the computational effort for a potential online application, and increases the accuracy of the estimated fringe parameters. The results in Fig. 5.5 indeed reveal a window size where the variance of the averaged sample sets yields a minimum. This corresponds to 600 samples, or about 2179 seconds.

The estimation is now repeated with a window size of 600 samples. The estimated parameters are depicted in Fig. 5.6. The amplitude reaches maximum values of about 0.12 close to the beginning of the experiment, and yields a minimum just below 0.08 at the middle section. The offset p_0 is relatively constant with values between 0.4 and 0.43 over the course of the experiment. The phase shift offset ϕ_0 varies over a total range of $0.5\,\mathrm{rad}$ between $-131.6\,\mathrm{rad}$ and $-132.1\,\mathrm{rad}$. A clear drifting behavior is inherent which likely results from the difference

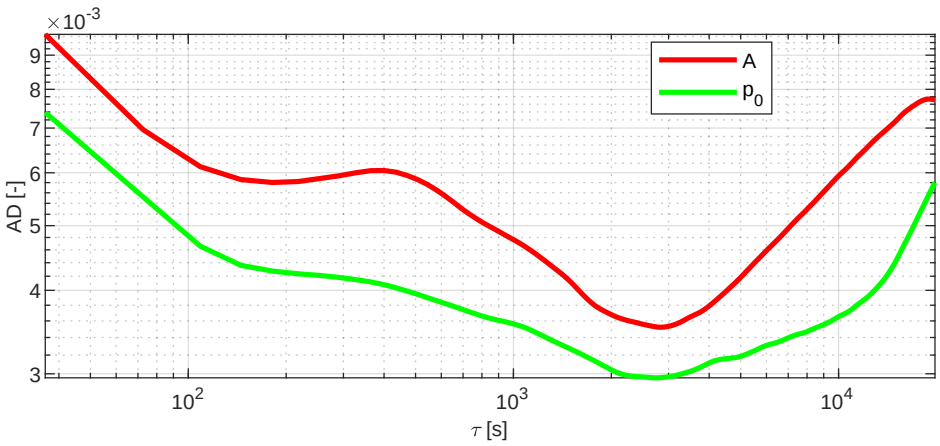

Figure 5.5: Overlapping Allan standard deviation of the fringe amplitude and offset. The amplitude A in blue and the offset p_0 in red show a distinct minimum at an averaging time of just above 2000 seconds, which corresponds to 600 samples. The amplitude furthermore reaches a first plateau at about 180 seconds.

of the predicted observation due to sensor drift of the Titan over time and the actual CAI measurement.

The estimated variances as produced from the LSE are depicted in Fig. 5.6 (right panels). The mean values for the standard deviation are 18.39° for the phase shift, 0.0294 for the amplitude, and 0.0208 for the offset p_0. The graphs of the results show that they are clearly correlated, which is mainly because they are all calculated on the same basis, i.e. the residual sum of squares. The method fails to identify the true source of the noise, i.e. phase noise or detection noise in the measurement.

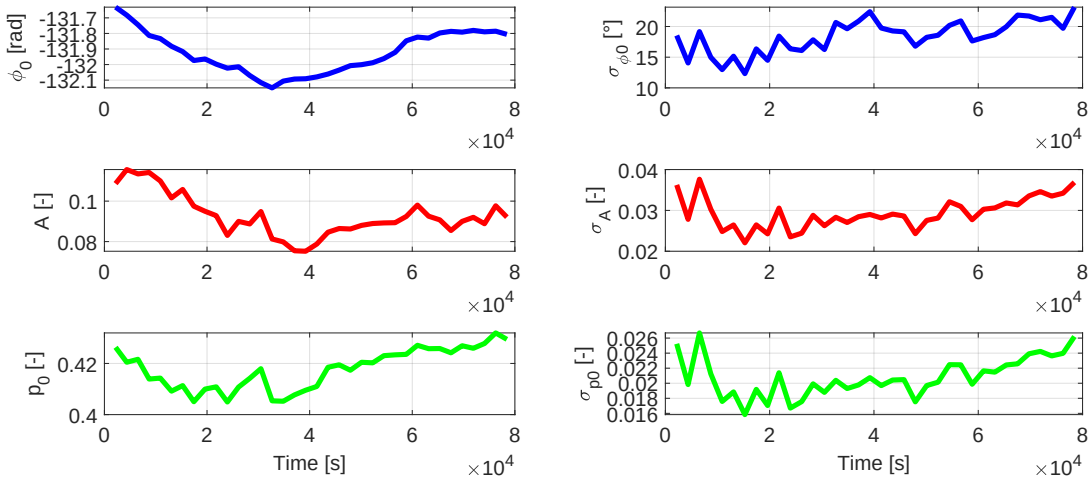

Figure 5.6: Fringe parameters estimated by a least-squares method with a window size of 600 samples. Left: estimated CAI fringe parameters. Right: estimates of the parameter standard deviations per CAI shot.

To summarize, the results show that the LSE method can be applied to the estimation of the fringe parameters. Furthermore, the accuracy of the estimates can be assessed through the parameter covariances in $\mathbf{P}$. While the variance estimate $\hat{\sigma}_p^2$ is reasonable, it is not possible to identify the correct variance components for phase noise $\sigma_{\phi_0}^2$ and detection noise $\sigma_{p_0}^2$, i.e., the true noise sources.

5.3 Maximum Likelihood Estimation of Fringe Parameter Uncertainty

In this section, MLE as an alternative method for the estimation of the variance components is applied. As a data basis, the residuals of the LSE are used again in order to compare the results of both methods.

5.3.1 Methodology

The likelihood L of a variance σ_i^2 and mean μ_i for a given sample x_i under the assumption of a Gaussian normal distribution with independent and identically distributed random variables reads

$$L(\mu_i, \sigma_i | x_i) = \frac{1}{\sqrt{2\pi}\sigma_i} \cdot \exp\left(-\frac{1}{2} \cdot \frac{(x_i - \mu_i)^2}{\sigma_i^2}\right). \tag{5.14}$$

The variance σ_i^2 of a sample is composed of the variances of the offset $\sigma_{p_0}^2$, the phase $\sigma_{\phi_0}^2$ as well as the amplitude σ_A^2. It can be computed by variance propagation of the single parameters according to

$$\sigma_i^2 = \left|\frac{\partial h}{\partial \phi_0}\right|^2 \cdot \sigma_{\phi_0}^2 + \left|\frac{\partial h}{\partial p_0}\right|^2 \sigma_{p_0}^2 + \left|\frac{\partial h}{\partial A}\right|^2 \cdot \sigma_A^2, \tag{5.15}$$

where h is the observation according to Eq. (5.1). The resulting equation for the variance is

$$\sigma_i^2 = A^2 \cdot \sin(\phi_i)^2 \cdot \sigma_{\phi_0}^2 + \sigma_{p_0}^2 + \cos(\phi_i)^2 \cdot \sigma_A^2. \tag{5.16}$$

The samples are now representing the residual process after the LSE fit, thus $\mu_i = 0$. A parameter vector $\boldsymbol{\theta}$ is defined as

$$\boldsymbol{\theta} = \begin{bmatrix} \sigma_{p_0} & \sigma_{\phi_0} & \sigma_A \end{bmatrix}^T. \tag{5.17}$$

The total likelihood of this parameter vector for a total of n samples is given by the product

$$L(\boldsymbol{\theta}|\mathbf{x}) = \prod_{i=1}^{n} \frac{1}{\sqrt{2\pi}\sigma_i} \cdot \exp\left(-\frac{1}{2} \cdot \frac{x_i^2}{\sigma_i^2}\right). \tag{5.18}$$

The log-likelihood, cf. Appendix A.7, is then given by

$$\ln L(\boldsymbol{\theta}|\mathbf{x}) = -\frac{1}{2} \ln 2\pi + \sum_{i=1}^{N} \left(-\ln \sigma_i - \frac{x_i^2}{2\sigma_i^2}\right). \tag{5.19}$$

A closed form solution for the maximum of the likelihood does not exist, since the composed variances σ_i^2 yield a dependency on the phase shift ϕ_i of the samples, cf. Eq. (5.16). Consequently, an iteration technique like gradient ascent is used.

The estimate $\hat{\boldsymbol{\theta}} = [\hat{\sigma}_{p_0}, \hat{\sigma}_{\phi_0}, \hat{\sigma}_A]^{\mathrm{T}}$ can be solved by the gradient ascent given the recursive equation

$$\hat{\boldsymbol{\theta}}^{(k)} = \hat{\boldsymbol{\theta}}^{(k-1)} + \boldsymbol{\beta}^{(k-1)} \mathbf{J}^{(k-1)}, \tag{5.20}$$

where

$$\mathbf{J}^{(k-1)} = \frac{\partial \ln L^{(k-1)}}{\partial \hat{\boldsymbol{\theta}}^{(k-1)}} \tag{5.21}$$

is a vector with derivatives of the log-likelihood function w.r.t. the three parameters, which are (without explicitly stating the index $k-1$) given by Eqs. (5.22) - (5.24),

$$\frac{\partial \ln L}{\partial \sigma_{p_0}} = \sum_{i=1}^{N} \left(-\frac{\sigma_{p_0}}{\sigma_i^2} + x_i^2 \frac{\sigma_{p_0}}{\sigma_i^4} \right), \tag{5.22}$$

$$\frac{\partial \ln L}{\partial \sigma_{\phi_0}} = \sum_{i=1}^{N} \left(-\frac{A^2 \sin(\phi_i)^2 \sigma_{\phi_0}}{\sigma_i^2} + x_i^2 \frac{A^2 \sin(\phi_i)^2 \sigma_{\phi_0}}{\sigma_i^4} \right), \tag{5.23}$$

$$\frac{\partial \ln L}{\partial \sigma_A} = \sum_{i=1}^{N} \left(-\frac{\cos(\phi_i)^2 \sigma_A}{\sigma_i^2} + x_i^2 \frac{\cos(\phi_i)^2 \sigma_A}{\sigma_i^4} \right). \tag{5.24}$$

After convergence, e.g. when the difference of two subsequent $\hat{\boldsymbol{\theta}}^{(k)} - \hat{\boldsymbol{\theta}}^{(k-1)}$ is sufficiently low, the recursion loop may be stopped. The step width $\boldsymbol{\beta}$ is defined by the inverse Hessian of the log-likelihood (Schweppe, 1973, p. 349),

$$\boldsymbol{\beta}^{(k-1)} = \left(\frac{\partial \mathbf{J}^{(k-1)}}{\partial \hat{\boldsymbol{\theta}}^{(k-1)}} \right)^{-1}, \tag{5.25}$$

with the derivatives being stated in detail in Appendix A.7.

The combined uncertainty of a single CAI observation, σ_p, can then be reconstructed from the estimated components,

$$\sigma_p^2 = A^2 \cdot \sin(\phi)^2 \cdot \hat{\sigma}_{\phi_0}^2 + \hat{\sigma}_{p_0}^2 + \cos(\phi)^2 \cdot \hat{\sigma}_A^2, \tag{5.26}$$

and applied on the main diagonal of the observation uncertainty matrix $\mathbf{R}$. Note that the phase ϕ in this particular calculation depends on the individual samples, but can be considered random and uniformly distributed for the set of samples that were used for the MLE. In case of a feedback mid fringe operation, the value can be set to the controlled point at $\phi = \frac{\pi}{2}$, and thus $\sin(\phi) = 1$ and $\cos(\phi) = 0$, the latter being a clear indicator that the uncertainty of the amplitude does not affect the observation uncertainty. However, in the randomly distributed case, the *root mean square* (RMS) of the sinusoidals can be used as an approximation. Here, the factor $\sin(\phi)$ is approximated by the RMS under the assumption of uniformly distributed phases, cf. Svitlov (2012), so that $\sin(\phi) = \cos(\phi) = \frac{1}{\sqrt{2}}$.

5.3.2 Application and Discussion

As a first demonstration of the method, a fringe signal is simulated. Additive white noise is applied on all three parameters. Fig. 5.7 shows the simulated signal with the noise parameters $\sigma_A = 0.03, \sigma_{p_0} = 0.05$ and $\sigma_{\phi_0} = 0.2618\,\text{rad}$. A total number of 500 samples are generated. For the initial parameter estimate $\hat{\boldsymbol{\theta}}_0$ of the gradient ascent method, the simulated values were applied with a deviation of $+100\,\%$. As the results indicate, it is possible to reconstruct all three parameters within a small error margin. The estimates converge quite fast after just ten iterations.

Application of the algorithm to the ATLAS data set is straight forward possible. First tests show that the parameter for σ_A is often estimated as zero. In order to reduce numerical issues, only the variances of ϕ and p_0 are estimated. A total of 20 iterations of Eq. (5.20) are processed. Fig. 5.8 displays the results for $\sigma_{\phi_0}^2$ and $\sigma_{p_0}^2$. The uncertainties and their standard deviation over the whole data set are $(11.397 \pm 3.667)^\circ$ for the phase shift and (0.0191 ± 0.0033) for the offset, respectively.

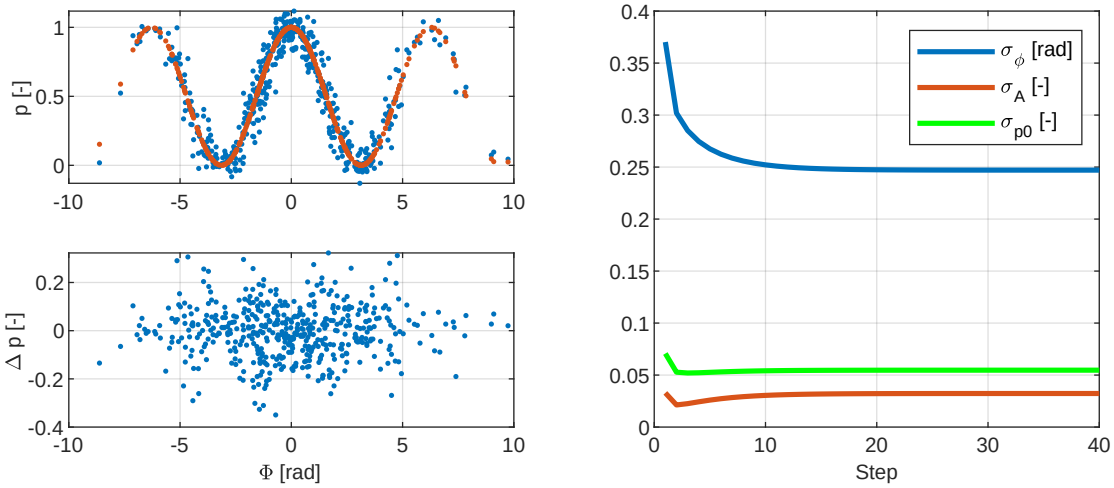

Figure 5.7: Simulated example of a fringe signal and the MLE results. Left panel: simulated fringe signal, with the reference in red color and the noisy signal in blue color. Below is the residual process from which the variance components are estimated. Right: variance components as reconstructed from the observations by the MLE and gradient ascent method.

For comparison, the STD estimates from the LSE are added in the figure. While σ_{p_0} is comparable, the LSE estimate for σ_{ϕ_0} is too large. Still, the direct juxtaposition of the total observation STD σ_p as computed by both methods shows that they are comparable. The estimate from the MLE method tends to be slightly larger than that of the LSE at some regions, e.g. the spike after 3×10^4 s. This difference likely results from the transformation step of the σ_{ϕ_0} term in Eq. (5.16), where the factor $\sin(\phi)$ is approximated by the RMS under the assumption of uniformly distributed phases.

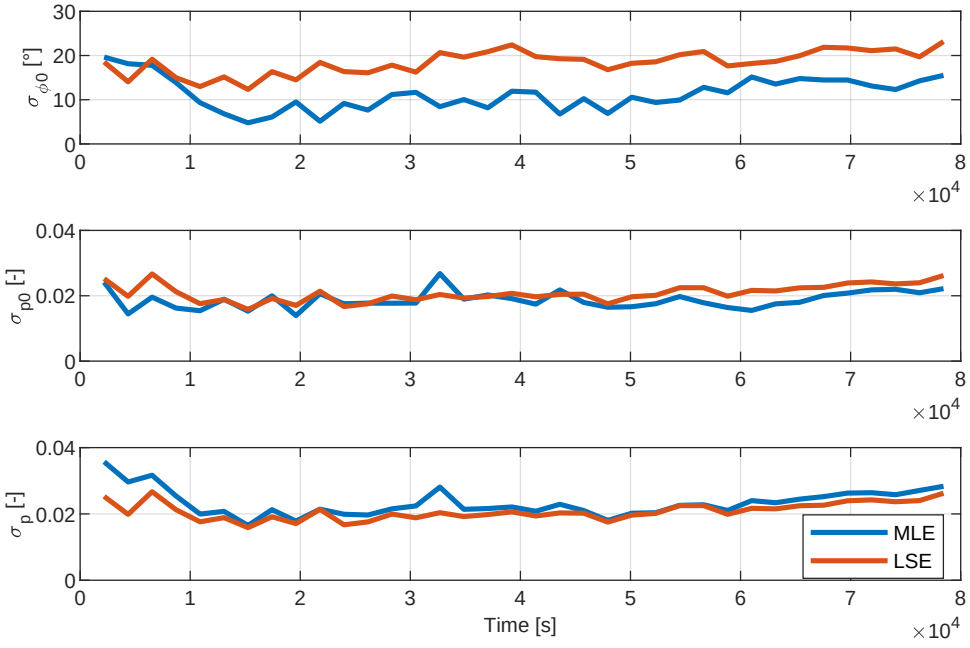

Figure 5.8: Comparison of the estimated fringe parameter variances as computed by MLE and LSE. The blue lines indicate the result from the maximum likelihood method and the red lines represent the empirical standard deviation from the least-squares estimation. The bottom figure shows the total uncertainty.

While the parameter estimation by maximum likelihood method is a valid method for the reconstruction of the variance components, the following drawbacks need to be considered:

- Estimation of parameters always includes uncertainty, which can be reduced with the number of samples for white, normally distributed processes.
- MLE is a biased estimator. This bias is reduced by the number of samples as well.
- As the gradient ascent method is a recursive procedure, there is always a chance to find a local maximum instead of the intended global maximum. This problem can be widely mitigated by using the prior variance component estimates.

It is quite clear that the LSE is less computationally demanding and in general sufficient when the goal is to produce an estimate of the total observation uncertainty of σ_p. This is especially true since the LSE is needed anyway in order to estimate the fringe parameters and the observation variance is merely a side product. The maximum likelihood method however is more suitable to find the source of the uncertainty, i.e. if the noise process is resulting from detection noise or from phase noise. This is important to identify the noise source, and ultimately enables more distinct fault detection.

As a final addition, by exactly controlling the phase shift it seems possible to get a proper estimate of the noise source with the LSE as well. A closer look at Eq. (5.16) under consideration of uncertainties in p_0 and phase noise,

$$\sigma_p^2 = A^2 \cdot \sin(\phi)^2 \cdot \sigma_{\phi_0}^2 + \sigma_{p_0}^2, \tag{5.27}$$

reveals that in case of $\phi = 0$ and thus $\sin(\phi) = 0$, σ_p^2 is entirely composed of $\sigma_{p_0}^2$ because at the top/bottom fringe the interferometer is not sensitive to the phase uncertainty. As a result, the detection noise can be identified. In subsequent measurements with arbitrary phase shift, the phase noise can be attained by subtracting the detection noise from the total noise. This approach however is only accurate if the noise is stationary, and as the prior analysis demonstrated, this is not necessarily the case.

5.4 Experimental Demonstration of the Hybridization

As a final study, the hybridization algorithm from Chap. 4 is now evaluated on the static data set. This will serve as a demonstration of the applicability of the algorithm and filter to real data of accelerometers and atom interferometers on a single axis. The EKF is utilized as described in Sec. 4.2.2. The process noise variance Q of the acceleration input is set to $5 \times 10^{-13}\,\mathrm{m^2/s^4}$, according to the white noise assessed from the data sheet (Nanometrics inc., 2023). The initial conditions at t_0 are defined as follows:

$$\begin{aligned} b_a(t_0) &= -0.0817\,\mathrm{m/s^2}, \\ P(t_0) &= 1 \times 10^{-8}\,\mathrm{m^2/s^4}. \end{aligned} \tag{5.28}$$

In this case, the initial bias $b_a(t_0)$ was determined during post-processing by taking the mean of the accelerations in Fig. 5.2. Note that the value of the parameter is much larger than the ambiguity range. In an online-scenario where the initial bias is unknown, intelligent adaption of the interrogation time is required in order to get a first lock-on on the bias induced phase shift, cf. Appendix A.8.1. The initial state variance $P(t_0)$ is set, so that the standard deviation is about two orders of magnitude above the uncertainty of the accelerometer. It is possible to apply larger values in order to improve the convergence time of the filter. Lower values however increase the convergence time and could lead to wrong estimates of the bias state, and thus a divergence of the filtered solution.

The amplitude and the uncertainty of the fringe pattern were computed before by means of LSE for chunks of subsequent measurements, and saved in order to reduce computation time. The σ_p uncertainty estimate of the MLE is saved as well. In order to bring the scenario as close to the resemblance of an online operation as possible, it is not allowed to define the initial values of A and p_0 based on the LSE estimates that were gained from *future* data. In a real online scenario, an initial data set needs to be taken before the kinematic experiment in order to produce a first estimate. In this case, the following values are set,

$$\begin{aligned} A(t_0) &= 0.11, \\ p_0(t_0) &= 0.42, \\ \phi_0(t_0) &= 0\,\text{rad}. \end{aligned} \tag{5.29}$$

Furthermore, the estimates of $\hat{\phi}_0$, which were computed by the LSE, now serve as a comparison for the *online* estimation of the phase shift by the EKF. For the transformation into the corresponding acceleration bias, Eq. (3.3) is applied.

The estimated acceleration bias and standard deviation are depicted in Fig. 5.9 and Fig. 5.10, respectively. Clearly, the bias can be tracked and the filter runs stable. The results of the EKF, which are computed with every new observation, comply with the ones from the LSE which were computed from sets of 600 data points. This means that online tracking of the bias is possible even though no mid fringe feedback operation of the laser phase is applied.

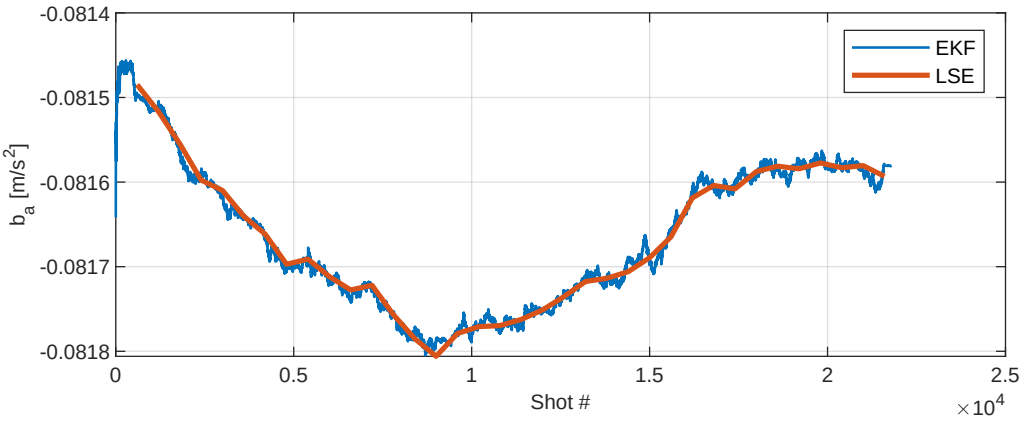

Figure 5.9: ATLAS: estimated Titan acceleration bias. The EKF result is depicted as blue line. This resembles the continuous estimation which can also be applied online. For comparison, the LSE ϕ_0 estimate, multiplied by the CAI scale factor to accelerations, is depicted as well as red line.

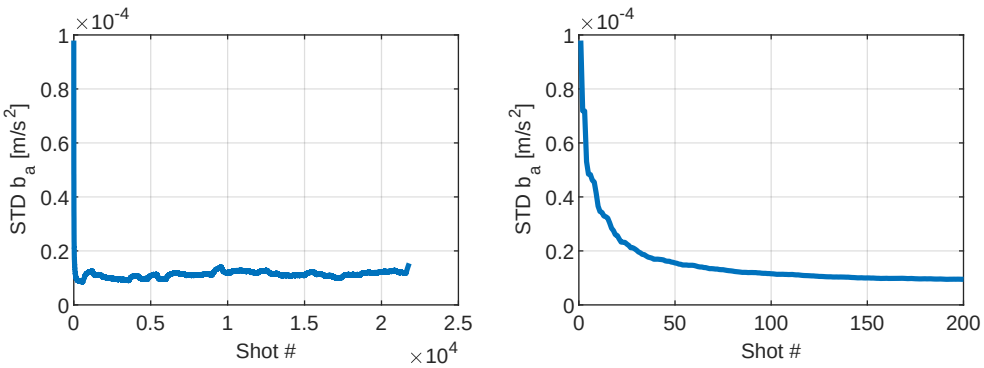

Figure 5.10: ATLAS: standard deviation of the estimated Titan acceleration bias (left), and a detailed view on the first filter time steps (right) to clarify the impact of the initial state variance on the convergence time.

The state standard deviation as computed from $\sqrt{P}$ is depicted in Fig. 5.10. The value converges to a steady state. The convergence speed depends mainly on the setting of the initial uncertainty $P(t_0)$. The small changes of the value after the convergence correspond to the different, time-depending, values of the measurement uncertainty R that are used in the EKF.

The stability of the filtered accelerations can be improved thanks to the reduction of the signal by the acceleration bias. This is demonstrated by computing the AD as depicted in Fig. 5.11. The flicker floor of the raw signal is reached after about 1×10^4 s at a value of $6 \times 10^{-4}\,\mathrm{m/s^2}$, while the flicker floor of the filtered signal does not seem to be reached in the time frame covered by the data. In fact, even after 4×10^4 seconds no clear drift is visible. Note that ambient vibrations overshadow the actual noise of the accelerometer in magnitude, which is why a difference caused by sensor noise is only visible well after 5000 seconds. Because of this circumstance, an accurate assessment of the white noise density is not possible with this method, and not further pursued.

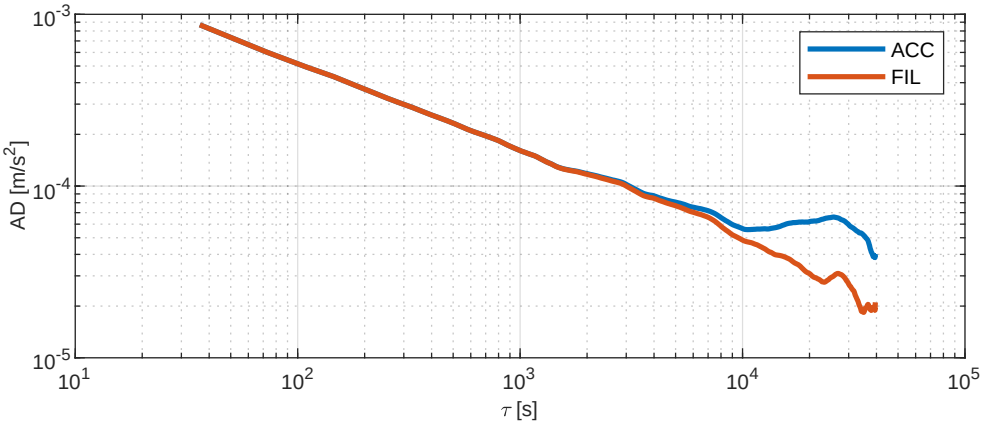

Figure 5.11: ATLAS: overlapping Allan deviation of the Titan and filtered acceleration data, indicating the performance gain by the EKF. Depicted are the overlapped Allan standard deviation results for the accelerometer data as blue line (ACC), as well as the corrected accelerations in red (FIL).

A final interesting option, especially for mere CAI gravimetry approaches in which ambient vibrations are corrected by high rate sensors, is the improvement of the CAI observation under the additional knowledge of the estimated phase shift offset ϕ_0. If the acceleration signal is not filtered before being convoluted with the CAI transfer function, in order to assign phase information to the measurement and reconstruct the fringe pattern, the CAI observation is affected by additional errors. If, however, the estimated phase offset is included in the reconstructed phase shift as gained by the convolution, the discrepancy of the actual CAI observation and the reconstructed fringe can, in this case, be reduced by 8.91 %. Both are illustrated in Fig. 5.12.

To conclude, the two-step method described here, i.e. the estimation of the fringe parameters and the *online* EKF phase shift error estimation, is a novel approach for an online operation of a QINS. Other experiments rely on a histogram fit (Richardson et al., 2020) of chunks of data, or solely on a least-squares fit of the data with a sinusoidal model. Those methods are often not considering the phase bias between the reconstructed fringe and the interferometer measurement.

One experiment closest in its core to the methods described in this thesis is the one presented in Cheiney et al. (2018), where data from a high-bandwidth classical sensor and a single-axis cold atom interferometer is combined in a regular Kalman filter. The major difference is that their state vector is composed of the three fringe parameters and additionally the rate of

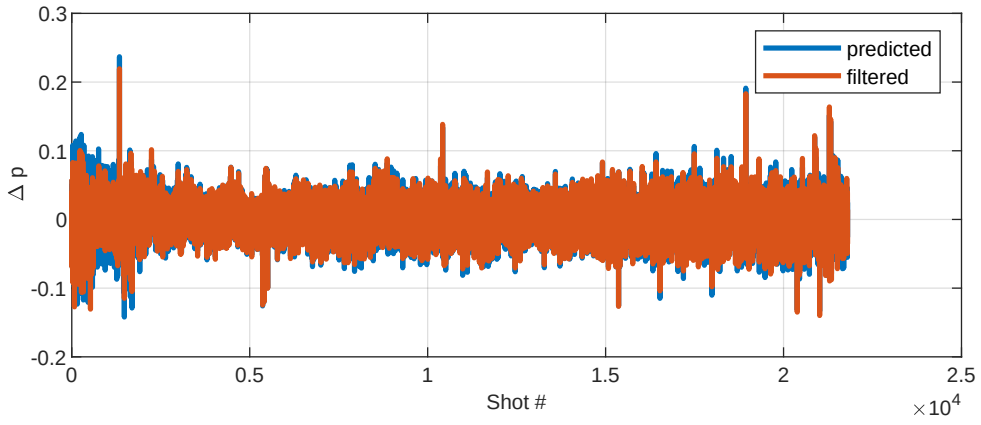

Figure 5.12: ATLAS: atom population error of the predicted and filtered model. Blue: error of the prediction model w.r.t. the CAI data. Red: model with corrected bias error.

change of the phase shift bias. They do not comment on the stability of their filter. In fact, using one observation for four (time-dependent) states at a time leads to an underdetermined system. This can only be justified for slowly changing values of the parameters and the phase shift error. Otherwise, batch estimation or other means of a reduction of the state vector are necessary. Nevertheless, it was discussed in Sec. 3.5 that the amplitude, or contrast, is a quantity that is strongly correlated with rotations. Thus, the augmentation of the state vector by the contrast should be further experimentally investigated, but with an additional focus on the stability of the filter.

Furthermore, the KF, which is applied in Cheiney et al. (2018), in truth suffers from the same inability to identify the true non-stationary driving noise processes as the LSE. In the simulated example, they show that the parameters of the variances of the driving noise processes are constant over time and quite similar in their order of magnitude. In the case of large deviations of the variances, the KF would fail to reconstruct all variances accordingly. The MLE presented here thus constitutes a valuable addition.

6

Summary and Outlook

In this thesis, a number of important topics on the steep road toward a quantum inertial navigation system have been discussed. A promising concept for the design of such a system has been presented. The main motivation being the limited bandwidth of CAI, as well as the circumstance that the observation is subject to an ambiguity, leading to a limited dynamic range of the sensor. There are four major accomplishments.

Result 1: Adapted Kinematic Model and Atom Strapdown

A kinematic model for the atoms has been elaborated, based on the Feynman path integral and the Bordé midpoint line theorem in conjunction. Under certain circumstances this allows to reduce complex quantum physics, necessary to describe the spatio-temporal evolution of the wave packet of two interferometer paths, to the arguably easier to handle kinematic differential motion equations of a single point mass. This methodology has been adapted to the kinematics that are relevant for high rate inertial navigation. To accomplish this, a sensor frame for the atom interferometer has been introduced for which the kinematics have been developed. This allows to apply inertial navigation methodology, i.e. the evaluation of the kinematic state of the point mass by using data of three accelerometers and gyroscopes alone in a classic strapdown navigation algorithm, to the case of a moving atom wave packet in a CAI. Consequently, the method is labeled Atom Strapdown. The major applications of this method are the following:

1. The formalism allows to include accelerations *and* angular rate measurements in the phase shift prediction, which means that it is in principle possible to use CAI without stabilization or means of compensation for external rotations, at least within the physical limits of the CAI. Furthermore, systematic errors between the CAI s-frame and the IMU b-frame are already part of the differential equation system. So far, the transfer function between the accelerometers and the CAI was often unknown and needed to be experimentally estimated, or completely avoided by bandpass filtering the acceleration signals, which in turn affected the bandwidth of the system.

   This culminates in the Atom Strapdown being a generalization and potential alternative to the basic correlation approach. As the fringe pattern can be reconstructed even for large scatter of phase shifts beyond the dynamic range, the method by itself already allows for a basic hybridization of CAI with classical IMUs.

2. It was discussed that the very same phase ambiguity problem, for which the hybridization with high rate classical sensors is the intended solution, is still present in shape of a phase shift error ambiguity problem. This phase shift error is the result of any accumulated systematic and stochastic errors between the reconstructed phase shift and the actual CAI observation. In order to further elaborate this topic, the error state kinematic

differential equations of the Atom Strapdown have been developed. This allows to point out the conditions under which the phase shift error exceeds the dynamic range limit posed by the fringe signal cosine flank. For terrestrial applications, the misalignment was identified as the major impact factor in this regard. For other applications like in space, parameter assessment for system integration, or in order to derive quality requirements for system calibration, the developed methods can readily be applied.

Result 2: Quantum Inertial Navigation System Based on Extended Kalman Filter

The Atom Strapdown can be utilized for a second hybridization technique. Rather than just reconstructing the fringe pattern by computing the phase shift, this second method allows to estimate the systematic offset of the classical sensors. This is realized by predicting the phase shift in the frame of an extended Kalman filter (EKF). The update step of the filter is essentially an attempt to distribute the phase shift error to certain states that are modeled in the system. The observation sensitivities, as derived from the explicit formulation of the phase shift in the solution of the Atom Strapdown differential equations, are acting as a weight for this distribution. In a sense, the EKF is a solution to the second ambiguity problem concerning the phase shift errors. Systematic effects and long term drift of the phase shift error can efficiently be removed, leaving the majority of remaining errors being caused by stochastic effects and systematics that depend on the trajectory dynamics.

This method was demonstrated for a minimum state vector configuration consisting of the biases of the classical accelerometers and gyroscopes. The system in this minimum configuration was shown to be stable. Furthermore, systematic effects like lever arm and misalignment between IMU and CAI were compensated with the bias states alone, as demonstrated by a scenario under dynamic conditions.

An extended observability study has revealed that it is not sufficient to have one or two counterpropagating CAI measuring sequentially in order to achieve a stable system in a six degree of freedom navigation case. The main reason for this is the ability of the atoms to move freely in space. The velocity and position of the atoms in the s-frame is affected by inertial effects on all axes. This generates a sensitivity to the accelerations and angular rates on all axes which builds up, the larger the velocity and position displacement of the atoms grows. Thus, the use of CAI that cover all six degrees of freedom seems pivotal.

The misalignment and lever arm as state vector augmentations have been discussed, and the observability conditions have been evaluated. This opens the possibility for an online estimation under certain dynamic conditions. Based on the results, strategies for initial calibration procedures of complete QINS can be elaborated.

Result 3: Limits and Uncertainty of CAI Related to Inertial Navigation

Another result of modeling the CAI is the restriction of the sensor in terms of dynamic range, which can be further differentiated in *soft limits* and *hard limits*. While the soft limits, defined by the phase shift ambiguity, can be removed by the use of high rate sensors in the frame of the QINS, the hard limits come in shape of actual physical restrictions of CAI. For measurements in laser direction the acceleration is only limited by the dimension of the vacuum chamber, which can be rather large. Accelerations perpendicular to the sensitive axis are limited by the width of the laser. Depending on the interrogation time, the lateral acceleration is limited to $25\,\mathrm{m/s^2}$, for $T = 10\,\mathrm{ms}$ and a laser width of 10 mm, while for interrogation times of 25 ms the limit is at $4\,\mathrm{m/s^2}$. For any non-constant acceleration signals over the course of the measurement it was demonstrated that CAI introduces systematic errors for any signals that are not point-

symmetric in time with respect to the mirror pulse at time T. Apart from that, CAI is essentially a low-pass filter for accelerations and angular rates, and additionally blocks certain signal frequencies.

The hard limit for angular rates is related to the contrast of the measurement. The contrast is reduced exponentially with the path separation, i.e. the distance of the two wave packets, at the second beam splitter pulse at time $2T$. A geometric approach to model this impact factor was presented. It can be shown that the path separation scales with the angular rate and the recoil velocity of the beam splitters. Depending on the interrogation time, the limitations to angular rates are very strict: an interrogation time of 10 ms yields a limit of 41.3 mrad/s, while for interrogation times of 25 ms that are needed to compare with classical navigation grade sensors, the limit is at a very low 6.6 mrad/s.

This model works quite well for most applications with short interrogation times. Longer times make the consideration of the thermal expansion of the wave packet necessary. In this regard, the contrast loss can as well be explained with the phase shift error due to uncertainty of the wave packet position and velocity. This was demonstrated using some simplified examples, but ultimately the complete distribution of the wave packets would need to be modeled, which is well beyond the scope of the *engineering approach* which is pursued in this thesis. Some studies, e.g. Rakholia et al. (2014), even mention that the contrast could benefit from a large spread of the wave packet since the overlap is partially recovered.

CAI data from a stationary experiment without stabilization have been analyzed. It was demonstrated that besides the phase shift also the amplitude and offset of the fringe pattern are time-varying. Further analysis has revealed that even the uncertainty of the parameters is varying, indicating the non-stationary nature of the noise processes over long periods of time.

These results show that dynamic experiments with time-depending rotation rates and accelerations are a necessity in order to further develop and adapt the models and ultimately to proceed in this field. For this static data set, the EKF was successfully applied and the online bias correction for the acceleration measurement was demonstrated. The methods that were used for the fringe pattern estimation and the uncertainty assessment can be further developed to allow an online fault detection of CAI.

Result 4: Solutions to QINS Related Trade-Offs

The CAI as inertial sensor was introduced as a system with a multitude of engineering options and optimization problems. The timing of the measurement cycle alone yields three major adjustments that were discussed. Here, the preparation time and the interrogation time have the largest impact.

The preparation time, required to prepare and cool the atoms, is related to the number of atoms that are incorporated in the wave packet and thus the quantum projection noise level. Thus, it correlates with the accuracy of the CAI. The combination with a complete classical IMU has the great advantage that a continuous measurement is available to cover the timespan in which the CAI is not measuring. It was shown that for sufficiently large bias stability, which is given by some tactical and most navigation grade sensors, this dead time is allowed to be quite large, up to several tens of seconds, so there is no limitation from the side of the QINS. In terms of the benefit to the CAI accuracy itself it was shown that the performance is limited by the laser phase noise. One of the largest preparation times reported in literature is 600 ms (Freier et al., 2016). Consequently, the preparation time should be chosen as long as necessary to reach the limit due to the laser phase noise and thus the maximum performance.

The second adjustment is the interrogation time T. Using CAI alone, the sensitivity to accelerations and angular rates scales with T^2, the dynamic range with $1/T^2$. With the proposed QINS this trade-off is already solved by the high rate IMU, and any additional systematic phase shift errors are removed by the EKF. Under the circumstance that the phase shift error is mainly composed of stochastic errors, an optimization problem between the quality of the classical sensors and the performance gain of the QINS has been revealed. Using steady state formulation of the EKF, models for improvement and a penalty factor related to the IMU noise have been established. This allows to find the optimal IMU for any specific CAI parameters, in terms of variance or power spectral density of the accelerations and angular rates. The location of the optimum mainly depends on the scale factor of the CAI, and to a lower degree on the signal to noise ratio (SNR) of the CAI. The sensitivity gain of the QINS over the IMU is entirely defined by the CAI SNR.

From a more general perspective, two different QINS designs based on the methods have been elaborated. It was shown that the CAI-based design with supporting accelerometers (QINS-C) yields the best sensitivity to accelerations measurements. The large CAI scale factor can only be supported with very high sensitivity classical acceleration sensors, that often go in hand with an unfavorable large bias drift. A continuous solution is thus not possible, and the main application appears to be a mere gravimetry operational mode, with the additional opportunity of providing angular rate measurements. The latter, however, is expected to be in the tactical/navigation grade quality range. The IMU-based design with supporting CAI (QINS-I) yields the best overall performance. The simulations have revealed that the *sensitivity* of CAI to accelerations and angular rates is not necessarily the main argument for its use in dynamic applications, since the gain is coupled to the quality of the classical sensor that is used for the hybridization. The real improvement results from the long term stability of the CAI by the bias estimation of the classical IMU. The total position error of the system is defined by the classical gyroscope thanks to the Schuler-bounding of accelerometer-related errors. Consequently, QINS is predestined to be used for high-accuracy, medium-term inertial navigation. For the QINS-I in combination with Q-Flex accelerometers and strategic grade FOG, a horizontal position error of below 10 m during the first hour of free inertial navigation seems plausible. For longer times, switching to gravimetry operation mode in conjunction with gravity maps could still limit the position error to the lower 100 m level (L. Wu et al., 2017). Combined operational modes with intelligent adaption might thus be worth considering in order to achieve the best possible overall performance.

A general framework for the hybridization of classical IMU and CAI has been developed, which is vital for first assessments of applications of CAI in navigation related tasks. The additional topics that have been discussed are significant tools for the planning of future integrated QINS designs. That being said, further steps toward an actual hardware platform include additional questions that cannot be answered by simulations alone. This especially involves the time synchronization of the systems, the cycle time of the integrated circuits of the navigation computer and the time delays of the laser feedback control. Furthermore, in-situ calibration of the CAI sensor and the complete QINS needs to be further evaluated and discussed in order to reduce the problems caused by a misalignment between the sensors. Sophisticated calibration procedures need to be established. At this stage, prototyping and experimental validation are essential in order to iterate to a final product.

A
Appendix

A.1 Physical and Technical Constants

Physical constants

Speed of light in vacuum

$$c = 299\,792\,458\,\mathrm{m/s}. \tag{A.1}$$

Planck constant

$$h = 6.626\,070\,15 \times 10^{-34}\,\mathrm{Js}. \tag{A.2}$$

Reduced Planck constant

$$\hbar = \frac{h}{2\pi} = 1.054\,571\,817 \times 10^{-34}\,\mathrm{Js}. \tag{A.3}$$

Boltzmann constant

$$k_\mathrm{B} = 1.380\,649\,1 \times 10^{-23}\,\mathrm{J/K}. \tag{A.4}$$

Unit atom mass

$$u = 1.660\,539\,066\,6 \times 10^{-27}\,\mathrm{kg}. \tag{A.5}$$

Earth rate

$$\Omega_{ie}^{e} = 7.292\,115 \times 10^{-5}\,\mathrm{rad/s}. \tag{A.6}$$

Reoccurring technical parameters

Effective wave number for ^{87}Rb

$$k_\mathrm{e} = 4\pi \cdot \frac{1}{780 \cdot 10^{-9}}\ \mathrm{m}^{-1}. \tag{A.7}$$

Recoil velocity for $|1\rangle \rightarrow |2\rangle$ state transition of ^{87}Rb

$$v_\mathrm{rec} = 11.8\,\mathrm{mm/s}. \tag{A.8}$$

Initial atom split velocity for multi axis design

$$v_{sa}^{s} = \pm 94\,\mathrm{mm/s}. \tag{A.9}$$

A.2 Laplace Correspondences

Laplace domain $F(s)$	Time domain $f(t)$
1	$\delta(t)$
e^{-as}	$\delta(t-a)$
$\frac{1}{s}$	1
$\frac{1}{s^2}$	t
$\frac{1}{s^n}$	$\frac{t^{n-1}}{(n-1)!}$
$\frac{1}{s+a}$	e^{-at}
$\frac{1}{s^2+a^2}$	$\frac{1}{a}\sin at$
$\frac{s}{s^2+a^2}$	$\cos at$
$sX(s)+x_0$	$\frac{\partial x(t)}{\partial t}$
$\frac{1}{s}X(s)$	$\int_0^t x(t)\,dt$
$F(s)G(s)$	$\int_0^t f(\tau)g(t-\tau)\,d\tau$

Table A.1: Laplace correspondences

A.3 Matrix Algebra

Derivative of a function with respect to a vector

Let f denote a scalar function depending on a vector $\mathbf{x} = [x_1, x_2, ..., x_n]^{\mathrm{T}}$, then the derivative $\boldsymbol{\nabla} f = \frac{\partial f}{\partial \mathbf{x}}$,

$$\boldsymbol{\nabla} f = \begin{bmatrix} \frac{\partial f}{\partial x_1} & \frac{\partial f}{\partial x_2} & ... & \frac{\partial f}{\partial x_n} \end{bmatrix}, \tag{A.10}$$

is a vector as well and represents the gradient of the function with respect to the single dimensions of the vector $\mathbf{x}$.

Derivative of a vector valued function

Let $\mathbf{f}$ denote a set of equations, depending on a vector $\mathbf{x} = [x_1, x_2, ..., x_n]^{\mathrm{T}}$,

$$\mathbf{f}(\mathbf{x}) = \begin{bmatrix} f_1(\mathbf{x}) \\ f_2(\mathbf{x}) \\ ... \\ f_n(\mathbf{x}) \end{bmatrix}. \tag{A.11}$$

Then the derivative $\mathbf{J} = \frac{\partial \mathbf{f}}{\partial \mathbf{x}}$ is composed of the individual functions with respect to the vector,

$$\mathbf{J} = \frac{\partial \mathbf{f}(\mathbf{x})}{\partial \mathbf{x}} = \begin{bmatrix} \frac{\partial f_1(\mathbf{x})}{\partial x_1} & \frac{\partial f_1(\mathbf{x})}{\partial x_2} & ... & \frac{\partial f_1(\mathbf{x})}{\partial x_N} \\ \frac{\partial f_2(\mathbf{x})}{\partial x_1} & \frac{\partial f_2(\mathbf{x})}{\partial x_2} & ... & ... \\ ... & ... & ... & ... \\ \frac{\partial f_n(\mathbf{x})}{\partial x_1} & ... & ... & \frac{\partial f_n(\mathbf{x})}{\partial x_n} \end{bmatrix}. \tag{A.12}$$

The derivative may be called the Jacobian of $\mathbf{f}$. One special case is the differentiation of an n-by-1 vector with respect to itself,

$$\frac{\partial \mathbf{a}}{\partial \mathbf{a}} = \frac{\partial [a_1, a_2, ..., a_n]^{\mathrm{T}}}{\partial [a_1, a_2, ..., a_n]^{\mathrm{T}}} = \begin{bmatrix} \frac{\partial a_1}{\partial a_1} & \frac{\partial a_1}{\partial a_2} & ... & \frac{\partial a_1}{\partial a_n} \\ \frac{\partial a_2}{\partial a_1} & \frac{\partial a_2}{\partial a_2} & ... & \frac{\partial a_2}{\partial a_n} \\ ... & ... & ... & ... \\ \frac{\partial a_n}{\partial a_1} & \frac{\partial a_n}{\partial a_2} & ... & \frac{\partial a_n}{\partial a_n} \end{bmatrix} = \begin{bmatrix} 1 & 0 & ... & 0 \\ 0 & 1 & ... & 0 \\ ... & ... & ... & ... \\ 0 & 0 & ... & 1 \end{bmatrix} = \mathbf{I}_{(nxn)}, \tag{A.13}$$

which yields the identity $\mathbf{I}$ with dimension n-by-n.

Hessian matrix

Let $\boldsymbol{\mathcal{H}}$ denote the second derivative of the function $\mathbf{f}$ w.r.t. the vector $\mathbf{x} = [x_1, x_2, ..., x_n]^{\mathrm{T}}$, then it is the same as the derivative of the Jacobian $\mathbf{J}$ with respect to the vector $\mathbf{x}$,

$$\boldsymbol{\mathcal{H}} = \frac{\partial \mathbf{J}(\mathbf{x})}{\partial \mathbf{x}} = \frac{\partial^2 \mathbf{f}(\mathbf{x})}{\partial \mathbf{x} \partial \mathbf{x}} = \begin{bmatrix} \frac{\partial^2 f_1(\mathbf{x})}{\partial x_1 \partial x_1} & \frac{\partial^2 f_1(\mathbf{x})}{\partial x_1 \partial x_2} & ... & \frac{\partial^2 f_1(\mathbf{x})}{\partial x_1 \partial x_n} \\ \frac{\partial^2 f_2(\mathbf{x})}{\partial x_2 \partial x_1} & \frac{\partial^2 f_2(\mathbf{x})}{\partial x_2 \partial x_2} & ... & ... \\ ... & ... & ... & ... \\ \frac{\partial^2 f_n(\mathbf{x})}{\partial x_n \partial x_1} & ... & ... & \frac{\partial^2 f_n(\mathbf{x})}{\partial x_n \partial x_n} \end{bmatrix}. \tag{A.14}$$

Note that the matrix is quadratic in this case.

Derivative of scalar products

Let $\mathbf{a}$ and $\mathbf{b}$ denote 3-by-1 vectors, and $\mathbf{c}$ is defined as the scalar product between $\mathbf{a}$ and $\mathbf{b}$ so that $\mathbf{c} = \mathbf{a} \cdot \mathbf{b}$. Then

$$\frac{\partial \mathbf{c}}{\partial \mathbf{a}} = \frac{\partial \begin{bmatrix} a_1 \\ a_2 \\ a_3 \end{bmatrix} \cdot \begin{bmatrix} b_1 \\ b_2 \\ b_3 \end{bmatrix}}{\partial \begin{bmatrix} a_1 \\ a_2 \\ a_3 \end{bmatrix}} = \frac{\partial \left(a_1 b_1 + a_2 b_2 + a_3 b_3\right)}{\partial \begin{bmatrix} a_1 \\ a_2 \\ a_3 \end{bmatrix}} = \begin{bmatrix} \frac{\partial \mathbf{c}}{\partial a_1} & \frac{\partial \mathbf{c}}{\partial a_2} & \frac{\partial \mathbf{c}}{\partial a_3} \end{bmatrix} = \begin{bmatrix} b_1 & b_2 & b_3 \end{bmatrix} = \mathbf{b}^{\mathrm{T}}. \tag{A.15}$$

Likewise, as the scalar product is commutative,

$$\frac{\partial \mathbf{c}}{\partial \mathbf{b}} = \mathbf{a}^{\mathrm{T}}. \tag{A.16}$$

Derivative of a cross product

Differentiation w.r.t. a vector in a cross product of two 3-by-1 vectors yields

$$\frac{\partial}{\partial \mathbf{a}} \left[\mathbf{a} \times \mathbf{b}\right] = -[\mathbf{b}\times] = [\mathbf{b}\times]^{\mathrm{T}}. \tag{A.17}$$

In detail, let $\mathbf{c} = \mathbf{a} \times \mathbf{b}$, then

$$\frac{\partial \mathbf{c}}{\partial \mathbf{a}} = \frac{\partial \begin{bmatrix} a_1 \\ a_2 \\ a_3 \end{bmatrix} \times \begin{bmatrix} b_1 \\ b_2 \\ b_3 \end{bmatrix}}{\partial \begin{bmatrix} a_1 \\ a_2 \\ a_3 \end{bmatrix}} = \frac{\partial \begin{bmatrix} a_2 b_3 - a_3 b_2 \\ a_3 b_1 - a_1 b_3 \\ a_1 b_2 - a_2 b_1 \end{bmatrix}}{\partial \begin{bmatrix} a_1 \\ a_2 \\ a_3 \end{bmatrix}} = \begin{bmatrix} \frac{\partial c_1}{\partial a_1} & \frac{\partial c_1}{\partial a_2} & \frac{\partial c_1}{\partial a_3} \\ \frac{\partial c_2}{\partial a_1} & \frac{\partial c_2}{\partial a_2} & \frac{\partial c_2}{\partial a_3} \\ \frac{\partial c_3}{\partial a_1} & \frac{\partial c_3}{\partial a_2} & \frac{\partial c_3}{\partial a_3} \end{bmatrix} = \begin{bmatrix} 0 & b_3 & -b_2 \\ -b_3 & 0 & b_1 \\ b_2 & -b_1 & 0 \end{bmatrix} = -[\mathbf{b}\times]. \tag{A.18}$$

Likewise

$$\frac{\partial}{\partial \mathbf{b}} \left[\mathbf{a} \times \mathbf{b}\right] = [\mathbf{a}\times]. \tag{A.19}$$

Derivative of concatenated cross products

Double cross product differentiated w.r.t. $\mathbf{a}$ via product rule:

$$\begin{aligned} \frac{\partial}{\partial \mathbf{a}} \left[\mathbf{a} \times (\mathbf{a} \times \mathbf{b})\right] &= \frac{\partial}{\partial \mathbf{a}} \mathbf{a} \times (\mathbf{a} \times \mathbf{b}) + \mathbf{a} \times \frac{\partial}{\partial \mathbf{a}} (\mathbf{a} \times \mathbf{b}) \\ &= -[(\mathbf{a} \times \mathbf{b})\times] - [\mathbf{a}\times][\mathbf{b}\times]. \end{aligned} \tag{A.20}$$

Double cross product differentiated w.r.t. $\mathbf{b}$ via product rule:

$$\begin{aligned} \frac{\partial}{\partial \mathbf{b}} \left[\mathbf{a} \times (\mathbf{a} \times \mathbf{b})\right] &= \frac{\partial}{\partial \mathbf{b}} \mathbf{a} \times (\mathbf{a} \times \mathbf{b}) + \mathbf{a} \times \frac{\partial}{\partial \mathbf{b}} (\mathbf{a} \times \mathbf{b}) \\ &= [\mathbf{a}\times][\mathbf{a}\times]. \end{aligned} \tag{A.21}$$

Double cross product with different factors $\mathbf{d} = \mathbf{a} \times (\mathbf{b} \times \mathbf{c})$, differentiated w.r.t. $\mathbf{a}$:

$$\frac{\partial \mathbf{d}}{\partial \mathbf{a}} = -[(\mathbf{b} \times \mathbf{c})\times]. \tag{A.22}$$

Similarly,

$$\frac{\partial \mathbf{d}}{\partial \mathbf{b}} = -[\mathbf{a}\times][\mathbf{c}\times]. \tag{A.23}$$

Triple cross product differentiated w.r.t. $\mathbf{a}$ via product rule:

$$\begin{aligned}\frac{\partial}{\partial \mathbf{a}}\left[\mathbf{a}\times(\mathbf{a}\times(\mathbf{a}\times\mathbf{b}))\right]\\ = \frac{\partial}{\partial \mathbf{a}}\mathbf{a}\times(\mathbf{a}\times(\mathbf{a}\times\mathbf{b})) + \mathbf{a}\times(\frac{\partial}{\partial \mathbf{a}}\mathbf{a}\times(\mathbf{a}\times\mathbf{b})) + \mathbf{a}\times(\mathbf{a}\times\frac{\partial}{\partial \mathbf{a}}(\mathbf{a}\times\mathbf{b}))\\ = -\left[(\mathbf{a}\times(\mathbf{a}\times\mathbf{b}))\times\right] - [\mathbf{a}\times]\left[(\mathbf{a}\times\mathbf{b})\times\right] - [\mathbf{a}\times][\mathbf{a}\times][\mathbf{b}\times].\end{aligned} \tag{A.24}$$

Triple cross product differentiated w.r.t. $\mathbf{b}$ via product rule:

$$\begin{aligned}\frac{\partial}{\partial \mathbf{b}}\left[\mathbf{a}\times(\mathbf{a}\times(\mathbf{a}\times\mathbf{b}))\right]\\ = \frac{\partial}{\partial \mathbf{b}}\mathbf{a}\times(\mathbf{a}\times(\mathbf{a}\times\mathbf{b})) + \mathbf{a}\times(\frac{\partial}{\partial \mathbf{b}}\mathbf{a}\times(\mathbf{a}\times\mathbf{b})) + \mathbf{a}\times(\mathbf{a}\times\frac{\partial}{\partial \mathbf{b}}(\mathbf{a}\times\mathbf{b}))\\ = [\mathbf{a}\times][\mathbf{a}\times][\mathbf{a}\times].\end{aligned} \tag{A.25}$$

Derivative of scalar triple products

Let $\mathbf{d} = \mathbf{a}\cdot(\mathbf{b}\times\mathbf{c})$, then

$$\begin{aligned}\frac{\partial \mathbf{d}}{\partial \mathbf{a}} &= \frac{\partial \begin{bmatrix}a_1\\a_2\\a_3\end{bmatrix}\cdot\left(\begin{bmatrix}b_1\\b_2\\b_3\end{bmatrix}\times\begin{bmatrix}c_1\\c_2\\c_3\end{bmatrix}\right)}{\partial \begin{bmatrix}a_1\\a_2\\a_3\end{bmatrix}} = \frac{\partial\left(a_1b_2c_3 - a_1b_3c_2 + a_2b_3c_1 - a_2c_3b_1 + a_3b_1c_2 - a_3b_2c_1\right)}{\partial \begin{bmatrix}a_1\\a_2\\a_3\end{bmatrix}}\\ &= \begin{bmatrix}\frac{\partial \mathbf{d}}{\partial a_1} & \frac{\partial \mathbf{d}}{\partial a_2} & \frac{\partial \mathbf{d}}{\partial a_3}\end{bmatrix} = \begin{bmatrix}b_2c_3 - c_2b_3 & b_3c_1 - b_1c_3 & b_1c_2 - b_2c_1\end{bmatrix} = [\mathbf{b}\times\mathbf{c}]^{\mathrm{T}} = -[\mathbf{b}\times\mathbf{c}].\end{aligned} \tag{A.26}$$

Likewise,

$$\frac{\partial \mathbf{d}}{\partial \mathbf{b}} = \begin{bmatrix}\frac{\partial \mathbf{d}}{\partial b_1} & \frac{\partial \mathbf{d}}{\partial b_2} & \frac{\partial \mathbf{d}}{\partial b_3}\end{bmatrix} = \begin{bmatrix}-a_2c_3 + c_2a_3 & -a_3c_1 + a_1c_3 & -a_1c_2 + a_2c_1\end{bmatrix} = -[\mathbf{a}\times\mathbf{c}]^{\mathrm{T}} = [\mathbf{a}\times\mathbf{c}], \tag{A.27}$$

and

$$\frac{\partial \mathbf{d}}{\partial \mathbf{c}} = \begin{bmatrix}\frac{\partial \mathbf{d}}{\partial c_1} & \frac{\partial \mathbf{d}}{\partial c_2} & \frac{\partial \mathbf{d}}{\partial c_3}\end{bmatrix} = \begin{bmatrix}a_2b_3 - a_3b_2 & a_3b_1 - a_1b_3 & a_1b_2 - a_2b_1\end{bmatrix} = [\mathbf{a}\times\mathbf{b}]^{\mathrm{T}} = -[\mathbf{a}\times\mathbf{b}]. \tag{A.28}$$

Furthermore it can be shown that

$$-[\mathbf{a}\times\mathbf{b}] = \mathbf{a}^{\mathrm{T}}[\mathbf{b}\times]. \tag{A.29}$$

Finally, let $\mathbf{d} = \mathbf{k}\cdot[\mathbf{a}\times(\mathbf{b}\times\mathbf{c})]$, then

$$\frac{\partial \mathbf{d}}{\partial \mathbf{a}} = -\mathbf{k}^{\mathrm{T}}[(\mathbf{b}\times\mathbf{c})\times]. \tag{A.30}$$

Another non-trivial derivative needed in Sec. 4.3.3 is $\mathbf{d} = ((\mathbf{I} - [\mathbf{a}\times])\mathbf{b}\times\mathbf{c})$. The term is first reformulated,

$$\begin{aligned}\mathbf{d} &= ((\mathbf{b} - \mathbf{a}\times\mathbf{b})\times\mathbf{c})\\ &= \mathbf{b}\times\mathbf{c} - (\mathbf{a}\times\mathbf{b})\times\mathbf{c}\\ &= \mathbf{b}\times\mathbf{c} + \mathbf{c}\times(\mathbf{a}\times\mathbf{b})\\ &= \mathbf{b}\times\mathbf{c} - \mathbf{c}\times(\mathbf{b}\times\mathbf{a}).\end{aligned} \tag{A.31}$$

The derivative with respect to $\mathbf{a}$ reads

$$\frac{\partial \mathbf{d}}{\partial \mathbf{a}} = -[\mathbf{c}\times][\mathbf{b}\times]. \tag{A.32}$$

Matrix Exponential

The matrix exponential $\exp \mathbf{A}$ can be evaluated as an infinite power series,

$$\exp \mathbf{A} = \sum_{k=0}^{\infty} \frac{1}{k!}\mathbf{A}^k, \tag{A.33}$$

if convergence is provided (Papula, 2007). The matrix $\mathbf{A}$ thus needs to be *nilpotent*, which is the case when $\mathbf{A}^k = \mathbf{0}$ for sufficiently large exponents k.

A.4 Stochastic Error Modelling

A.4.1 Allan Variance

In order to associate a variance to the spectral density, the following integral needs to be evaluated (Schweppe, 1973):

$$\sigma^2 = \int_{-\infty}^{\infty} S(f)\, df. \tag{A.34}$$

The classical Allan variance AV_c can be defined by transferring the spectral density S_y into time domain

$$AV_c(\tau) = \int_0^{f_c} S_y(f) \cdot 4\frac{sin^4(\pi\tau f)}{(\pi\tau f)^2}\, df, \tag{A.35}$$

with the cut-off frequency f_c used as upper limit, and zero as lower limit for the integral. Apart from that, the equation is essentially Eq. (A.34) with a windowing function $4\sin^4(\pi\tau f)/(\pi\tau f)^2$. This windowing function introduces a time constant τ, and acts as weight for certain frequency ranges. The lower τ is, the wider the spectrum that is covered. For large τ, a small region at low frequencies is weighted larger.

A modification that is often considered superior with respect to the classical AV_c is the overlapping Allan variance (AV). Based on a set of phase data x, the overlapping Allan variance reads (Riley, 2008):

$$AV(\tau) = \frac{1}{2(n-2m)\tau^2} \sum_{i=1}^{n-2m} \left[x_{i+2m} - 2x_{i+m} + x_i\right]^2. \tag{A.36}$$

Here, n is the number of measurements, τ_0 corresponds to the data rate and $\tau = m\tau_0$ is the averaging time, where the integer m represents the size of the averaging window.

A.4.2 Response of a LTI System to Random Perturbation Input

The response $y(t)$ of a causal system $f(t)$ to an input $x(t)$ is given by

$$y(t) = \int_0^t f(t-\tau)x(\tau)\, d\tau. \tag{A.37}$$

The autocorrelation φ_{yy} of $y(t)$ reads

$$\varphi_{yy}(t_2 - t_1) = E\left\langle \int_0^{t_1} f(t_1 - \tau_1)x(\tau_1)\, d\tau_1 \int_0^{t_2} f(t_2 - \tau_2)x(\tau_2)\, d\tau_2 \right\rangle. \tag{A.38}$$

The response function is identical for each sample so that the integrals can be combined,

$$\varphi_{yy}(t_2 - t_1) = \int_0^{t_1} \int_0^{t_2} f(t_1 - \tau_1)f(t_2 - \tau_2)E\langle x(\tau_1)x(\tau_2)\rangle\, d\tau_1 d\tau_2. \tag{A.39}$$

For an input consistent of an ensemble of constant functions with MSE $\langle x_0^2\rangle$, the following MSE of the output can be stated (Maybeck, 1979)

$$E\langle y^2(t)\rangle = \int_{\tau_2=0}^{\tau_2=t} \int_{\tau_1=0}^{\tau_1=t} f(t - \tau_1)f(t - \tau_2)E\langle x_0^2\rangle\, d\tau_1 d\tau_2. \tag{A.40}$$

which results in

$$E\langle y^2(t)\rangle = E\langle x_0^2\rangle \int_0^t f^2(t - \tau)\, d\tau. \tag{A.41}$$

As an example, for white noise with PSD N^2 the autocorrelation function reads (Britting, 1971)

$$\varphi_{xx}(t_2 - t_1) = N^2\delta(t_2 - t_1), \tag{A.42}$$

so that the output results in

$$E\langle y^2(t)\rangle = N^2 \int_0^t f^2(t - \tau)\, d\tau. \tag{A.43}$$

In the case that $f = 1$, which represents an integrator, the result is the random walk process

$$E\langle y^2(t)\rangle = N^2 t. \tag{A.44}$$

A.4.3 Discrete Time vs. Continuous Time White Noise

Following Farrell et al. (2022), let a measurement denoted by $\tilde{a}(t)$ be composed of the true signal $a(t)$ and a white noise process $q(t)$, then

$$\tilde{a}(t) = a(t) + q(t). \tag{A.45}$$

The discrete time measurement yields

$$\tilde{a}(k) = \frac{1}{T} \int_{t_k}^{t_{k+1}} (a(\tau) + q(\tau))\ \mathrm{d}\tau, \tag{A.46}$$

where T is the time between t_k and t_{k+1}, i.e. sample time. The Eq. (A.46) can be divided into two terms,

$$\tilde{a}(k) = \bar{a}(k) + q_d(k). \tag{A.47}$$

The first term resembles the mean $\bar{a}(k)$ of the interval, the second one $q_d(k)$ reads

$$q_d(k) = \frac{1}{T} \int_{t_k}^{t_{k+1}} q(\tau)\, \mathrm{d}\tau. \tag{A.48}$$

The variance can now be stated,

$$E\langle q_d^2(k)\rangle = \frac{1}{T^2} \int_{t_k}^{t_{k+1}} N^2\, \mathrm{d}\tau. \tag{A.49}$$

For a constant N^2, this results in the following representation of the discrete process noise variance

$$Q_k(k) = E\langle q_d^2(k)\rangle = \frac{1}{T}N^2. \tag{A.50}$$

A.5 Error State Kinematics

The derivation of the error state differential equations for the QINS is summarized in this section. In order to reduce unnecessary complexity, it is assumed that $\mathbf{C}_b^s = \mathbf{I}$, meaning that the s- and the b-frame are considered to be aligned, up to an error due to misalignment. The indices are furthermore reduced, so that the specific forces and angular rates read $\mathbf{f}^b$ and $\boldsymbol{\omega}^b$, respectively. It was established in Eq. (4.6) and Eq. (4.7) that for a rigid connection between the s- and the b-frame $\mathbf{f}_{is}^b = \mathbf{f}_{ib}^b$ and $\boldsymbol{\omega}_{is}^b = \boldsymbol{\omega}_{ib}^b$. According to the definition of the sensor frame in Sec. 3.4 it is furthermore assumed that the initial atom position is $\mathbf{x}_{sa}^s = \mathbf{0}$.

Case 1: No displacement and misalignment between s-frame and b-frame

The equations for the velocity $\dot{\mathbf{v}}_{sa}^s$ and nominal velocity $\dot{\tilde{\mathbf{v}}}_{sa}^s$ under the assumption of perfect alignment and without lever arms are

$$\dot{\mathbf{v}}_{sa}^s = -(\mathbf{f}^s + \mathbf{b_a}) + 2(\boldsymbol{\omega}^s + \mathbf{b_g}) \times \mathbf{v}_{sa}^s, \tag{A.51}$$

$$\dot{\tilde{\mathbf{v}}}_{sa}^s = -(\mathbf{f}^s + \tilde{\mathbf{b}_\mathbf{a}}) + 2(\boldsymbol{\omega}^s + \tilde{\mathbf{b}_\mathbf{g}}) \times \tilde{\mathbf{v}}_{sa}^s. \tag{A.52}$$

The nominal values are defined as follows, whereas the δ indicates the corresponding error state:

$$\tilde{\mathbf{v}}_{sa}^s = \mathbf{v}_{sa}^s - \delta\mathbf{v}_{sa}^s, \qquad \tilde{\mathbf{b}_\mathbf{a}} = \mathbf{b_a} - \delta\mathbf{b_a}, \qquad \tilde{\mathbf{b}_\mathbf{g}} = \mathbf{b_g} - \delta\mathbf{b_g}.$$

The effect of the change of orientation between $\mathbf{f}^s$ and $\boldsymbol{\omega}^s$ is neglected in the frame of the error state kinematic equations. The error equations are

$$\delta\mathbf{v}_{sa}^s = \mathbf{v}_{sa}^s - \tilde{\mathbf{v}}_{sa}^s, \tag{A.53}$$

$$\delta\dot{\mathbf{v}}_{sa}^s = \dot{\mathbf{v}}_{sa}^s - \dot{\tilde{\mathbf{v}}}_{sa}^s. \tag{A.54}$$

This means for the ODE of $\delta\dot{\mathbf{v}}_{sa}^s$:

$$\begin{aligned}
\delta\dot{\mathbf{v}}_{sa}^s &= -(\mathbf{f}^s + \mathbf{b_a}) + 2\boldsymbol{\omega}^s \times \mathbf{v}_{sa}^s - 2\mathbf{b_g} \times \mathbf{v}_{sa}^s \\
&\quad - (-(\mathbf{f}^s + \tilde{\mathbf{b}_\mathbf{a}}) + 2\boldsymbol{\omega}^s \times \tilde{\mathbf{v}}_{sa}^s - 2\tilde{\mathbf{b}_\mathbf{g}} \times \tilde{\mathbf{v}}_{sa}^s) \\
&= \mathbf{f}^s + \mathbf{b_a} - 2\boldsymbol{\omega}^s \times \mathbf{v}_{sa}^s - 2\mathbf{b_g} \times \mathbf{v}_{sa}^s \\
&\quad - (\mathbf{f}^s + \mathbf{b_a} - \delta\mathbf{b_a} - 2\boldsymbol{\omega}^s \times (\mathbf{v}_{sa}^s - \delta\mathbf{v}_{sa}^s) - 2(\mathbf{b_g} - \delta\mathbf{b_g}) \times (\mathbf{v}_{sa}^s - \delta\mathbf{v}_{sa}^s)) .
\end{aligned} \tag{A.55}$$

The equation is now expanded. Products of error terms are neglected. The resulting equation is

$$\begin{aligned}
\delta\dot{\mathbf{v}}_{sa}^s &= -\delta\mathbf{b_a} + 2\boldsymbol{\omega}^s \times \delta\mathbf{v}_{sa}^s + 2\mathbf{b_g} \times \delta\mathbf{v}_{sa}^s + 2\delta\mathbf{b_g} \times \mathbf{v}_{sa}^s \\
&= -\delta\mathbf{b_a} + 2(\boldsymbol{\omega}^s + \mathbf{b_g}) \times \delta\mathbf{v}_{sa}^s + 2\delta\mathbf{b_g} \times \mathbf{v}_{sa}^s.
\end{aligned} \tag{A.56}$$

Case 2: Error state kinematics including lever arm and misalignment

Let the true alignment $\mathbf{C}_b^s$ be composed of the nominal value $\tilde{\mathbf{C}}_b^s$ and the orientation error $\delta\mathbf{C}_b^s$,

$$\mathbf{C}_b^s = \tilde{\mathbf{C}}_b^s \delta\mathbf{C}_b^s. \tag{A.57}$$

The orientation error is expressed as matrix exponential with the misalignment, $\delta\mathbf{C}_b^s = \exp[\boldsymbol{\gamma}_b^s\times]$, and truncated after the first order term,

$$\delta\mathbf{C}_b^s = \mathbf{I} - [\boldsymbol{\gamma}_b^s\times]. \tag{A.58}$$

The nominal value can thus be expressed as

$$\tilde{\mathbf{C}}_b^s = (\mathbf{I} - [\boldsymbol{\gamma}_b^s\times])\mathbf{C}_b^s. \tag{A.59}$$

This equation can be solved for the misalignment,

$$[\boldsymbol{\gamma}_b^s\times] = \mathbf{I} - \mathbf{C}_b^s\tilde{\mathbf{C}}_b^s. \tag{A.60}$$

The ODE for the velocities read

$$\dot{\mathbf{v}}_{sa}^s = -\left((\mathbf{f}^b + \mathbf{b_a}) - 2(\boldsymbol{\omega}^b + \mathbf{b_g})\times\mathbf{v}_{sa}^s - (\boldsymbol{\omega}^b + \mathbf{b_g})\times[(\boldsymbol{\omega}^b + \mathbf{b_g})\times\mathbf{x}_{bs}^b]\right), \tag{A.61}$$

$$\begin{aligned}\dot{\tilde{\mathbf{v}}}_{sa}^s = &-\Big((\mathbf{I} - [\boldsymbol{\gamma}_b^s\times])(\mathbf{f}^b + \tilde{\mathbf{b_a}}) - 2((\mathbf{I} - [\boldsymbol{\gamma}_b^s\times])(\boldsymbol{\omega}^b + \tilde{\mathbf{b_g}}))\times\tilde{\mathbf{v}}_{sa}^s \\ &- (\mathbf{I} - [\boldsymbol{\gamma}_b^s\times])((\boldsymbol{\omega}^b + \tilde{\mathbf{b_g}})\times[(\boldsymbol{\omega}^b + \tilde{\mathbf{b_g}})\times\tilde{\mathbf{x}}_{bs}^b])\Big).\end{aligned} \tag{A.62}$$

Compared to the prior example, there are two major differences. Namely, the inclusion of the misalignment $\boldsymbol{\gamma}_b^s$ and the centrifugal term caused by the lever arm $\mathbf{x}_{bs}^b$. The additional nominal value of the lever arm is defined as:

$$\tilde{\mathbf{x}}_{bs}^b = \mathbf{x}_{bs}^b - \delta\mathbf{x}_{bs}^b.$$

Starting with the term associated with the specific forces first,

$$\begin{aligned}\dot{\delta\mathbf{v}}_{sa}^s &= \dot{\mathbf{v}}_{sa}^s - \dot{\tilde{\mathbf{v}}}_{sa}^s \\ &= -(\mathbf{f}^b + \mathbf{b_a}) - \Big(-(\mathbf{I} - [\boldsymbol{\gamma}_b^s\times])(\mathbf{f}^b + \mathbf{b_a} - \delta\mathbf{b_a})\Big) \\ &= -\mathbf{f}^b - \mathbf{b_a} + \mathbf{f}^b + \mathbf{b_a} - \delta\mathbf{b_a} - [\boldsymbol{\gamma}_b^s\times]\mathbf{f}^b - [\boldsymbol{\gamma}_b^s\times]\mathbf{b_a} + [\boldsymbol{\gamma}_b^s\times]\delta\mathbf{b_a}.\end{aligned}$$

The equation is now further evaluated. Products of error terms are neglected. The resulting equation under the assumption that $\mathbf{C}_b^s = \mathbf{I}$, meaning that the systems are aligned, is

$$\dot{\delta\mathbf{v}}_{sa}^s = -\delta\mathbf{b_a} - \boldsymbol{\gamma}_b^s\times(\mathbf{f}^b + \mathbf{b_a}). \tag{A.63}$$

The error state term associated with the Coriolis effect reads

$$\begin{aligned}\dot{\delta\mathbf{v}}_{sa}^s &= \dot{\mathbf{v}}_{sa}^s - \dot{\tilde{\mathbf{v}}}_{sa}^s \\ &= -(-2(\boldsymbol{\omega}^b + \mathbf{b_g})\times\mathbf{v}_{sa}^s) - 2\left[((\mathbf{I} - [\boldsymbol{\gamma}_b^s\times])(\boldsymbol{\omega}^b + \mathbf{b_g} - \delta\mathbf{b_g}))\times(\mathbf{v}_{sa}^s - \delta\mathbf{v}_{sa}^s)\right].\end{aligned}$$

Expanding the equation and neglecting the products of error terms yields

$$\dot{\delta\mathbf{v}}_{sa}^s = 2\boldsymbol{\omega}^b\times\delta\mathbf{v}_{sa}^s + 2\mathbf{b_g}\times\delta\mathbf{v}_{sa}^s + 2\delta\mathbf{b_g}\times\mathbf{v}_{sa}^s + 2(\boldsymbol{\gamma}_b^s\times\boldsymbol{\omega}^b)\times\mathbf{v}_{sa}^s + 2(\boldsymbol{\gamma}_b^s\times\mathbf{b_g})\times\mathbf{v}_{sa}^s. \tag{A.64}$$

The final term of the velocity error state ODE is associated with the centrifugal term due to the lever arm. It reads

$$\begin{aligned}\dot{\delta\mathbf{v}}_{sa}^s &= \dot{\mathbf{v}}_{sa}^s - \dot{\tilde{\mathbf{v}}}_{sa}^s \\ &= -\Big(-(\boldsymbol{\omega}^b + \mathbf{b_g})\times(\boldsymbol{\omega}^b + \mathbf{b_g})\times\mathbf{x}_{bs}^b\Big) \\ &\quad -\Big(-(\mathbf{I} - [\boldsymbol{\gamma}_b^s\times])(-(\boldsymbol{\omega}^b + \mathbf{b_g} - \delta\mathbf{b_g})\times(\boldsymbol{\omega}^b + \mathbf{b_g} - \delta\mathbf{b_g})\times(\mathbf{x}_{bs}^b - \delta\mathbf{x}_{bs}^b))\Big).\end{aligned}$$

Again, expanding the equation and neglecting the products of error terms results in

$$\begin{aligned}\dot{\delta\mathbf{v}}_{sa}^s = &\boldsymbol{\omega}^b\times\boldsymbol{\omega}^b\times\delta\mathbf{x}_{bs}^b + \boldsymbol{\omega}^b\times\mathbf{b_g}\times\delta\mathbf{x}_{bs}^b + \mathbf{b_g}\times\boldsymbol{\omega}^b\times\delta\mathbf{x}_{bs}^b + \mathbf{b_g}\times\mathbf{b_g}\times\delta\mathbf{x}_{bs}^b \\ &+ \boldsymbol{\omega}^b\times\delta\mathbf{b_g}\times\mathbf{x}_{bs}^b + \delta\mathbf{b_g}\times\boldsymbol{\omega}^b\times\mathbf{x}_{bs}^b + \mathbf{b_g}\times\delta\mathbf{b_g}\times\mathbf{x}_{bs}^b + \delta\mathbf{b_g}\times\mathbf{b_g}\times\mathbf{x}_{bs}^b \\ &+ \boldsymbol{\gamma}_b^s\times\boldsymbol{\omega}^b\times\boldsymbol{\omega}^b\times\mathbf{x}_{bs}^b + \boldsymbol{\gamma}_b^s\times\boldsymbol{\omega}^b\times\mathbf{b_g}\times\mathbf{x}_{bs}^b + \boldsymbol{\gamma}_b^s\times\mathbf{b_g}\times\boldsymbol{\omega}^b\times\mathbf{x}_{bs}^b + \boldsymbol{\gamma}_b^s\times\mathbf{b_g}\times\mathbf{b_g}\times\mathbf{x}_{bs}^b.\end{aligned} \tag{A.65}$$

The total velocity error ODE under inclusion of Eq. (A.63), Eq. (A.64) and Eq. (A.65) finally reads

$$\begin{aligned}
\dot{\delta\mathbf{v}}^s_{sa} = &-\delta\mathbf{b_a} - \boldsymbol{\gamma}^s_b \times (\mathbf{f}^b + \mathbf{b_a}) \\
&+ 2(\boldsymbol{\omega}^b + \mathbf{b_g}) \times \delta\mathbf{v}^s_{sa} + 2\delta\mathbf{b_g} \times \mathbf{v}^s_{sa} \\
&+ 2\mathbf{v}^s_{sa} \times (\boldsymbol{\omega}^b + \mathbf{b_g}) \times \boldsymbol{\gamma}^s_b \\
&+ \boldsymbol{\omega}^b \times \delta\mathbf{b_g} \times \mathbf{x}^b_{bs} + \delta\mathbf{b_g} \times \boldsymbol{\omega}^b \times \mathbf{x}^b_{bs} \\
&+ \mathbf{b_g} \times \delta\mathbf{b_g} \times \mathbf{x}^b_{bs} + \delta\mathbf{b_g} \times \mathbf{b_g} \times \mathbf{x}^b_{bs} \\
&+ \boldsymbol{\gamma}^s_b \times \boldsymbol{\omega}^b \times \boldsymbol{\omega}^b \times \mathbf{x}^b_{bs} + \boldsymbol{\gamma}^s_b \times \boldsymbol{\omega}^b \times \mathbf{b_g} \times \mathbf{x}^b_{bs} \\
&+ \boldsymbol{\gamma}^s_b \times \mathbf{b_g} \times \boldsymbol{\omega}^b \times \mathbf{x}^b_{bs} + \boldsymbol{\gamma}^s_b \times \mathbf{b_g} \times \mathbf{b_g} \times \mathbf{x}^b_{bs} \\
&+ \boldsymbol{\omega}^b \times \boldsymbol{\omega}^b \times \delta\mathbf{x}^b_{bs} + \boldsymbol{\omega}^b \times \mathbf{b_g} \times \delta\mathbf{x}^b_{bs} \\
&+ \mathbf{b_g} \times \boldsymbol{\omega}^b \times \delta\mathbf{x}^b_{bs} + \mathbf{b_g} \times \mathbf{b_g} \times \delta\mathbf{x}^b_{bs}.
\end{aligned} \tag{A.66}$$

A.6 CAI Penalty Model

A.6.1 CAI Linearization Error

In order to model the penalty of the CAI observations for cases in which the actual measurement is far off the mid fringe operating point, the linearization error of the measurement sensitivity is used as a basis. The error of the linearization of the measurement equation can be assessed as follows. Let $h(x)$ be the measurement equation, x the state and Δx a distance, i.e. error, to the state. The function $h(x)$ is linearized around the state x to first order,

$$h(x + \Delta x) = h(x) + H(x) \cdot \Delta x, \tag{A.67}$$

with the linearized function $H = \partial h / \partial x$. The error e of this linearization is then the difference between the linearized model on the right side of the minus sign and the original model on the left side:

$$e = h(x + \Delta x) - (h(x) + H(x) \cdot \Delta x). \tag{A.68}$$

In case of the atom interferometer measurement equation (3.10) at the mid fringe operation point $\frac{1}{2}\pi$, the error can be approximated by

$$e = A\cos(\frac{\pi}{2} + \delta\phi) - \left(A\cos(\frac{\pi}{2}) - A\sin(\frac{\pi}{2})\delta\phi\right). \tag{A.69}$$

Following the trigonometric addition theorem,

$$\cos(a + b) = \cos(a)\cos(b) - \sin(a)\sin(b), \tag{A.70}$$

the formulation can be simplified,

$$e = A\left(\cos(\frac{\pi}{2})\cos(\delta\phi) - \sin(\frac{\pi}{2})\sin(\delta\phi)\right) - \left(A\cos(\frac{\pi}{2}) - A\sin(\frac{\pi}{2})\delta\phi\right). \tag{A.71}$$

Evaluating the sinusoidal terms at $\frac{\pi}{2}$ leads to the compact form

$$e = A(\delta\phi - \sin(\delta\phi)). \tag{A.72}$$

For small phase shifts $\sin\delta\phi \approx \delta\phi$ takes effect and the expression in the brackets is zero, while for $\delta\phi = \pi$ the error is $A\pi$. For very large values of $\delta\phi$ the function is asymptotic to $A\delta\phi$.

A.6.2 Variance Propagation

The phase shift error $\delta\phi$ is related to the incoming acceleration bias error δb_a via

$$\delta\phi = -k_\mathrm{e} T^2 \delta b_a.$$

The variance is propagated by

$$\sigma_{e_y}^2 = \left|\frac{\partial e_y}{\partial \delta b_a}\right|^2 \sigma_{\delta b_a}^2. \tag{A.73}$$

The derivative of Eq. (A.73) is evaluated as follows:

$$\frac{\partial e_y}{\partial \delta b_a} = \frac{\partial}{\partial \delta b_a} A\left(k_\mathrm{e} T^2 \delta b_a - \sin\left(-k_\mathrm{e} T^2 \delta b_a\right)\right) = A\left(k_\mathrm{e} T^2 + k_\mathrm{e} T^2 \cos\left(-k_\mathrm{e} T^2 \delta b_a\right)\right).$$

By rearranging and using the symmetry of the cosine, the result reads

$$\frac{\partial e_y}{\partial \delta b_a} = A(k_\mathrm{e} T^2)\left(\cos\left(k_\mathrm{e} T^2 \delta b_a\right) - 1\right). \tag{A.74}$$

The cosine can be represented by McLaurin series expansion,

$$\cos\left(k_\mathrm{e} T^2 \delta b_a\right) = 1 - \frac{(k_\mathrm{e} T^2 \delta b_a)^2}{2} + ... + \mathcal{O}((k_\mathrm{e} T^2 \delta b_a)),$$

so that, after truncation of the series, Eq. (A.74) can be simplified to

$$\frac{\partial e_y}{\partial \delta b_a} \approx A k_\mathrm{e} T^2 \left(1 - \frac{(k_\mathrm{e} T^2 \delta b_a)^2}{2} - 1\right) \approx \frac{A}{2}(k_\mathrm{e} T^2)^3 \delta b_a^2.$$

Recalling Eq. (A.73), the variance of the linearization error reads

$$\sigma_{e_y}^2 = \left|\frac{A}{2}(k_\mathrm{e} T^2)^3 \delta b_a^2\right|^2 \sigma_{\delta b_a}^2.$$

For a zero mean noise process in δb_a, it can be stated that $\delta b_a^2 = \sigma_{\delta b_a}^2$. The variance of the linearization error $\sigma_{e_y}^2$ can finally be formulated as the CAI penalty model $R_\mathrm{pen} = \sigma_{e_y}^2$ as follows:

$$R_\mathrm{pen} = \kappa \frac{A^2}{4}(k_\mathrm{e} T^2)^6 \sigma_{\delta b_a}^6. \tag{A.75}$$

A factor κ is additionally introduced to compensate for certain flaws of using the closed solution of the steady state variance of the Kalman filter. It will soon be discussed.

A.6.3 Optimum of $\mathcal{R}$

The penalty model R_pen in Eq. (A.75) can only grow with increasing values of $\sigma_{\delta b_a}$, which is assumed to be caused by the input acceleration uncertainty σ_a entirely. The optimum is thus evaluated by setting $\sigma_p^2 = R_\mathrm{pen}$. This is the point after which the total observation uncertainty of CAI $R = \sigma_p^2 + R_\mathrm{pen}$ will considerably increase with growing accelerometer uncertainty.

$$\begin{aligned} R_\mathrm{pen} &= \sigma_p^2 \\ \kappa \frac{A^2}{4}(k_\mathrm{e} T^2)^6 \sigma_a^6 &= \sigma_p^2 \\ \sigma_a^6 &= \frac{\sigma_p^2}{\frac{1}{4}\kappa A^2 (k_\mathrm{e} T^2)^6} \\ \sigma_a^* &= \frac{1}{k_\mathrm{e} T^2} \sqrt[3]{\frac{2}{\sqrt{\kappa}} \frac{\sigma_p}{A}}. \end{aligned} \tag{A.76}$$

This value represents the optimal acceleration noise level for the hybridization and is thus marked with the $*$ superscript. The next step is the evaluation of the performance gain at this value of σ_a^*. It was already established that

$$R = \sigma_p^2 + R_{\text{pen}} = 2\sigma_p^2$$

since σ_p^2 is equal to R_{pen} at the optimal value. With this piece of information, the steady state variance for the accelerations of Eq. (4.94) can be simplified substantially,

$$P_{a,\infty} = -\frac{1}{2}\sigma_a^2 + \sqrt{\frac{\sigma_a^4}{4} + \frac{2\sigma_p^2\sigma_a^2}{H_a^2}}. \tag{A.77}$$

For convenience, let σ_a^2 be factored out from the expression under the root,

$$P_{a,\infty} = -\frac{1}{2}\sigma_a^2 + \sigma_a^2\sqrt{\frac{1}{4} + \frac{2\sigma_p}{\sigma_a^2 H_a^2}}.$$

The focus is now the evaluation of the fraction under the root, with H_a^2 according to Eq. (4.35) and under insertion of the optimal value of σ_a^* from Eq. (A.76),

$$\begin{aligned}\frac{2\sigma_p}{\sigma_a^2 H_a^2} &= \frac{2\sigma_p}{\frac{1}{(k_e T^2)^2}\sqrt[3]{\frac{4}{\kappa}\frac{\sigma_p^2}{A^2}}(Ak_eT^2)^2} \\ &= \frac{2\sigma_p}{\sqrt[3]{\frac{4}{\kappa}\frac{\sigma_p^2}{A^2}}A^2} \\ &= \sqrt[3]{2\kappa\left(\frac{\sigma_p}{A}\right)^4}.\end{aligned} \tag{A.78}$$

This expression is included in Eq. (A.77), and subsequently inserted in Eq. (4.104), resulting in the following model for the performance gain $\mathcal{R}$:

$$\begin{aligned}\mathcal{R}^2 = \frac{\sigma_a^2}{P_{a,\infty}} &= \frac{\sigma_a^2}{-\frac{1}{2}\sigma_a^2 + \sigma_a^2\sqrt{\frac{1}{4} + \sqrt[3]{2\kappa\left(\frac{\sigma_p}{A}\right)^4}}} \\ &= \frac{1}{-\frac{1}{2} + \sqrt{\frac{1}{4} + \sqrt[3]{2\kappa\left(\frac{\sigma_p}{A}\right)^4}}}.\end{aligned} \tag{A.79}$$

When comparing the model with the trivial factor of $\kappa = 1$ with the empirical results of the performance gain $\mathcal{R}$, cf. Fig. A.1, the model does not quite coincide with the empirical data. The major reason for this is that the closed solution of the steady state variance that is used for the calculation of the value $\mathcal{R}$ represents the limit to which the variance converges to in order to reach its equilibrium state after several measurement updates. In the case of just a single CAI measurement, there is only one filter update which is applied, meaning that the state variance did not reach its steady state value yet, in which the Kalman filter is in equilibrium.

In order to compensate for this insufficiency of the model, the factor κ was included in R_{pen}. It is now estimated by a numerical optimization approach in which samples with uniformly distributed values between 1 and 2 are generated. A cost function based on the difference of the model $\mathcal{R}$ and the empirical result of the simulated data $\tilde{\mathcal{R}}$,

$$\text{cost} = \sum_{k=1}^{N}\left[(\mathcal{R}_k - \tilde{\mathcal{R}}_k)^2\right], \tag{A.80}$$

is evaluated for each sample. The value of κ with the best fit yields approximately

$$\kappa = \frac{5}{3}.$$

Note that the variance of the CAI observation is set to a low value of $\sigma_p^2 = 9 \times 10^{-8}$. Fig. A.2 shows two different examples. For large values $\sigma_p^2 = 1 \times 10^{-1}$, the steady state variance is not representative enough as a basis for the model. On the other hand, for even lower values of $\sigma_p^2 = 1 \times 10^{-12}$ the estimate of κ stays at a value of about $\frac{5}{3}$.

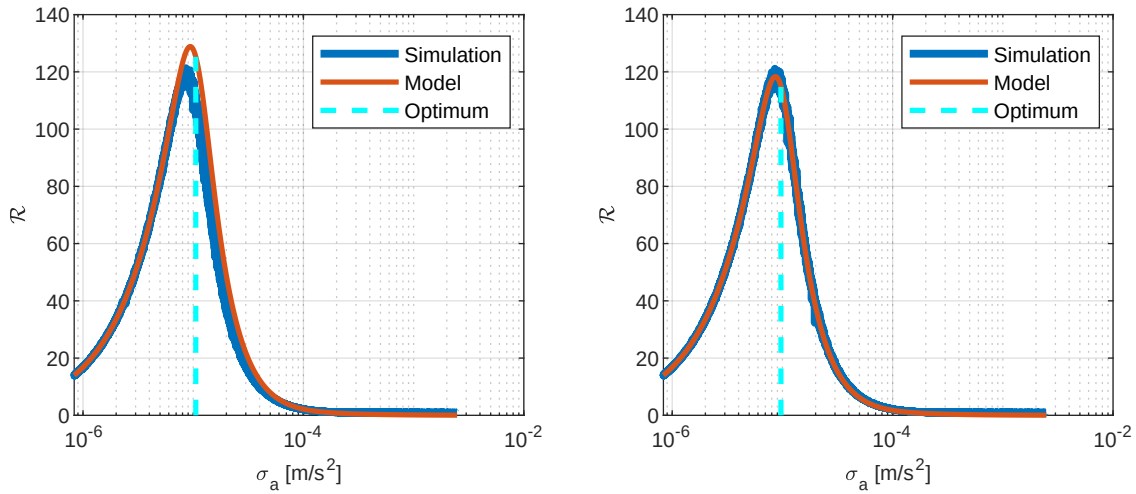

Figure A.1: QINS sensitivity gain model with and without correction parameter. The empirical sensitivity gain $\mathcal{R}$ (blue) is compared to the model (red). CAI parameters: $\sigma_p^2 = 9 \times 10^{-8}$, $T = 25\,\text{ms}$. Left: $\kappa = 1$. Right: $\kappa = 5/3$.

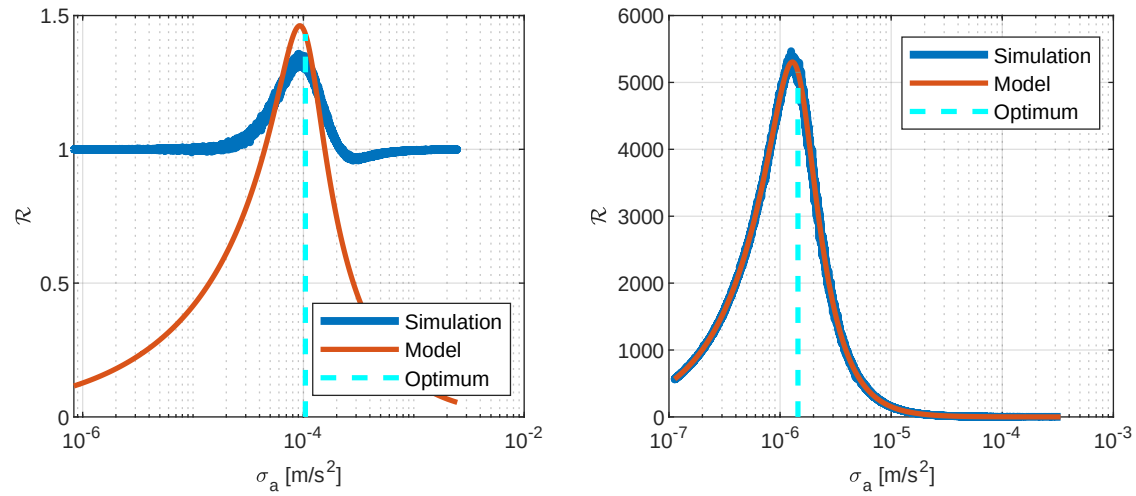

Figure A.2: QINS sensitivity gain model for different CAI variances. The empirical sensitivity gain $\mathcal{R}$ (blue) is compared to the model (red). CAI parameters: $T = 25\,\text{ms}$. Left: $\sigma_p^2 = 1 \times 10^{-1}$, estimated $\kappa = 1.20$. Right: $\sigma_p^2 = 1 \times 10^{-12}$, estimated $\kappa = 1.67$.

A.6.4 Series Expansion of $\mathcal{R}$

By substituting

$$x = \sqrt[3]{2\kappa \left(\frac{\sigma_p}{A}\right)^4},$$

and evaluation of Eq. (4.109) by using Wolfram Alpha LLC (2024), the following result can be achieved by McLaurin series expansion:

$$\mathcal{R}^2 \approx \frac{1}{x} + 1 - x + 2x^2 - 5x^3 + \mathcal{O}(x^5). \tag{A.81}$$

By substituting back and truncation of the series, the following approximation for $\mathcal{R}$ can be stated,

$$\mathcal{R}^2 \approx 1 + \sqrt[3]{\frac{1}{2\kappa}\left(\frac{A}{\sigma_p}\right)^4}. \tag{A.82}$$

A.7 Maximum Likelihood Estimation

General Formalism

The likelihood L of a single observation x_i with index i and a corresponding mean value μ_i and variance σ_i^2 reads:

$$L(\mu_i, \sigma_i | x_i) = \frac{1}{\sqrt{2\pi}\sigma_i} \cdot \exp\left(-\frac{1}{2} \cdot \frac{(x_i - \mu_i)^2}{\sigma_i^2}\right). \tag{A.83}$$

For n parameters it is the following:

$$L(\boldsymbol{\mu}, \boldsymbol{\sigma} | x_1 ... x_n) = \frac{1}{\sqrt{2\pi}\sigma_1} \exp\left(-\frac{1}{2} \cdot \frac{(x_1 - \mu_1)^2}{\sigma_1^2}\right) \cdot ... \cdot \frac{1}{\sqrt{2\pi}\sigma_n} \exp\left(-\frac{1}{2} \cdot \frac{(x_n - \mu_n)^2}{\sigma_n^2}\right), \tag{A.84}$$

or written as a product,

$$L(\boldsymbol{\mu}, \boldsymbol{\sigma} | \boldsymbol{x}) = \prod_{i=1}^{n} \frac{1}{\sqrt{2\pi}\sigma_i} \cdot \exp\left(-\frac{1}{2} \cdot \frac{(x_i - \mu_i)^2}{\sigma_i^2}\right). \tag{A.85}$$

For each observation i, the expression can be reformulated under the further consideration that $\ln(\exp(a)) = a$,

$$\begin{aligned}
\ln\left(\frac{1}{\sqrt{2\pi}\sigma_i} \exp\left(-\frac{1}{2} \cdot \frac{(x_i - \mu_i)^2}{\sigma_i^2}\right)\right) &= \ln\left(\frac{1}{\sqrt{2\pi}\sigma_i}\right) + \ln\left(\exp\left(-\frac{1}{2}\frac{(x_i - \mu_i)^2}{\sigma_i^2}\right)\right) \\
&= -\frac{1}{2}\ln\left(2\pi\sigma_i^2\right) - \frac{1}{2}\frac{(x_i - \mu_i)^2}{\sigma_i^2} \\
&= -\frac{1}{2}\ln(2\pi) - \frac{1}{2}\ln(\sigma_i^2) - \frac{1}{2}\frac{(x_i - \mu_i)^2}{\sigma_i^2} \\
&= -\frac{1}{2}\ln(2\pi) - \ln(\sigma_i) - \frac{1}{2}\frac{(x_i - \mu_i)^2}{\sigma_i^2}.
\end{aligned} \tag{A.86}$$

Where $\ln(1/\sqrt{x}) = -1/2\ln(x)$ and $\ln(\exp(x)) = x$. In logarithmic expression, for the total likelihood of all samples the product becomes a sum,

$$\begin{aligned}\ln L(\boldsymbol{\mu}, \boldsymbol{\sigma}|\boldsymbol{x}) = &\ln\left(\frac{1}{\sqrt{2\pi}\sigma_1}\exp\left(-\frac{1}{2}\cdot\frac{(x_1-\mu_1)^2}{\sigma_1^2}\right)\right)\\ &+ ...\\ &+ \ln\left(\frac{1}{\sqrt{2\pi}\sigma_n}\exp\left(-\frac{1}{2}\cdot\frac{(x_n-\mu_n)^2}{\sigma_n^2}\right)\right).\end{aligned} \tag{A.87}$$

With the adaptions from Eq. (A.86),

$$\ln L(\boldsymbol{\mu}, \boldsymbol{\sigma}|\boldsymbol{x}) = -\frac{1}{2}\ln(2\pi) - \ln(\sigma_1) - \frac{1}{2}\frac{(x_1-\mu_1)^2}{\sigma_1^2} - ... - \frac{1}{2}\ln(2\pi) - \ln(\sigma_n) - \frac{1}{2}\frac{(x_n-\mu_n)^2}{\sigma_n^2}, \tag{A.88}$$

the following compact sum equation results,

$$\ln L(\boldsymbol{\mu}, \boldsymbol{\sigma}|\boldsymbol{x}) = -\frac{n}{2}\ln(2\pi) + \sum_{i=1}^{n}\left(-\ln\sigma_i - \frac{(x_i-\mu_i)^2}{2\sigma_i^2}\right), \tag{A.89}$$

which cannot be simplified further. The reason is that the variance σ_i^2 as well as the expectation value μ_i may be depending on a control value that is different for every new sample, i.e. the phase information ϕ_i in Eq. (A.91). No closed solution for the sum term, nor the maximum of the likelihood, can be given for this reason.

Application to CAI Parameters

Let the variances $\boldsymbol{\sigma}(\boldsymbol{\theta})$ be dependent on a parameter vector $\boldsymbol{\theta} = [\sigma_{p_0}^2, \sigma_A^2, \sigma_{\phi_0}^2]^{\mathrm{T}}$. The partial derivative of the likelihood with respect to the parameter vector reads

$$\frac{\partial \ln L(\boldsymbol{\theta}|\mathbf{x})}{\partial\boldsymbol{\theta}} = \sum_{i=1}^{n}\left(-\frac{1}{\sigma_i}\frac{\partial\sigma_i}{\partial\boldsymbol{\theta}} - \frac{(x_i-\mu_i)}{\sigma_i^2}\frac{\partial\mu_i}{\partial\boldsymbol{\theta}} + \frac{(x_i-\mu_i)^2}{\sigma_i^3}\frac{\partial\sigma_i}{\partial\boldsymbol{\theta}}\right). \tag{A.90}$$

The remaining partial derivatives have to be calculated based on the equations for μ_i,

$$\mu_i = A\cdot\cos(\phi_i + \phi_0) + p_0, \tag{A.91}$$

and σ_i^2,

$$\sigma_i^2 = A^2\cdot\sin^2(\phi_i+\phi_0)\cdot\sigma_\phi^2 + \sigma_{p0}^2 + \cos^2(\phi_i+\phi_0)\cdot\sigma_A^2, \tag{A.92}$$

or as standard deviation,

$$\sigma_i = \sqrt{A^2\cdot\sin^2(\phi_i+\phi_0)\cdot\sigma_\phi^2 + \sigma_{p0}^2 + \cos^2(\phi_i+\phi_0)\cdot\sigma_A^2}. \tag{A.93}$$

Since Eq. (A.91) does not yield any dependencies on the variance components, all derivatives associated with μ_i are zero. The derivatives of the composed variance w.r.t. the fringe parameters variance components read

$$\begin{aligned}\frac{\partial\sigma_i}{\partial\sigma_{p_0}^2} &= \frac{1}{2\sigma_i}\cdot\frac{\partial\sigma_i^2}{\partial\sigma_{p_0}^2}\\ &= \frac{1}{2\sigma_i},\end{aligned} \tag{A.94}$$

$$\frac{\partial \sigma_i}{\partial \sigma_{\phi_0}^2} = \frac{1}{2\sigma_i} \cdot \frac{\partial \sigma_i^2}{\partial \sigma_{\phi_0}^2} = \frac{1}{2\sigma_i} \cdot A^2 \cdot \sin^2(\phi_i + \phi_0), \tag{A.95}$$

$$\frac{\partial \sigma_i}{\partial \sigma_A^2} = \frac{1}{2\sigma_i} \cdot \frac{\partial \sigma_i^2}{\partial \sigma_A^2} = \frac{1}{2\sigma_i} \cdot \cos^2(\phi_i + \phi_0). \tag{A.96}$$

With those derivatives clarified, the sensitivity of the total likelihood with respect to the three parameters are the following,

$$\frac{\partial \ln L(\boldsymbol{\theta}|\mathbf{x})}{\partial \sigma_{p0}^2} = \sum_{i=1}^{n} \left(-\frac{1}{\sigma_i} \frac{\partial \sigma_i}{\partial \sigma_{p0}^2} - \frac{(x_i - \mu_i)}{\sigma_i^2} \frac{\partial \mu_i}{\partial \sigma_{p0}^2} + \frac{(x_i - \mu_i)^2}{\sigma_i^3} \frac{\partial \sigma_i}{\partial \sigma_{p0}^2} \right) = \sum_{i=1}^{n} \left(-\frac{1}{2\sigma_i^2} + (x_i - \mu_i)^2 \frac{1}{2\sigma_i^4} \right). \tag{A.97}$$

The second partial derivative reads

$$\frac{\partial^2 \ln L(\boldsymbol{\theta}|\mathbf{x})}{\partial \sigma_{p0}^2 \partial \sigma_{p0}^2} = \sum_{i=1}^{n} \left(\frac{1}{\sigma_i^3} \frac{\partial \sigma_i}{\partial \sigma_{p0}^2} - \frac{2(x_i - \mu_i)^2}{\sigma_i^5} \frac{\partial \sigma_i}{\partial \sigma_{p0}^2} \right) = \sum_{i=1}^{n} \left(\frac{1}{2\sigma_i^4} - (x_i - \mu_i)^2 \frac{1}{\sigma_i^6} \right). \tag{A.98}$$

The first and second partial derivative of the likelihood with respect to $\sigma_{\phi_0}^2$ are

$$\frac{\partial \ln L(\boldsymbol{\theta}|\mathbf{x})}{\partial \sigma_{\phi_0}^2} = \sum_{i=1}^{n} \left(-\frac{1}{\sigma_i} \frac{\partial \sigma_i}{\partial \sigma_{\phi_0}^2} - \frac{(x_i - \mu_i)}{\sigma_i^2} \frac{\partial \mu_i}{\partial \sigma_{\phi_0}^2} + \frac{(x_i - \mu_i)^2}{\sigma_i^3} \frac{\partial \sigma_i}{\partial \sigma_{\phi_0}^2} \right) = \sum_{i=1}^{n} \left(-\frac{A^2 \sin^2(\phi_i + \phi_0)}{2\sigma_i^2} + (x_i - \mu_i)^2 \frac{A^2 \sin^2(\phi_i + \phi_0)}{2\sigma_i^4} \right), \tag{A.99}$$

$$\frac{\partial^2 \ln L(\boldsymbol{\theta}|\mathbf{x})}{\partial \sigma_{\phi_0}^2 \partial \sigma_{\phi_0}^2} = \sum_{i=1}^{n} \left(-\frac{1}{\sigma_i} \frac{\partial \sigma_i}{\partial \sigma_{\phi_0}^2} - \frac{(x_i - \mu_i)}{\sigma_i^2} \frac{\partial \mu_i}{\partial \sigma_{\phi_0}^2} + \frac{(x_i - \mu_i)^2}{\sigma_i^3} \frac{\partial \sigma_i}{\partial \sigma_{\phi_0}^2} \right) = \sum_{i=1}^{n} \left(\frac{A^4 \sin^4(\phi_i + \phi_0)}{2\sigma_i^4} - (x_i - \mu_i)^2 \frac{A^4 \sin^4(\phi_i + \phi_0)}{\sigma_i^6} \right). \tag{A.100}$$

The first and second partial derivative of the likelihood with respect to σ_A^2 are

$$\frac{\partial \ln L(\boldsymbol{\theta}|\mathbf{x})}{\partial \sigma_A^2} = \sum_{i=1}^{n} \left(-\frac{1}{\sigma_i} \frac{\partial \sigma_i}{\partial \sigma_A^2} - \frac{(x_i - \mu_i)}{\sigma_i^2} \frac{\partial \mu_i}{\partial \sigma_A^2} + \frac{(x_i - \mu_i)^2}{\sigma_i^3} \frac{\partial \sigma_i}{\partial \sigma_A^2} \right) = \sum_{i=1}^{n} \left(-\frac{\cos^2(\phi_i + \phi_0)}{2\sigma_i^2} + (x_i - \mu_i)^2 \frac{\cos^2(\phi_i + \phi_0)}{2\sigma_i^4} \right), \tag{A.101}$$

$$\frac{\partial^2 \ln L(\boldsymbol{\theta}|\mathbf{x})}{\partial \sigma_A^2 \partial \sigma_A^2} = \frac{\partial}{\partial \sigma_A^2} \sum_{i=1}^{n} \left(-\frac{\cos^2(\phi_i + \phi_0)}{2\sigma_i^2} + (x_i - \mu_i)^2 \frac{\cos^2(\phi_i + \phi_0)}{2\sigma_i^4} \right) = \sum_{i=1}^{n} \left(\frac{\cos^4(\phi_i + \phi_0)}{2\sigma_i^4} - (x_i - \mu_i)^2 \frac{A^4 \cos^4(\phi_i + \phi_0)}{\sigma_i^6} \right). \tag{A.102}$$

The remaining entries of the Hessian matrix are the following:

$$\begin{aligned}\frac{\partial^2 \ln L(\boldsymbol{\theta}|\mathbf{x})}{\partial\sigma_{p0}^2\partial\sigma_{\phi_0}^2} &= \frac{\partial}{\partial\sigma_{p0}^2}\sum_{i=1}^{n}\left(-\frac{A^2\sin^2(\phi_i+\phi_0)}{2\sigma_i^2}+(x_i-\mu_i)^2\frac{A^2\sin^2(\phi_i+\phi_0)}{2\sigma_i^4}\right)\\ &= \sum_{i=1}^{n}\left(\frac{A^2\sin^2(\phi_i+\phi_0)}{\sigma_i^3}\frac{\partial\sigma_i}{\partial\sigma_{p0}^2}-(x_i-\mu_i)^2\frac{A^2\sin^2(\phi_i+\phi_0)}{\sigma_i^5}\frac{\partial\sigma_i}{\partial\sigma_{p0}^2}\right)\\ &= \sum_{i=1}^{n}\left(\frac{A^2\sin^2(\phi_i+\phi_0)}{2\sigma_i^4}-(x_i-\mu_i)^2\frac{A^2\sin^2(\phi_i+\phi_0)}{\sigma_i^6}\right),\end{aligned} \tag{A.103}$$

$$\begin{aligned}\frac{\partial^2 \ln L(\boldsymbol{\theta}|\mathbf{x})}{\partial\sigma_{A}^2\partial\sigma_{\phi_0}^2} &= \frac{\partial}{\partial\sigma_{A}^2}\sum_{i=1}^{n}\left(-\frac{A^2\sin^2(\phi_i+\phi_0)}{2\sigma_i^2}+(x_i-\mu_i)^2\frac{A^2\sin^2(\phi_i+\phi_0)}{2\sigma_i^4}\right)\\ &= \sum_{i=1}^{n}\left(\frac{A^2\sin^2(\phi_i+\phi_0)}{\sigma_i^3}\frac{\partial\sigma_i}{\partial\sigma_{A}^2}-(x_i-\mu_i)^2\frac{A^2\sin^2(\phi_i+\phi_0)}{\sigma_i^5}\frac{\partial\sigma_i}{\partial\sigma_{A}^2}\right)\\ &= \sum_{i=1}^{n}\left(\frac{A^2\sin^2(\phi_i+\phi_0)\cos^2(\phi_i+\phi_0)}{2\sigma_i^4}-(x_i-\mu_i)^2\frac{A^2\sin^2(\phi_i+\phi_0)\cos^2(\phi_i+\phi_0)}{\sigma_i^6}\right),\end{aligned} \tag{A.104}$$

$$\begin{aligned}\frac{\partial^2 \ln L(\boldsymbol{\theta}|\mathbf{x})}{\partial\sigma_{A}^2\partial\sigma_{p_0}^2} &= \frac{\partial}{\partial\sigma_{p_0}^2}\sum_{i=1}^{n}\left(-\frac{A^2\sin^2(\phi_i+\phi_0)}{2\sigma_i^2}+(x_i-\mu_i)^2\frac{A^2\sin^2(\phi_i+\phi_0)}{2\sigma_i^4}\right)\\ &= \sum_{i=1}^{n}\left(\frac{A^2\sin^2(\phi_i+\phi_0)}{\sigma_i^3}\frac{\partial\sigma_i}{\partial\sigma_{p_0}^2}-(x_i-\mu_i)^2\frac{A^2\sin^2(\phi_i+\phi_0)}{\sigma_i^5}\frac{\partial\sigma_i}{\partial\sigma_{p_0}^2}\right)\\ &= \sum_{i=1}^{n}\left(\frac{A^2\cos^2(\phi_i+\phi_0)}{2\sigma_i^4}-(x_i-\mu_i)^2\frac{A^2\cos^2(\phi_i+\phi_0)}{\sigma_i^6}\right),\end{aligned} \tag{A.105}$$

$$\frac{\partial^2 \ln L(\boldsymbol{\theta}|\mathbf{x})}{\partial\sigma_{\phi_0}^2\partial\sigma_{A}^2} = \frac{\partial^2 \ln L(\boldsymbol{\theta}|\mathbf{x})}{\partial\sigma_{A}^2\partial\sigma_{\phi_0}^2}, \tag{A.106}$$

$$\frac{\partial^2 \ln L(\boldsymbol{\theta}|\mathbf{x})}{\partial\sigma_{\phi_0}^2\partial\sigma_{p_0}^2} = \frac{\partial^2 \ln L(\boldsymbol{\theta}|\mathbf{x})}{\partial\sigma_{p_0}^2\partial\sigma_{\phi_0}^2}, \tag{A.107}$$

$$\frac{\partial^2 \ln L(\boldsymbol{\theta}|\mathbf{x})}{\partial\sigma_{p_0}^2\partial\sigma_{A}^2} = \frac{\partial^2 \ln L(\boldsymbol{\theta}|\mathbf{x})}{\partial\sigma_{A}^2\partial\sigma_{p_0}^2}. \tag{A.108}$$

A.8 Additional Aspects

A.8.1 Automatic Adaption of the Interrogation Time

The error state of the acceleration and angular rate biases in the QINS is estimated with each new CAI measurement. Smaller errors indicate a better prediction based on the IMU data. It was demonstrated in Sec. 4.5 that reasons for an increase of the bias error can be large spikes of the dynamics on multiple axes, in which case the integrated noise of the IMU is scaled directly due to the angular rates and accelerations on one side, but also due to misalignment

and to a degree by the lever arm on the other side. An increase of the bias error state, which can be directly related to an increase of the phase shift error, is a clear indicator that the QINS is in such an unfavorable situation and a loss of the ambiguity solution might be imminent.

One option to directly counteract the increase of the error is to reduce the interrogation time, which consequently reduces the scale factor between the bias error state and the phase shift error. In Tennstedt and Schön (2023) a method is published in which the adaption of the interrogation time, and subsequently the scale factor, is performed by a state automaton, cf. Fig. A.3. On the example of the acceleration bias on one axis, the bias error is compared to two thresholds. If the error is too large, the interrogation time is reduced. If it is below a certain threshold, the interrogation time can be increased again. At this rate, a high level of sensitivity can be kept even in the light of changing situations, cf. Fig. A.4. If the CAI is measuring again after a long dead time, the automaton can be reset by an initialization with a low T_f.

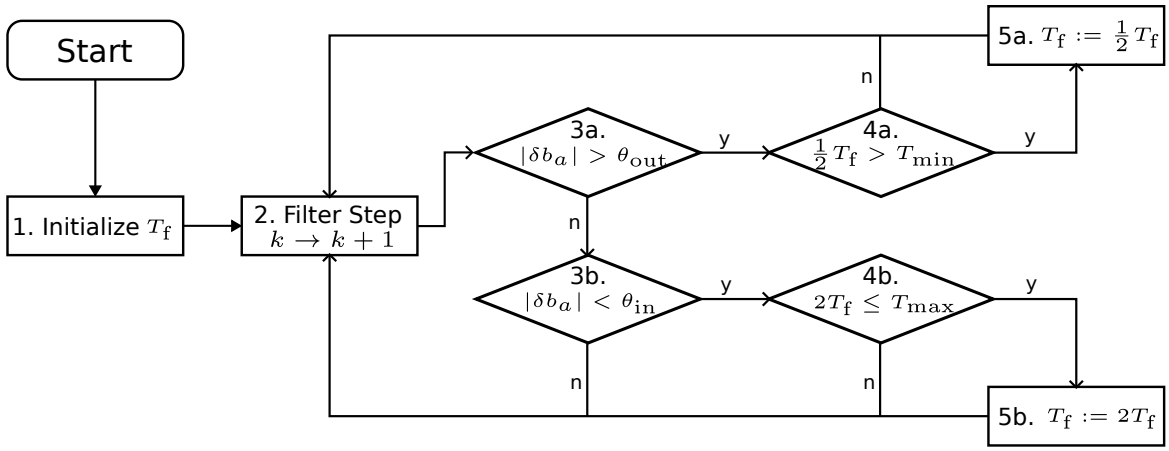

Figure A.3: Intelligent adaption of the interrogation time. Scheme for a state automaton for the adaption of the interrogation time based on the bias error.

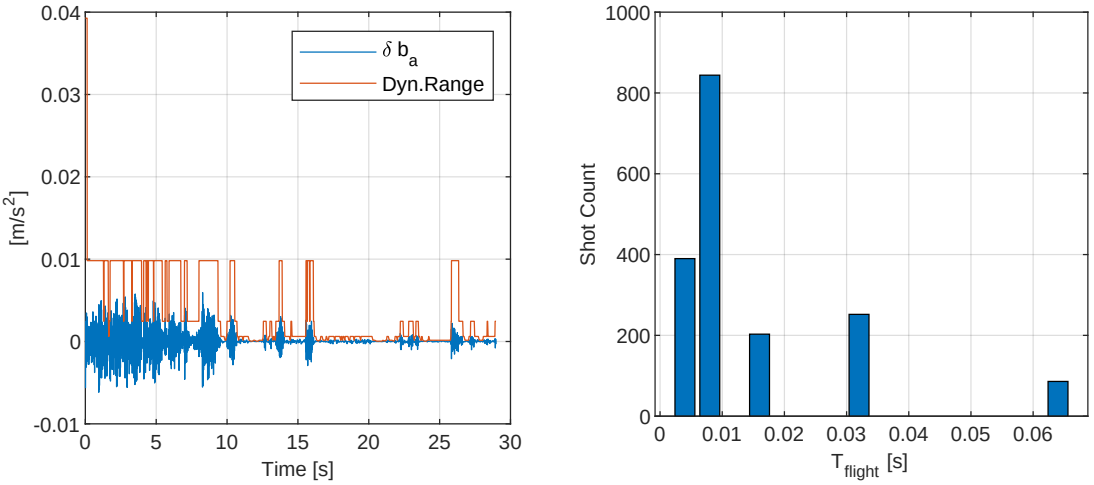

Figure A.4: Effect of the state automaton on the dynamic range and CAI scale factor. Left: illustration of the dynamic range (red line) and and the estimated bias error (blue line) on the basis of a static data set recorded with a navigation grade sensor and a simulated CAI observation. A smaller dynamic range means higher atom flight times and thus a larger scale factor. Right: histogram showing the amount of CAI shots for each setting of the flight time that was achieved in the scenario.

A.8.2 QINS Transfer Function

The differential equation for a scalar state under steady state conditions, which is driven by an input process only, reads:

$$\dot{x} = u + K(z - Hx), \tag{A.109}$$

or in error state notation,

$$\delta\dot{x} = \delta u + K\delta z. \tag{A.110}$$

The Laplace domain representation, by omitting initial conditions, and considering that $\delta z = H\delta x$, is

$$s\delta X = \delta U - KH\delta X. \tag{A.111}$$

Solving the equation for δX yields:

$$\delta X(sI + KH) = \delta U, \tag{A.112}$$

so that

$$\frac{\delta X}{\delta U} = \frac{1}{s + KH}. \tag{A.113}$$

The time domain representation of the transfer function is

$$T(t) = e^{-KHt}, \tag{A.114}$$

which is characterized by an exponential dampening for growing frequencies. As such, the Kalman filter under steady state conditions is essentially acting like a low pass filter with a time constant τ_K of $1/(KH)$. The Kalman gain K is given by

$$K = \frac{PH}{R}.$$

For the acceleration bias state, $H_a = Ak_eT^2$, the time constant thus yields

$$\tau_K = \frac{R}{PH_a^2}. \tag{A.115}$$

This general filter equation can be applied to CAI in a one dimensional case. With the transfer function from Sec. 3.3,

$$\frac{1}{s^2}[1 - e^{-2sT}]^2,$$

and an additional factor due to the dead time,

$$e^{-sT_d},$$

the following QINS transfer function can be assembled,

$$\frac{\delta X}{U} = \frac{1}{s^2} \cdot \frac{[1 - e^{-2sT}]^2}{s + KH} \cdot e^{-sT_d}. \tag{A.116}$$

The total response of the QINS to accelerations can thus be regarded as a second order integrator with latency T_d. After the cutoff frequency at KH it behaves like an integrator of third order. This cutoff frequency, due to the large scale factor included in H, is considerably larger than the CAI cutoff frequency at $1/T$. Signals of high frequencies that are already dampened by the CAI transfer function, have their magnitude reduced even more in a QINS.

Bibliography

Abend, S., Allard, B., Arnold, A. S., Ban, T., Barry, L., Battelier, B., Bawamia, A., Beaufils, Q., Bernon, S., Bertoldi, A., Bonnin, A., Bouyer, P., Bresson, A., Burrow, O. S., Canuel, B., Desruelle, B., Drougakis, G., Forsberg, R., Gaaloul, N., Gauguet, A., Gersemann, M., Griffin, P. F., Heine, H., Henderson, V. A., Herr, W., Kanthak, S., Krutzik, M., Lachmann, M. D., Lammegger, R., Magnes, W., Mileti, G., Mitchell, M. W., Mottini, S., Papazoglou, D., Pereira dos Santos, F., Peters, A., Rasel, E., Riis, E., Schubert, C., Seidel, S. T., Tino, G. M., Van Den Bossche, M., von Klitzing, W., Wicht, A., Witkowski, M., Zahzam, N. & Zawada, M. (2023). Technology roadmap for cold-atoms based quantum inertial sensor in space. *AVS Quantum Science*, *5* (1), 019201. doi: 10.1116/5.0098119

Abend, S., Gebbe, M., Gersemann, M., Ahlers, H., Müntinga, H., Giese, E., Gaaloul, N., Schubert, C., Lämmerzahl, C., Ertmer, W., Schleich, W. & Rasel, E. (2016). Atom-chip fountain gravimeter. *Physical Review Letters*, *117* (20), 203003. doi: 10.1103/physrevlett.117.203003

Adams, C. S., Pfau, T. & Mlynek, J. (1993). Atomic beam splitters based on light. In *AIP Conference Proceedings* (pp. 200–213). AIP. doi: 10.1063/1.43798

Allan, D. (1966). Statistics of atomic frequency standards. *Proceedings of the IEEE*, *54* (2), 221–230. doi: 10.1109/proc.1966.4634

Altorio, M., Sidorenkov, L. A., Gautier, R., Savoie, D., Landragin, A. & Geiger, R. (2020). Accurate trajectory alignment in cold-atom interferometers with separated laser beams. *Physical Review A*, *101* (3), 033606. doi: 10.1103/PhysRevA.101.033606

Altshuler, S. & Frantz, L. (1972). *Matter wave interferometric apparatus* (No. US3761721A). U.S. Patent and Trade-mark Office.

Antoine, C. (2007). Rotating matter-wave beam splitters and consequences for atom gyrometers. *Physical Review A*, *76* (3), 033609. doi: 10.1103/physreva.76.033609

Antoine, C. & Bordé, C. J. (2003). Quantum theory of atomic clocks and gravito-inertial sensors: An update. *Journal of Optics B: Quantum and Semiclassical Optics*, *5* (2), 199–207. doi: 10.1088/1464-4266/5/2/380

Baggott, J. (2020). *The quantum cookbook*. Oxford University Press. doi: 10.1093/oso/9780198827856.001.0001

Barrett, B., Cheiney, P., Battelier, B., Napolitano, F. & Bouyer, P. (2019). Multidimensional atom optics and interferometry. *Physical Review Letters*, *122* (4), 043604. doi: 10.1103/physrevlett.122.043604

Barrett, B., Gominet, P.-A., Cantin, E., Antoni-Micollier, L., Bertoldi, A., Battelier, B., Bouyer, P., Lautier, J.-M. & Landragin, A. (2014). Mobile and remote inertial sensing with atom interferometers. *Proceedings of the International School of Physics "Enrico Fermi"*, *188*, 493-555. doi: 10.3254/978-1-61499-448-0-493

Battelier, B., Barrett, B., Fouché, L., Chichet, L., Antoni-Micollier, L., Porte, H., Napolitano, F., Lautier, J., Landragin, A. & Bouyer, P. (2016). Development of compact cold-atom sensors for inertial navigation. In J. Stuhler & A. J. Shields (Eds.), *Proceedings of SPIE, Quantum Optics, 9900,* 990004. SPIE. doi: 10.1117/12.2228351

Beaufils, Q., Lefebve, J., Baptista, J. G., Piccon, R., Cambier, V., Sidorenkov, L. A., Fallet, C., Lévèque, T., Merlet, S. & Pereira Dos Santos, F. (2023). Rotation related systematic effects in a cold atom interferometer onboard a nadir pointing satellite. *npj Microgravity*, *9* (1). doi: 10.1038/s41526-023-00297-w

Becker, M., Bestmann, U., Schwithal, A. & Hecker, P. (2010). Observability of integrated navigation system states under varying dynamic conditions and aiding techniques. In *IEEE/ION Position, Location and Navigation Symposium* (pp. 632–638). IEEE. doi: 10.1109/plans.2010.5507185

Bencze, W., Eglington, M., Brumley, R. & Buchman, S. (2007). Precision electrostatic suspension system for the Gravity Probe B relativity mission's science gyroscopes. *Advances in Space Research*, *39* (2), 224–229. doi: 10.1016/j.asr.2006.09.020

Berg, P. (2014). *Ein rauscharmes Materiewellen-Gyroskop hoher Genauigkeit* (Doctoral dissertation, Gottfried Wilhelm Leibniz Universität Hannover, Fakultät für Mathematik und Physik). url: `https://www.repo.uni-hannover.de/bitstream/handle/123456789/8277/779792319.pdf` (visited 09.05.2024)

Berg, P., Abend, S., Tackmann, G., Schubert, C., Giese, E., Schleich, W. P., Narducci, F. A., Ertmer, W. & Rasel, E. M. (2015). Composite-light-pulse technique for high-precision atom interferometry. *Physical Review Letters*, *114* (6), 063002. doi: 10.1103/PhysRevLett.114.063002

Bertoldi, A., Minardi, F. & Prevedelli, M. (2019). Phase shift in atom interferometers: Corrections for nonquadratic potentials and finite-duration laser pulses. *Physical Review A*, *99* (3), 033619. doi: 10.1103/PhysRevA.99.033619

Bidel, Y., Zahzam, N., Blanchard, C., Bonnin, A., Cadoret, M., Bresson, A., Rouxel, D. & Lequentrec-Lalancette, M. F. (2018). Absolute marine gravimetry with matter-wave interferometry. *Nature Com-*

munications, *9* (627). doi: 10.1038/s41467-018-03040-2

Bidel, Y., Zahzam, N., Bresson, A., Blanchard, C., Cadoret, M., Olesen, A. V. & Forsberg, R. (2020). Absolute airborne gravimetry with a cold atom sensor. *Journal of Geodesy*, *94* (2). doi: 10.1007/s00190-020-01350-2

Biedermann, G. W., Wu, X., Deslauriers, L., Roy, S., Mahadeswaraswamy, C. & Kasevich, M. A. (2015). Testing gravity with cold-atom interferometers. *Physical Review A*, *91* (3), 033629. doi: 10.1103/physreva.91.033629

Bittanti, S., Laub, A. J. & Willems, J. C. (1991). *The Riccati equation.* Berlin, Heidelberg: Springer Berlin Heidelberg. doi: 10.1007/978-3-642-58223-3

Black, A. T., Kwolek, J., Fancher, C. & Bashkansky, M. (2020). Decoherence and dynamics in continuous 3D-cooled atom interferometry. In S. M. Shahriar & J. Scheuer (Eds.), *Optical, Opto-Atomic, and Entanglement-Enhanced Precision Metrology II*. SPIE. doi: 10.1117/12.2552540

Blankinship, K. G. (2008). A general theory for inertial navigator error modeling. In *2008 IEEE/ION Position, Location and Navigation Symposium* (pp. 1152–1166). IEEE. doi: 10.1109/plans.2008.4570002

BMBF. (2022). *Quantengravimetrie für den Einsatz in Flugzeugen.* url: `https://www.quantentechnologien.de/fileadmin/public/Redaktion/Dokumente/PDF/Projekte/230105_BMBF_QuanTech_Projektumrisse_AeroQGrav_C1.pdf` (visited 09.05.2024)

Bochkati, M., Schön, S., Schlippert, D., Schubert, C. & Rasel, E. (2017). Could cold atom interferometry sensors be the future inertial sensors? — First simulation results. In *2017 DGON Inertial Sensors and Systems (ISS)* (pp. 1–20). IEEE. doi: 10.1109/inertialsensors.2017.8171500

Bongs, K., Launay, R. & Kasevich, M. (2006). High-order inertial phase shifts for time-domain atom interferometers. *Applied Physics B*, *84* (4), 599–602. doi: 10.1007/s00340-006-2397-5

Bortz, J. (1971). A new mathematical formulation for strapdown inertial navigation. *IEEE Transactions on Aerospace and Electronic Systems*, *AES-7* (1), 61–66. doi: 10.1109/TAES.1971.310252

Britting, K. R. (1971). *Inertial navigation systems analysis.* New York: Wiley-Interscience.

Brown, R. G. & Hwang, P. Y. C. (2012). *Introduction to random signals and applied Kalman filtering: With MATLAB exercises* (4. ed.). Hoboken, NJ: Wiley.

Cadoret, M., Zahzam, N., Bidel, Y., Diboune, C., Bonnin, A., Théron, F. & Bresson, A. (2016). Phase shift formulation for n-light-pulse atom interferometers: application to inertial sensing. *Journal of the Optical Society of America B*, *33* (8), 1777. doi: 10.1364/josab.33.001777

Canuel, B., Leduc, F., Holleville, D., Gauguet, A., Fils, J., Virdis, A., Clairon, A., Dimarcq, N., Bordé, C. J., Landragin, A. & Bouyer, P. (2006). Six-axis inertial sensor using cold-atom interferometry. *Physical Review Letters*, *97* (1), 10402. doi: 10.1103/physrevlett.97.010402

Casimir, H. B. G. (1981). Die Bedeutung des Stern-Gerlach-Experimentes für die Entwicklung der Quantentheorie. *Physikalische Blätter*, *37* (3), 57–58. doi: 10.1002/phbl.19810370303

Cheinet, P., Canuel, B., Pereira Dos Santos, F., Gauguet, A., Yver-Leduc, F. & Landragin, A. (2008). Measurement of the sensitivity function in a time-domain atomic interferometer. *IEEE Transactions on Instrumentation and Measurement*, *57* (6), 1141–1148. doi: 10.1109/TIM.2007.915148

Cheiney, P., Fouché, L., Templier, S., Napolitano, F., Battelier, B., Bouyer, P. & Barrett, B. (2018). Navigation-compatible hybrid quantum accelerometer using a Kalman filter. *Physical Review Applied*, *10* (3), 034030. doi: 10.1103/physrevapplied.10.034030

Christophe, B., Boulanger, D., Foulon, B., Huynh, P.-A., Lebat, V., Liorzou, F. & Perrot, E. (2015). A new generation of ultra-sensitive electrostatic accelerometers for grace follow-on and towards the next generation gravity missions. *Acta Astronautica*, *117*, 1–7. doi: 10.1016/j.actaastro.2015.06.021

Cordova, A., Patterson, R. A., Rahn, J., Lam, L. K. & Rozelle, D. M. (1996). Progress in navigation-grade IFOG performance. In E. Udd, H. C. Lefevre & K. Hotate (Eds.), *Fiber Optic Gyros: 20th Anniversary Conference* (pp. 207–217). SPIE. doi: 10.1117/12.258181

Cronin, A. D., Schmiedmayer, J. & Pritchard, D. E. (2009). Optics and interferometry with atoms and molecules. *Reviews of Modern Physics*, *81* (3), 1051–1129. doi: 10.1103/revmodphys.81.1051

Delhaye, F. (2018). HRG by SAFRAN: The game-changing technology. In *2018 IEEE International Symposium on Inertial Sensors and Systems (INERTIAL)* (pp. 1–4). IEEE. doi: 10.1109/ISISS.2018.8358163

Dickerson, S. M., Hogan, J. M., Sugarbaker, A., Johnson, D. M. S. & Kasevich, M. A. (2013). Multiaxis inertial sensing with long-time point source atom interferometry. *Physical Review Letters*, *111* (8), 083001. doi: 10.1103/physrevlett.111.083001

Dubetsky, B. & Kasevich, M. A. (2006). Atom interferometer as a selective sensor of rotation or gravity. *Physical Review A*, *74* (2), 023615. doi: 10.1103/PhysRevA.74.023615

Durfee, D. S., Shaham, Y. K. & Kasevich, M. A. (2005). Long-term stability of an area-reversible atom-interferometer sagnac gyroscope. *Physical Review Letters*, *97* (24), 240801. doi: 10.1103/physrevlett.97.240801

Dutta, I., Savoie, D., Fang, B., Venon, B., Garrido Alzar, C. L., Geiger, R. & Landragin, A. (2016). Continuous cold-atom inertial sensor with 1 nrad/sec rotation stability. *Physical Review Letters*, *116* (18), 183003. doi: 10.1103/physrevlett.116.183003

El-Sheimy, N. & Youssef, A. (2020). Inertial sensors technologies for navigation applications: State of the art and future trends. *Satellite Navigation*, *1* (2). doi: 10.1186/s43020-019-0001-5

Fang, B., Dutta, I., Gillot, P., Savoie, D., Lautier, J., Cheng, B., Alzar, C. L. G., Geiger, R., Merlet, S., Santos, F. P. D. & Landragin, A. (2016). Metrology with atom interferometry: Inertial sensors from laboratory to field applications. *Journal of Physics: Conference Series*, *723*, 012049. doi: 10.1088/1742-6596/723/1/012049

Fang, B., Mielec, N., Savoie, D., Altorio, M., Landragin, A. & Geiger, R. (2018). Improving the phase response of an atom interferometer by means of temporal pulse shaping. *New Journal of Physics*, *20* (2), 023020. doi: 10.1088/1367-2630/aaa37c

Farrell, J. (2008). *Aided navigation: GPS with high rate sensors*. New York: McGraw-Hill.

Farrell, J., Silva, F. O., Rahman, F. & Wendel, J. (2022). Inertial measurement unit error modeling tutorial: Inertial navigation system state estimation with real-time sensor calibration. *IEEE Control Systems*, *42* (6), 40–66. doi: 10.1109/mcs.2022.3209059

Freier, C., Hauth, M., Schkolnik, V., Leykauf, B., Schilling, M., Wziontek, H., Scherneck, H.-G., Müller, J. & Peters, A. (2016). Mobile quantum gravity sensor with unprecedented stability. *Journal of Physics: Conference Series*, *723*, 012050. doi: 10.1088/1742-6596/723/1/012050

French, A. P., Taylor, E. F. & Brown, L. S. (1979). An introduction to quantum physics. *American Journal of Physics*, *47* (1), 121–122. doi: 10.1119/1.11656

Gauguet, A., Canuel, B., Lévèque, T., Chaibi, W. & Landragin, A. (2009). Characterization and limits of a cold-atom Sagnac interferometer. *Physical Review A*, *80* (6), 063604. doi: 10.1103/physreva.80.063604

Geiger, R., Landragin, A., Merlet, S. & Pereira Dos Santos, F. (2020). High-accuracy inertial measurements with cold-atom sensors. *AVS Quantum Science*, *2* (2). doi: 10.1116/5.0009093

Geiger, R., Ménoret, V., Stern, G., Zahzam, N., Cheinet, P., Battelier, B., Villing, A., Moron, F., Lours, M., Bidel, Y., Bresson, A., Landragin, A. & Bouyer, P. (2011). Detecting inertial effects with airborne matter-wave interferometry. *Nature Communications*, *2*, 474. doi: 10.1038/ncomms1479

Gelb, A. (2001). *Applied optimal estimation* (16. ed.). Cambridge, Mass.: MIT Press.

Gerberding, O., Guzmán Cervantes, F., Melcher, J., Pratt, J. R. & Taylor, J. M. (2015). Optomechanical reference accelerometer. *Metrologia*, *52* (5), 654–665. doi: 10.1088/0026-1394/52/5/654

Gersemann, M., Gebbe, M., Abend, S., Schubert, C. & Rasel, E. M. (2020). Differential interferometry using a Bose-Einstein condensate. *The European Physical Journal D*, *74* (10). doi: 10.1140/epjd/e2020-10417-8

Goodman, J. (2009). Apollo 13 guidance, navigation, and control challenges. In *AIAA SPACE 2009 Conference & Exposition*. Reston, Virigina: American Institute of Aeronautics and Astronautics. doi: 10.2514/6.2009-6455

Goshen-Meskin, D. & Bar-Itzhack, I. Y. (1990). Observability analysis of piece-wise constant systems with application to inertial navigation. In *29th IEEE Conference on Decision and Control* (p. 821-826 vol.2). IEEE. doi: 10.1109/cdc.1990.203702

Gouët, J. L., Mehlstäubler, T., Kim, J., Merlet, S., Clairon, A., Landragin, A. & Santos, F. P. D. (2008). Limits to the sensitivity of a low noise compact atomic gravimeter. *Applied Physics B*, *92* (2), 133–144. doi: 10.1007/s00340-008-3088-1

Groves, P. D. (2013). *Principles of GNSS, inertial, and multisensor integrated navigation systems* (2. ed.). Artech House.

Groves, P. D. (2015). Navigation using inertial sensors [Tutorial]. *IEEE Aerospace and Electronic Systems Magazine*, *30*, 42–69. doi: 10.1109/MAES.2014.130191

Gustavson, T. L., Bouyer, P. & Kasevich, M. A. (1997). Precision rotation measurements with an atom interferometer gyroscope. *Physical Review Letters*, *78* (11), 2046–2049. doi: 10.1103/physrevlett.78.2046

Gustavson, T. L., Landragin, A. & Kasevich, M. A. (2000). Rotation sensing with a dual atom-interferometer sagnac gyroscope. *Classical and Quantum Gravity*, *17* (12), 2385. doi: 10.1088/0264-9381/17/12/311

Han, C., Li, C., Zhao, Y. & Li, B. (2021). High-stability quartz resonant accelerometer with micro-leverages. *Journal of Microelectromechanical Systems*, *30* (2), 184–192. doi: 10.1109/JMEMS.2020.3036121

Heller, E. J. (1975). Time-dependent approach to semiclassical dynamics. *The Journal of Chemical Physics*, *62* (4), 1544–1555. doi: 10.1063/1.430620

Hofmann-Wellenhof, B., Lichtenegger, H. & Collins, J. (2001). *GPS: Theory and practice* (5., revised ed.). New York: Springer.

Honeywell. (2018). *HG9900 inertial measurement unit* (No. N61-1638-001-002). url: `https://aerospace.honeywell.com/content/dam/aerobt/en/documents/learn/products/sensors/brochures/N61-1638-000-000-hg9900inertialmeasurementunit-bro.pdf` (visited 07.11.2024)

Honeywell. (2020). *Q-Flex QA-3000 accelerometer* (No. N61-2546-000-000). url: `https://aerospace.honeywell.com/content/dam/aerobt/en/documents/learn/products/sensors/brochures/N61-2546-000-000_9521-QA-3000-bro.pdf` (visited 09.05.2024)

HosseiniArani, A., Tennstedt, B., Schilling, M., Knabe, A., Wu, H., Schön, S. & Müller, J. (2023). Kalman-filter based hybridization of classic and cold atom interferometry accelerometers for future satellite gravity missions. In J. T. Freymueller & L. Sánchez (Eds.), *Geodesy for a Sustainable Earth* (Vol. 154, pp. 221–231). Cham: Springer International Publishing. doi: 10.1007/1345_2022_172

IEEE. (2006). IEEE standard specification format guide and test procedure for single-axis laser gyros. *IEEE*

Std 647-2006 (Revision of IEEE Std 647-1995). doi: 10.1109/IEEESTD.2006.246241

IEEE. (2019). IEEE standard specification format guide and test procedure for linear single-axis, nongyroscopic accelerometers. *IEEE Std 1293-2018 (Revision of IEEE Std 1293-1998)*. doi: 10.1109/IEEESTD.2019.8653544

IEEE. (2021). IEEE standard for specifying and testing single-axis interferometric fiber optic gyros. *IEEE Std 952-2020 (Revision of IEEE Std 952-1997)*. doi: 10.1109/IEEESTD.2021.9353434

Igel, H., Schreiber, K. U., Gebauer, A., Bernauer, F., Egdorf, S., Simonelli, A., Lin, C.-J., Wassermann, J., Donner, S., Hadziioannou, C., Yuan, S., Brotzer, A., Kodet, J., Tanimoto, T., Hugentobler, U. & Wells, J.-P. R. (2021). ROMY: a multicomponent ring laser for geodesy and geophysics. *Geophysical Journal International*, *225* (1), 684–698. doi: 10.1093/gji/ggaa614

iMAR. (2017a). *iIMU-FSAS-NG-EI-SN-E FOG based IMU with trigger and integrated power regulation - special edition for NovAtel's SPAN applications only* - (No. DOC151009039). url: `https://www.imar-navigation.de/downloads/IMU_FSAS_NG_EI_SN.pdf` (visited 07.11.2024)

iMAR. (2017b). *iNAT-RQT-4002-4003 inertial INS/GNSS navigation system for advanced applications* (No. DOC130724827). url: `https://www.imar-navigation.de/downloads/NAT_RQT_4003_en.pdf` (visited 09.05.2024)

Itano, W. M., Bergquist, J. C., Bollinger, J. J., Gilligan, J. M., Heinzen, D. J., Moore, F. L., Raizen, M. G. & Wineland, D. J. (1993). Quantum projection noise: Population fluctuations in two-level systems. *Physical Review A, Atomic, Molecular, and Optical Physics*, *47* (5), 3554–3570. doi: 10.1103/physreva.47.3554

Itō, K. & McKean, H. P. (1996). *Diffusion processes and their sample paths*. Springer.

Jacobs, E. D. (1972). *Accelerometer* (No. US3702073A). U.S. Patent and Trade-mark Office.

Jekeli, C. (2001). *Inertial navigation systems with geodetic applications*. De Gruyter. doi: 10.1515/9783110800234

Jekeli, C. (2005). Navigation error analysis of atom interferometer inertial sensor. *Navigation*, *52* (1), 1–14. doi: 10.1002/j.2161-4296.2005.tb01726.x

Jerebets, S. A. (2007). Gyro evaluation for the mission to Jupiter. In *2007 IEEE Aerospace Conference* (pp. 1–9). IEEE. doi: 10.1109/aero.2007.352660

Karcher, R., Imanaliev, A., Merlet, S. & Santos, F. P. D. (2018). Improving the accuracy of atom interferometers with ultracold sources. *New Journal of Physics*, *20* (11), 113041. doi: 10.1088/1367-2630/aaf07d

Kasdin, N. J. (1995). Discrete simulation of colored noise and stochastic processes and $1/f^{\alpha}$ power law noise generation. *Proceedings of the IEEE*, *83* (5), 802–827. doi: 10.1109/5.381848

Kasevich, M. & Chu, S. (1991). Atomic interferometry using stimulated Raman transitions. *Physical Review Letters*, *67* (2), 181–184. doi: 10.1103/PhysRevLett.67.181

Kasevich, M. & Chu, S. (1992). Measurement of the gravitational acceleration of an atom with a light-pulse atom interferometer. *Applied Physics B*, *54*, 321-332. doi: 10.1007/BF00325375

Kasevich, M., Weiss, D. S., Riis, E., Moler, K., Kasapi, S. & Chu, S. (1991). Atomic velocity selection using stimulated Raman transitions. *Physical Review Letters*, *66* (18), 2297–2300. doi: 10.1103/physrevlett.66.2297

Kennard, E. H. (1927). Zur Quantenmechanik einfacher Bewegungstypen. *Zeitschrift für Physik*, *44* (4-5), 326–352. doi: 10.1007/BF01391200

Knabe, A., Schilling, M., Wu, H., HosseiniArani, A., Müller, J., Beaufils, Q. & Santos, F. P. d. (2022). The benefit of accelerometers based on cold atom interferometry for future satellite gravity missions. In *Geodesy for a Sustainable Earth* (pp. 213–220). Springer International Publishing. doi: 10.1007/1345_2022_151

Koch, K.-R. (1999). *Parameter estimation and hypothesis testing in linear models*. Berlin, Heidelberg: Springer. doi: 10.1007/978-3-662-03976-2

Korkishko, Y. N., Fedorov, V. A., Prilutskiy, V. E., Ponomarev, V. G., Fedorov, I. V., Kostritskii, S. M., Morev, I. V., Obuhovich, D. V., Prilutskiy, S. V., Zuev, A. I. & Varnakov, V. K. (2017). Highest bias stability fiber-optic gyroscope SRS-5000. In *2017 DGON Inertial Sensors and Systems (ISS)* (pp. 1–23). IEEE. doi: 10.1109/InertialSensors.2017.8171490

Krasnov, A. A. & Rozentsvein, V. G. (2022). Electrostatic accelerometers for space applications: Modern state and prospects of development. *Gyroscopy and Navigation*, *13* (2), 59–81. doi: 10.1134/s2075108722020043

Lam, Q., Stamatakos, N., Woodruff, C. & Ashton, S. (2003). Gyro modeling and estimation of its random noise sources. In *AIAA Guidance, Navigation, and Control Conference and Exhibit.* Reston, Virigina: American Institute of Aeronautics and Astronautics. doi: 10.2514/6.2003-5562

Lan, S.-Y., Kuan, P.-C., Estey, B., Haslinger, P. & Müller, H. (2012). Influence of the Coriolis force in atom interferometry. *Physical Review Letters*, *108* (9), 090402. doi: 10.1103/PhysRevLett.108.090402

Landau, L. D. & Lifšic, E. M. (2011). *Mechanics* (3., reprinted ed., Vol. 1). Elsevier Butterworth-Heinemann.

Lautier, J., Volodimer, L., Hardin, T., Merlet, S., Lours, M., Pereira Dos Santos, F. & Landragin, A. (2014). Hybridizing matter-wave and classical accelerometers. *Applied Physics Letters*, *105* (14), 144102. doi: 10.1063/1.4897358

Lawrence, A. (2001). *Modern inertial technology: Navigation, guidance, and control* (2. ed.). Springer.

Lefevre, H., Steib, A., Claire, A., Sekeriyan, A., Couderette, A., Pointel, A.-L., Viltard, A., Bonnet, A.,

Frénois, A., Gandoin, A., Laurent, A., Luton, A., Galbès, A., Escarnot, A., Cadier, B., Kerouanton, B., Lhermitte, B., Bonnafé, B., Stuber, C., Ortiz, C., Moluçon, C., Allano, C., Dunette, C., Ollivier, C., Guyot, C., Vercambre, C., Ponceau, D., Ramecourt, D., de Toldi, E., Peter, E., Ducloux, E., Vassilakis, E., Colliou, F., Napolitano, F., Lauvinerie, F., Guattari, F., Fauquert, G., Mélin, G., Hardy, G., Lecamp, G., Porte, H., Jaheny, H., Boiron, H., Bonnefois, J.-J., Michel, J.-P., Périot, J.-P., Pillon, J., Hauden, J., Honthaas, J., Aubry, K., Gauthier, K., Lablonde, L., Ly, L., Lhomme, L., Poulain, L., Girault, M., Mancini, M., Goudron, M., Duplaquet, M.-L., Bernasconi, M., Collignon, M., Dacheux, M., Rattier, M., Marta, M., Faussot, N., Grossard, N., Pirrone, N., Jolly, O., Rabine, O., Guitton, P., Mollier, P., Simonpiétri, P., Buisson, P., Cheiney, P., Chakma, P., Taibi, R., Blondeau, R., Shariati, S., Boisgontier, S., Ferrand, S., Keller, S., Huet, S., Chouvin, S., Meyer, S., Puille, S., Ustaze, S., Bénard, S., Clémenceau, S., Laudat, T., Guettler-Sergeant, T., Dos Santos, T., Peou-Sanson, T., Robin, T., Buret, T., Loret, T., Villedieu, T., Ferreira, V., Pham, V. D., Rumoroso, V., Paturel, Y. & Arditty, H. (2020). The fiber optic gyro 'adventure' at Photonetics, iXsea and now iXblue. In G. A. Sanders, R. A. Lieberman & I. U. Scheel (Eds.), *Optical Waveguide and Laser Sensors* (pp. 10–29). SPIE. doi: 10.1117/12.2560791

Lohmeier, D. (Ed.). (1992). *Einstein, Anschütz und der Kieler Kreiselkompaß: Der Briefwechsel zwischen Albert Einstein und Hermann Anschütz-Kaempfe und andere Dokumente* (Vol. 16). Heide in Holstein: Westholstein. Verl.-Anst. Boyens.

Lunze, J. (2008). *Regelungstechnik 2: Mehrgrößensysteme, Digitale Regelung* (5. ed.). Berlin, Heidelberg: Springer Berlin Heidelberg. doi: 10.1007/978-3-540-78463-0

Macek, W. M. & Davis, D. T. M. (1963). Rotation rate sensing with traveling-wave ring lasers. *Applied Physics Letters*, *2* (3), 67–68. doi: 10.1063/1.1753778

Magnus, K. (1971). *Kreisel: Theorie und Anwendungen*. Springer Berlin Heidelberg. doi: 10.1007/978-3-642-52162-1

Matthews, A. & Rybak, F. (1992). Comparison of hemispherical resonator gyro and optical gyros. *IEEE Aerospace and Electronic Systems Magazine*, *7* (5), 40–46. doi: 10.1109/62.257091

Maybeck, P. S. (1979). *Stochastic models, estimation, and control* (Vol. 1). New York: Acad. Press.

Mead, D. T. & Mosor, S. (2020). Progress with interferometric fiber optic gyro at Honeywell. In R. A. Lieberman, G. A. Sanders & I. U. Scheel (Eds.), *Optical waveguide and laser sensors* (Vol. 11405, pp. 7 – 22). SPIE. doi: 10.1117/12.2561135

Merlet, S., Le Gouët, J., Bodart, Q., Clairon, A., Landragin, A., Pereira Dos Santos, F. & Rouchon, P. (2009). Operating an atom interferometer beyond its linear range. *Metrologia*, *46* (1), 87–94. doi: 10.1088/0026-1394/46/1/011

Moler, K., Weiss, D. S., Kasevich, M. & Chu, S. (1992). Theoretical analysis of velocity-selective Raman transitions. *Physical Review A, Atomic, Molecular, and Optical Physics*, *45*, 342–348. doi: 10.1103/physreva.45.342

Muquans. (2019). *Absolute quantum gravimeter.* url: https://www.muquans.com/wp-content/uploads/2019/03/muquans_aqg.pdf (visited 09.05.2024)

Mustafazade, A., Pandit, M., Zhao, C., Sobreviela, G., Du, Z., Steinmann, P., Zou, X., Howe, R. T. & Seshia, A. A. (2020). A vibrating beam MEMS accelerometer for gravity and seismic measurements. *Scientific Reports*, *10* (1). doi: 10.1038/s41598-020-67046-x

Nanometrics inc. (2023). *Titan accelerometer* (No. 1002.15.10). url: https://nanometrics.ca/hubfs/Downloads/DataSheets/titan.pdf?hsLang=en-ca (visited 09.05.2024)

Narducci, F. A., Black, A. T. & Burke, J. H. (2022). Advances toward fieldable atom interferometers. *Advances in Physics: X*, *7* (1). doi: 10.1080/23746149.2021.1946426

Niebauer, T. M., Sasagawa, G. S., Faller, J. E., Hilt, R. & Klopping, F. (1995). A new generation of absolute gravimeters. *Metrologia*, *32* (3), 159-180. doi: 10.1088/0026-1394/32/3/004

Niemeier, W. (2008). *Ausgleichungsrechnung: Statistische Auswertemethoden* (2. ed.). Berlin: De Gruyter.

Papula, L. (2007). *Mathematik für Ingenieure und Naturwissenschaftler: Ein Lehr- und Arbeitsbuch für das Grundstudium; mit zahlreichen Beispielen aus Naturwissenschaft und Technik* (11. ed., Vol. 1). Wiesbaden: Vieweg.

Paturel, Y., Honthaas, J., Lefèvre, H. & Napolitano, F. (2014). One nautical mile per month FOG-based strapdown inertial navigation system: A dream already within reach? *Gyroscopy and Navigation*, *5* (1), 1–8. doi: 10.1134/s207510871401009x

Peters, A., Chung, K. Y. & Chu, S. (2001). High-precision gravity measurements using atom interferometry. *Metrologia*, *38* (1), 25–61. doi: 10.1088/0026-1394/38/1/4

Plaszczynski, S. (2007). Generating long streams of $1/f^{\alpha}$ noise. *Fluctuation and Noise Letters*, *7* (1), 1–13. doi: 10.1142/s0219477507003635

Post, E. J. (1967). Sagnac effect. *Reviews of Modern Physics*, *39*, 475–493. url: https://link.aps.org/doi/10.1103/RevModPhys.39.475 doi: 10.1103/RevModPhys.39.475

Raab, E. L., Prentiss, M., Cable, A., Chu, S. & Pritchard, D. E. (1987). Trapping of neutral sodium atoms with radiation pressure. *Physical Review Letters*, *59* (23), 2631-2634. doi: 10.1103/physrevlett.59.2631

Rakholia, A. V., McGuinness, H. J. & Biedermann, G. W. (2014). Dual-axis high-data-rate atom interferometer via cold ensemble exchange. *Physical Review Applied*, *2* (5), 054012. doi: 10.1103/physrevapplied.2.054012

Richardson, L. L., Rajagopalan, A., Albers, H., Meiners, C., Nath, D., Schubert, C., Tell, D., Wodey, É., Abend, S., Gersemann, M., Ertmer, W., Rasel, E. M., Schlippert, D., Mehmet, M., Kumanchik, L., Colmenero, L., Spannagel, R., Braxmaier, C. & Guzmán, F. (2020). Optomechanical resonator-enhanced atom interferometry. *Communications Physics*, *3* (1). doi: 10.1038/s42005-020-00473-4

Riehle, F., Kisters, T., Witte, A., Helmcke, J. & Bordé, C. J. (1991). Optical Ramsey spectroscopy in a rotating frame: Sagnac effect in a matter-wave interferometer. *Physical Review Letters*, *67* (2), 177–180. doi: 10.1103/physrevlett.67.177

Riley, W. J. (2008). *Handbook of frequency stability analysis* (No. SP 1065). Gaithersburg, MD: National Institute of Standards and Technology. doi: 10.6028/nist.sp.1065

Roura, A., Zeller, W. & Schleich, W. P. (2014). Overcoming loss of contrast in atom interferometry due to gravity gradients. *New Journal of Physics*, *16* (12), 123012. doi: 10.1088/1367-2630/16/12/123012

Roussel, C., Verdun, J., Cali, J., Maia, M. & d'EU, J. F. (2015). Integration of a strapdown gravimeter system in an autonomous underwater vehicle. *The International Archives of the Photogrammetry, Remote Sensing and Spatial Information Sciences*, *XL-5/W5*, 199–206. doi: 10.5194/isprsarchives-XL-5-W5-199-2015

Rozelle, D. M. (2009). The hemispherical resonator gyro: From wineglass to the planets. In *Proc. 19th AAS/AIAA Space Flight Mechanics Meeting* (Vol. 134, pp. 1157–1178).

Rudolf, F., Gonseth, S., Brisson, R. & Krebs, P. (2014). New generation of high performance/high reliability MEMS accelerometers for harsh environment. In *2014 IEEE/ION Position, Location and Navigation Symposium (PLANS)* (pp. 7–11). IEEE. doi: 10.1109/PLANS.2014.6851350

Sakurai, J. J. (2011). *Modern quantum mechanics* (2. ed.). Boston: Addison-Wesley.

Santarelli, G., Audoin, C., Makdissi, A., Laurent, P., Dick, G. J. & Clairon, A. (1998). Frequency stability degradation of an oscillator slaved to a periodically interrogated atomic resonator. *IEEE Transactions on Ultrasonics, Ferroelectrics, and Frequency Control*, *45*, 887–894. doi: 10.1109/58.710548

Santarelli, G., Laurent, P., Lemonde, P., Clairon, A., Mann, A. G., Chang, S., Luiten, A. N. & Salomon, C. (1999). Quantum projection noise in an atomic fountain: A high stability cesium frequency standard. *Physical Review Letters*, *82* (23), 4619-4622. doi: 10.1103/physrevlett.82.4619

Savage, P. G. (1998a). Strapdown inertial navigation integration algorithm design part 1: Attitude algorithms. *Journal of Guidance, Control, and Dynamics*, *21* (1), 19–28. doi: 10.2514/2.4228

Savage, P. G. (1998b). Strapdown inertial navigation integration algorithm design part 2: Velocity and position algorithms. *Journal of Guidance, Control, and Dynamics*, *21* (2), 208–221. doi: 10.2514/2.4242

Savage, P. G. (2000). *Strapdown analytics* (Vol. 1). Maple Plain, Minn.: Strapdown Associates.

Savoie, D., Altorio, M., Fang, B., Sidorenkov, L. A., Geiger, R. & Landragin, A. (2018). Interleaved atom interferometry for high-sensitivity inertial measurements. *Science Advances*, *4* (12), eaau7948. doi: 10.1126/sciadv.aau7948

Saywell, J., Carey, M., Belal, M., Kuprov, I. & Freegarde, T. (2020). Optimal control of raman pulse sequences for atom interferometry. *Journal of Physics B: Atomic, Molecular and Optical Physics*, *53* (8), 085006. doi: 10.1088/1361-6455/ab6df6

SBG-Systems. (2022). *Apogee Surface series ultimate accuracy MEMS inertial sensors user manual* (No. APOGEEHM.1.7). url: `https://support.sbg-systems.com/sc/hp/files/latest/102924765/102924758/3/1721636024593/Apogee+2+-+Hardware+Manual+v1.7.pdf` (visited 07.11.2024)

Schweppe, F. C. (1973). *Uncertain dynamic systems*. Englewood Cliffs, NJ: Prentice-Hall.

Serrano, D. E., Jeong, Y., Keesara, V., Sung, W. K. & Ayazi, F. (2014). Single proof-mass tri-axial pendulum accelerometers operating in vacuum. In *2014 IEEE 27th International Conference on Micro Electro Mechanical Systems (MEMS)* (p. 28-31). doi: 10.1109/MEMSYS.2014.6765565

Simon, D. (2006). *Optimal state estimation: Kalman, H-∞, and nonlinear approaches*. Hoboken, NJ: Wiley-Interscience.

Snadden, M., McGuirk, J., Bouyer, P., Haritos, K. & Kasevich, M. (1998). Measurement of the Earth's gravity gradient with an atom interferometer-based gravity gradiometer. *Physical Review Letters*, *81* (5), 971–974. doi: 10.1103/physrevlett.81.971

Storey, P. & Cohen-Tannoudji, C. (1994). The Feynman path integral approach to atomic interferometry. A tutorial. *Journal de Physique II*, *4* (11), 1999–2027. doi: 10.1051/jp2:1994103

Svitlov, S. (2012). Frequency-domain analysis of absolute gravimeters. *Metrologia*, *49* (6), 706–726. doi: 10.1088/0026-1394/49/6/706

Tackmann, G., Berg, P., Schubert, C., Abend, S., Gilowski, M., Ertmer, W. & Rasel, E. M. (2012). Self-alignment of a compact large-area atomic sagnac interferometer. *New Journal of Physics*, *14* (1), 015002. doi: 10.1088/1367-2630/14/1/015002

Tazartes, D. (2014). An historical perspective on inertial navigation systems. In *2014 International Symposium on Inertial Sensors and Systems (ISISS)* (pp. 1–5). IEEE. doi: 10.1109/isiss.2014.6782505

Templier, S., Cheiney, P., d'Armagnac de Castanet, Q., Gouraud, B., Porte, H., Napolitano, F., Bouyer, P., Battelier, B. & Barrett, B. (2022). Tracking the vector acceleration with a hybrid quantum accelerometer triad. *Science Advances*, *8* (45), eadd3854. doi: 10.1126/sciadv.add3854

Tennstedt, B., Rajagopalan, A., Weddig, N. B., Abend, S., Schön, S. & Rasel, E. M. (2023). Atom strapdown: Toward integrated quantum inertial navigation systems. *Navigation*, *70* (4), navi.604. doi: 10.33012/

navi.604

Tennstedt, B. & Schön, S. (2020). Dedicated calculation strategy for atom interferometry sensors in inertial navigation. In *2020 IEEE/ION Position, Location and Navigation Symposium (PLANS)* (pp. 755–764). IEEE. doi: 10.1109/PLANS46316.2020.9110142

Tennstedt, B. & Schön, S. (2021a). *Entwicklung und Test einer für Quantensensoren adäquaten Berechnungsstrategie für die Inertialnavigation : Schlussbericht zum Vorhaben 50NA1805.* Leibniz Universität Hannover. doi: 10.2314/KXP:1780396740

Tennstedt, B. & Schön, S. (2021b). Integration of atom interferometers and inertial measurement units to improve navigation performance. In *2021 28th Saint Petersburg International Conference on Integrated Navigation Systems (ICINS)* (pp. 1–9). IEEE. doi: 10.23919/ICINS43216.2021.9470809

Tennstedt, B. & Schön, S. (2023). *Verfahren und Vorrichtung zur inertialen sensorischen Messung sowie Computerprogramm* (No. DE 10 2022 109 438.3). Deutsches Patent- und Markenamt. url: `https://register.dpma.de/DPMAregister/pat/register?AKZ=1020221094383` (visited 09.05.2024)

Tennstedt, B., Weddig, N. & Schön, S. (2021). Improved inertial navigation with cold atom interferometry. *Gyroscopy and Navigation*, *12* (4), 294-307. doi: 10.1134/S207510872104009X

Thong, Y., Woolfson, M., Crowe, J., Hayes-Gill, B. & Jones, D. (2004). Numerical double integration of acceleration measurements in noise. *Measurement*, *36* (1), 73–92. doi: 10.1016/j.measurement.2004.04.005

Titterton, D. H. & Weston, J. L. (2009). *Strapdown inertial navigation technology* (2. ed., Vol. 17). Stevenage: The Inst. of Engineering and Technology.

Vali, V. & Shorthill, R. W. (1976). Fiber ring interferometer. *Applied Optics*, *15* (5), 1099–1100. doi: 10.1364/ao.15.001099

VectorAtomic. (2023). *Vector Atomic validates quantum navigation sensor at sea.* url: `https://www.businesswire.com/news/home/20230327005642/en/Vector-Atomic-Validates-Quantum-Navigation-Sensor-at-Sea` (visited 09.05.2024)

Vermeulen, P., Lemoignc, N., Mcnoret, V., Busquet, C., Dcsruellc, B., Laurier-Gaud, J., Merlet, S., Landragin, A., Cook, A. K. & Bonvalot, S. (2018). Evaluating the performances of an operational absolute quantum gravimeter. In *2018 Conference on Precision Electromagnetic Measurements (CPEM 2018)* (pp. 1–2). IEEE. doi: 10.1109/CPEM.2018.8501047

Wagner, J. F. (2003). *Zur Verallgemeinerung integrierter Navigationssysteme auf räumlich verteilte Sensoren und flexible Fahrzeugstrukturen: Zugl.: Hamburg-Harburg, Techn. Univ., Arbeitsbereich Mechanik und Meerestechnik, Habil.-Schr., 2003* (Vol. 1008). Düsseldorf: VDI-Verlag.

Wang, X., Kealy, A., Gilliam, C., Haine, S., Close, J., Moran, B., Talbot, K., Williams, S., Hardman, K., Freier, C., Wigley, P., White, A., Szigeti, S. & Legge, S. (2023). Improving measurement performance via fusion of classical and quantum accelerometers. *Journal of Navigation*, *76* (1), 91-102. doi: 10.1017/s0373463322000637

Weber, H. & Ulrich, H. (2017). *Laplace-, Fourier- und z-Transformation: Grundlagen und Anwendungen* (10. ed.). Wiesbaden and Heidelberg: Springer Vieweg.

Weddig, N. B., Tennstedt, B. & Schön, S. (2022). Challenges for a hybrid CAI-based INS due to trajectory dynamics derived from real inertial datasets. In *2022 DGON Inertial Sensors and Systems (ISS)* (pp. 1–20). IEEE. doi: 10.1109/ISS55898.2022.9926311

Wolfram Alpha LLC. (2024). *Wolfram|Alpha.* url: `https://www.wolframalpha.com/input?i=1%2F(-1%2F2+%2B++sqrt(1%2F4++%2B++x))` (visited 01.05.2024)

Wright, M. J., Anastassiou, L., Mishra, C., Davies, J. M., Phillips, A. M., Maskell, S. & Ralph, J. F. (2022). Cold atom inertial sensors for navigation applications. *Frontiers in Physics*, *10*, 994459. doi: 10.3389/fphy.2022.994459

Wu, L., Wang, H., Chai, H., Zhang, L., Hsu, H. & Wang, Y. (2017). Performance evaluation and analysis for gravity matching aided navigation. *Sensors*, *17* (4), 769. doi: 10.3390/s17040769

Wu, X., Zi, F., Dudley, J., Bilotta, R. J., Canoza, P. & Müller, H. (2017). Multiaxis atom interferometry with a single-diode laser and a pyramidal magneto-optical trap. *Optica*, *4* (12), 1545. doi: 10.1364/optica.4.001545

Yoder, C. F., Williams, J. G. & Parke, M. E. (1981). Tidal variations of Earth rotation. *Journal of Geophysical Research: Solid Earth*, *86* (B2), 881–891. doi: 10.1029/jb086ib02p00881

Zahzam, N., Christophe, B., Lebat, V., Hardy, E., Huynh, P.-A., Marquet, N., Blanchard, C., Bidel, Y., Bresson, A., Abrykosov, P., Gruber, T., Pail, R., Daras, I. & Carraz, O. (2022). Hybrid electrostatic–atomic accelerometer for future space gravity missions. *Remote Sensing*, *14* (14), 3273. doi: 10.3390/rs14143273

Zetie, K. P., Adams, S. F. & Tocknell, R. M. (2000). How does a Mach-Zehnder interferometer work? *Physics Education*, *35* (1), 46-48. doi: 10.1088/0031-9120/35/1/308

Zhang, L., Gao, W., Li, Q., Li, R., Yao, Z. & Lu, S. (2019). A novel monitoring navigation method for cold atom interference gyroscope. *Sensors*, *19* (2), 222. doi: 10.3390/s19020222

List of Figures

List of Tables

Acknowledgement

My work in the field of atom interferometry started in the QuSI (50NA1805) project (Tennstedt & Schön, 2021a) with the goal to examine how a CAI would function as inertial sensor, and what steps needed to be done to compute a conventional strapdown navigation solution. It was clear very early, that conventional strapdown methodology was not applicable to a low datarate sensor which on top also has a dynamic range which fails to even resolve slow and steady maneuvers. Thus, the motivation to integrate CAI with high rate sensors to a combined QINS was established.

The first working version of the hybrid navigation algorithm was presented in Tennstedt and Schön (2020). At this time, the CAI was used to correct the errors of the IMU directly and, partially due to the lack of proper modelling of the CAI, systematic errors in case of changing dynamics were present that were not quite understood at that time. Based on that work, in the Master thesis of Nicolai the design was adapted for a 3-dimensional simulation which spearheaded the further work on including a more comprehensive IMU error model. In parallel, I was working on including the Bordé midpoint line model in the equations which largely improved the capabilities of the CAI model in the light of changing dynamics. This resulted in Tennstedt and Schön (2021b), including a more detailed analytical observability study of the IMU errors. The structure of the algorithms, even though already quite similar to the form presented here, was still sketchy and a lot of important things, like the correct description of the coordinate systems, were rather ill-defined. Furthermore, the CAI was assumed to be a perfect sensor, so the paper was more of a proof-of-concept for the stability of the hybrid navigation solution.

A bit later that year I was able to analyze some raw data of an actual atomic interferometer, thanks to Ashwin who helped in understanding and preparing the data. This resulted in the updated navigation filter, including a proper uncertainty model for the CAI as presented in Tennstedt et al. (2021). After that, it was time to develop a proper mathematical framework of the filter, including the phase prediction step. This resulted in the Atom Strapdown (Tennstedt et al., 2023), which was the gateway to a proper mathematical description of the navigation filter. From that point on, it was possible to derive physically meaningful results from the simulations.

This thesis now ties together all lose knots and unifies the description of the hybrid navigation algorithm to a QINS, while going one step further and draw the correct conclusions for real life applications of such a system. This research was financially enabled by the QGyro (50RK1957) and QGyro+ (50NA2106) projects. Here, I would like to thank the QGyro team for the fruitful discussions. Additional thanks to Sven for the review of chapter 3, Thomas for the detailed feedback on chapter 5, Nicolai and Alireza for the remarks on chapters 2 and 4, respectively, and Tobi for the LaTeXblueprint. Special thanks go to my supervisor Steffen Schön for the discussions and feedback, and quite generally for providing me the opportunity to work in this exciting field, as well as my co-reviewers for their patience in having to read through this perhaps not always easily accessible work. Last but certainly not least, Karin for her patience and her valuable final proof read which gave me the confidence to finish this off.